

Fall 2016

A Precision Measurement of the Weak Charge of Proton at Low Q^2 : Kinematics and Tracking

Siyuan Yang

College of William and Mary, sxyang@email.wm.edu

Follow this and additional works at: <https://scholarworks.wm.edu/etd>



Part of the [Physics Commons](#)

Recommended Citation

Yang, Siyuan, "A Precision Measurement of the Weak Charge of Proton at Low Q^2 : Kinematics and Tracking" (2016). *Dissertations, Theses, and Masters Projects*. Paper 1477068332.

<http://doi.org/10.21220/S2B88Z>

This Dissertation is brought to you for free and open access by the Theses, Dissertations, & Master Projects at W&M ScholarWorks. It has been accepted for inclusion in Dissertations, Theses, and Masters Projects by an authorized administrator of W&M ScholarWorks. For more information, please contact scholarworks@wm.edu.

A Precision Measurement of the Weak Charge of the
Proton at Low Q^2 : Kinematics and Tracking

Siyuan Yang
Chongqing, China

A Dissertation presented to the Graduate Faculty
of the College of William and Mary in Candidacy for the Degree of
Doctor of Philosophy

Department of Physics

The College of William and Mary
August, 2016

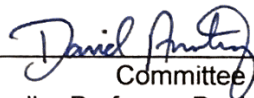
APPROVAL PAGE

This Dissertation is submitted in partial fulfillment of
the requirements for the degree of

Doctor of Philosophy

Siyuan Yang

Approved by the Committee, May, 2016

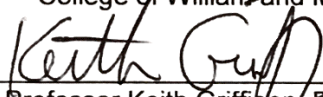


Committee Chair

Chancellor Professor David Armstrong, Physics
College of William and Mary




Assistant Professor Wouter Deconinck, Physics
College of William and Mary



Professor Keith Griffioen, Physics
College of William and Mary



Professor Marc Sher, Physics
College of William and Mary



Professor Mark Pitt, Physics
Virginia Polytechnic Institute and State University

ABSTRACT

The Standard Model of particle physics represents our present best understanding of the elementary particles and three of the four fundamental forces. One of the most important and challenging tasks of modern particle physics is to test and to find the evidence for new physics not contained in the Standard Model. One such test, the Qweak experiment, was conducted at JLab in Newport News, VA, from 2010 to 2012. The goal of the experiment is to measure the value of the weak charge of proton, Q_{weak} to a 4% precision, which, if it confirms the Standard Model prediction, will provide tighter constraints on new physics; or, if it is in disagreement with that prediction, will provide evidence for new physics. In this experiment, an 85% polarized electron beam with $150 \mu A$ current is used on a 35 cm thick hydrogen target to make elastic electron-proton scattering happen at a four-momentum transfer $Q^2 = 0.03 \text{ GeV}/c^2$. To determine the weak charge, we must also precisely determine the kinematics of the scattering process, namely, the Q^2 . In order to reach this goal, the hardware, a particle tracking system and special analysis software, the Qweak Tracking Reconstruction software, are both needed. In this dissertation, a full description of the tracking software and the preliminary analysis of the Q^2 and the first subset of production data will be given. The proton's weak charge Q_{weak}^p was measured to be 0.064 ± 0.012 , which is consistent with the prediction of the Standard Model.

TABLE OF CONTENTS

Acknowledgements	vi
Dedications	vii
List of Tables	viii
List of Figures	x
CHAPTER	
1 Theory	1
1.1 Standard Model of Particle Physics	1
1.2 The Theory of Electroweak Unification	4
1.3 Electromagnetic Interaction	7
1.4 Neutral Current Weak Interaction	9
1.5 The Parity-Violating Asymmetry in the Qweak Experiment	11
1.6 Hadronic Form Factor $B(Q^2)$	14
1.7 Radiative Corrections and Higher order effects	15
1.8 Running of the Weak Mixing Angle $\sin^2\theta_W$	17
1.9 Beyond the Standard Model	20
1.10 Other Related Experiments	23

1.10.1	Measurement of $\sin^2 \theta_W$ at LEP and SLC	24
1.10.2	NuTeV Experiment	26
1.10.3	Moller Scattering Experiment	28
1.10.4	Atomic Parity Violation	29
1.11	Models of Possible New Physics	31
2	Qweak Experiment Equipment	34
2.1	Experimental Overview	34
2.2	Experimental Timeline	39
2.3	CEBAF Accelerator	40
2.4	Liquid Hydrogen Target System	44
2.5	QTOR Magnet	48
2.6	Collimators	50
2.7	Detector System	54
2.7.1	Main Detectors	54
2.7.2	Tracking Detectors	58
2.7.3	Trigger Scintillators (TS)	64
2.7.4	The Focal Plane Scanners	65
2.8	The Data Acquisition Systems	67
2.9	Beam Instrumentation	70
2.9.1	Beam Current Monitors	70
2.9.2	Beam Position Monitors	73
2.9.3	Luminosity Monitors	75

2.9.4	Halo Monitors	77
2.10	Precision Beam Polarimetry	79
2.10.1	Hall C Møller Polarimeter	79
2.10.2	Hall C Compton Polarimeter	81
3	Qweak Tracking Software	85
3.1	Overview of Qweak Track Reconstruction software	85
3.2	Overview of QTR Workflow	86
3.3	Coordinate Systems	88
3.4	Calibration Methods	90
3.4.1	F1TDC Reference Time Correction	91
3.4.2	t_0 correction	93
3.4.3	Time to Distance Conversion	95
3.5	Pattern Recognition Algorithm	99
3.6	Detector Tracking	103
3.6.1	HDCs	104
3.6.2	VDCs	108
3.7	Three-Dimensional (3D) Least Square Fitting Algorithm	111
3.8	Momentum Determination	117
3.9	Geometry File	120
4	Tracking Data Analysis and Kinematics	133
4.1	Overview	133

4.2	Q^2 results	135
4.2.1	Geometry of Tracking System and Projection	136
4.2.2	Cuts	144
4.3	Systematic Uncertainties	149
4.3.1	Beam Properties	150
4.3.2	Beam energy measurement	160
4.3.3	Energy loss in the target	161
4.3.4	Octant Variance	162
4.3.5	Stability	163
4.4	Light-weighting effect on Q^2	165
4.5	The Summary of Error Sources for Q^2	166
4.6	Path Forward to 0.5% precision	167
5	Parity Data Analysis	168
5.1	Overview of the Data	168
5.2	Data Processing Scheme for Parity Data	170
5.3	Data Quality	170
5.4	The Measurement of the Raw Asymmetry A_{raw}	173
5.5	Polarization	174
5.6	Corrections for Helicity-related Beam Properties	175
5.7	Corrections for Backgrounds	183
5.7.1	Aluminum Target Window and Dilution	184
5.7.2	Inelastic Backgrounds	186

5.7.3	Soft Backgrounds	188
5.8	Transverse Asymmetry	190
5.9	Physics Asymmetry	192
6	Result and Outlook	196
6.1	The 25% measurement of Q_W^p	196
6.2	More recent results and path to the 4% result	197
APPENDIX A		
	Details of Parameter Files and Running Options in QTR	200
A.1	Parameter Files	200
A.2	Running Options	201
APPENDIX B		
	Details of Geometry File in QTR	203
APPENDIX C		
	Hall C beamline apparatus layout	209
APPENDIX D		
	Projections of Reconstructed Tracks for all Ocants	211
APPENDIX E		
	Personal Contributions to Qweak	216
BIBLIOGRAPHY		217

ACKNOWLEDGMENTS

I would like to start thanking my advisor, Professor David Armstrong for his seven years' mentoring in my career as a graduate student. His enthusiasm for the research area for over 20 years always inspires me to be a person, like him, who loves your work and always keep curiosity. His broad understanding of physics along with his lively personality makes him a perfect guidance and I am therefore benefited from countless insightful discussions he provided about research. I am also very grateful to Professor Wouter Deconick, who helped me to fix errors in the tracking software I was mainly focused on. Also I want to thank Professor Mark Pitt, who provided numerous suggestions and ideas to help me to improve the result from the tracking software. I would like to thank the members of PhD committee, Professor Mark Pitt, Wouter Deconinck, Marc Sher and Keith Griffioen, for their time to review my thesis and valuable suggestions.

I want to thank Qweak collaboration, who has been doing an excellent job, especially considering this is an big and complicated experiment. Without the contribution from each group member, I won't get any result in this dissertation. People I want to thank includes, but not limited to, Dave Mack, Greg Smith, Roger Carlini, Brad Sawatzky, Dave Gaskell.

I am also grateful to graduate and undergraduate students and postdocs whom I worked with since the beginning of this experiment and the people who put a lot of effort on the data analysis. They are John Leckey, Josh Hoskins, Josh Magee, Juan Carlos Cornejo, Jim Dowd, Katherine Myers, John Leacock, Scott Macewan, Don Jones, Rakitha Beminiwattha, Buddhini Waidyawansa, Jeong Han Lee, Rob Marhurin and Jean-Francois Rajotte.

I'll also thank my wife, Ji Liu, for her love and urging me on to finish this dissertation. At last, I want to thanks for my parents, who always stand behind to support me through my life.

To My Parents

List of Tables

2.1	Overview of the Qweak data set	39
3.1	Classes used in the Pattern Recognition Algorithm	104
3.2	Some methods used in Pattern Recognition Algorithm	105
3.3	List of available filters in <i>QwBridgingTrackFilter.Filter</i> function	117
4.1	The overview of the tracking data set	134
4.2	Summary of projection result to a thin Al target from run 13722	140
4.3	Fitted Z location for 1,3,5 optics target from run 15112.	140
4.4	Summary of measured Z vertex distribution	142
4.5	The summary of slopes for beam position study.	155
4.6	Results from beam energy measurements	161
4.7	Contributions to the uncertainty in $\langle Q^2 \rangle$	167
5.1	the criterion of the data quality	172
5.2	Helicity-correlated differences in the 25% measurement averaged out on the slug basis for two different IHWP states.	177
5.3	Variables used in std, 5+1, set3, set5, set6 and set7 regression schemes.	180

5.4	Total corrections of 5+1 and set3 to raw asymmetry, in ppb, for two correction schemes. All the total corrections shown in the next few tables are handled in the same way.	181
5.5	Total corrections of set5 and set7 to raw asymmetries, in ppb, for two correction schemes.	182
5.6	Total corrections of set3 and set6 to raw asymmetries, in ppb, for two correction schemes.	182
5.7	Total corrections of set5 and set3 to raw asymmetry, in ppb, for two correction schemes.	183
5.8	Asymmetry under different regression schemes for slugs 31-40, in ppb.	183
5.9	Summary of the values of the “null” test and the true physics asymmetry for slugs 31-40 before and after the standard regression scheme is applied, in ppb.	192
5.10	Summary of the error on each individual background correction in ppb and its relative uncertainties on A_{ep} for the 25% measurement, in ppb.	193
5.11	Summary of each individual correction and its relative uncertainties on A_{ep} for the 25% measurement, in ppb.	194

List of Figures

1.1	The lowest-order Feynman diagrams for electron-proton scattering.	12
1.2	Fitting of normalized parity-violating asymmetry using all current word data from parity-violating electron-proton scattering experiments.	16
1.3	Higher-order correction to the electron proton scattering	18
1.4	Calculated running of the weak mixing angle	19
1.5	Constraints of the mass scale in new physics beyond the Standard Model	22
1.6	Knowledge of the C_{1u} and C_{1d}	23
2.1	A schematic overview of the CEBAF at Jefferson Lab.	41
2.2	Qweak Target Cell	46
2.3	Target boiling study results	48
2.4	QTOR magnet separates elastic and inelastic electrons while focusing the elastic ones onto the main detectors.	51
2.5	CAD drawing of the locations of the collimator system	52
2.6	CAD drawing of the primary collimator	53
2.7	CAD drawing of the main detector	55
2.8	The schematic of the HDCs	60

2.9	The schematic of the VDCs	61
2.10	The concept of the MUX system used in the VDCs	63
2.11	The schematic of the Trigger Scintillators.	66
2.12	Schematic of the Focal Plane Scanner.	67
2.13	Layout of the 4-wire BPM.	73
2.14	Locations of the upstream and downstream luminosity monitors.	77
2.15	The schematic overview of the Hall C Møller Polarimeter.	81
2.16	The schematic overview of the Compton Polarimeter.	83
3.1	Overview of the working flow of the main function in QTR.	89
3.2	Overview of Coordinate systems	90
3.3	The procedure on how to select hits in the F1TDCs	91
3.4	The relationship between raw drift-time and reference time.	92
3.5	Typical drift-time distribution before and after the t_0 correction.	94
3.6	The correlation between t_0 value and wire number in a single plane	96
3.7	The relationship between drift-time and drift-distance drawn from the entries in the look-up table for the VDCs.	122
3.8	The relationship between drift-time and drift-distance drawn from the entries in the look-up table for the HDCs.	123
3.9	A typical VDC drift-distance distribution obtained by numerical in- tegration of the time spectrum.	124
3.10	Schematic of the creation of pattern database.	125
3.11	The tree structure of pattern database.	125

3.12	In order to save space as well as speed up the tree search process, bit patterns with only minor difference are considered as one.	126
3.13	Schematic overview of the tree-search algorithm in the case of the HDCs.	126
3.14	Conversion of hits into bit pattern in the case of the HDCs.	127
3.15	Selection of appropriate hits based on the initial condition of treelines.	127
3.16	Pattern Recognition Method for VDCs	128
3.17	The schematic of the method <i>QwTrackingTreeMatch.MatchRegion3</i>	128
3.18	Overview of the relationship between “plane 0” treeline and wire planes	129
3.19	The calculation of difference between hit position and track position	130
3.20	the definition of the $\Delta\phi_{front}$ used in the track reconstruction filter	131
3.21	Using signed residual of a plane to adjust the internal wire plane’s position	132
4.1	Change of projections to the aluminum target by changing the po- sitions of the HDC chambers.	137
4.2	Q^2 dependence on the positions of the HDC chambers.	138
4.3	Projection of aluminum run to the target plane.	139
4.4	Measured Z vertex in package 1 from run 15112	141
4.5	Projection result from package 1 in run 13653	143
4.6	The MD cut used in the tracking data analysis.	145

4.7	The ϕ distribution from reconstructed tracks within and outside the MD "prompt" window from package 1 in run 13653.	145
4.8	The θ distribution from reconstructed tracks within and beyond the MT cut from package 1 in run 13653.	146
4.9	The valid hits distribution from package 1 in run 13653.	147
4.10	The θ distribution from reconstructed tracks within and outside the MD "prompt" window from package 1 in run 13653.	147
4.11	The ϕ distribution from reconstructed tracks within and beyond the MT cut from package 1 in run 13653.	148
4.12	The distribution of the DirectionThetaOff variable in run 13653.	149
4.13	Q^2 dependence on the beam raster size	151
4.14	Q^2 dependence on the beam position in the X direction when detectors are at octant 1 and 5.	153
4.15	Q^2 dependence on the beam position in the Y direction when detectors are at octant 1 and 5.	154
4.16	Q^2 dependence on the beam angle in the Y direction when detectors are at octant 3 and 7.	154
4.17	Q^2 dependence on the beam rate in runs 13723 to 13726	156
4.18	Q^2 dependence on the beam rate in runs 15137 to 15140	157
4.19	Q^2 dependence on the beam angle in the Y direction	159
4.20	Q^2 dependence on the beam angle in the X direction	159
4.21	Q^2 dependence on octant	162

4.22	Q^2 dependence on octant pair.	163
4.23	Q^2 from different data-taking period.	164
5.1	Data process scheme in the Qweak experiment	171
5.2	Møller Polarimetry results for the 25% measurement	176
5.3	Møller Polarimetry results for the 25% measurement	177
5.4	MD sensitivity determined from linear regression, to position X for individual Main detectors in slug 35.	178
5.5	MD sensitivity to position Y for individual Main detectors in slug 35.	179
5.6	The regressed value of the parity-violating asymmetry of aluminum.	187
5.7	The fit of the asymmetry against the octant number on the elastic horizontal and vertical LH_2 data sets.	191
5.8	Raw asymmetry A_{ep} for slugs 31-40.	194
5.9	Asymmetry A_{ep} after applying the standard regression for slugs 31-40.	195
6.1	Updated current world data from parity-violating electron-proton experiment.	198
B.1	Layout of two ν planes from both packages in the VDCs. They are placed at octant 1 and 5.	206
B.2	Layout of two u planes from both packages in the VDCs. They are placed at octant 1 and 5.	207
B.3	Layout of the u plane in the HDCs.	207
B.4	Layout of the ν plane in the HDCs.	208
C.1	The side view of the layout of Hall C beamline elements.	210

D.1	Projection result from package 2 in run 13653	212
D.2	Projection result from package 1 in run 13671	212
D.3	Projection result from package 2 in run 13671	213
D.4	Projection result from package 1 in run 13674	213
D.5	Projection result from package 2 in run 13674	214
D.6	Projection result from package 1 in run 13676	214
D.7	Projection result from package 2 in run 13676	215

CHAPTER 1

Theory

1.1 Standard Model of Particle Physics

Our present best understanding of the elementary particles and three of the four fundamental forces of nature is described in the Standard Model of Particle Physics. The three kinds of elementary particles contained in the Standard Model are leptons, quarks and force mediators, while the three fundamental forces (interactions) are the electromagnetic, weak and strong interactions. The only force we are familiar with that is absent from the current Standard Model is gravitation, which is described by General Theory of Relativity separately.

All the visible matter in our universe is made up of leptons and quarks while the mediators are responsible for the non-gravitational interactions between them. Up to the present date, there are a total number of 61 elementary particles existing in the Standard Model. They include 12 leptons ($e, \mu, \tau, \nu_e, \nu_\mu, \nu_\tau$ and their

antiparticles), 36 quarks (u, d, c, s, t, b) with three different color charges and their antiparticles), 12 mediators (8 gluons, W^+, W^-, Z bosons and photon) and one Higgs Boson, which was recently confirmed to exist [1].

In addition to the description of elementary particles, the Standard Model also provides the main theoretical framework for each force such as quantum electrodynamics (QED) for the electromagnetic force and quantum chromodynamics (QCD) for the strong force. The weak force, which is outlined in the unified theory of the electroweak force, will be discussed more in detail in the next section and is the basis of the Qweak experiment. In each theory, the force occurs due to the exchange of corresponding mediators: the electromagnetic force is carried by the photon, the weak interaction is carried by charged and neutral weak vector bosons and the strong force is carried by gluons. The property of the mediators largely determines the features of the force, such as its strength and range. The dimensionless effective coupling constant, which is used to describe the relative strength of different types of interactions, varies from 1 in the strong interaction to 10^{-6} in the weak interaction. Similarly, the force range can change from infinity in the electromagnetic interaction to order of femtometers in the strong interaction.

Another important aspect of the Standard Model lies in the concept of symmetry; the Standard Model assumes an $SU(3) \times SU_L(2) \times U(1)$ gauge symmetry. The Lagrangian density is constructed under various scenarios through this principle of symmetry. For example, the successful electroweak theory, which will be discussed in Sec. 1.2, is based on the unified $SU_L(2) \times U(1)$ gauge groups.

Although the Standard Model represents our best understanding of elementary particles and forces of nature so far, most physicists are convinced that it is not the final solution to describe the whole picture. As mentioned before, gravitation is not included in the Standard Model due to the lack of an acceptable quantum theory of gravity. Continuous attempts over many years to incorporate gravity into the Standard Model have not led to a final solution. The Dark Matter, which accounts for the dominant form of masses in our universe, is another aspect that the Standard Model does not fully explain. Last but not least, a more inherent reason that leads physicists to think the Standard Model is not an ultimate optimal theory is that it contains too many arbitrary parameters: 19 arbitrary parameters (masses, weak mixing angles and gauge couplings etc.) are included currently. Numerous evidences of the deficiencies of the Standard Model lead physicists to believe that in order to better understand this universe, new and presently unknown physics beyond the Standard Model seems to be inevitable and searching for it will keep playing an integral role in physicists' work in the future.

One thing that needs to be noticed is that the deficiencies of the Standard Model do not necessarily mean that the Standard Model is wrong. On the contrary, no failure of the Standard Model has been undeniably seen yet for any predictions so far. Therefore, from here on, unless explicitly stated otherwise, we assume the validity of the Standard Model in our derivations.

1.2 The Theory of Electroweak Unification

Although electromagnetism and the weak interaction seem to be quite different in terms of the magnitude and force range at first glance, they can be described in a unified theory called the electroweak theory, where each of those two effective interactions are just different manifestations of the same electroweak force. An early attempt to unify electromagnetism and the weak interaction was made by Glashow in 1961 [2]. In addition to the two W^+ , W^- intermediate bosons, he also predicted the existence of one additional neutral intermediary. Then, in 1967, Weinberg and Salam improved the theory by modeling it into the gauge field theory where the symmetry between the two interactions is spontaneously broken in order to interpret the obvious differences in the masses of the photon and intermediate bosons [3, 4]. This theory, which is called the Glashow-Weinberg-Salam (GWS) theory today, together with QCD, consists of the cornerstone of the Standard Model.

The GWS theory asserts that apart from the $SU_L(2)$ gauge boson vector fields, an additional isosinglet vector boson field B_μ is also introduced, to give rise to the massless field when the symmetry is spontaneously broken. Then the covariant derivative of the Higgs field ϕ becomes

$$D_\mu\phi = (\partial_\mu - igW_\mu^a\tau^a - \frac{i}{2}g'B_\mu)\phi, \quad (1.1)$$

where g and g' are the $SU_L(2)$ and $U(1)$ coupling constants and τ_a is equal to half of the corresponding Pauli spin matrix $\sigma^a/2$. Note here that when mentioning the

SU_L symmetry, we always put a subscript in order to emphasize that it involves left-handed states only. If ϕ acquires a vacuum expectation value v and we replace that value into Eq. 1.1, the relevant Lagrangian becomes

$$\frac{1}{8}g^2v^2 [(W_\mu^1)^2 + (W_\mu^2)^2] + \frac{1}{8}v^2(gW_\mu^3 + g'B_\mu)^2. \quad (1.2)$$

We see immediately that for the first two terms in Eq. 1.2, two charged weak bosons W^+ , W^- can be derived through the transformation

$$W_\mu^\pm = \frac{1}{\sqrt{2}}(W_\mu^1 \mp iW_\mu^2) \quad (1.3)$$

with mass

$$M_W = \frac{1}{2}gv.$$

The last quadratic term in Eq. 1.2 contains the mixture of two neutral vector bosons W_μ^3 and B_μ . By solving the mass matrix, two eigenstates are generated in terms of those two vector fields as follows:

$$Z_\mu = \frac{1}{\sqrt{g^2 + g'^2}}(gW_\mu^3 + g'B_\mu), \quad (1.4)$$

$$A_\mu = \frac{1}{\sqrt{g^2 + g'^2}}(-g'W_\mu^3 + gB_\mu). \quad (1.5)$$

By substituting Eqs. 1.4-5 into Eq. 1.2, the last term becomes

$$\frac{1}{8}v^2(g^2 + g'^2)Z_\mu Z^\mu,$$

so it is quite obvious that the newly derived vector fields have the masses

$$M_Z = \frac{1}{2}v\sqrt{g^2 + g'^2},$$

$$M_A = 0.$$

The field A_μ is just the photon field of QED which characterizes the electromagnetic interaction and the field Z_μ is identified as the neutral weak boson Z^0 . To further simplify Eqs. 1.4-5, a free parameter, the weak mixing angle θ_W , is introduced through

$$\begin{pmatrix} Z_\mu \\ A_\mu \end{pmatrix} = \begin{pmatrix} \cos \theta_W & \sin \theta_W \\ -\sin \theta_W & \cos \theta_W \end{pmatrix} \begin{pmatrix} W_\mu^3 \\ B_\mu \end{pmatrix}, \quad (1.6)$$

where

$$\cos \theta_W = \frac{g}{\sqrt{g^2 + (g')^2}}, \quad \sin \theta_W = \frac{g'}{\sqrt{g^2 + (g')^2}}.$$

Notice that the g and g' are not the physical coupling constants of the weak and electromagnetic interactions; in order to get the physical coupling constants, we can use Eqs. 1.3-5 in the gauge equations and derive the following relationship between the coupling constants, by directly comparing with the electric current for the leptons [5]:

$$g_W = \frac{g_e}{\sin \theta_W},$$

$$g_Z = \frac{g_e}{\sin \theta_W \cos \theta_W}.$$

This also relates the tree-level masses of the charged and neutral weak bosons through

$$M_Z = \frac{M_W}{\cos \theta_W}. \quad (1.7)$$

The neutral current was first observed in the Gargamelle bubble chamber at CERN in 1973 through the $\nu p \rightarrow \nu X$ process [6]. In 1978, another cornerstone experiment E122 was carried out at SLAC by Charles Prescott and collaborators [7].

This experiment made the first observation of the parity-violating asymmetry effect in a weak neutral interaction and therefore established the validity of the weak neutral current in the Standard Model. In 1983, the W^\pm and Z^0 bosons were discovered by the UA1 and UA2 experiments at CERN [8, 9], which further validated the electroweak theory.

1.3 Electromagnetic Interaction

The lowest-order scattering amplitude for an electromagnetic process in which an electron is scattered from a proton is calculated in terms of the electric current as

$$\mathcal{M}_\gamma = -\frac{4\pi\alpha}{q^2} \mathcal{J}^{\mu e} \mathcal{J}_\mu^p, \quad (1.8)$$

where α is fine structure constant, q^2 is the four-momentum transfer and $\mathcal{J}^{\mu e}$ is the electron current, which is defined as

$$\mathcal{J}^{\mu e} = \bar{u}(l') \gamma^\mu u(l), \quad (1.9)$$

whereas the proton current, which contains the form factor representing how the photon couples to the composite structure of the proton, is expressed as

$$\mathcal{J}_\mu^p = \bar{u}(p') (F_1^p(q^2) \gamma_\mu + F_2^p(q^2) \frac{i\sigma_{\mu\nu} q^\nu}{2M_p}) u(p), \quad (1.10)$$

where M_p is the mass of the proton and $F_1^p(q^2)$ and $F_2^p(q^2)$ are called Dirac and Pauli form factors, respectively, which are normalized to unity and to the anomalous magnetic moment of the proton, respectively, when q^2 is taken in the limit to 0. Notice here that we write the kinematic of each particle, which consists of the

four parameters $p \equiv (E/c, \mathbf{p})$, in a more compact form as l, l', p, p' , shown in the above equations. Linear combinations of those two form factors give rise to the Sachs form factors [10]:

$$G_E^p = F_1^p - \frac{Q^2}{4M_p^2} F_2^p \quad (1.11)$$

$$G_M^p = F_1^p + F_2^p \quad (1.12)$$

where $Q^2 = -q^2 > 0$, whereas Q_E^p and Q_M^p are named as the electric form factor and magnetic form factor, which describe the spatial distribution of electric charge and current inside the proton, and only depend on the Q^2 .

For those form factors, each individual quark flavour contributes in terms of their relevant electric charge to the proton's form factors, like

$$G_{E,M}^p \simeq \frac{2}{3} G_{E,M}^{p,u} - \frac{1}{3} (G_{E,M}^{p,d} + G_{E,M}^{p,s}).$$

Two things need to be noticed here: first, for the proton, only u and d quarks are present both as sea and valence quarks, while the s quark is only present in the quark sea; second, we only consider three light quarks: u, d, s here because the masses of the heavier quarks are much larger than Λ , where Λ is a constant to parameterize the strength of strong coupling constant in terms of q^2 and which appears to be $\simeq 250$ MeV. In the regime of $q^2 \gg \Lambda$, the strong coupling constant decreases and the interaction between quarks becomes relatively weak, which makes the contribution from heavy quarks negligible.

1.4 Neutral Current Weak Interaction

Now, it is time to take a look at the more complicated scattering amplitude in which the neutral weak boson Z^0 is involved. Similar to the Eq. 1.8, we can write the scattering amplitude as

$$\mathcal{M}_Z = -\sqrt{2}G_F \mathcal{J}^{\mu eZ} \mathcal{J}_\mu^{pZ}, \quad (1.13)$$

where G_F is the Fermi constant. The $\mathcal{J}^{\mu eZ}$ describes how the Z^0 is coupled to the electron

$$J^{\mu eZ} = \bar{u}(l')\gamma^\mu(c_V - c_A\gamma^5)u(l), \quad (1.14)$$

where c_V and c_A are the coefficients of vector and axial components in this coupling. In the Standard Model, their values are equal to

$$c_V = -\frac{1}{2} + 2\sin^2\theta_W \text{ and } c_A = -\frac{1}{2};$$

putting those values into Eq. 1.14, we get the current

$$J^{\mu eZ} = -\frac{1}{2}\bar{u}(l')\gamma^\mu(1 - 4\sin^2\theta_W - \gamma^5)u(l). \quad (1.15)$$

Not to mention the proton's internal structure, the coupling between the Z^0 and the proton is more complicated because of the emergence of the axial vector component. However, similar to Eq. 1.10, we can write down the corresponding current as

$$\mathcal{J}_\mu^p = \bar{u}(p')(F_1^{pZ}(q^2)\gamma_\mu + F_2^{pZ}(q^2)\frac{i\sigma_{\mu\nu}q^\nu}{2M_p} + \gamma_\mu\gamma^5 G_A^Z(q^2))u(p), \quad (1.16)$$

where the additional axial vector form factor $G_A^Z(q^2)$ is added here. Following Eqs. 1.11-12, the electric and magnetic form factors can be made by the same linear

combinations of F_1^{pZ} and F_2^{pZ} here. Instead of the electric charge, quark flavor contributes to the vector form factors in the proton and Z^0 coupling according to the neutral weak vector charges, as

$$G_{E,M}^{p,Z} = \left(1 - \frac{8}{3} \sin^2 \theta_W\right) G_{E,M}^{p,u} + \left(-1 + \frac{4}{3} \sin^2 \theta_W\right) (G_{E,M}^{p,d} + G_{E,M}^{p,s}). \quad (1.17)$$

Again, we only include the light quarks here for the same reasoning when we express $G_{E,M}^p$ in Sec. 1.3. Similarly, the axial vector form factor can be identified as

$$G_A^{p,Z} = G_A^{p,u} - (G_A^{p,d} + G_A^{p,s}). \quad (1.18)$$

At $Q^2 = 0$ (GeV/c)², since there is no net strangeness appearing in the proton, one expects that the contribution from strange quarks in Eq. 1.17 should be $G_E^s(q^2) = 0$ and $G_M^s(q^2) = \mu_s$, where μ_s is the strangeness magnetic moment of the proton. However, from the analysis of the previous experimental data taken at $Q^2 \approx 0.1$ (GeV/c)² by using different targets [11], $G_{E,M}^s$ have different values, which are functions of transferred four-momentum Q^2 , due to their existence in the “quark-gluon sea”. Therefore, we need to precisely determine the contribution from strange quark in our range of $Q^2 \approx 0.026$ (GeV/c)². We can obtain this goal by separating the strange quarks effect from the other two valence quarks u and d and then incorporating it into the so-called hadronic form factor $B(Q^2)$. As we will see in Sec. 1.6, we rely on the existing experiments’ results to extrapolate the value of $B(Q^2)$ to the Q^2 of our interest, which contains the correct value of $G_{E,M}^s$. In short, we do not measure $G_{E,M}^s$ specifically but instead calculate them as a component in $B(Q^2)$.

1.5 The Parity-Violating Asymmetry in the Qweak Experiment

From Eq. 1.17, by ignoring the contribution of strange quarks, one could easily write down the weak charge of proton in the Standard Model as

$$Q_W^p \approx 2\left(1 - \frac{8}{3} \sin^2 \theta_W\right) + \left(-1 + \frac{4}{3} \sin^2 \theta_W\right) = 1 - 4 \sin^2 \theta_W. \quad (1.19)$$

This quantity happens to be suppressed to be rather small (≈ 0.07), therefore providing a chance for a sensitive probe of the weak mixing angle $\sin^2 \theta_W$, if there is any observed deviation from the theoretical value predicted by the Standard Model. In this section, we will describe how the quantity is measured in the Qweak experiment.

The Qweak experiment employs a 1.165 GeV longitudinally-polarized electron beam, scattering off of an unpolarized proton in a fixed target of liquid hydrogen and then the scattered electron flux is detected. The helicity of the electron beam is rapidly reversed and the scattered electron flux in each helicity is integrated in order to effectively count the number of scattered electrons in each state. The asymmetry A , which is the difference in the cross section for each beam helicity state, is defined as

$$A_{LR}^p = \frac{\sigma_R - \sigma_L}{\sigma_R + \sigma_L}, \quad (1.20)$$

where σ_R and σ_L are the cross sections for the right-handed and left-handed electrons, respectively. In the lowest-level Feynman diagram, the elastic scattering

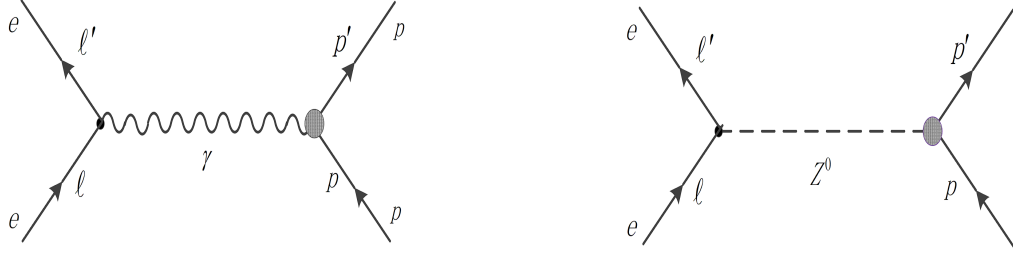


FIG. 1.1: The lowest-order Feynman diagrams to the electron-proton scattering, where either the photon or neutral weak boson Z^0 are exchanged.

of an electron from a proton is a mixture of two interactions: the electromagnetic interaction in which photon is exchanged and the weak interaction in which the neutral weak boson Z^0 serves as the mediator, as in Figure 1.1 . Therefore, the scattering amplitude \mathcal{M} can be expressed as

$$\mathcal{M} = \mathcal{M}_\gamma + \mathcal{M}_Z. \quad (1.21)$$

Rewriting Eq. 1.20 in terms of the scattering amplitude and substituting Eq. 1.21 into the rewritten form, we get

$$A_{LR}^p = \left[\frac{|\mathcal{M}_\gamma + \mathcal{M}_{Z,R}| - |\mathcal{M}_\gamma + \mathcal{M}_{Z,L}|}{|\mathcal{M}_\gamma + \mathcal{M}_{Z,R}| + |\mathcal{M}_\gamma + \mathcal{M}_{Z,L}|} \right]^2. \quad (1.22)$$

Eq. 1.22 can be further simplified based on the following assumptions: first, $\mathcal{M}_\gamma \gg \mathcal{M}_Z$. This is because in the low Q^2 region where the value of Q^2 for Q_{weak} is roughly equal to 0.026 (GeV/c)^2 , the mass term appearing in the denominator of the propagator will make the magnitude of $\mathcal{M}_\gamma \simeq 10^7$ times bigger than \mathcal{M}_Z . Therefore, the terms like \mathcal{M}_Z^2 are ignored and we are able to get

$$A_{LR}^p = -2 \frac{\text{Re}(\mathcal{M}_\gamma^* \mathcal{M}_Z)}{|\mathcal{M}_\gamma|^2}. \quad (1.23)$$

The numerator part does not cancel out during the subtraction because the cou-

pling of quarks and leptons to the Z^0 has the $V - A$ form like

$$\frac{-ig_Z}{2}\gamma^\mu(c_V^f - c_A^f\gamma^5), \quad (1.24)$$

whereas the combination of vector γ^μ and axial vector $\gamma^\mu\gamma^5$ term violates the conservation of the parity. So the only work left to do is to calculate the scattering amplitude of the electromagnetic and neutral weak interaction during the elastic electron-proton scattering respectively.

So based on the results from Sec. 1.3 and Sec. 1.4, we can write Eq 1.22 as [12]

$$A_{LR}^p = -\left(\frac{G_F Q^2}{4\pi\alpha\sqrt{2}}\right) \frac{\epsilon(\theta) G_E^\gamma G_E^Z + \tau G_M^\gamma G_M^Z - (1 - 4\sin^2\theta_W)\epsilon' G_M^\gamma G_A^Z}{\epsilon(\theta)(G_E^\gamma)^2 + \tau(G_M^\gamma)^2}, \quad (1.25)$$

where we define the kinematic factors as

$$\begin{aligned} \tau &= \frac{Q^2}{4M_p^2}, \\ \epsilon(\theta) &= [1 + 2(1 + \tau) \tan^2 \frac{\theta}{2}]^{-1}, \\ \epsilon'(\theta) &= \sqrt{\tau(1 + \tau)(1 - \epsilon^2(\theta))}, \end{aligned}$$

where θ is the lab scattering angle and M_p is the proton's mass. It is obvious from Eq. 1.25 that the parity-violating asymmetry contains three terms, each of which manifests the interference between electromagnetic and neutral weak interactions. It is also noted that the asymmetry depends on θ .

For Qweak, the scattered electrons are only measured at a very small forward angle, so we can regard $\theta \rightarrow 0^\circ$. Consequently, one has $\epsilon(\theta) \approx 1$ and $\epsilon' \simeq 0$, so

the term with axial form factor G_A^Z becomes negligible, leading to

$$A_{LR}^p \simeq -\left(\frac{G_F Q^2}{4\pi\alpha\sqrt{2}}\right) \frac{\epsilon(\theta) G_E^\gamma G_E^Z + \tau G_M^\gamma G_M^Z}{\epsilon(\theta)(G_E^\gamma)^2 + \tau(G_M^\gamma)^2}. \quad (1.26)$$

At very low momentum transfer $Q^2 \approx 0.03 \text{ (GeV/c)}^2$, one also has $\tau \approx 0$ so we can even further simplify Eq. 1.25 by expanding the denominator in terms of $\mathcal{O}(\tau)$,

$$A_{LR}^p = -\left(\frac{G_F Q^2}{4\pi\alpha\sqrt{2}}\right) \left(\frac{G_E^Z}{G_E^\gamma} + \tau \frac{G_M^\gamma(G_M^Z G_E^\gamma - G_E^Z G_M^\gamma)}{\epsilon(G_E^\gamma)^3} + \mathcal{O}(\tau^2) + \mathcal{O}(\tau^3) + \dots\right). \quad (1.27)$$

Remembering that at $Q^2 \rightarrow 0$, G_E^γ is normalized to unity and $G_E^Z = 1 - 4 \sin^2 \theta_W$ is normalized to the weak charge of the proton at tree level, this leads to

$$A_{LR}^p = -\left(\frac{G_F}{4\pi\alpha\sqrt{2}}\right) (Q^2 Q_W^p + Q^4 B(Q^2)). \quad (1.28)$$

Here, $B(Q^2)$ depends on the nucleon electromagnetic and strange quark form factors, which will be detailed in the next section. Eq. 1.28 also explains how we extract the weak charge of the proton from the measured parity-violating asymmetry in the Qweak experiment. Of course we need to carefully design the experiment so that the Q^2 chosen is within a range where it is small enough so that the uncertainty of $B(Q^2)$ is comfortably constrained while big enough so that the asymmetry is measurable to the desired statistical precision.

1.6 Hadronic Form Factor $B(Q^2)$

Although it is suppressed by the very small momentum transfer Q^2 , the hadronic form factor $B(Q^2)$ still plays an important role in extracting the weak charge of proton to a high precision. It is thus worthwhile to devote some effort to get the correct

$B(Q^2)$. From Eqs. 1.26-7, one can see that the hadronic form factor depends on both $G_{E,M}^\gamma$ and $G_{E,M}^Z$. Since all the form factors are functions of momentum transfer Q^2 , the hadronic form factor $B(Q^2)$ is also a function of Q^2 .

One can see that Eq. 1.28 can be rewritten as

$$A_{LR}^p \simeq A_0(Q^2 Q_W^p + Q^4 B(Q^2)), \quad (1.29)$$

where the overall normalization is decided by $A_0 = -G_F/(4\pi\alpha\sqrt{2})$. A number of parity-violating electron-proton (PVES) experiments have been carried out over a wide range of momentum transfers Q^2 and so one can fit the correlation between the normalized data $\overline{A_{LR}^p} \equiv A_{LR}^p/(A_0 Q^2)$ from Eq. 1.29 and Q^2 . Note that the intercept at $Q^2 = 0$ would directly give the value of Q_W^p . Furthermore, the value of $B(Q^2)$ at the Q^2 of our interest can be deduced by extrapolating from the results of the fit.

Figure 1.2 depicts how we determine the $B(Q^2)$ using the results of these earlier experiments.

1.7 Radiative Corrections and Higher order effects

At tree level, the weak charge of the proton is given by

$$Q_W^p = 1 - 4 \sin^2 \theta_W. \quad (1.30)$$

With electroweak radiative corrections included, the term can be expressed up to one loop as [15]

$$Q_W^p = [\rho_{NC} + \Delta e][1 - 4 \sin^2 \hat{\theta}_W(0) + \Delta e'] + \square_{WW} + \square_{ZZ} + \square_{\gamma Z}, \quad (1.31)$$

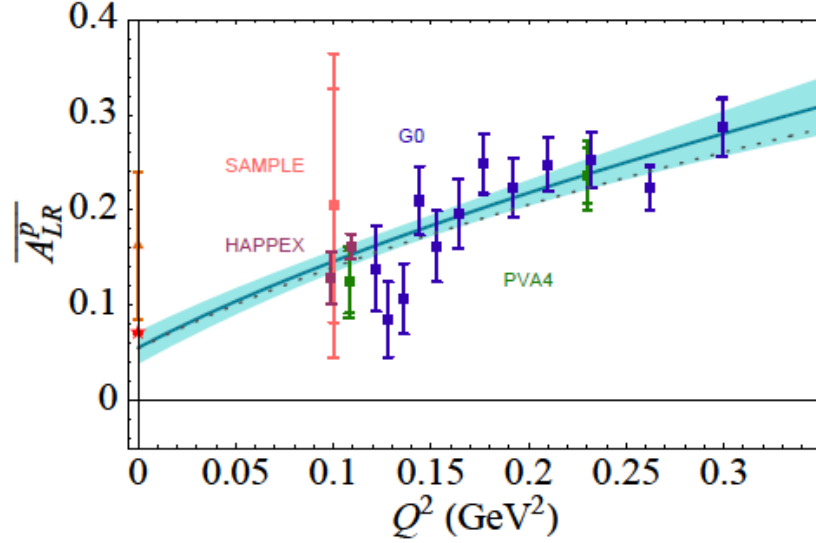


FIG. 1.2: The correlation between the normalized, parity-violating asymmetry and the momentum transfer using an analysis of all previous world data from parity-violating electron-proton experiments [13]. The extrapolation to $Q^2 = 0$ yields the weak charge of the proton Q_W^p , which will be used as the main method to determine the weak charge of proton after Qweak. The orange triangle point indicates the prior knowledge of Q_W^p before adding the relatively new results from SAMPLE at MIT-Bates, PVA4 at Mainz and the HAPPEX and G0 Collaborations at Jefferson Lab. The star point is the predicted value from the Standard Model. The solid blue line and the shaded blue band are the best fit and $1\text{-}\sigma$ bound of the current world data, respectively. The dotted line is the best fit if theoretical estimates of the anapole form factor are incorporated [14].

where higher-order contributions from vertex corrections, vacuum polarization and box diagrams are considered. It is possible to predict ρ_{NC} , Δe and $\Delta e'$ quite precisely, all of which arise from the standard electroweak radiative corrections. Additionally, two-boson exchange brings about box diagram corrections as the last three terms in Eq 1.30 indicate. The WW and ZZ diagrams, where two massive bosons are involved, are rather small and well predicted here at the region of low Q^2 of our interest [15]. Consequently, those box diagrams involving at least one photon ($\gamma\gamma$, γZ) as the last term in Eq. 1.30 describes are the main

concern, because they are larger corrections. For the γZ box diagram, extensive work has been carried out to calculate this value during the past few years [16, 17, 18, 19, 20, 21]. Result from Gorchtein and Horowitz showed that the relative correction of the γZ box diagram to Q_W^p is $(7.6 \pm 2.8\%)$ [20]. The work from Sibirtsev *et al.* [18], however, suggested a smaller uncertainty $\sim 1.5\%$ related with the γZ correction compared with the 2.8% uncertainty showed before. Carlson and Rislow's work [19] agreed with the Sibirtsev *et al.* result within the uncertainty limits and also claimed a smaller uncertainty than Gorchtein and Horowitz's result. The latest result, from Hall *et al.* shows the correction [21], at the kinematics of the Qweak experiment, is $7.8 \pm 0.5\%$.

For $\gamma\gamma$ corrections, their effect on the asymmetry can be denoted as $Z(\gamma\gamma)$ and $\gamma(\gamma\gamma)$, which represent the interference between single Z^0 and photon exchange and the $\gamma\gamma$ exchange amplitude. A calculation by Tjon *et al.* [22] showed that $Z(\gamma\gamma)$ and $\gamma(\gamma\gamma)$ will particularly cancel in their effect on A_{LR} and the work also indicated that at the Q^2 region of our interest and in the forward angle limit, the correction to Q_W^p is negligible.

1.8 Running of the Weak Mixing Angle $\sin^2\theta_W$

The Qweak experiment will measure the weak charge of the proton $Q_W^p = 1 - 4\sin^2\theta_W$ to 4% precision within the context of the Standard Model; this will also

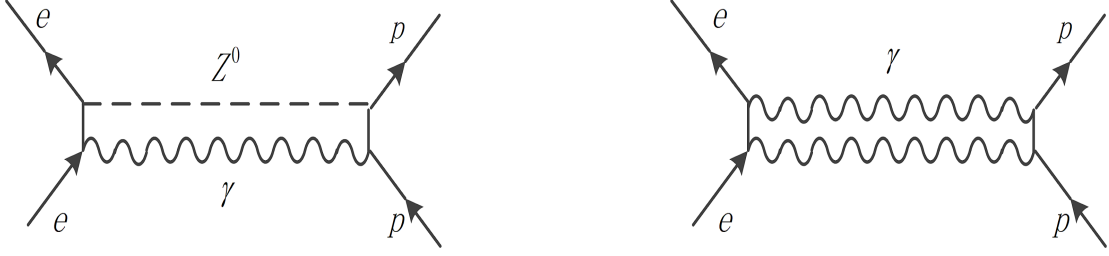


FIG. 1.3: Two types of higher order corrections of the Feynman diagrams to the electron-proton scattering: the left is the γZ box diagram while the right represents the $\gamma\gamma$ diagram.

constitute a precision measurement of the weak mixing angle $\sin^2 \theta_W$, providing a direct probe of the running of $\sin^2 \theta_W$ as predicted by the Standard Model at low Q^2 .

Similar to the well-known phenomenon of the running of $\alpha(Q^2)$ in QED, the value of the weak mixing angle $\sin^2 \theta_W$, which is defined as the mixing ratio between the third component of the isotriplet vector boson W and the isosinglet B in GWS theory, also depends on momentum transfer Q^2 and thus the effect is referred as the “running of $\sin^2 \theta_W$ ”.

The variation of $\sin^2 \theta_W$ stems largely from the large logarithm term, resulting from the one-loop level radiative correction. Czarnecki and Marciano [23] found that it is possible to replace the tree-level weak charge of the proton by

$$1 - 4\kappa(Q^2) \sin^2 \hat{\theta}_W(M_Z) \equiv 1 - 4 \sin^2 \theta_W(Q^2). \quad (1.32)$$

where the caret sign indicates the quantities under the minimum subtraction ($\overline{\text{MS}}$) renormalization scheme and $\kappa(Q^2)$ represents the Q^2 -dependent shift in the effective $\sin^2 \theta_W(Q^2)$ due to loop effects. In Eq. 1.31 $\sin^2 \hat{\theta}_W(M_Z)$ is the value of the weak mixing angle at the Z^0 -pole, where $Q^2 = M_Z^2$ under the $\overline{\text{MS}}$ scheme and

$\sin^2 \theta_W(Q^2)$ is the running parameter depending on Q^2 .

Figure 1.4 displays the predicted running of $\sin^2 \theta_W(Q^2)$ as well as the results of several precision electroweak experiments which were carried out at different Q^2 and which will be discussed more in detail in Sec. 1.10.

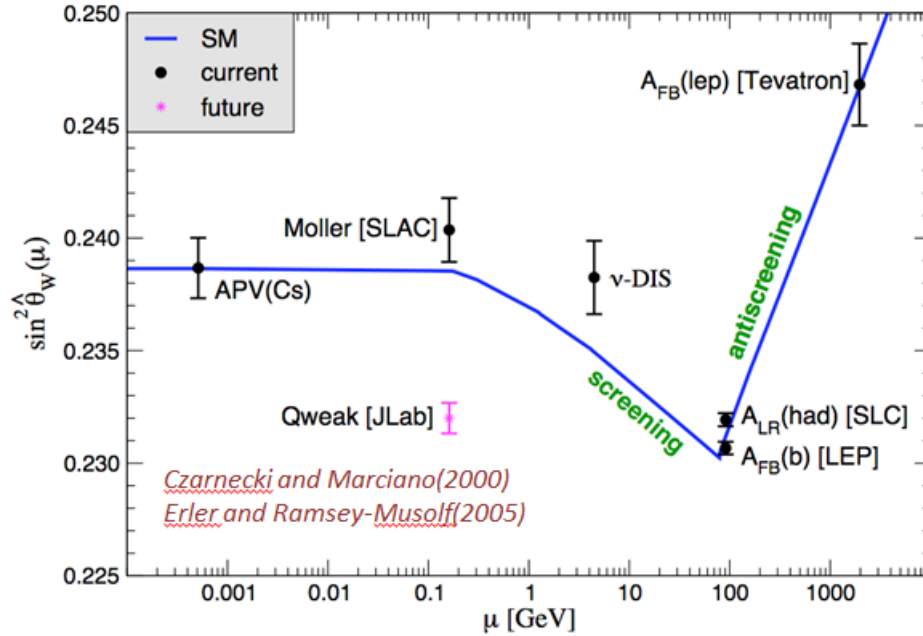


FIG. 1.4: The calculated running of the weak mixing angle $\sin^2 \theta_W$ in the Standard Model (blue solid line), as defined in the $\overline{\text{MS}}$ renormalization scheme [23, 24], whereas the thickness of the blue curve describes the uncertainty of the prediction. The existing data are displayed as black points with error bars on the graph. They are from atomic parity violation [25], SLAC Moller scattering experiment [26], NuTeV deep inelastic neutrino scattering experiment [27], Tevatron [28], LEP and SLC Z^0 -pole experiments [29]. The anticipated result from the Qweak experiment, which is outlined as a pink point and placed at an arbitrary position, could either confirm the expected value of $\sin^2 \theta_W$ from the Standard Model or indicate new physics.

1.9 Beyond the Standard Model

A precision measurement of the weak charge of the proton along with any deviation from the theoretical prediction in the Standard Model can be used to test for possible new physics up to high energy scales. To calculate the quantitative implication of the proposed 4% precision measurement of Q_W^p , it is useful to consider a model-independent Lagrangian in terms of an effective contact interaction of the form $A(e) \times V(q)$ [15]:

$$\mathcal{L}^{eH} = \mathcal{L}_{SM}^{PV} + \mathcal{L}_{NEW}^{PV}, \quad (1.33)$$

where

$$\mathcal{L}_{SM}^{eH} = -\frac{G_F}{\sqrt{2}} \bar{e} \gamma_\mu \gamma_5 e \sum_q C_{1q} \bar{q} \gamma^\mu q \quad (1.34)$$

$$\mathcal{L}_{NEW}^{eH} = \frac{g^2}{4\Lambda^2} \bar{e} \gamma_\mu \gamma_5 e \sum_f h_V^q \bar{q} \gamma^\mu q \quad (1.35)$$

and where g , Λ and h_V^q are the coupling constant, mass scale and effective coefficients related with parity-violating new physics, respectively. The effective coefficients are of order of unity and are set by $h_V^u = \cos \theta_h$ and $h_V^d = \sin \theta_h$, where θ_h is called the flavor mixing angle [13]. Any discrepancy between the measured value and the theoretical value of Q_W^p , which represents the new physics component, can be expressed as

$$(Q_W^p)_{NEW} = (Q_W^p)_{Exp} - (Q_W^p)_{SM}. \quad (1.36)$$

The uncertainty of the above equation is

$$\Delta(Q_W^p)_{NEW} \simeq \Delta(Q_W^p)_{Exp}, \quad (1.37)$$

where the uncertainty of $(Q_W^p)_{SM}$ is ignored because it is relatively small. Using the Lagrangians from Eqs. 1.32-4, the ratio between the deviation from the theoretical value and its own uncertainty associated with new physics becomes

$$S = \frac{(Q_W^p)_{NEW}}{\Delta(Q_W^p)_{NEW}} = \frac{(Q_W^p)_{NEW}}{\Delta(Q_W^p)_{Exp}} = \left(\frac{g^2}{4\Lambda^2} (Q_W^p)_{NEW} \right) / \left(\frac{G_F}{\sqrt{2}} (\Delta Q_W^p)_{Exp} \right). \quad (1.38)$$

Consequently, the energy scale to which our measurement can probe can be written in the following form, by rearranging the above equation

$$\frac{\Lambda^2}{g^2} = - \frac{1}{2\sqrt{2}} \frac{(Q_W^p)_{NEW}}{S G_F (\Delta Q_W^p)_{Exp}}, \quad (1.39)$$

where $(Q_W^p)_{NEW} = -2(2h_V^u + h_V^d)$. If we take the further assumption of a significance of $S = 2$, which corresponds to 95% confidence level (2σ), then a 4% measurement of Q_W^p will yield the energy scale up to

$$\frac{\Lambda}{g} = \frac{1}{\sqrt{2}\sqrt{2}} \frac{1}{\sqrt{2} G_F (\Delta Q_W^p)_{Exp}} = 2.3 \text{ TeV}. \quad (1.40)$$

Figure 1.5 displays bounds of new physics that could be set by a proposed 4% precision measurement of Q_W^p along with other previous measurements.

Although up to now our analysis is model-independent, it is easy to extend to a model-dependent analysis by specifying a different coupling constant g . For instance, the sensitivity to a non-perturbative theory with $g \sim 2\pi$ would enhance the mass scale up to 14 TeV. Another way of interpreting a precision measurement

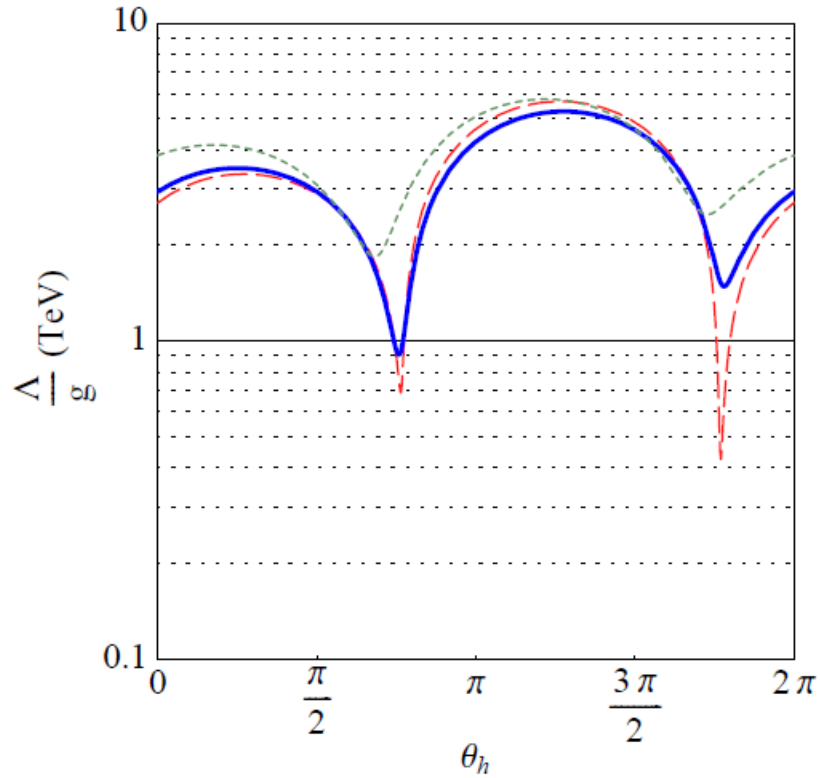


FIG. 1.5: The correlation between various constraints of the mass scale for new parity-violating physics beyond the Standard Model and the flavor mixing angle θ_h [13] (see Sec. 1.9). The dashed red line describes the old limit reported in the PDG [30]. The solid blue line is the limit if relatively new results from parity-violating electron scattering experiments are incorporated. Finally, the short-dashed green line would be the new constraint when the result from Qweak is revealed, assuming a value in agreement with the Standard Model.

of Q_W^p lies in the fact that the Q_W^p can be decomposed as the linear combination of C_{1u} and C_{1d} ,

$$Q_W^p = -2(2C_{1u} + C_{1d}), \quad (1.41)$$

which are defined in Eq. 1.34 and therefore has the capability of testing the theoretical value of those two variables predicted by the Standard Model. Existing world data, as summarized by the PDG [30], provides information on various linear combinations of C_{1u} and C_{1d} , therefore constraining the correlation between

$C_{1u} + C_{1d}$ and $C_{1u} - C_{1d}$ as Figure 1.6 illustrates.

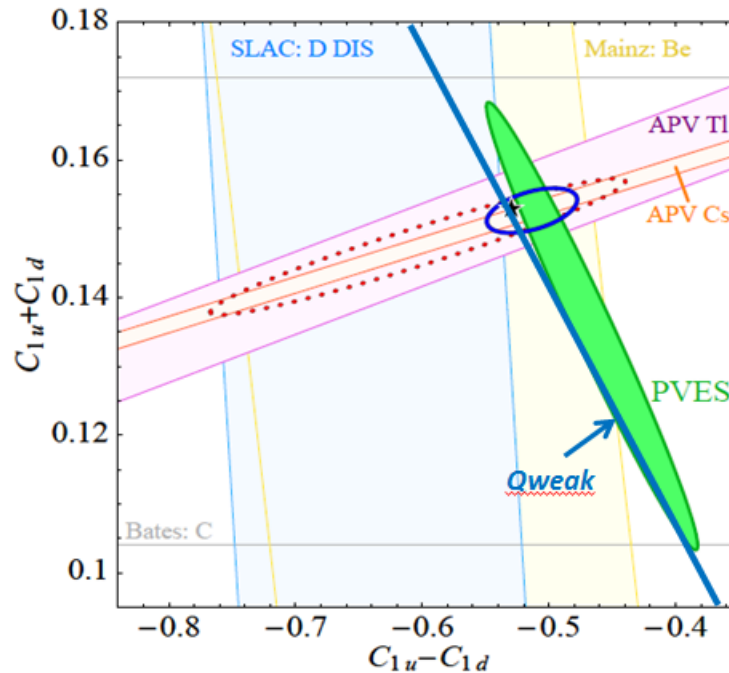


FIG. 1.6: Constraints on the value of C_{1u} and C_{1d} [13] from current world data. The dotted contour depicts the constraints (95% CL) reported in 2006 PDG [30]. The black star is the position predicted by the Standard Model. The filled green ellipse represents the 68% CL constraints of results from relatively new PVES measurements on hydrogen, deuterium and helium targets. The blue solid contour is the 95% CL constraint if the proposed precision of 4% Q_{W}^p is included, assuming its agreement with the Standard Model.

1.10 Other Related Experiments

Over the past decade, precision measurements played an important role in laying out the structure of the electroweak interaction. In this section, several important experiments, with their results of testing the weak mixing angle being shown in Fig 1.4, including a Moller scattering experiment, neutrino-nucleon scattering experiment and an atomic parity-violation experiment will be briefly overviewed, and

the implications for precision tests of the Standard Model will be discussed, as well as those of certain high-energy experiments.

1.10.1 Measurement of $\sin^2 \theta_W$ at LEP and SLC

A number of experiments, which enabled the precision measurement of the value of $\sin^2 \theta_W$, were carried out at the LEP and SLC e^+e^- colliders during 1989 to 1998 at the center-of-mass energy of approximately 91 GeV, which is close to the mass of the Z^0 boson. All of the experiments utilized the process $e^+e^- \rightarrow Z^0 \rightarrow f\bar{f}$ where f represents all known fermions, except the top quark, which is too heavy to be produced in Z^0 decay.

With the unpolarized beam at LEP, the *forward-backward asymmetries* for different identified fermion final states can be defined as

$$A_{FB}^f = \frac{\sigma_F^f - \sigma_B^f}{\sigma_F^f + \sigma_B^f} = \frac{3}{4} A_e A_f, \quad (1.42)$$

where A_e and A_f can be expressed as

$$A_e = \frac{2v_e a_e}{v_e^2 + a_e^2} \quad \text{and} \quad A_f = \frac{2v_f a_f}{v_f^2 + a_f^2}, \quad (1.43)$$

where v_f and a_f are vector and axial vector couplings of the Z^0 to the fermion and v_e and a_e stand for specifically the vector and axial vector couplings of the electron to the Z^0 . Note here the concept of “forward” is defined as that the produced fermion (anti-fermion) is in the hemisphere determined by the incident direction of the electron (positron) beam, where the scattering angle $\theta < \pi/2$. Similarly, “backward” means the scattering angle $\theta > \pi/2$. Since all those couplings depend

on $\sin^2 \theta_W$, the value of $\sin^2 \theta_W$ can be thus extracted through A_{FB}^f . Rather than integrating the cross section over the whole range of scattering angle θ , A_{FB}^f is actually obtained from maximum-likelihood fits to the measured differential cross-section with respect to the angle θ :

$$\frac{d\sigma}{d\cos\theta} \propto 1 + \cos^2\theta + \frac{8}{3}A_{FB}^f \cos\theta. \quad (1.44)$$

The result from LEP shown in Figure 1.4 was calculated based on the event selection where the final state involved b quarks, $Z^0 \rightarrow b\bar{b}$.

With the availability of a highly polarized beam at SLC, the SLD collaboration [31] was able to perform a the measurement of the *left-right asymmetry* in the $e^+e^- \rightarrow Z^0 \rightarrow f\bar{f}$ process

$$A_{LR} = \frac{\sigma_L - \sigma_R}{\sigma_L + \sigma_R} = P_e A_e, \quad (1.45)$$

where P_e is the electron polarization. The value of A_{LR} is only in terms of the coupling of the electron to the Z^0 , irrespective of the final state couplings, and thus great statistics can be reached. Since A_e is quite sensitive to $\sin^2 \theta_W$, the precision measurement of A_{LR} yielded a stringent test of the theoretical value from the Standard Model. Finally, the combined results from LEP and SLC showed an average value of the weak mixing angle at [32]

$$\sin^2 \theta_W = 0.23153 \pm 0.00016. \quad (1.46)$$

However, a discrepancy of 2.1σ between the SLD and LEP $\sin^2 \theta_W$ still remains (see Fig 1.4), which is hoped to be resolved based on data from future precision experiments, such as the proposed MOLLER experiment at Jefferson Lab [33].

1.10.2 NuTeV Experiment

NuTeV was a deep-inelastic neutrino scattering experiment and one of its primary goals was to measure the electroweak parameter $\sin^2 \theta_W$ through the quantity R^- expressed in Eq. 1.47. In order to calculate that quantity, ratios of neutral current to charged current cross sections for ν and $\bar{\nu}$ scattering from isoscalar targets of u and d quarks were both measured at a momentum-transfer $Q^2 \approx 20 \text{ (GeV/c)}^2$. The experiment was carried out during the 1996-1997 run at the Fermilab Tevatron.

The NuTeV experiment employed high-purity ν and $\bar{\nu}$ beams generated from the decay of pions and kaons resulting from applying 800 GeV protons on a BeO target. A magnet was used to select the specific charged particles by bending others away from the detector system. The neutrino interactions were measured in the NuTeV detector, which was placed 1450 m downstream of the target and consisted of a steel-scintillator target followed by an iron-toroid spectrometer.

The value of $\sin^2 \theta_W$ was extracted through the observable suggested by Paschos and Wolfenstein [34]

$$R^- \equiv \frac{\sigma(\nu_\mu N \rightarrow \nu_\mu X) - \sigma(\bar{\nu}_\mu N \rightarrow \bar{\nu}_\mu X)}{\sigma(\nu_\mu N \rightarrow \mu^- X) - \sigma(\bar{\nu}_\mu N \rightarrow \mu^+ X)} \quad (1.47)$$

in order to suppress the contribution from charm quarks, which are the same for neutrino and anti-neutrino interactions. Ignoring quark mass differences and assuming that the u - and d - distributions from a isoscalar target are identical [35], the quantity R^- depends upon $\sin^2 \theta_W$ through

$$R^- = \frac{1}{2} - \sin^2 \theta_W. \quad (1.48)$$

Initially, the analysis of data from the NuTeV collaboration indicated an approximately 3σ deviation from the theoretical value predicted in the Standard Model [27], which was an obvious indication of new physics. Since then, many attempts have been suggested to either understand this deviation in light of extensions of the Standard Model or correct this anomaly within the Standard Model. The primary corrections considered so far are focused on three aspects: 1) charge symmetry violation (CSV) arising from, for example, the difference in mass of \bar{u} and \bar{d} quarks, 2) the steel target used in NuTeV experiment which was not iso-scalar (more neutrons than protons), leading to a possible isovector EMC effect, which could modify the parton distribution function of all the nucleons, and 3) despite the equal number of strange and anti-strange quarks $s\bar{s}$ in the nucleon, to conserve the strangeness quantum number, the symmetry in the strange quark sea distribution, *i.e.* $s(x) = \bar{s}(x)$ could be violated, which could shift the extracted value of $\sin^2 \theta_W$ because neutrinos and antineutrinos interact differently with s and \bar{s} . One recent study shows, after incorporating all those independent corrections, that the result extracted from NuTeV experiment's data matches the theoretical value well [36], however, those attempts of solving the anomaly are quite model-dependent and therefore need more precise data which is anticipated in future experiment to verify those effects.

1.10.3 Moller Scattering Experiment

The Moller scattering experiment (E-158), which was performed at SLAC, was a precision experiment which aimed at measuring the electron's weak charge by scattering a longitudinally-polarized electron beam off a liquid hydrogen target at low $Q^2 \approx 0.026 \text{ (GeV/c)}^2$ [26]. Unlike the Qweak experiment, in which only electrons scattered from a proton target through an elastic process are detected by the main detector system, the calorimeters of the Moller experiment was divided into four regions, of which the innermost was responsible for detecting the Moller scattering events. After measuring the parity-violating asymmetry A_{PV} , the weak charge of the electron Q_W^e is extracted through [23]

$$A_{PV} = \frac{G_F Q^2}{\sqrt{2}\pi\alpha} \frac{1-y}{1+y^4+(1-y)^4} Q_W^e, \quad (1.49)$$

where

$$y \equiv \frac{1 - \cos \theta_{CM}}{2}.$$

The θ_{CM} term in above expression refers to the center-of-momentum scattering angle.

The data for the Moller scattering experiment was collected through distinct periods spanning from 2001 to 2003. The E-158 collaboration reported a final value of the weak mixing angle at $Q^2 = 0.026 \text{ (GeV/c)}^2$ [37]:

$$\sin^2 \theta_W(Q^2) = 0.2397 \pm 0.0010(\text{stat.}) \pm 0.008(\text{syst.}), \quad (1.50)$$

which is consistent with the value predicted by the Standard Model.

1.10.4 Atomic Parity Violation

In an atomic system, unlike the usual Coulomb interaction which describes the potential between electrons and nucleus for a pure electromagnetic process, the potential with Z^0 involved, V_{pv} , is parity-violating and is proportional to the weak charge of the nucleus, defined as

$$Q_W = (2Z + N)Q_W^u + (Z + 2N)Q_W^d. \quad (1.51)$$

Notice that the weak charges of the quarks rely on $\sin^2 \theta_W$ in the Standard Model and therefore, Eq 1.44 can be also expressed as

$$Q_W(SM) = -N - Z(4 \sin^2 \theta_W - 1). \quad (1.52)$$

It was initially noticed that the range of V_{pv} was much smaller than the atomic scale, which makes the observation of parity-violating effect in atoms extremely difficult. However, after the Z^3 enhancement law was discovered by Bouchiat [38], the experiment of measuring the parity non-conservation (PNC) in atoms became plausible. This Z^3 law states that the electroweak effects in atoms should grow a little faster than the cube of the atomic number Z . This also makes ^{133}Cs , which has a large Z and simple atomic structure, with only one valence electron, an ideal candidate for such an experiment. In the same work, Bouchiat recognized that the parity-forbidden $6S_{1/2} \rightarrow 7S_{1/2}$ transition for Cesium was a good candidate for observing PNC. The $6S_{1/2} \rightarrow 7S_{1/2}$ transition is forbidden because both states have the same parity, however, the involvement of the Z^0 breaks the parity by

slightly mixing the S and P states in the atom. Finally, in 1982, PNC was first measured in Cesium by the Paris group [39] and an improved version was carried out by the Boulder group in 1997 [40]. In both experiments, the so-called Stark-interference technique was employed. In this technique, an external electrical field was applied when the beam of Cesium atoms went through to induce the parity-allowed transition. By reversing the handedness of the applied field, the transition rate related with PNC changed while the induced parity-allowed transition was kept the same. Consequently, by measuring the difference in the transition rate of those two different settings divided by their sums, A_{PV} was determined.

In order to translate the measured A_{PV} into an electroweak observable, like the weak mixing angle $\sin^2 \theta_W$, a computation of A_{PV} is required, in which $\sin^2 \theta_W$ is treated as an input parameter. However, the computation itself might seem to be intractable because the electronic many-body problem is involved: for Cs, one needs to solve the correlated motion of 55 electrons. The computation is simplified by being treated within many-body perturbation theory [41], where most of the higher-rank excitations are suppressed. Based on those assumptions, the most accurate to-date measurement, with claimed 0.35% and 0.4% experimental and systematic uncertainty, respectively, from the Boulder group [39] initially reported a 2.6σ deviation from the theoretical value predicted by the Standard Model in $\sin^2 \theta_W$. However, later theoretical work, which takes advantage of more modern computing resources to enable to account for the effects of higher-rank excitations, has readjusted the result to be in an agreement with the Standard

Model [42].

1.11 Models of Possible New Physics

As we see in Figure 1.5, several PVES experiments provided or will provide complementary probes of different possible scenarios of new physics. Before ending the first chapter, we briefly discuss how the elastic ep asymmetry, which the Qweak experiment is based on, is sensitive to different prospective models in new physics. Note that only a few such models are mentioned here.

1) Additional neutral gauge bosons

Additional neutral gauge bosons arise from the spontaneous symmetry breaking in E_6 theories, which are grand unified theories based on the E_6 gauge group and which have been widely analyzed [43]. They may also arise in left-right symmetric models [44]. Here, we only discuss one of those acceptable low energy models, in which E_6 breaks down to $SO(10) \times U(1)_\psi$ and then to $SU(5) \times U(1)_\chi \times U(1)_\psi$. A general representation of such a new boson, Z' , can be written as [45]

$$Z' = \cos \phi Z_\psi + \sin \phi Z_\chi, \quad (1.53)$$

where ϕ is a parameter to represent different symmetry breaking scenarios, similar to the role of the flavor mixing angle θ_h in Sec. 1.9. Since Z_ψ is not present in the parity-violating asymmetry at tree-level level, the only possible contribution to our measured asymmetry at low-energy level would be from Z_χ with a rather low

mass. The previous PVES data provided a constraint on the mass of such a Z_χ ≥ 1 TeV [45].

2) Leptoquark and R-parity violating Supersymmetry (SUSY)

Leptoquarks (LQ), which carry both the lepton- and baryon- numbers, are predicted in certain Grand Unification Theories (GUT), in technicolor theories, as well as in R-parity violating SUSY models [46]. The low-energy PV observable provides a probe of LQ interactions, and recent data analysis from ZEUS experiment at HERA indicated that the lower limit mass range of LQ ranged from 290 to 699 GeV [47]. Similar to LQ, their analogs in the SUSY can be present as R-parity violating (RPV) or R-parity conserving (RPC) effects. The Qweak experiment could probe the loop effect in RPC effects as well as tree-level contribution in RPV via the precise measurement of the weak charge. The loop corrections in RPC can be as large as $\sim 4\%$ (Q_W^p), while the effect of RPV could be up to $\sim 15\%$ of Q_W^p [48]. The value of $\delta Q_W^p / Q_W^p$, combined with the value of $\delta Q_e^p / Q_e^p$ from the SLAC E158 measurement (see Sec.1.10.3), could determine if SUSY is preferred over other new physics scenarios as well as if the R-parity is conserved or not.

3) Fermion compositeness

In the Standard Model, both fermions and bosons are assumed to be pointlike. However, the possibility that they have some substructure would make their constituents interact in a process, like dilepton production, where pointlike quark and

antiquark pairs annihilate to produce lepton pairs. Therefore, any significant deviation from the Standard Model predicted value in that process could indicate the possible presence of substructure. An analysis of data by the CDF collaboration showed the Λ , the mass scale of such new physics, is in the range of 3.5-6.0 TeV and the upper limit of R is 5.6×10^{-17} cm, where R^2 is the mean-square radius of the quark and lepton [49]. A more precise low-energy parity-violating variable, such as the one in the Qweak experiment, is expected to yield a stronger bounds on those variables [45].

CHAPTER 2

Qweak Experiment Equipment

2.1 Experimental Overview

The Qweak experiment aims at measuring the value of the weak charge of the proton to a high precision, $\sim 4\%$. In this experiment, an 85% polarized electron beam with beam energy of 1.165 GeV at as high as 180 μA current from the Thomas Jefferson National Accelerator Facility (JLab) is used on a 35 cm thick hydrogen target to make elastic electron-proton (ep) scattering happen at a four-momentum transfer $Q^2 \simeq 0.03 (\text{GeV}/c)^2$.

The major components of the experiment include: the polarized beam source, the beam monitors, the beam polarimetry, the QTOR magnet, the detector system and a liquid hydrogen (LH_2) target system [50]. The experimental actually ran under two different modes: event-mode and current-mode. In event-mode, low beam current was used and tracking detectors were put within the elastic beam

envelope to collect information on elastic electrons which travel through, to determine the kinematics. In order to ensure that only the information from elastic electrons are measured, the QTOR magnet was used to bend most of the inelastic electrons away from the detector acceptance. This mode was primarily devoted to measuring the Q^2 and was carried out once every few months. In current-mode, high current beam was used to hit the target to produce the elastic ep scattering events and then the QTOR magnet focused this elastic peak onto the eight symmetrical main detector bars. Most of the experiment's running time was under the current-mode.

The main idea of extracting the weak charge of the proton is simple and can be outlined in Eq. 1.28. However, to complete the proposed 4% precise measurement on Q_W^p presents many experimental challenges, which mainly come from the requirement of precise measurements of the following three quantities: 1) the parity-violating asymmetry A_{LR}^p 2) the beam polarization P_e and 3) the Q^2 . Here, I briefly discuss some of the most important challenges and also show how we designed or made basic choices of experimental apparatus based upon those challenges. Some other challenges will be mentioned separately in subsystem sections later.

The very first basic challenge comes from how we calculate the Q_W^p precisely from our measurement. From Eq. 1.28, one can see that even if we can measure the physics asymmetry and Q^2 to the proposed precision, we still need to calculate the value with the uncertainty from the hadronic form factor $B(Q^2)$, which

is discussed in detail in Sec. 1.6. In order to suppress its effect, we decided to run the experiment at forward scattering angle and low Q^2 . At forward angle, the contribution of the axial form factor component to $B(Q^2)$ becomes negligible and in the region of low Q^2 , the contribution of terms with $B(Q^2)$ is suppressed due to a higher-order of Q^4 as one can see in Eq 1.28. However, the adverse impact of the small scattering angle is that if it is too small, it will make the parity-violating asymmetry too small to be measured with the proposed precision in the given running time. Therefore, $5.8^\circ \rightarrow 11.2^\circ$ is chosen to be the final scattering angle acceptance.

Another challenge in the experiment is the requirement of high statistics, due to the fact that, because of the dominance of the much stronger electromagnetic effect in the process of ep scattering, the parity-violating asymmetry, which is the result of the interference between electromagnetic and neutral weak interactions, is very small and is measured in terms of hundreds of ppb (parts-per-billion) in this experiment. The final statistical error, σ , depends upon the uncertainty in a single measurement as well as the total number of measurements, like

$$\sigma = \frac{\sigma_{\text{single}}}{\sqrt{N}}. \quad (2.1)$$

In order to meet the proposed 2.1% statistical uncertainty on Q_W^p , we proposed the running time of the experiment to be 2200 hours under the current-mode. To keep the experiment running continuously at 180 μA beam current for such a long time, several decisions have been also made upon the design of subsystems. For instance, quartz is chosen to be used as the material of the main detector, because

of its radiation hardness property, which makes it be able to operate normally under high current in the current-mode. In doing so, we chose to integrate the main detector's signals over the helicity window, instead of counting the individual events to collect signals as much as possible per unit time so as to enhance the statistics. Besides increasing the experiment's running time, one can conclude from Eq. 2.1 that another way to yield the small statistical error is to minimize σ_{single} , the uncertainty in a single measurement. In our experiment, σ_{single} can be outlined as

$$\sigma_{\text{single}}^2 = \sigma_{\text{counting}}^2 + \sigma_{\text{electronic}}^2 + \sigma_{\text{target}}^2 + \sigma_{\text{BCM}}^2 + \sigma_{\text{detector}}^2. \quad (2.2)$$

Here σ_{counting} is the Poisson counting statistics, σ_{target} is the target boiling noise and the rest of the σ is the resolution in each subsystem. The 35 cm long liquid hydrogen target was used so as to both increase the scattering rate and minimize the boiling in the target, thereby reducing the σ_{target} (see Sec. 2.4). Other uncertainties, like σ_{BCM} , the resolution in the BCMs, were also monitored and measured in our experiment.

The magnet used in the experiment must satisfy the following three requirements: 1) its field will bend the incident electrons in the dispersive direction and the extent of the bending is based upon the electron's kinematics, 2) its field must be self-contained, which, in other words, means the field must not affect the working mechanism of other apparatus, 3) the cost is affordable and the operation is reliable. Those three considerations made a resistive toroidal magnet the final choice. The first two requirements rule out the possibility of a dipole magnet be-

cause its field has the potential to affect the target, which could then make the proton polarized. The third point shows the advantage of a resistive magnet over a superconducting magnet. In addition to the listed three requirements, we also needed to ensure that the magnet was iron-free for two reasons: the first is to prevent any false asymmetry related with any spin-dependent interactions; the second is to allow an easier way to calculate and manipulate the magnetic field, which is much more complicated when hysteresis occurs in ferromagnetic materials.

The challenge of measuring the Q^2 and P_e will be addressed by using the tracking system and two polarimeters, respectively. The reason to choose two polarimeters is because while one technique (Møller polarimetry) can measure the beam polarization to a high precision, it is invasive, while the other (Compton polarimetry) can perform noninvasive measurements of P_e but it takes longer to achieve high statistical accuracy.

In addition to the statistical uncertainty related with the measured parity-violating asymmetry, one of the biggest challenges in the Qweak experiment is how to reduce the systematic errors on the asymmetry, which mainly come from backgrounds and helicity-correlated false asymmetries. For instance, the pedestals, which is the output signal of the electronics (ADCs, BCMs, *etc*) when beam is absent, can change over time and therefore its magnitude can be helicity-correlated. This requires us to monitor the change and make necessary correction to get the real signal. Furthermore, we also need to carefully study and calibrate

TABLE 2.1: Overview of the Qweak data set

Data set	Time
Commissioning Run	Fall 2010
25% measurement	Jan 2011 to Feb 2011
Run I	Feb 2011 to May 2011
Run II	Nov 2011 to May 2012

each of the electronic devices used in the experiment to ensure that we thoroughly understand their noise level ($\sigma_{\text{electronic}}$).

2.2 Experimental Timeline

The data for the Qweak experiment were collected over four distinct periods. Table 2.1 presents the basic information of each of the running periods. The last three data sets belong to the production data; for each data set, there were some changes, including to both the hardware and software. For instance, in the “25% measurement” and Run I, we mainly relied on BCM 1 and BCM 2 (see Sec. 2.8.1) to monitor the activity of the beam current while in Run II, we also used BCM 5 and BCM 6. Note here that for each distinct data set, the blinding factor (see Chapter 5) is also different so as to allow the data sets to be analyzed independently.

This dissertation covers only the 25% measurement, which is the first section of the production data. This data set was named this way as the anticipated statistical precision was such that it should allow a measurement of $Q_W^p \simeq 25\%$ precision. The analysis of the Run I and Run II is still underway.

2.3 CEBAF Accelerator

The CEBAF (Continuous Electron Beam Accelerator Facility) accelerator at JLab is a five-pass racetrack accelerator which is able to deliver spin-polarized electron beam with energy up to a maximum of 6 GeV at the time of the Qweak experiment. Its main components include the polarized electron source, injector, and two linear superconducting radiofrequency accelerators connected by two arc sections of steering magnets.

Initially, the electrons are generated from a photocathode hit by laser light before going into the injector where they are accelerated up to 67 MeV. Then the electrons are directed into the North Linac where they gain energy up to 667 MeV. After traversing the North Linac, the electrons meet the arc section where the bending magnets are and they are reoriented by 180° through an orbit and are brought back to the linear section of the South Linac for further acceleration. The beam gains another 600 MeV in the South Linac before going into the second magnetic arc section located at the end of South Linac. The electrons will traverse the orbit and are brought back to the axis of the North Linac again. Each electron can repeat this process as many as five times and eventually is able to obtain up to an energy of 6 GeV. The accelerated electron beam is composed of 3 interlaced variable-intensity beams that can be independently directed from any of the five passes to any of the three experimental halls (Hall A, Hall B and Hall C). The accelerator can deliver only a single energy to any one experimental hall at one

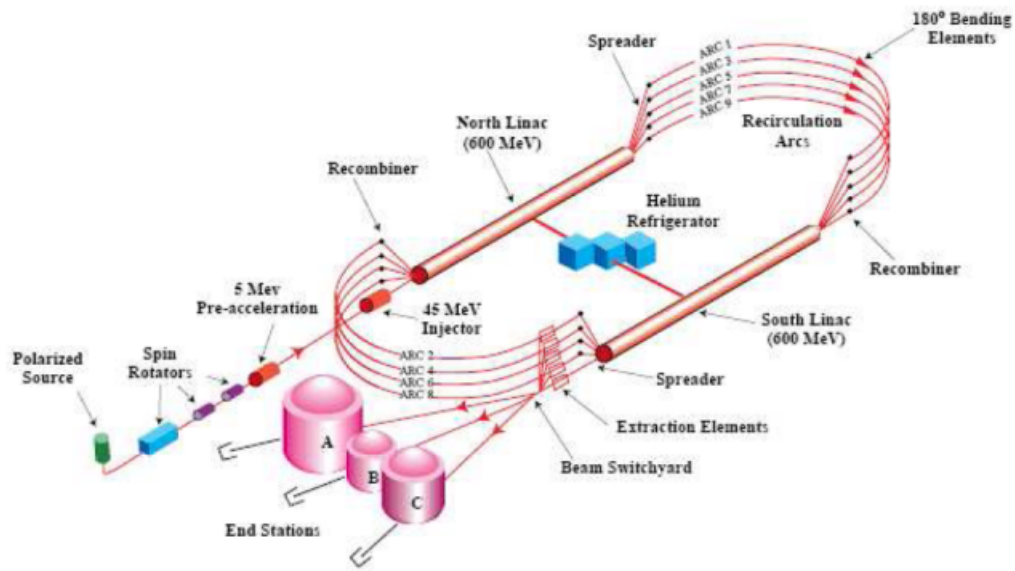


FIG. 2.1: A schematic overview of the CEBAF at Jefferson Lab.

time or the maximum energy (6 GeV) to all three experimental halls. A schematic of the CEBAF accelerator is shown in Figure 2.1.

In addition to the energy requirement for the present experiment, the accelerator must provide an electron beam with high polarization as well as the capability of flipping the electron spin direction from parallel to anti-parallel to the direction of beam motion, or vice versa, at some specific frequency. The first task can be achieved by applying a circularly polarized laser beam with specific helicity state to the photocathode to generate highly polarized electrons through the photoelectric effect. A wafer of GaAs/GaAsP, with a strained-superlattice structure [51], is presently employed as the photocathode in CEBAF as the electron source. The second task can be implemented by changing the helicity state of the circularly polarized laser beam, which will be directed onto the photocathode and therefore determines the polarization of the emitting electrons, through reversing the

voltage applied to an electro-optical device, referred to as a Pockels Cell. The Pockels Cell can flip the polarization of the laser beam at up to 1 kHz and just meets requirement of Qweak experiment, in which the helicity flipping rate is 960 Hz. The helicity signal is generated in a quartet pattern: +- -+ or -++- by choosing the first state randomly and the next one opposite. The reason to choose such a helicity pattern is to compensate any slow linear drift over time during collecting of the signal, as this will cancel out when we calculate the asymmetry, which is defined as

$$A_{Quartet} = \frac{(\sigma^1 + \sigma^4) - (\sigma^2 + \sigma^3)}{(\sigma^1 + \sigma^4) + (\sigma^2 + \sigma^3)}, \quad (2.3)$$

where the superscript i represents the i th helicity state in a quartet, and σ is the cross section.

The Qweak experiment also uses an insertable half-wave plate (IHWP) to change the helicity of the electron beam less frequently, at a period of about every 8 hours. The IHWP can be inserted and removed from the path of the laser to mechanically flip the helicity of the polarized laser. Consequently, the helicity states of the electrons are also flipped. In other words, the helicity signal as recorded in the electronics will be preserved while the true beam asymmetry will be reversed under the influence of the IHWP. In addition, if there is no helicity-correlation in electronics, the average over the measured asymmetries from the two states with IHWP in and out should be zero. Therefore, this provides a powerful tool to detect any false asymmetries brought by the electronics and to calculate the true physics asymmetry. Furthermore, this technique also cancels certain beam-related false

asymmetries, which could be caused by many reasons. For instance, if the Pockels cell is not aligned properly, when its high voltage reverses to change the helicity state, the position and angle of the laser light to enter and exit the Pockels cell might change, which would produce a helicity-correlated beam property and then a false asymmetry. Another false asymmetry, related with the helicity-correlated change in the beam current, arises due to the difference in the voltages, which were applied on the Pockels cell between helicity states. A charge feedback system was then introduced to make small adjustments on the voltages, according to the difference in the produced charge between helicity states.

In addition to the IHWP, the electron helicity can be also slowly reversed by using a spin flipper, which is composed of two orthogonal Wien filters and two solenoid magnets [52]. Unlike the IHWP, which operates on the laser, the spin flipper operates directly on the electrons and therefore brings the benefit of suppressing any potential impacts the IHWP can not address. To accomplish the spin flip, the first Wien filter is used to rotate the electron spin from being in the plane of accelerator by 90° to be in the vertical direction. Then the solenoid is orientated to rotate the spin 90° “left” or “right” back to the in-plane direction. The second Wien filter is set to cancel out the spin processing introduced by the CEBAF transport magnets to make sure the electron beam is longitudinally polarized with only 180° reversed polarization. This second slow reversal technique was typically used about once every month in the Qweak experiment and we assigned a different number to the running period if we used this reversal technique. For instance,

during the 25% measurement, the setting of Wien flipper did not change and we call it “Wien 0”.

2.4 Liquid Hydrogen Target System

The Qweak experiment used a closed-loop circulating liquid hydrogen (LH₂) target, which contains 55 liters of LH₂. The main components of the target system include a He heat exchanger, a 35 cm long target cell, a centrifugal pump and a heater. Under the nominal running conditions, the pressure of the LH₂ flow is between 30 to 35 psia and the volume flow rate is settled to 15 l/s. This flow rate is maintained by the centrifugal pump which is connected to the loop through flanges at one corner of the loop and which turns at 30 Hz. The liquid hydrogen in the target loop is kept at the temperature of 20 K. In order to make the liquid hydrogen run smoothly at the nominal condition with a beam energy of 1.165 GeV at 180 μA , the total amount of 2500 Watts of cooling power is required. This makes Qweak target system the highest power cryogenic target in the world so far. 85% of the cooling power requirement of the Qweak target system comes from the energy deposited in the target, dominated by the ionization energy loss at $4.65 \text{ MeV}/(\text{g}/\text{cm})^3$ for every passing electron at the beam incident energy. The rest of the cooling power requirement stems from heat load for the circulation fan, conductive heat losses, viscous heating, and heat load for the heater feedback circuit which controls the temperature of the target. In order to achieve the goal

of this challenging cooling power, two independent subsystems are employed to provide the liquid Helium which serves as the heat exchange medium. One is the more traditional JLab End Station Refrigerator (ESR), which at its maximum working load, can supply 25 g/s of 15 K Helium coolant, which corresponds to 775 W cooling power. The other is the JLab Central Helium Liquefier (CHL), which is able to supply 25 g/s of 4 K Helium coolant to the experimental Halls from its excessive capacity, which is equal to 2575 W of cooling power. Although the CHL itself seems to be enough for our cooling goal, the Qweak experiment adopted the design of running parallel subsystems for two reasons: one was to make sure the target ran stably and safely even under some extreme cases; the second was to provide more flexibility to reach the equilibrium between the two independent refrigerators by adjusting the working load of the heat exchangers installed in individual refrigerators. The combination of these two cooling sources is obtained through a novel hybrid heat exchanger, which is made of three coolant circuits arranged in three sections. There is another component, called the high power heater, used in the loop to regulate the loop temperature, especially to compensate for the loss of beam heat when the beam is away, in order to prevent the hydrogen in the heat exchanger from freezing.

The design of the target cell was instructed by the use of Computational Fluid Dynamics codes to try to minimize the boiling in the target. The final design chosen was a cell consisting of a conical shape with transverse flow of LH_2 with respect to the axis of the beam, as Figure 2.2 shows. This design also steers most

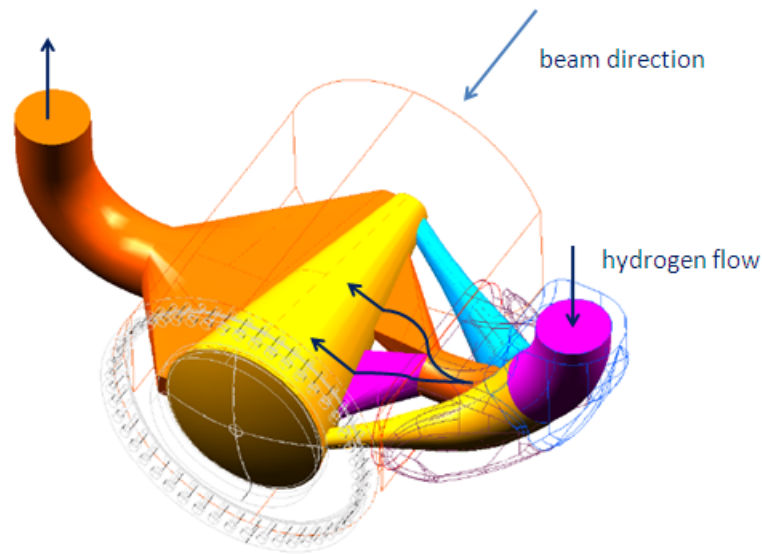


FIG. 2.2: The overview of 7.5 liters of flow space inside the liquid hydrogen target cell. The liquid hydrogen flow is in the transverse direction to the beam axis, the overall length of the target cell is 35 cm and the target cell block itself is depicted as the outer wireframe [53].

of the scattered electrons out in a direction normal to the exit window. The target cell has one entrance (upstream) and one exit (downstream) window, which are primarily made of Aluminum. Both of those two windows are made as thin as possible, with the upstream window thickness of 0.097 mm and downstream window of 0.127 mm, to reduce the ep elastic scattering rate in the Aluminum, which is considered as the biggest background source in the Qweak experiment. Note that the thickness of the exit window is not a constant number. The bulk of the window was 0.635 mm in thickness, however, a thin 0.127 mm nipple with 1.58 mm in diameter, was machined at the very center of the window. This design was to minimize the aluminum background from that region where most of the electrons pass through [53].

To study the background contribution from the aluminum cell windows, two thin aluminum targets are placed at upstream and downstream z locations which are the same as the z location of the hydrogen cell windows. Additional optics targets are used, primarily to test and tune the vertex construction from our horizontal drift chambers. The Al targets, optics targets, various solid targets, along with other ancillary targets were all arranged in a ladder frame, which could be moved in either the horizontal or vertical direction to put each of targets onto the beamline.

One of the key factors which needs to be considered is the target boiling while the incident beam is heating it and therefore changing its density, which will lead to the increasing target boiling noise. This noise will contribute to the asymmetry width and thus has the potential to increase the experiment's running time. This effect can be mitigated in three ways: enlarging the beam raster size, increasing the flow rate of LH_2 in the target loop associated with the pump speed and increasing the helicity reversal frequency. The raster is a magnet system which will direct the beam into an uniform square area on the target. The reason to use a raster is that the unrastered beam has a rather small diameter $\sim 150 \mu\text{m}$ and will consequently produce huge local heating effect which could drill a hole in the aluminum target window. In nominal running conditions, the raster size is usually between $3 \times 3 \text{ mm}^2$ to $5 \times 5 \text{ mm}^2$. The design goal of the target is to make sure the target boiling noise should not increase the experiment's running time by more than 10%, which implies ≤ 125 ppm boiling noise at the nominal running

condition. Special tests were conducted to study the correlation between each of those factors and the contribution from density fluctuations to the width of the asymmetry distributions measured in the main detector. These studies indicated an overall asymmetry width due to boiling $\sigma_{boiling} \simeq 48$ ppm is expected at our normal running condition (170 μA beam current, 4×4 mm² raster size, 30 Hz pump speed and reversal frequency 960 Hz), which met the design goal of the target. Results from some of those studies can be seen in Fig. 2.3.

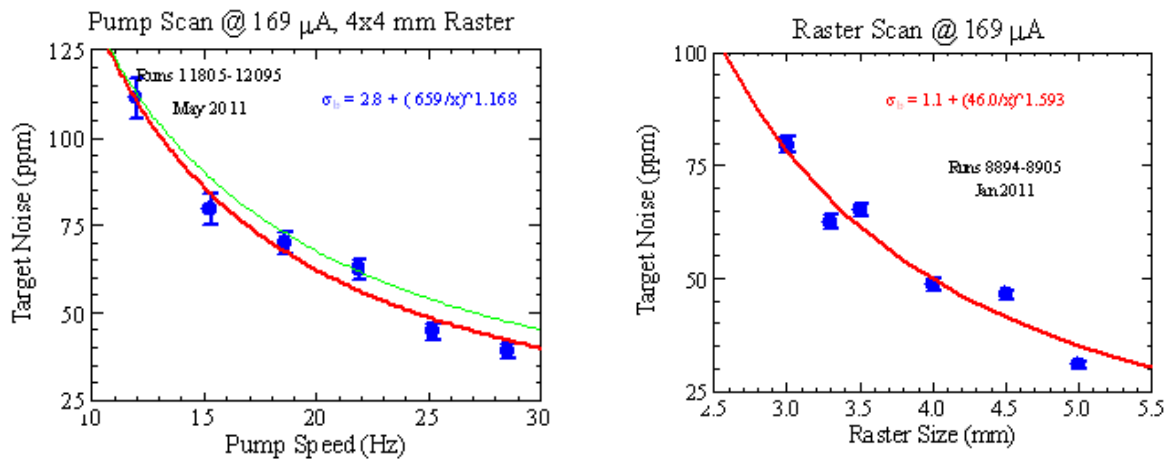


FIG. 2.3: Target boiling noise study at 170 μA with varying pump speed and raster size, respectively. They show that at the nominal pump speed 30 Hz and raster size 4×4 mm², the target noise is well below 50 ppm.

2.5 QTOR Magnet

One of the key components in the Qweak experiment is the magnetic spectrometer 'QTOR'. Its most important function is to focus the elastic electrons onto a set of eight main quartz Čerenkov detectors while bending the inelastic electrons away from the detectors. Due to the requirement of high statistics, the spectrom-

eter had to be designed to have an open geometry which allows the maximum detector solid angle. The axially symmetric acceptance in this geometry also is a desirable feature because it reduces the systematic error related with helicity-correlated motion of the beam. A resistive spectrometer magnet with water-cooled coils, under those considerations, was chosen for the additional reason of the low cost and comparative reliability compared with superconducting solutions.¹

The main purpose of the eight coils with a racetrack shape is to generate the magnetic field. The total DC current to drive the coils under the nominal conditions was 8921 A. The knowledge of the magnetic field was obtained by using a technique called zero-crossing method, which was initially developed for the G^0 experiment [54]. This technique was to find out many points in space where the magnetic field is zero from the experimental data. Since those zero-crossing points were quite sensitive to the actual coil locations, determining the zero-crossing points allowed us to find out the coil locations in reality. Once the real positions or the alignment of the coils were determined, the magnetic field at any point, generated by the current in those coils, could be calculated using the Biot-Savart law.

The physics behind the working mechanism of the spectrometer is quite elegant and straightforward, which can be described using

$$\Delta\theta\frac{p}{e} = \int B_{\perp} dl, \quad (2.4)$$

where B_{\perp} is the magnetic field perpendicular to the scattered electrons' path, θ is

¹Although the magnet itself ran reliably during the experiment, the power supply for the magnet was not running so smoothly and therefore caused the loss of several weeks of running time.

the bending angle, p is momentum of an electron, e is the charge of the proton and d/l represents paths of the electrons. The inelastic electrons' scattered momentum $p_{inelastic}$ is smaller than that from electrons from the elastic process $p_{elastic}$. This, in turn, will give rise to $\Delta\theta_{elastic} < \Delta\theta_{inelastic}$. Therefore, inelastic electrons with smaller momentum will end up having a bigger radius or, bending more drastically, while elastic electrons with bigger momentum will bend less.

Since the scattered elastic electrons have a range of scattered angles, in order to focus them onto the main detectors with finite size, the QTOR magnet had to have a radius-dependent magnetic field, in other words, $\partial B/\partial r$ is not equal to zero. The actual curve is shown in the Figure 2.4. The elastic electrons with smaller angle will experience a larger azimuthal magnetic field when entering into the QTOR while ones with larger angle will experience a smaller azimuthal field. The overall effect is to focus those electrons with different angles onto a certain area, which is where the main detectors are placed.

2.6 Collimators

The collimator system in Qweak experiment plays an essential role in determining the Q^2 acceptance as well as minimizing the background perceived by the main detectors. The design of the collimator system is instructed by GEANT simulation on the basis of consideration of keeping the contribution to the rate on main detectors from inelastic electrons reasonably low while maintaining the rate from

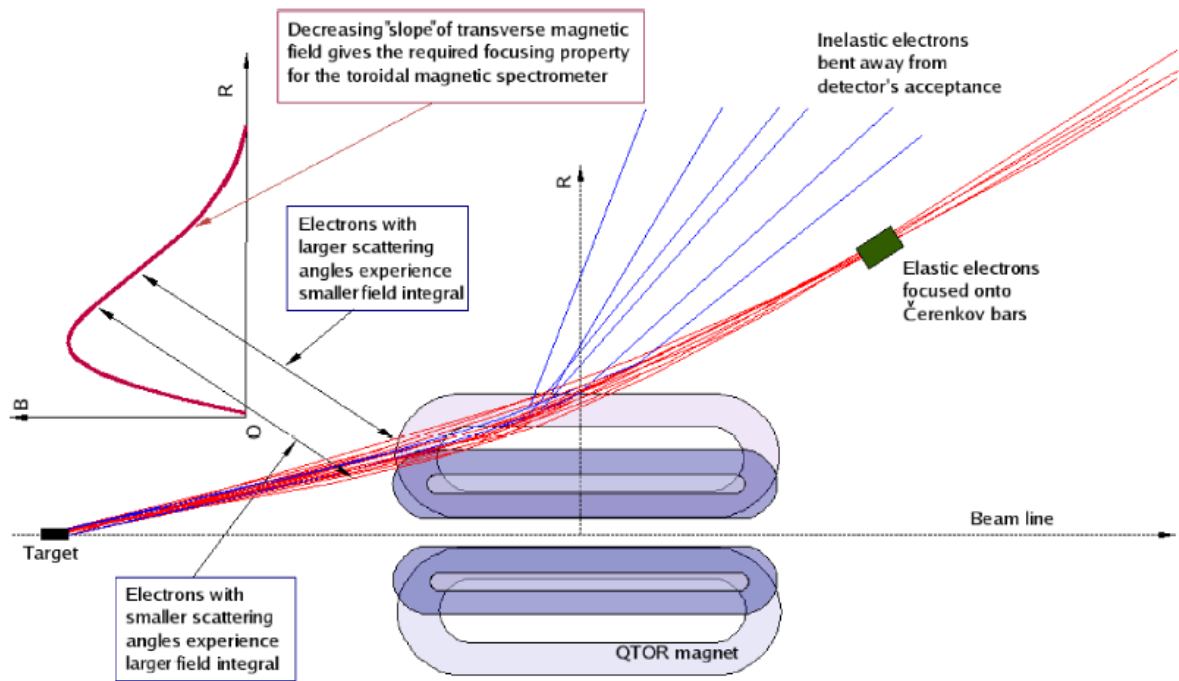


FIG. 2.4: QTOR magnet separates elastic and inelastic electrons while focusing the elastic ones onto the main detectors.

elastic electrons acceptably maximum.

The collimator system consists of three sequential parts (see Figure 2.5), each made of lead antimony (95.5% Pb, 4.5% Sb), the second of which is the acceptance-defining collimator located ~ 30 cm before the first plane of the Horizontal Drift Chambers. The other two are employed for the purpose of “screening background events”, namely, to prevent direct line-of-sight from target to detectors and thus to suppress neutral backgrounds, which mainly consist of photons and neutrons. Each of the collimators has eight azimuthally symmetric openings, as Fig 2.6 shows. The thickness of the primary collimator (collimator 2) is 15 cm, the area of each of its eight openings is around 400 cm^2 , and the radial distance from the center position of the openings to the beamline axis is approximately

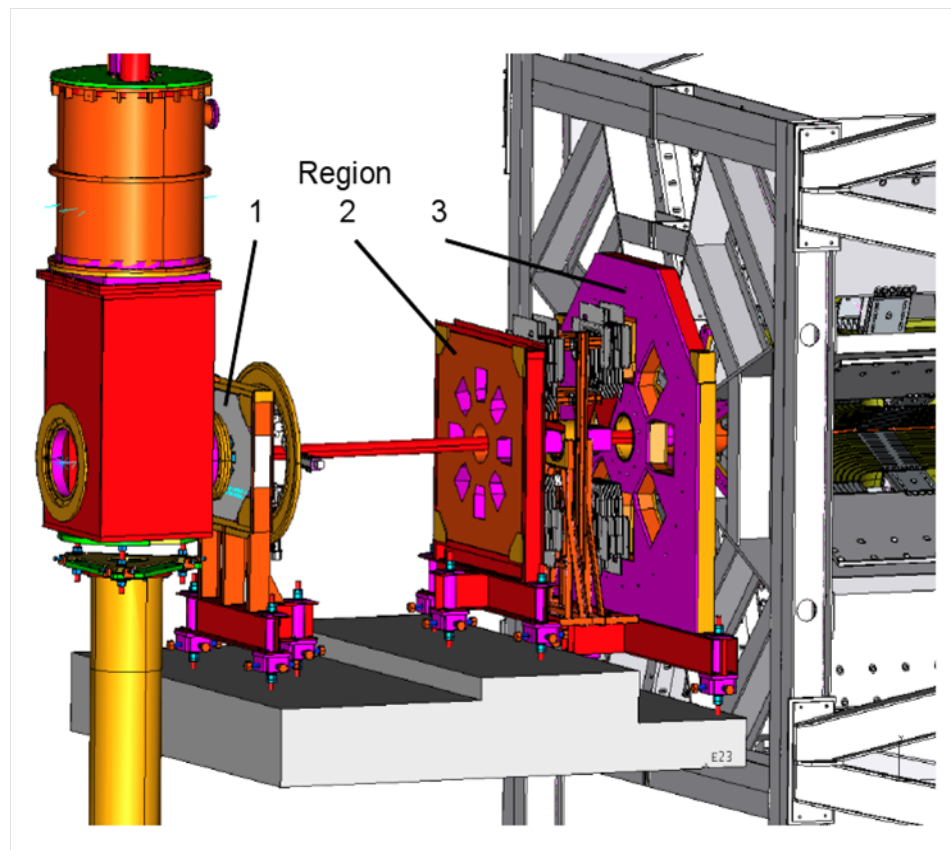


FIG. 2.5: CAD drawing of the locations of the collimator system, which consists of three separate parts.

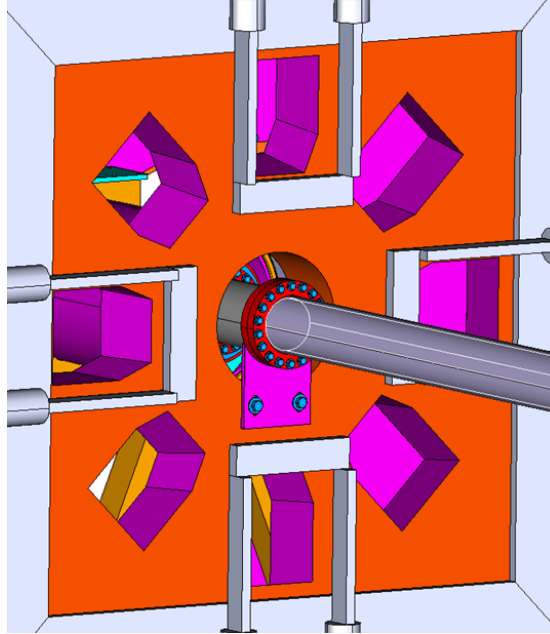


FIG. 2.6: CAD drawing of the primary collimator, which has eight openings and are placed azimuthally symmetric along with the beam line.

35 cm. The positions of the collimators, especially the primary collimator, were measured from a precision survey; the reason to do that is because the position of the collimator largely determined our elastic electrons' profile and therefore the scattering angles, which the measurement of the Q^2 relies upon.

In addition, a water-cooled tungsten plug was installed about 1 meter downstream of the target in order to prevent the small-angle $0.75^\circ \rightarrow 4^\circ$ scattered particles from interacting with the downstream beamline in the region, where secondary scatterings could then hit the main detectors.

2.7 Detector System

The Qweak experiment, as described before, was designed to run under two modes: current-mode and event-mode. Different detectors with different configuration were employed under those two running conditions. Under current-mode, in which high current beam was used, the main detectors, consisting of eight fused silica bars, were responsible for detecting the elastic electrons focused by the QTOR magnet and generating the output signal through integration of the detector response. The tracking detectors, combined with main detectors running under conventional pulse data collecting mode, were only employed under event-mode, in which few pA to 100 nA magnitude of current beam was supplied to detect the elastic ep scattered electrons on an event-by-event basis and therefore provided an opportunity to study the four-momentum transfer Q^2 as well as some background contributions.

2.7.1 Main Detectors

The Qweak experiment used eight Čerenkov detectors, which are positioned symmetrically about the beam axis downstream of the QTOR magnet, ~ 1229 cm from the center of the target. Each Čerenkov detector was made by gluing two 1 meter long, thin rectangular fused silica radiators (Spectroil 2000 material) together to form the final size: 200 cm (L) \times 18 cm (W) \times 1.25 cm (T). Each of the eight fused silica bars were placed in a light-tight box to reduce the background and

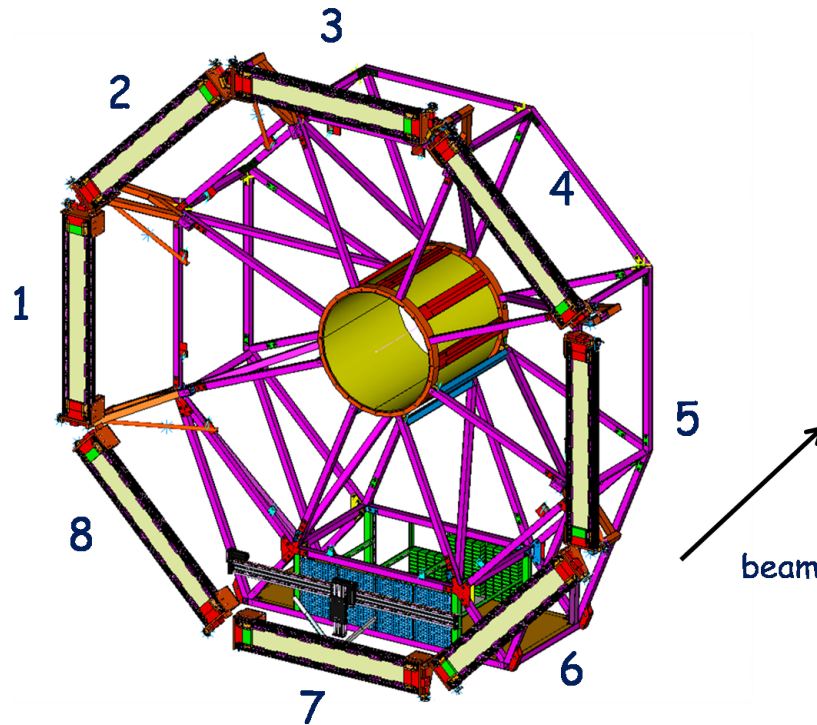


FIG. 2.7: CAD drawing of the main detector system. Eight fused silica bars were installed on a Ferris wheel to support them at desired positions. The numbers were used to distinguish distinct main detectors depending on their position. In this dissertation, this number scheme is used when referring to specific main detectors.

were installed on a Ferris wheel structure to hold them at desired positions, as Figure 2.7 shows.

Čerenkov radiation occurs when charged particles pass through a dielectric medium at a velocity bigger than the speed of light in the same medium. Some of the photons emitted during the radiation will be directed via total internal reflection towards the end of the detector bars and can therefore be collected by one of two 5 inch Photomultiplier tubes (PMTs), one each installed at either end of the bar. These are located away from the scattered electron beam envelope in order to prevent the scattered electrons from directly interacting in the PMTs. In order to

further reduce interaction from the background in the PMTs, a 5 cm thick lead brick was mounted before each PMT. A light-tight housing made of aluminum was also used as an electrostatic, magnetic and physical protection. The PMTs are Electron Tubes model D753WKB with S20 photocathode, SbCs dynodes and UV glass windows. The PMTs were operated with two different settings: one with nominal gain during current-mode and another with high gain for event-mode data taking. Under event-mode running, the event rate in each of the main detectors was less than 1 MHz. The signal was read out for every event and the PMT's bases were switched to high gain, which was as high as 10^7 to guarantee enough sensitivity. For current-mode, the event rate generated in each of the main detectors was as high as 800 MHz so that the PMT's anode current would be $6.4 \mu\text{A}$ if we assume that 50 photoelectrons are generated for every incident primary electron. The PMT's bases therefore had to be switched to a mode with a low gain of 1000, so as to keep a low enough current to maintain an adequate lifetime for the PMTs during the experiment's running time. Then the signal was sent to a high gain I-to-V operational amplifier to convert it to a voltage signal. Finally, the signal is fed into an Analog to Digital Converter (ADC) (see Sec. 2.7) to get the integrated digital signal.

One of the most major source of noise that could contaminate the signal from the main detectors is "soft" background. Although low-energy photons do not produce Čerenkov light in the main detector, high-energy photons, such X or γ rays, can create electrons with high velocities through either electron-positron pairs or

the Compton effect. These electrons and positrons can generate Čerenkov light when passing through the main detector. In order to reduce this effect, 2 cm thick lead pre-radiators were installed in front of the main detectors and were used to reduce the flux of high-energy photons. Apart from reducing the soft background, there is another benefit of using pre-radiators: the scattered electrons going into the pre-radiators will cause electromagnetic showers, thereby creating many secondary electrons, each of which can generate Čerenkov light in the detectors. This shower effect increased the signal size by a factor of 6~7 compared to the use of “bare” detectors. However, we must consider the excessive noise brought by this shower, which will cause more statistical error. Extensive GEANT simulations were carried out to determine the optimal thickness of pre-radiator which would cause the minimum excessive noise width. The final result determined 2 cm to be the optimal thickness, which results in 12% excess noise, or equivalently, an additional 25% in running time. At the beginning, due to this high cost of additional running time, we did not plan to use pre-radiators in the experiment, but during the initial commissioning data-taking period, the collaboration found out the “soft” backgrounds were ~ 10 times bigger than expected and therefore the use of the pre-radiators was essential.

Pedestals from the main detectors, which are the output of its electronics when the beam is absent, is also must be carefully monitored and subtracted from the raw signal when calculating the yield from the main detectors. The pedestal appears as a peak in the ADC spectrum. Therefore, pedestal runs were taken at

least once per day or whenever the beam was not available to gather as much data as possible to get the most updated values.

2.7.2 Tracking Detectors

As already mentioned, the Qweak experiment was designed to run in two modes: event-mode and current-mode. The tracking detectors described here could only be used under event-mode, in which a current of order of ≤ 100 nA was employed. The main purpose of the tracking detectors was to determine the kinematics of the scattered electrons, therefore to deduce the four-momentum transfer Q^2 to the required precision. Notice here that the Q^2 , before being used in the Eq. 1.28, needs to be weighted by the analog response of the main detector, because the parity-violating asymmetry was measured under the current-mode. The tracking detectors consisted of two regions of wire chambers: Horizontal Drift Chamber (HDCs) and Vertical Drift Chambers (VDCs). One additional instrument, a focal plane scanner, was located in one octant (octant 7) and could be positioned either upstream or downstream of the main detector in that octant.

Horizontal Drift Chambers

Two pairs of HDCs were built by Virginia Tech collaborators and were installed on the opposite sides of a rotating support structure, located just before the entrance of the QTOR magnet but behind the primary collimator, see Figure 2.8. The HDCs could cover two opposite octants at one time but also had the capability of being

rotated to cover all eight octants, as well as to be moved radially outward to a “parking” position, which is out of the acceptance during current-mode running. There was also a pair of octants (2 and 6) that could be covered redundantly by either pair. The main purpose of the HDCs was to reconstruct the trajectory of the scattered electrons and therefore determine their kinematic information, such as their scattering angle, point of origin in the target, etc. Each package of HDCs contained two sets of chambers, separated by around 4 cm in z in order to provide an angular resolution of ≈ 0.6 mrad and position resolution of $\approx 200 \mu\text{m}$. A 2050 V voltage was applied onto the aluminum-coated Mylar foils in the HDCs to create the electrostatic field to make them operate. Each wire plane had 32 gold-plated tungsten sense wires with $20 \mu\text{m}$ diameter and each sense wire was separated by 1.1684 cm.

Each chamber consisted of six wire planes (in the order of $xuvx'u'v'$) where the orientation of u and v planes have a tilted angle of 53° with respect to the short side of the plane. The gas mixture used in the testing period at Virginia Tech was Argon-65%-Ethane-35% and in the experiment running time at JLab, Argon-50%-Ethane-50% were used for the 25% measurement and Run I. In Run II, bottled Argon-65%-Ethane-35% was used.

Vertical Drift Chambers

Five Vertical Drift Chambers were designed and built by our group at the College of William and Mary. More details regarding the building and testing of the VDCs

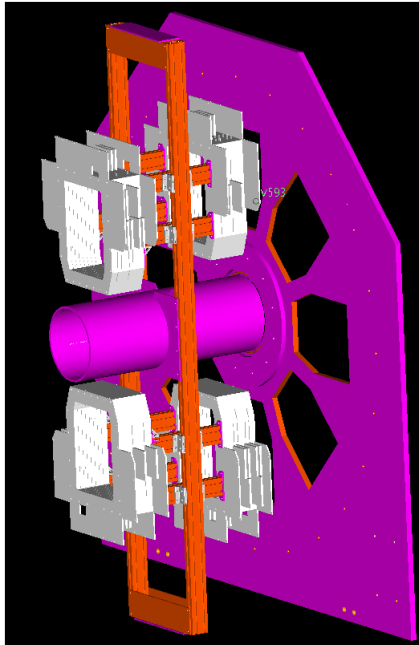


FIG. 2.8: The schematic of the HDCs, installed on a rotating system, covering octant 3 and 7 in the figure.

can be found in [55]. Four VDCs were shipped to JLab in May of 2010 and two sets (each set has two VDCs) were installed on the opposite sides of a rotator in front of the main detectors. Just as for the HDCs, they could be rotated about the axis of beam line so as to cover all eight octants, as Figure 2.9 shows. In addition, one pair of octants (3 and 7) could be covered redundantly with either package to make sure there was no bias brought by the individual properties of the packages. The term “package” here refers to each pair of VDCs and this term was also used for HDCs. The VDCs could also be removed radially inward along the rotator’s arms to avoid damage in the current-mode because of the high rate electron flux and to prevent interaction of the primary electrons in the VDCs.

The purpose of the VDCs is to ensure that detected electrons are truly from elastic events and also to characterize the particle trajectories entering the main

detector. The main components of each VDC are two wire planes with different wire orientations (noted as u and v , each tilted at 26° with respect to the long side of the plane). Unlike the alignment with the HDCs, which were placed normal to the beamline axis, the angle between the VDCs' wire planes and the beamline axis is $\sim 65.5^\circ$. The sense wires used were gold-plated tungsten wires with $25 \mu\text{m}$ diameter, each separated by 0.4921 cm in the perpendicular direction to the wire. Each plane had 279 sense wires which adds up to 2232 wires in total for all eight wire planes.

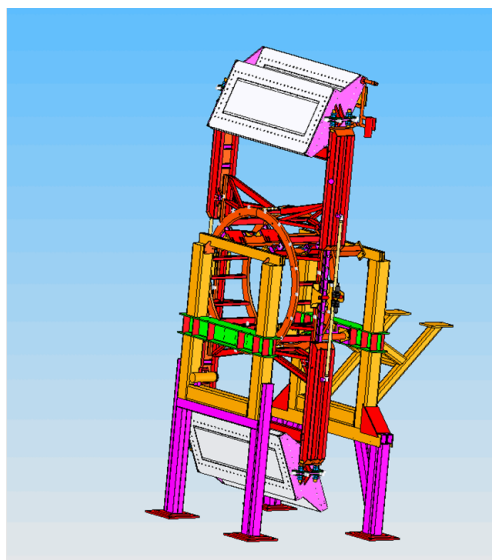


FIG. 2.9: The schematic of the VDCs, installed on the Ferris wheel, covering octant 3 and 7 in the figure.

Each VDC also had three high voltage planes made of aluminum-coated Mylar foil. When in operation, a negative high voltage as high as 3900 V was applied to those planes. Along with the grounded sense wires, this provides the electric field needed for the electrons after the initial ionization to drift towards the sense wire, undergoing repeated collisions with the gas molecules. If the electric field is

strong enough, another electron can be knocked out from the gas molecule which can repeat the process to ionize more gas molecules and therefore produce more electrons. This effect is called an avalanche and it is essential for the drift chamber to work, because when all the electrons from the avalanche are collected by wires, a measurable current is obtained. In order to generate ionization when the charged primary particle is passing through, gas is needed to fill up the chamber to provide such source of the ionized electrons. Cosmic ray data, combined with the Garfield [56] simulation helped us to pick Argon-50%-Ethane-50% , which was bubbled through isopropyl alcohol, to be the final gas mixtures used in the experiment due to some good features, such as high efficiency.

The amplifier/discriminator chips (MAD) [57] serve as the central part of the front-end electronics of the VDCs. Each MAD card has 16 channels, with a sense wire attached to each channel, and was mounted on the circuit board. After the sense wire is hit, the analog signal is amplified, discriminated and then converted to a TTL logic signal by the MAD chip, which are installed on a JLab customized pre-amp discriminator board, and then converted to a Low-voltage differential signal (LVDS) through a driver to feed twisted-pair cables carrying pulses with opposite signs, which have been used to reduce the radiated electromagnetic noise. The twisted-pair cables were referred as ribbon cables and their length is approximately 45 m. Then the signal was converted into Emitter-Coupled Signal (ECL) and duplicated. Those duplicated signals then went through digital delay lines equipped with a string of hex buffer logic chips serving as delay chips, each of

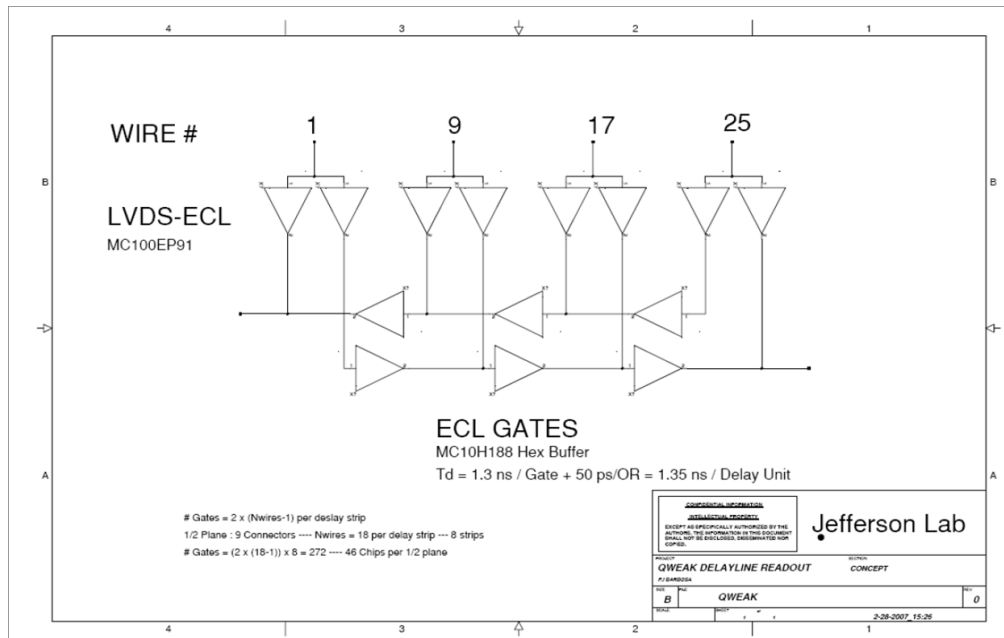


FIG. 2.10: The layout of the multiplexing (MUX) system used in the VDCs. The LVDS signal for each wire is split into two identical ECL signals. Then the ECL signals pass through two delay lines (“left” and “right”), equipped with a series of hex buffer chips used to generate discrete steps of time delay.

which provided a 1.3 ns delay (see Figure ??).

This is where the technique of multiplexing comes in. Instead of connecting every wire with a single time to digital converter (TDC) channel, we grouped 18 wires, each separated by eight wires, into two delay lines and connected the ends of each delay line with two different TDC channels (referred as “left” and “right”). Therefore, which wires are grouped together are determined by the first wire number, giving by

$$w_i = w_0 + 8 * (i - 1), \quad i = 1, 2, 3 \dots 18.$$

By calculating the time difference between the signals from the left and right channels, the wire number can be deduced and the timing information can be assigned to that wire. By adopting this technique, we saved the number of TDC channels

needed by a factor of 9, and thereby reduced the cost of the VDC electronics considerably.

The typical single-wire efficiency of the VDCs was $98.55 \pm 0.05\%$ [55]. During the Run I, the VDCs behaved very stably and reached the expected resolution $\sim 260 \mu\text{m}$. More of the tracking-related performance result will be shown in the fourth chapter.

2.7.3 Trigger Scintillators (TS)

Two plastic scintillation counters were used to provide the trigger in event-mode data taking, as well as the reference time for the tracking drift chambers. They were designed and built by collaborators from George Washington University. One was mounted on one arm of the VDC's rotators and the other was mounted on the other arm. Therefore, the scintillators could rotate along with the VDCs to cover all of the octants. Each scintillator was made from BC408 (a solid solution of organic scintillating molecules in a polymerized solvent) made by Saint-Gobain and was 218.45 cm long, 30.48 cm wide, and 1 cm thick. The size of the scintillator was larger than the Čerenkov bars to make sure that all the elastic electrons that hit the main detectors must generate a signal at the scintillators.² Two Photonic XP 4312B PMTs with 3 inch diameter were coupled to each of the scintillators at two ends (referred to as "left" and "right"). Then it could provide a high gain

²In the Qweak experiment, we chose to use only one TS per octant to minimize the material in beam profile. At low beam currents $\simeq 50 \text{ pA}$, the trigger rate was dominated by false triggers due to cosmic rays and room background. In hindsight, 2 layers would have perhaps better effect because it would get rid of those false triggers and thus obtain more clean triggers.

($\sim 10^7$), which allowed us to see around 100 to 300 pC of charge of the signal with a full width half maximum (FWHM) of 3.5 ns for a single photoelectron. On each end of the scintillator, there are six “finger” light guides (see Figure 2.11). The reason to choose this kind of light guide is because it could collect more light and provided better timing resolution compared with other types.

The TS also utilized a Constant Fraction Discriminator to reduce the “time-walk” effect, in which the pulse output time depends on the pulse amplitude. It also used a mean-timer to average the logic signals from both PMTs at the two ends. The output pulse was therefore essentially independent of the timing difference between the two input signals, which were caused by hit position dependence. The resolution of the mean-timer TS output signal was measured to be 460 ps (rms value). During the production running, the typical efficiency for the TS was about 98%~99%. For more information regarding the TS subsystem, see [58].

2.7.4 The Focal Plane Scanners

As discussed, the tracking system could only be operated at low beam current (≤ 100 nA) and could map the light weighted $\langle Q^2 \rangle$ over the main Čerenkov detectors. However, in the current-mode with high current, in which the parity-violating asymmetry was measured, the tracking system could not be operated. However, the focal plane scanner, which could be employed under both modes, provided an elegant way of indirectly measuring the $\langle Q^2 \rangle$. Therefore, we took the scanner data both at event-mode and current-mode to ensure the light-weighted Q^2 is the

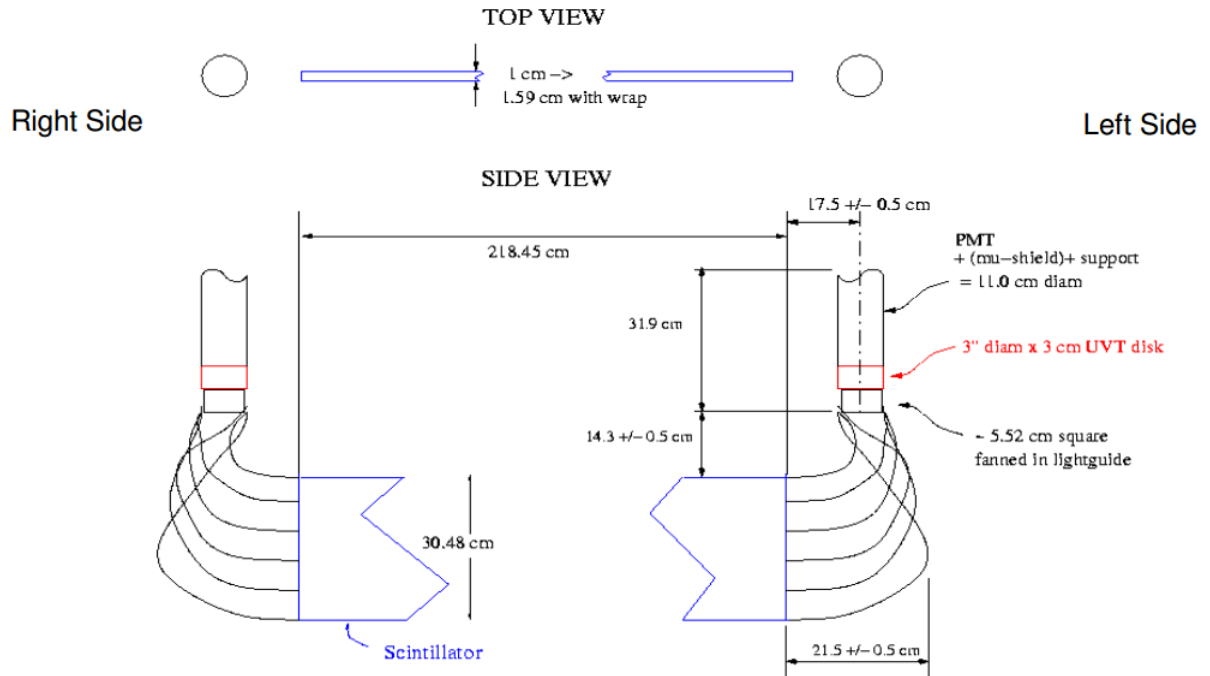


FIG. 2.11: The schematic of the Trigger Scintillators and their light guides.

same under both modes.

The focal plane scanner consisted of two quartz Čerenkov detectors with 1 cm thickness, one placed on top of the other, with a $1 \times 1 \text{ cm}^2$ active area. Two quartz detectors were used here to get rid of background noise and could be operated in the condition where the signal rate is as high as 1 MHz. Each quartz detector was coupled to a PMT by an air light guide and the PMT were thus used as the read out device. The scanner motion system could move detectors slowly at a steady rate across the fiducial area of one main Čerenkov detector and to count the rate at which it was hit. By doing this, we could get the light-weighted rate distribution over that Čerenkov detector. By comparing with the distribution under the event-mode, if we find them to agree with each other at high precision level, then we can safely conclude that the $\langle Q^2 \rangle$ directly determined at event-mode can

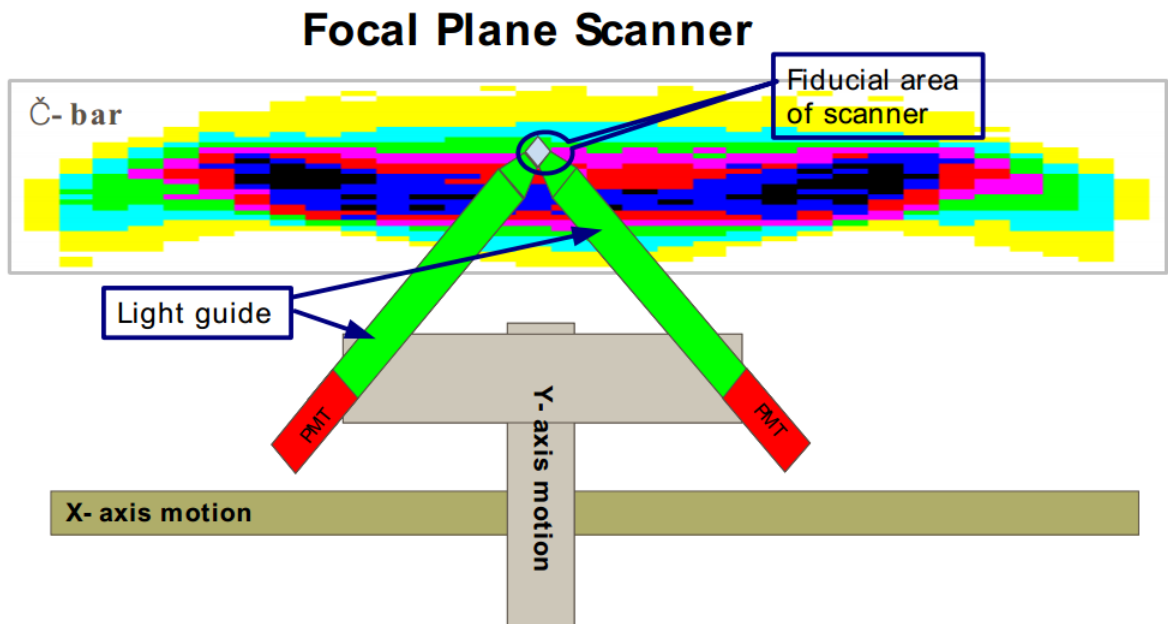


FIG. 2.12: The schematic of the Focal Plane Scanner. Two $1 \times 1 \times 1 \text{ cm}^3$ quartz detectors were overlaid to get rid of background noise. Each individual PMT, as a read out, was coupled to each piece of detector through an air light guide.

be used under current-mode. A schematic of the Focal Plane Scanner is shown in Figure 2.12.

2.8 The Data Acquisition Systems

The Data Acquisition System (DAQ) consisted of two parallel subsystems: one for current-mode integrating of the signals from the main detector and beam instrumentation and the other with event-mode collecting the signals from the tracking system as well as beamline instrumentation. These two DAQ systems were implemented in two distinct crates and used distinct DAQ analysis software.

The essential parts of the current-mode data taking were the 18 bit, 500 kHz

sampling ADCs built by TRIUMF. Their main purposes were to integrate and digitize the signal from the main detectors' PMTs. The integration must be implemented for each helicity state because we need to calculate the difference between positive and negative helicity states. This was achieved by using the MPS (~ 960 Hz) as the trigger for each integration period. Under that integration rate, the data rate was 4.5 MB/s, independent of the beam current. The same type of ADCs were also used to collect the digital signal from beamline monitors (BCMs and BPMs) in the accelerator injector as well as in Hall C. The beam monitors and the main detectors were digitized in separate crates, so as to minimize cross-talk which could cause helicity information from beam monitors to generate false asymmetries in the main detector's signals.

Under event-mode, the scattered electron rate was much slower, so we were able to record individual particle's amplitude and timing information, and the tracking DAQ system behaves like a conventional spectrometer DAQ. In order to fulfill this task, individual electrons triggered the recording of information from what has been defined as one event, which normally lasts around 400 ns (determined by maximum drift time in the drift chamber). The front-end electronics of the tracking DAQ was all based on VME, using the JLab F1TDC [59] to record the timing signals from the HDCs and VDCs as well as the trigger scintillators and the main detectors. The tracking system also employed ADCs for the main detectors and the trigger scintillators to record the signal amplitude from their PMTs. SIS3801 scalers from JLab [60] were used to digitize various rates. The beamline informa-

tion from the same VME crate can be accessed by the tracking DAQ system for the same purpose under the current-mode. The tracking DAQ could be operated at rates up to 6 kHz, at which rate the DAQ was saturated with $\simeq 100\%$ dead-time. For a typical Q^2 measurement, the beam current was about 50 pA and the rate recorded by both TS was ~ 1 kHz, which caused no problem for the tracking DAQ system. However, the current could be as high as ~ 100 nA for certain studies in the tracking runs and the rate in both TS was then ~ 50 kHz, which exceeded the maximum rates the tracking DAQ could handle. In order to solve this problem at higher current, we prescaled the incoming data to lower the rate by a certain factor. After prescaling, the rate was dropped down to $1 \rightarrow 2$ kHz in order to minimize the dead-time.

All the data collected by our DAQ system was streamed into raw data files in the CODA (CEBAF Online Data Acquisition System) format [61]. CODA is a software tool along with highly modular hardware and is used for all three Halls. The basic unit of CODA is the read-out controller, also known as the ROC, which generally runs VxWorks or Unix to communicate with the Unix processes on the host CPU. Each DAQ subsystem has its own corresponding ROC number and the ROC number is stored into the data file and therefore can be used by the analysis software to connect the information with individual piece of equipment.

2.9 Beam Instrumentation

One of the most biggest systematic error sources in a parity-violation experiment is a false asymmetry, which can be caused by a helicity-related beam property change. The Qweak experiment is no exception, and the proposed experimental precision requires any individual beam-related false asymmetry to be $\lesssim 1$ ppb. In order to meet this requirement, beam monitors are needed which can provide relatively precise, non-invasive continuous measurement of beam properties over the entire experiment's running time. Those beam properties include beam charge and its helicity-correlated difference ΔQ ; beam energy E and the energy difference ΔE ; beam position and angle at target X, Y, X', Y' and their differences $\Delta X, \Delta Y, \Delta X'$ and $\Delta Y'$.

2.9.1 Beam Current Monitors

The asymmetry used in our experiment is based on normalized yields given by

$$A_{ep} = \frac{Y^+ - Y^-}{Y^+ + Y^-}, \quad (2.5)$$

where Y is value of main detector's yield after being normalized to the beam charge. As we mentioned before, we used a charge feedback system (see Sec. 2.3) to control the charge asymmetry, and this normalization is meant to further reduce the effect of any helicity-correlated change in beam charge. However, a false asymmetry still might occur when there is a nonlinearity in either the main

detector response or the charge monitor. Therefore, in order to reduce such false asymmetry and to measure the beam current precisely, cavity-style beam charge monitors (BCMs) are used in Hall C for a noninvasive, stable and linear beam current measurement. The working mechanism is implemented by using a cylindrical cavity that is resonant with the transverse magnetic mode TM_{010} at the frequency of 1479 kHz [62]. When the beam passes through the cavity, it will be slowed by an infinitesimal amount because of the electric field, from which power will be extracted from the beam and stored in the cavity temporarily. Half of the stored radiofrequency (RF) power will be extracted magnetically by a loop antenna and then sent to the electronics for later processing. The output RF signal can be processed to lower frequency, filtered to enhance the signal/noise ratio and then converted to a DC signal, which is then digitized and recorded.

Since the output RF signal is only proportional to the beam intensity, but does not provide an absolute calibration, we must use an Unser monitor to allow an absolute measurement of the beam current, based on the relative measurement of the BCMs [63]. The Unser monitor is a toroidal transformer designed to make stable direct measurement of the beam current at high currents. The Hall C BPMs are normally calibrated with respect to the Unser monitor at high currents and thus have the capability to provide a direct measurement of the beam current over the entire experiment period except for the tracking runs (due to the too low current) because of the linear and stable measurement of the BCMs over a large dynamic range.

Distinct BCMs were employed in the Qweak experiment for different running periods. For the 25% measurement and Run I, two BCMs (BCM1 and BCM2) with analog receivers were used as the main current monitors in the Run I. They are separated by 1 meter and positioned in the beam line with one (BCM1) in front and the other behind the Unser monitor. The cavity and Unser monitor are enclosed in a grey box to provide good magnetic and temperature stabilizations. The resolution of BCM 1 and 2 were approximately 100 ppm (at 960 Hz) during the Run I, which contributed to the width of asymmetry distribution in main detectors as excess noise and was equal to a loss of $\sim 10\%$ of total experiment's running time. In order to improve the resolution, we decided to use four BCMs (BCM 5,6,7,8) with new JLab-designed digital receivers for Run II [64]. The data showed they outperformed the old BCM 1 and 2, with resolutions ≤ 65 ppm. In addition to the resolution of the BCMs, the nonlinearity issue for the BCMs were also taken care of because it might produce the false asymmetry through any nonlinear relationship between true beam current and measured current in BCMs, like

$$I_{BCM} = I_{true}(1 + \alpha I_{true}), \quad (2.6)$$

where α is just a parameter to indicate how big the nonlinearity is. Note Eq. 2.4 is just a simple example of the linearity and the relationship between true beam current and measured value might be much more complicated than Eq. 2.4. Special tests were carried out to study the nonlinearity in BCMs and the conclusion was that, over the full dynamic range of $10 \rightarrow 180 \mu A$ in current-mode, the degree of nonlinearity in the BCMs was pretty small, with a residual varying at $\sim \pm 0.4 \mu A$

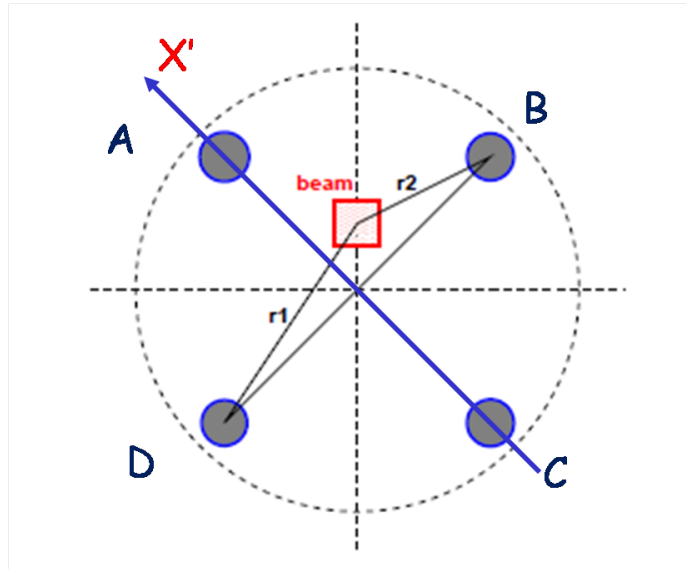


FIG. 2.13: Layout of the 4-wire BPM. The grey circle indicates where the stripline wire is located while the rastered beam is shown as a red box which is away from the central axis of the BPM

level [65].

2.9.2 Beam Position Monitors

In addition to knowledge of current intensity, beam position must be determined to some precision as well, in order to reduce the false asymmetry caused by helicity-related beam position and angle change. Beam position measurements are carried out along the beamline at different positions by using the stripline beam position monitors (BPMs).

A stripline BPM consists of 4 quarter-wave antennae, labeled as X^+ , X^- , Y^+ , Y^- . Each antennae is positioned at 90° to each other, and are rotated 45° about the axis of beam line, as Figure 2.13 shows. When the electron beam passes through the BPM can, currents are induced on the stripline, which picks up the fundamen-

tal frequency of 1497 MHz of the beam. The intensity of induced current on an individual stripline is proportional to r to the first order, where r is the distance from the beam position to the stripline. The difference between signals from the opposite striplines, which are 180° apart, will determine the relative offset along the axis which connecting those striplines after divided by their sum. As Figure 2.13 shows, the beam position along with the X' axis, which is the straight line that passes through stripline A and C, can be deduced by

$$X' \propto \frac{V_A - V_C}{V_A + V_C}, \quad (2.7)$$

where V is amplitude of the signal collected on the stripline. Similarly, the beam position along with the other axis connecting B and D can also be determined. Then a 45° rotation can be made in order to calculate the position in the lab-based coordinates (X, Y) from the wire-based coordinates (X', Y') . However, if there is a difference in the gains between the signals of two opposite striplines, a bias in the measurement occurs. In order to reduce this effect, the switched electrode electrode (SEE) technique was used in the Hall C BPMs. The main idea of this technique is to sequentially connect the opposite striplines to the same RF front-end electronics through a pair of GaAsFET switches. Consequently, a series of signal from opposite striplines are produced and they are insensitive to any changes in gains of electronics. The SEE BPMs also have a wide dynamic range, which allow them to operate at currents inside a range between $1\mu A$ and $1000\mu A$.

Similarly to the nonlinearity issue for the BCMs (see Sec. 2.9.1), a false asymmetry might arise due to the dependence of the measured value in BPMs on

the beam current. However, it can be shown that the false asymmetry may exist but with a negligible contribution to our measured asymmetry [66].

For both the BCMs and BPMs, the pedestals need to be measured for the purpose of an unbiased output. In the case of the BCMs, the Unser monitor is employed which could provide a pedestal calibrated read out. By changing the beam current, linear fitting of the BCM and the Unser signal could be performed, and the intercept is equal to the BCM pedestal value. In order to extract the BPM pedestals, the signals of the wires over a range of currents were plotted and extrapolation to zero current was carried out. This method also applied to the extraction of the luminosity monitors pedestals, which will be described in the next section.

2.9.3 Luminosity Monitors

Qweak employed two sets of luminosity monitors (“Lumis”): four at an upstream position, each oriented at 90° to each other and mounted to the upstream face of the primary collimator (see Figure 2.6); another eight were at a position 17 m downstream of the target, oriented at 45° to each other (see Figure 2.14). All of them were put at the position which was close to the beam axis and thus have higher counting rates compared with the main detectors. Each luminosity monitor is a Čerenkov detector built from fused quartz with an active area $4\text{ cm} \times 3\text{ cm} \times 1.5\text{ cm}$ for the upstream set and $25\text{ cm} \times 7\text{ cm} \times 2\text{ cm}$ for the downstream set.

We must make sure that any fluctuation in the density of the hydrogen target

caused by the incident electrons does not broaden the experimental asymmetry width in the final asymmetry measurement. The upstream luminosity monitors, which were placed at a scattering angle of 5° , were expected to give about 6 times smaller statistical error than the main detectors and are employed as a monitor for target density fluctuations. Since the total width of the measured asymmetry distribution is the quadrature sum of the statistical error, the width due to density fluctuations in the target, and other noise, by decreasing the statistical error, the total width of the upstream luminosity monitors becomes more and more sensitive to any density fluctuation compared to the width of the main detectors. However, during the experiment, the width of the asymmetry distribution observed in the upstream Lumi was approximately the same level as that in the main detectors ~ 200 ppm, which was mainly due to the electronic noise in the Lumi's signal chain.

As mentioned before, the downstream luminosity monitors were put at a distant downstream position (see Figure 2.14) and thus could monitor the scattered electrons at a very small angle $\sim 0.5^\circ$. At such small angle, they were expected to have negligible physics asymmetry compared with that in the main detectors and they were also very sensitive to any helicity-correlated beam changes, like beam angle or beam position. Therefore, the downstream luminosity monitors could serve as a powerful "null asymmetry monitor" to monitor any presence of false helicity-correlated asymmetry in our experiment if it was non-zero. Furthermore, they could provide an independent test on the systematic errors after the linear

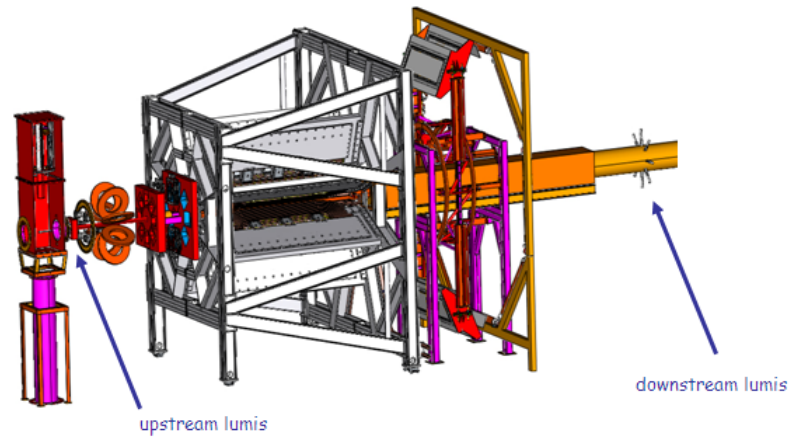


FIG. 2.14: Locations of two sets of luminosity monitors used in the experiment.

regression, which was expected to remove most of the false asymmetries due to any helicity-correlated changes in various beam properties. However, similar to the upstream Lumis, this set of Lumis also suffered from the unexpectedly high width problem in the experiment, where the width was at the same level of that in the main detectors. The reason for this issue is unknown at this moment and therefore needs further investigation [67].

2.9.4 Halo Monitors

The possible causes of beam halo in an electron accelerator can be attributed to several reasons [68], but not limited to: scraping between the electron beam and beam pipe, scattering against the stray gas in the beamline enclosure, self-interaction of beam electrons, and hits on the photocathode surface by scattered laser light in the electron source. In our experiment, the beam halo could increase

the rate of aluminum background either through scraping against the target cell wall or interacting in the target exit window. The increase in the Al background would dilute our measured asymmetry and cause a false asymmetry. The Al backgrounds, which are elastic electrons, could not be reduced by the QTOR and the halo monitors were thus used as a background monitor to monitor any primary beam well outside the “Gaussian” tail of the beam.

The way the halo is measured is to let the beam pass through the halo target, which is a 2 mm thick aluminum piece with two holes: one 8 mm square hole used for specific “spot check” and the other one is a circular hole, 13 mm in diameter employed for continuously monitoring during the production running without any scraping. If the beam halo increases, more scraping will take place and the increased rate caused by the shower will be detected by the following halo monitors. In the Qweak experiment, six halo monitors are employed and each are given a number to distinguish from each other. The most useful two monitors (halo monitor 3 and 4) were placed upstream of the LH_2 target. Both of halo monitor 3 and 4 were PMTs each attached to a piece of Lucite, while halo monitor 4 had a 2 cm thick lead pre-radiator. During the 25% measurement and Run I, the halo monitors were installed but the halo target could not be inserted because the center of the halo target hole was found to be 3.8 mm from our nominal beam trajectory. During the down period of 2011, an offset halo target was machined to resolve this issue. In the Run II, the halo monitors were found to be useful for monitoring the beam quality, especially when the quality became bad.

2.10 Precision Beam Polarimetry

The anticipated dominant systematic error source for the Qweak experiment comes from the uncertainty of the beam polarimetry. In order to meet the proposed error budget, Qweak requires measurement of the beam polarization to $\Delta P/P = 1\%$. The strategy used to achieve a 1% error in measurement of the beam polarization involves using both the Hall C Møller Polarimeter and the new Hall C Compton Polarimeter. Each of these devices is described in turn below.

2.10.1 Hall C Møller Polarimeter

The Hall C Møller Polarimeter [69], has the capability of measuring the absolute polarization of the electron beam going through Hall C to under 1% precision at low beam currents. Its operation is based on the spin-dependent Møller scattering process $\vec{e} + \vec{e} \rightarrow e + e$. The cross section for spin-dependent ee scattering can be expressed as [70]

$$\left(\frac{d\sigma}{d\Omega}\right)_{\text{CM}} = \left(\frac{d\sigma_0}{d\Omega}\right)_{\text{CM}} \left(1 + \sum_{ij} P_i^b A_{ij} P_j^t\right), \quad (2.8)$$

where P_i^b is the i th component of beam polarization, P_j^t is the j th component of target polarization and subscript CM means the center-of-mass frame. A_{ij} is called the analyzing power, which is dependent on the scattering angle θ_{CM} . $(d\sigma_0/d\Omega)$ is the unpolarized differential cross section. For the measurement of longitudinal beam polarization with a longitudinally polarized target, the expression above can

be simplified as

$$\left(\frac{d\sigma}{d\Omega}\right)_{\text{CM}} = \left(\frac{d\sigma_0}{d\Omega}\right)_{\text{CM}} (1 + P_z^b A_{zz} P_z^t), \quad (2.9)$$

where A_{zz} is given by

$$A_{zz} = -\sin^2\theta_{\text{CM}} \frac{7 + \cos^2\theta_{\text{CM}}}{(3 + \cos^2\theta_{\text{CM}})^2}. \quad (2.10)$$

The analyzing power reaches a maximum when the scattered angle of the Møller electrons is 90° in the center of mass frame. In order to determine the polarization, the rate of the scattered electrons is measured in one helicity and then with reverting the helicity and measuring the rate again. By subtracting those two rates, one get the asymmetry

$$A_R = \frac{\frac{d\sigma^{\uparrow\downarrow}}{d\Omega} - \frac{d\sigma^{\uparrow\uparrow}}{d\Omega}}{\frac{d\sigma^{\uparrow\downarrow}}{d\Omega} + \frac{d\sigma^{\uparrow\uparrow}}{d\Omega}} = P_z^b A_{zz} P_z^t. \quad (2.11)$$

Therefore, the beam polarization can be deduced by

$$P_z^b = \frac{A_R}{A_{zz} P_z^t}. \quad (2.12)$$

The Hall C Møller Polarimeter, as Figure 2.15 shows, consists of a thin pure Fe target, which can provide its outer shell electrons polarized either parallel or anti-parallel to the beam by a 4 Tesla magnetic field, which is provided by a superconducting solenoid. The reason to choose the pure Fe is because its polarization in saturation is known to great precision, so that the uncertainty of target polarization used in the previous expression can be tightly constrained under 0.4% [71]. The effect of beam-current-induced target temperature increase must also be considered, because the target depolarizes if the temperature is too high. For the Hall C

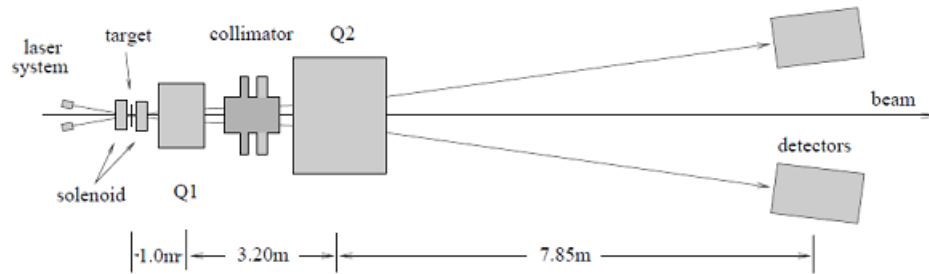


FIG. 2.15: The schematic overview of the Hall C Møller Polarimeter. Q1 and Q2 are the two quadrupole magnets. Two lead-glass electron detectors were placed on the left and right side of the beam for a coincidence measurement in order to suppress the background. They were located ~ 50 cm from the beamline so as to maximize the counting rate.

Møller Polarimeter, several μAs is the safe region for its normal operation where target depolarization due to heating is acceptably low. Other components include a small quadrupole to focus the scattered Møller electrons first, a series of tungsten alloy collimators to define the azimuthal acceptance, followed by a larger quadrupole magnet to defocus the envelope of scattered Møller electrons. Two lead-glass electron detectors were placed on the opposite side of the beam to measure the scattering rate. The design of using two symmetric detectors was to reduce the background noise by means of only counting the coincident rate seen by both detectors.

2.10.2 Hall C Compton Polarimeter

Although the Hall C Møller Polarimeter can measure the beam polarization to less than 1% error, it still has some properties which prevent it from being used as the

only polarimeter in our experiment. The most severe problems are that it can not be used at high current, due to the beam-heating induced depolarization of the target and that it is an invasive measurement due to the placement of the target, which means a cost of many hours of production running. In order to overcome those limitations, a new polarimeter with different working mechanism must be employed and this is where the Compton Polarimeter comes in. It was commissioned and used for the first time in the Qweak experiment and will also be used in future experiments in the Hall C.

The Compton Polarimeter is based on the spin-related Compton scattering, where the polarized beam electrons collide with polarized photons, $\vec{e} + \vec{\gamma} \rightarrow e + \gamma$. Similar to the Møller polarimetry, the polarization of the beam can be deduced from the difference of rates before and after reversing the electron beam's polarization, as the following expression shows

$$A_R = \frac{\frac{d\sigma^{\uparrow\downarrow}}{d\Omega} - \frac{d\sigma^{\uparrow\uparrow}}{d\Omega}}{\frac{d\sigma^{\uparrow\downarrow}}{d\Omega} + \frac{d\sigma^{\uparrow\uparrow}}{d\Omega}} = P_e P_\gamma A_I;$$

notice that here only the longitudinal part of the beam polarization is addressed. A_I is known as the theoretical asymmetry, which mainly depends on the angle of the back-scattering photons, given fixed incident beam and photon energy. In the Qweak experiment the scattered electrons and photons have only a very small angle in the Compton scattering, so in order to prevent those particles from contaminating the original beam, we need to use a magnetic chicane system.

The magnetic chicane used in Qweak consists of four dipole magnets as Figure 2.16 shows. The purpose of the first two magnets is to displace the beam

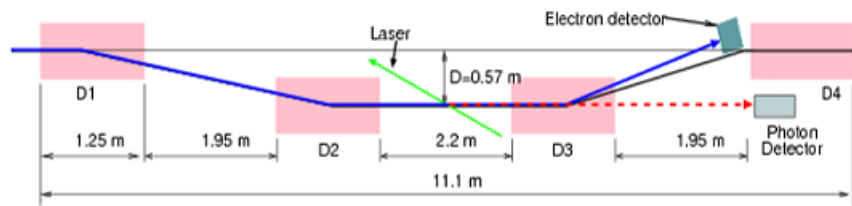


FIG. 2.16: The schematic overview of the Compton Polarimeter with a chicane consisting of four dipole magnets, labeled as D1, D2, D3, D4 respectively.

57 cm vertically from its original place. Then the electron beam is directed to interact with the laser beam where the Compton scattering can happen. The laser used here is a 10 W continuous wave laser whose wavelength is 532 nm, coupled to a low gain, external cavity. The third magnet separates the scattered electrons from those unaffected ones due to the fact that the scattered electrons have smaller momentum and thus are bent more drastically. The fourth magnet is employed to bend the unscattered electron beam out of the Compton chicane and back to the nominal direction.

The detector system of the Compton polarimeter consists of two independent parts: a photon detector and an electron detector. Several kinds of crystals were used as the photon detectors during the run I, including the original candidate PbWO_4 , and a $\text{GSO}(\text{Gd}_2\text{SiO}_5)$ crystal borrowed from Hall A. The backscattered photons cause scintillation in the crystal and thus the output signal can be generated through photomultiplier tubes. The electron detectors were built in collaboration between groups from the Universities of Winnipeg, Manitoba, TRIUMF and Mississippi State University. It used four diamond-strip solid-state electron detectors to detect the scattered electrons. Each detector's active width is $21 \text{ mm} \times 21$

mm and has 96 horizontal micro-strips.

In summary, as mentioned before, the Compton polarimeter can provide non-invasive, continuous measurement of the beam polarization at high current, which could not be achieved using the Møller polarimeter. It also produces two independent measurements using the electron and photon detectors, respectively. In the nominal conditions of the Qweak experiment, the electron detector can get a $\sim 1\%$ statistical error in approximately 20 minutes, while for the photon detector, it needed a longer time, $\sim 2-3$ hours. The goal of the systematic error is $\leq 1\%$, which is approximately the same as the Møller polarimeter. From the preliminary analysis of the Compton data, it should have no problem to reach that goal [72].

CHAPTER 3

Qweak Tracking Software

3.1 Overview of Qweak Track Reconstruction software

The Qweak Track Reconstruction (QTR) software package was originally based on the development of the software for the HERMES experiment [73]. Both experiments used upstream and downstream tracking detectors to detect signals from the scattered particles and then to derive the kinematics of the charged particles by connecting the front and rear part of the trajectory, separated by a magnet. Unlike the HERMES experiment, which needed an algorithm to identify different hadrons, the QTR only needs to rebuild the trajectory of scattered electrons to measure the momentum and scattering angle. The QTR was implemented by using C++ to make it more object-oriented and to reflect the data handling among

different components of the tracking system in a less abstract and clearer way. In addition, writing in C++ also provided access to full-fledged and highly efficient libraries, such as the Standard Template Library (STL) [74] and the Boost Library [75]. The QTR utilized a pattern recognition algorithm combined with a tree search algorithm as the core part to select the good tracks from a set of raw hits from individual detector on an event-by-event basis. Furthermore, due to the fact that we need to determine the four-momentum transfer Q^2 within an accuracy of 0.5%, the QTR must utilize the full capacity of each tracking detector and also requires careful calibration routines which include reference time correction, t_0 correction, drift-time to drift-distance conversion and the extraction of geometry numbers from survey data. In this chapter, details of the QTR as well as calibration methods will be discussed.

3.2 Overview of QTR Workflow

The main function of the QTR is in the **QwTracking.cc** file under **Tracking/main** directory and it consists of three consecutive steps. The first step is to load detector information, program options, the pattern recognition database and the QTR magnetic field map, if momentum reconstruction is required.

The detector information is calculated in advance through calibration methods and is saved in various parameter files under the **Tracking/priminput** directory. A description of those parameter files is given in Appendix A.1. The

program options utilize the features provided by the `program_options` library in Boost [75], which allow program developers to obtain program options, that is (name, value) pair, via two conventional ways: by configuration files or using the command line. The most important configuration file for the QTR is **Tracking/priminput/detectors.map**, which stores the name of the detector files for each subsystem to load. QTR provides a rich set of command line options which can be specified when the main function is run. A list of some options can be found in Appendix A.2. To see a full list of these options, you can type:

qwtracking - -help

The pattern recognition database is constructed the first time you run the QTR or when explicitly requiring QTR to reconstruct the database by specifying “yes” to the - **QwTracking.regenerate** option. More details will be discussed in Sec. 3.5.

The QTOR magnet field map stores the magnetic field strength vectors B_x, B_y, B_z for many discrete field points within the QTOR range in cylindrical coordinates R, Z, ϕ . When the momentum reconstruction is turned on by specifying “no” to the - **QwTracking.**

disable-momentum option, this file will be loaded, because connecting the front track with rear track requires the field information from QTOR magnet.

The second step of the main function is to iteratively load the raw hit information from every event and then to map the electronics information such as raw time, electronic channel to detector information, such as wire number and drift-

distance. A hit means a signal from a given wire that could either comes from a collision between the incident particle and gas molecules or, just noise. The drift-distance is the perpendicular distance from the trajectory to the wire plane.

Next it will call the **QwTrackingWorker** class, which is mainly responsible for the track reconstruction job, to loop through the detector types, and each of two octants, to get the upstream (HDCs) and downstream (VDCs) track segments.

The third step of the main function is a natural follow-up to the second. It attempts to connect the HDCs and VDCs track segments by using the so-called “shooting method” (see Sec. 3.8), in which the inelastic events will fail to connect but the elastic events will succeed. Once being connected, the four-momentum transfer Q^2 and the scattering angle from the elastic events will be thus determined.

The working flow of the main function of QTR with basic steps is illustrated in Figure 3.1.

3.3 Coordinate Systems

Before delving into the details of track reconstruction, it is necessary to take a look at the two coordinate systems used in the QTR: one is the local coordinates and the other is the global coordinates. An overview of those two coordinates can be found in Figure 3.2, where the beam direction is into the paper. Each octant of the spectrometer has its own local coordinates. The local coordinates are attached

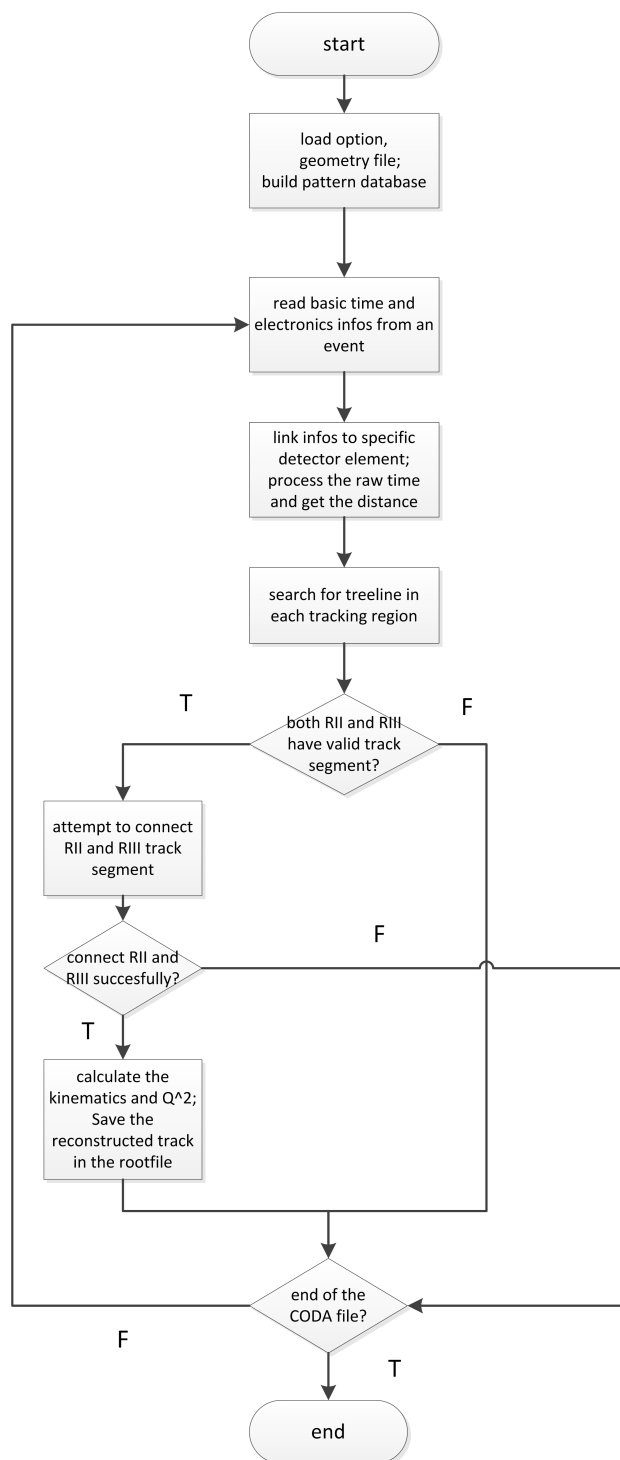


FIG. 3.1: Overview of the working flow of the main function in QTR.

to the wire planes, therefore, the origin of the local coordinates is at the center of the first wire plane in a given package and the local z direction is normal to the wire plane.

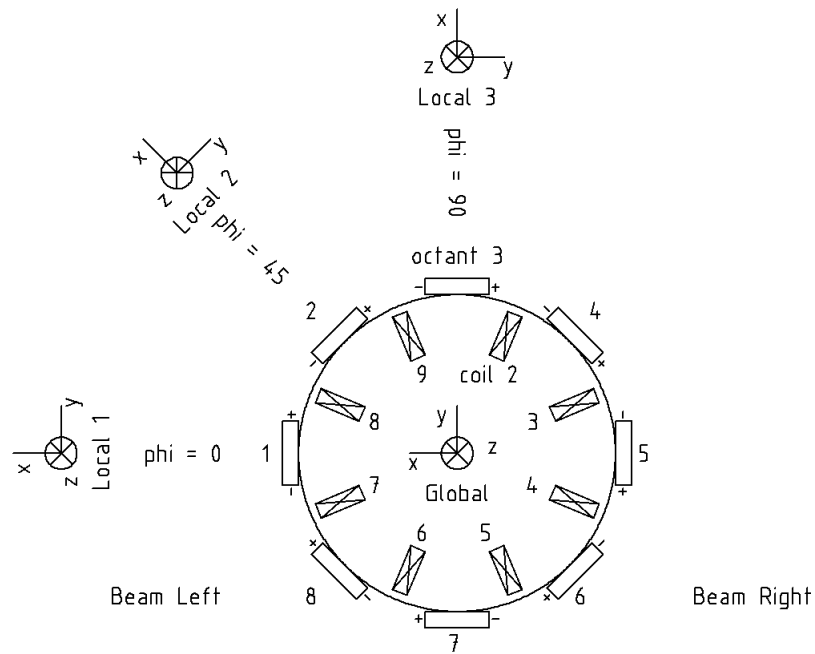


FIG. 3.2: The overview of the coordinate system used in the QTR. The global coordinates is placed at the center of diagram. Each octant has its own local coordinates attached to the center of the plane [76].

3.4 Calibration Methods

Although building the pattern database precedes the calibration procedures, some of the parameter files involved in those procedures, such as t_0 map and drift-time to drift-distance table, are made even before the main function starts. So the calibration methods, which are used to convert the raw drift-time to drift-distance

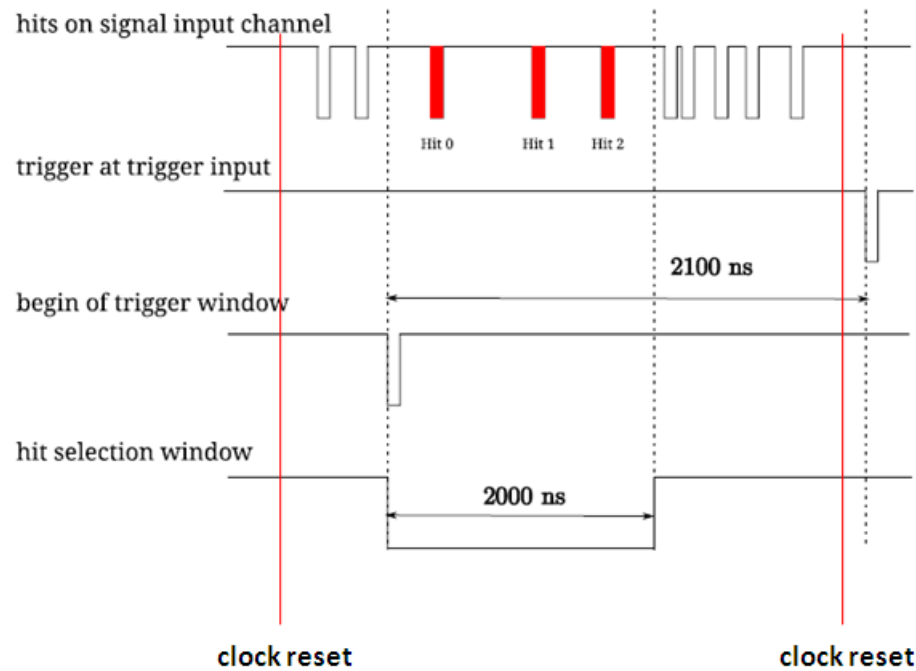


FIG. 3.3: The procedure on how to select hits in the F1TDCs is shown here. For a given series of hits, a trigger at trigger input is generated first to serve as a “stop” time. Then a hit selection window, where reference time and regular hit reside, can be decided.

used in the later tracking-search procedures, are discussed in this section at first.

3.4.1 F1TDC Reference Time Correction

The raw drift-time information, which is read directly from the F1TDC channel, requires the so-called reference time correction to measure the real time of flight from the trigger of the trigger scintillator (reference time) to the arrival of the signal on the wires (raw drift-time). But even before that, those hits needs to be selected from a series of input signal. The F1TDC used in our experiment is operated in common-stop mode and the procedure of selection of hits is shown in Figure 3.3. Another important feature of the JLab F1TDC is that the value directly read out

from the channel will be cycled for every period of time, which is referred to as “rollover” (see the “clock reset” in 3.3). Consequently, before simply subtracting the reference time from raw drift-time, a rollover check is required to see if any of the reference time and raw drift-time needs the rollover compensation. In our case, the $t_{rollover} = 65341$ bins and the trigger window is set to 12896 bins [77]. Three possible cases are illustrated in Figure 3.4. Also in [77] can be found that the trigger window, which is the length of acceptable time after the initialization of the trigger, is set to 2000 ns.



FIG. 3.4: Three possible cases are shown here. In the top diagram, the raw drift-time and reference time appear in the same time window, so the direct subtraction is sufficient; for the middle diagram, the reference time and raw drift-time are in different window, so in order to calculate their difference, an offset must be added to reference time, thus: $\Delta t = t_{reference} + t_{rollover} - t_{raw}$; for the bottom diagram, similar to the second case, the offset must be added to the raw drift-time in order to get the right difference: $\Delta t = t_{raw} + t_{rollover} - t_{reference}$.

The reference time subtraction procedure is handled by the *SubtractReferenceTime* function in each detector’s class.

Notice that up to now, all the time information is recorded in the unit of a TDC bin. The function *ApplyTimeCalibration* of each detector class is called to convert bins to ns for each drift-time. After that, the only step left to be applied to the drift-

time is t_0 correction, which will fix the offset brought by the cable length, which is the subject of next section.

3.4.2 t_0 correction

The time information extracted from CODA file for the VDCs after the reference-time correction is not the real drift-time, but is the sum of the real drift-time and the relative signal processing time, which is called t_0 . The value of t_0 is largely determined by the length of the cable, which connects the MAD pre-amplifier/discriminator cards with the F1TDC module via multiplexing crates and therefore can be regarded as a constant. Since not only the cable length of each wire is slightly different, but most important of all, the speed of propagation variation is also quite different in different cable and electronics, it is necessary to find t_0 for every wire in order to determine the real drift-time precisely. The t_0 algorithm, which will be described below, is employed to fulfill the task.

Figure 3.5 is a typical drift-time distribution for a single wire before t_0 correction. Notice that the reference time is already subtracted from the raw drift-time so that the shorter drift-time appears as smaller TDC value. The most important assumption we make here is that the shortest physical drift-time should be zero. Therefore the offset, which is equal to t_0 , should be located at the leftmost of the spectrum. However, the leftmost individual hits along the time axis, in most cases, can be mistaken as the t_0 value because they are likely just random noise in the electronics or are hits not related with the event. In order to screen those low-rate

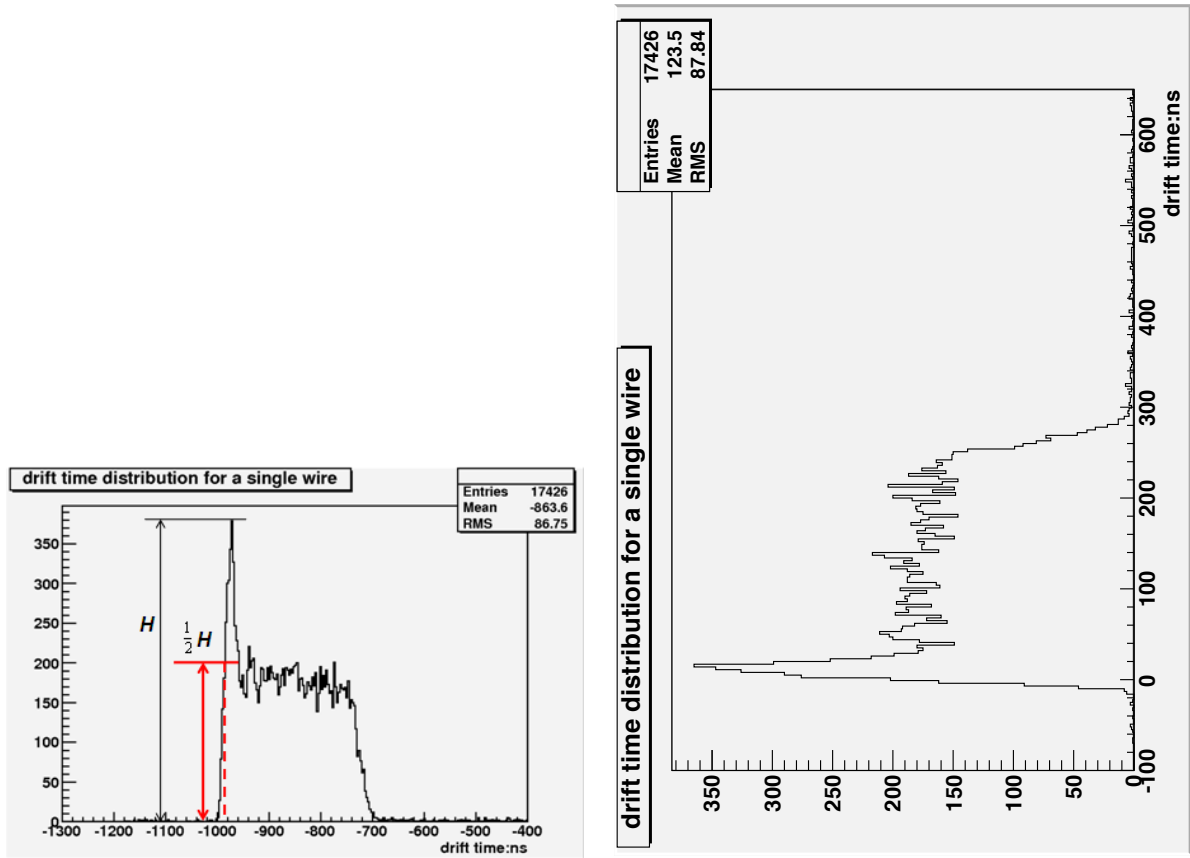


FIG. 3.5: The left diagram is a typical drift-time distribution for a single wire before t_0 correction. Although the shape is correct, the absolute value is not right. After the t_0 correction, the drift-time distribution is shown as in the right diagram.

unphysical signals, a cut-off threshold is needed and its value is set as the product of a preset ratio value and the peak value in the drift-time distribution. Once the cut-off threshold is applied, the t_0 is determined as the smallest value which satisfies the condition that is equal or greater than the threshold. For the case of VDCs, the preset ratio is set to 0.5 by default and a detailed example is shown on the left side of Figure 3.5. The red vertical arrow describes the threshold, which is equal to half of the maximum height in the distribution. The red dot line indicates the position of t_0 for the given wire. The reason to choose 0.5 as the preset

are twofold: firstly, it sets a high enough value to screen those low rate unphysical signal. Secondly, due to the time resolution from F1TDC, the sampling data from region where $t_{real}=0$ would appear as a gaussian distribution like the time distribution from very early stage presented in Figure 3.5 and the FWHM of this distribution defines the error in experimental t_0 value for every wire.

For a given VDC plane, the correlation between the t_0 value and the wire number is shown in Figure 3.6. The fluctuation of the t_0 at very low and very high wire numbers is due to the poor statistics related with the geometry where few hits are expected. This wouldn't cause us a problem because the number of valid tracks with hits in those areas is quite small. For where most of the hits come from, the t_0 stays fairly constant and the only big change in the middle of the plane indicates a change of cable length.

The procedure of finding out the t_0 for every wire is implemented in the independent ROOT macro script named **Finding_t0.C** under **Extensions/Macros/Tracking directory**. The values are saved in **Tracking/priminput/R3_timeoffset.map** which is loaded using the *QwDriftChamberVDC.LoadTimeWireOffset* function. The t_0 is subtracted from each specific wire's initial drift-time using the *QwDriftChamberVDC.SubtractWireTimeOffset* function.

3.4.3 Time to Distance Conversion

One essential part of the QTR is to convert the drift-time, measured by the TDCs, into drift-distance. Many algorithms exist for converting the drift-time to drift-

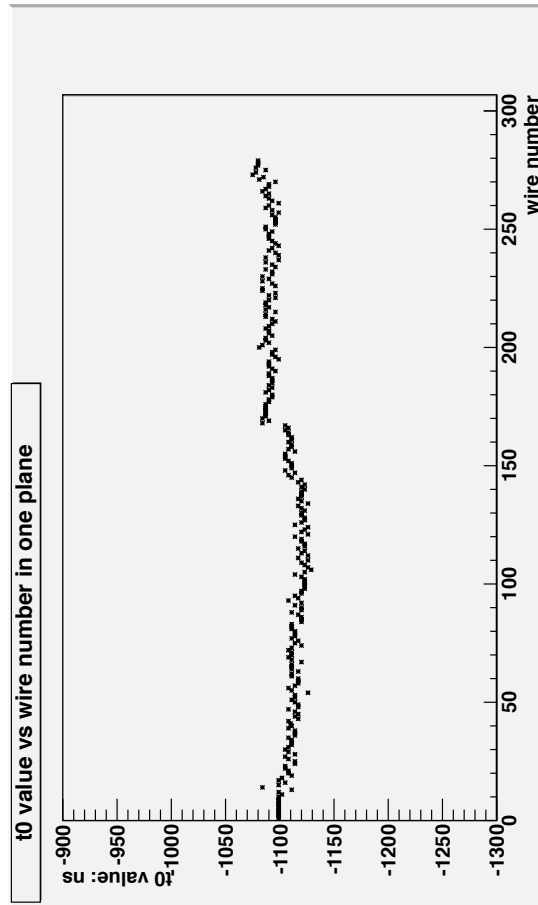


FIG. 3.6: The correlation between t_0 value and different wire number in a single plane of one VDC.

distance; for the Qweak experiment, we decided to use the same method as Hall A applied on its VDCs [78]. It is called a “flat-box” algorithm, because the final drift-distance distribution is expected to be almost flat based on the assumption that the volume of each drift “cell” should be uniformly illuminated under normal conditions without loss of efficiency for long drift times. The drift-distance can be calculated by integrating the drift-time distribution dN/dt . The starting point is that we can rewrite the time distribution as

$$\frac{dN}{dt} = \frac{dN}{dD(t)} \times \frac{dD(t)}{dt}. \quad (3.1)$$

Next, given the assumption that the drift cell is spatially uniformly hit, which gives rise to a constant value for $dN/dD(t)$, we can find that the drift velocity $dD(t)/dt$ is only proportional to the time distribution dN/dt . By integrating the time distribution and normalizing properly, the relation between the drift-distance and the drift-time can be given as

$$D(t) = \frac{d_{max}}{N_{total}} \int_0^t \frac{dN}{dt'} dt', \quad (3.2)$$

where

$$N_{total} = \int_0^{t_{max}} \frac{dN}{dt'} dt'.$$

In the above two equations, d_{max} is the largest drift distance and t_{max} is the largest drift-time. N_{total} is the total number of hits within the time range from the $t = 0$ to $t = t_{max}$. Since the dN/dt is always a positive number, so $D(t)$ increases monotonically along with the increasing of the drift-time and reaches the maximum value of d_{max} at $t = t_{max}$ (this can be verified by putting $t = t_{max}$ into Eq. 3.2).

Since the drift-time spectrum in our cases is not in a simple analytical form, a numerical method is thus employed to implement the integration in Eq. 3.2. We first divide the whole range of drift-time into numerous bins, width of each is 0.5 ns. Then by integrating the number of hits from each bin, the drift-distance is obtained for each specific drift-time and thus a look-up table containing the entries of drift-time and corresponding drift-distance can be constructed. However, since the number of entries in the table is finite, we need to use linear interpolation to calculate the drift-distance if the drift-time falls between two characteristic drift-

times, as followings

$$D(t) = D(t_{i-1}) + \frac{t - t_{i-1}}{t_i - t_{i-1}} \times (D(t_i) - D(t_{i-1})), \quad (3.3)$$

where

$$t_{i-1} < t < t_i.$$

The relationship between drift-time and drift-distance for the case of the VDCs and HDCs are shown in Figure 3.7 and Figure 3.8 respectively. The construction of the look-up table is implemented by the **Convert_vari.C** ROOT macro script under **Extensions/Macros/Tracking** directory. *QwDriftChamberVDC.LoadTtoDparameters* and *QwDriftChamberHDC.LoadTtoDparameters* functions are called to load their own look-up table, *QwDriftChamberVDC.CalculateDriftDistance* and *QwDriftChamberHDC.CalculateDriftDistance* functions are then called to use the value of the look-up table in every event to deduce the drift-distance. An example of the distribution of drift-distance in the case of VDCs after applying the look-up table is shown in Figure 3.9 and the reason that the distribution is not perfectly flat is probably because of the excessive noise and the angle-depedent time to distance effect described in the next paragraph.

Notice that in the scope of this dissertation, a preliminary, single drift-time to drift-distance table in the QTR was used for both the VDCs and HDCs. This approach assumes every wire in the tracking detector bears the same drift-time to drift-distance property. Another more profound factor that might influence the final result is addressed as follows. The track angle of the trajectories changes across the wire plane. Since the time measured in the TDCs is the time of electrons gen-

erated through the ionization process, triggered by a particle passing through, to travel from the trajectory to the sense wire along the least-time path, the correlation between drift-time and drift-distance depends on the track angle. For the HDCs, since the range of the accepted track angle is rather small, $7^\circ \rightarrow 11^\circ$, assuming the same relationship between drift-time and drift-distance of all of the tracks in the HDCs is reasonable. However, the change of the track angle in the VDCs is $45^\circ \rightarrow 55^\circ$, therefore, a more precise way to convert the drift-time and drift-distance is to use different tables as a function of track angle. This approach was not implemented in the QTR when this dissertation was written.

3.5 Pattern Recognition Algorithm

The pattern recognition algorithm uses the template matching technique, which was used in the ARGUS experiment [79], to identify an acceptable straight line segment, which is also referred to as a **treeline**. In this technique, a template, which is created from hits in an event, is compared with patterns created from a valid track, which has been saved in advance in a database. The algorithm employed in the QTR here consists of two basic steps: 1) creation of a pattern database and 2) the search for straight line segments in the database according to the signals in an event.

Since the pattern recognition algorithm is only employed to identify two-dimensional straight lines, therefore, detectors with the same wire orientation, the same de-

tor type, and the same octant number will be grouped into a single database. Consequently, instead of being one single file, the database is comprised of several files.

Creation of the Pattern Database

Each type of tracking detector consists of a number of layers, however, the definition of a layer is different between the HDCs and the VDCs. For the HDCs, a layer means a single wire plane, where the number of layers is set to 4 because there are four wire planes of the same orientation in one package. For the VDCs, a layer represents a wire cell, where the number of layers is set to 279 for the case of the VDCs but we only store the maximum number of 8 layers' information because eight is equal to the maximum number of wires being hit from a valid track in a given wire plane. Keep in mind that only one hit is allowed per layer in a given pattern. In the patterns, each layer is divided into a number of bins and each of those bins represents a range of position values along the plane for the HDCs, while in the case of the VDCs, each individual bin means a range of distances perpendicular to the wire plane. Each bin has a bit value 0 or 1, which indicates if a hit occurs in that range of position of the plane or not (if it is 0). The number of bins in each layer depends upon the maximum depth specified by the user at the very beginning of the database construction, and the spatial resolution is given by

$$\delta r = \frac{W_{layer}}{N_b}, \quad (3.4)$$

where W_{layer} is the width of layer and N_b is the total number of bins in that level. Since the pattern database is stored in terms of a tree structure (refer to the next section for more details), the number of bins in one level L is 2^L , and according to Eq. 3.4, changing the level by 1 corresponds to a factor of 2 change in the spatial resolution. The level starts at 0 and goes further by 1 each time until it reaches the maximum depth. For every level, each layer has the option of assigning the hit represented by bit value 1 to the lower or upper half of the old hit position in bins (illustrated in Figure 3.10). We can use 0 or 1 to describe the option as lower or upper half respectively, so if 1 has been chosen, the position with a hit will be updated to $2 \times bit_{old} + 1$, where bit_{old} is the old hit position in bins. Consequently, there is a total number of 16 possible descendants for a particular bit pattern in the case of the HDCs and all the possible combinations in the finer resolution level are covered. However, we are only interested in straight lines, so those descendants with a bit pattern that no straight line can pass through will not be saved. Since the detector layer has a finite spatial resolution determined by our maximum level, the number of valid bit patterns for all levels is also a finite number and all of them can be found by repeating the procedure described above.

Therefore, the procedure of creating the pattern database is highly recursive and the tree is a suitable data structure for storing the pattern database. For each valid bit pattern matrix, a node is created for storing the bit array value and the organization of the node is displayed in 3.11. In addition to the suitable data structure, another feature of our pattern database construction is based on the

fact that some of the bit patterns only differ by a single bin shift or are just the mirror image of another pattern, therefore we can regard those bit patterns as a single case only with different flip and shift properties, as Figure 3.12 shows. By using this optimization, the disk space used for storing the pattern database was reduced and the speed of treeline search procedure was accelerated.

Searching for the Treeline

For each event, a two-dimensional bit pattern matrix is created from the set of hits which enables us to search the equivalent in the pattern database to see if that set of hits corresponds to a valid track. The basic searching strategy used here is to start from a very coarse resolution (in our case the root of the tree) and to proceed using the depth-first strategy (DFS) until the same bit pattern is found at the deepest level [80, 81]. If the bit pattern is not found at a certain level, the algorithm will traverse roots in the same level until either 1) exhausting all the available roots and still not finding the matching bit pattern, then it will return “false” to declare no **treeline** has been found for this event, or 2) finding one root which has the matching bit pattern and then proceeding using DFS again. Once found, the valid **treeline** will be constructed and appended into a linked list for the later procedures. A brief schematic illustration in Figure 3.13 shows how this procedure works in the case of the HDCs.

It is worthwhile to mention that for a given event, the above procedure does not require that every hit is in a bit pattern in the database, because the possibility

of noise hits must be taken into consideration. On the contrary, it does require that a successful search in an event has every hit in the filled database pattern correspond to a hit in the event. The QTR can also handle the case when there are more than one **treeline** in an event. As mentioned before, they are stored in a linked list.

Overview of the related classes and methods

The classes used in the pattern recognition algorithm are listed in Table 3.1. The most important ones are: **QwTrackingTree**, which is responsible for creating, saving and loading the pattern database; **QwTrackingTreeSearch** classes, which is responsible for searching for the tree lines given the bit pattern from the hits in an event.

The most crucial functions in **QwTrackingTree** and **QwTrackingTreeSearch** classes are listed with a brief introduction in Table 3.2. Brief descriptions of all the functions from the two classes can be found in their source files (under **Tracking/src/** directory).

3.6 Detector Tracking

The term **partial track** in QTR is defined as a straight line three-dimensional track going through a specific detector region, which also serves as a prerequisite for the final track reconstruction. This section will mainly discuss details of how to

TABLE 3.1: Classes used in the Pattern Recognition Algorithm

QwTrackingTree	creates the pattern database
QwHitPattern	creates two-dimensional bit pattern based on the hit information in an event
QwTrackingTreeSearch	helper class to perform the tree search algorithm to find if the bit pattern from signals in an event has an equivalent pattern in the pattern database
QwTrackingTreeLine	a linked list to store the found treeline
treenode	contains the bits which represent a valid pattern; also contains arrays of nodenode s which represent this node's children
nodenode	pointer, used to link treenode with its siblings
shorttree	similar to treenode , used when reading a tree in tree search process to minimize the memory overhead
shortnode	similar to nodenode , used along with shorttree

reconstruct the **partial track** in each detector region given the hit information from an event. The procedures used for the HDCs and the VDCs are different, due to the different chamber geometry, and each are described in turn in the following.

3.6.1 HDCs

As described in the previous section, the starting point for **partial track** reconstruction for the HDCs is to map hits from the event into the bit pattern matrix. For each wire plane, a one-dimensional bit array will be created, given the hits in this plane. The drift-distance derived from the drift-time (see Sec. 3.4.3 for more details) can only provide the absolute value of the distance parallel to the wire plane from where the hit occurs to the closest sense wire. This undetermined

TABLE 3.2: Some methods used in Pattern Recognition Algorithm

<i>marklin</i>	this is a recursive function which is responsible for generating the pattern database. For a parent node, it generates 2^{layer} possible son patterns. Each son pattern will be checked through the <i>consistent</i> function to see if it corresponds to a straight line.
<i>consistent</i>	this function validates a possible hit pattern by checking if the hit pattern is consistent with a straight line, given the detector geometry information.
<i>_ SearchTreeLines()</i>	highly recursive function employed to search if the equivalent of the bit pattern from a event exists in the database; uses DFS method for tree search.

sign leads to a left-right ambiguity in which, for a single hit, two possible hit positions are generated, as illustrated in Figure 3.14. By taking the spatial resolution of the hits into account, each left or right hit can span more than 1 bin, as Figure 3.14 shows. The size of the bit array for one layer is $\sum_{i=0}^{i=max} 2^i$ where *max* is equal to the deepest level. The reason for that is, unlike the node in the pattern database, which only stores the position of the bin with value 1 for a single level, the bit array mapped from an event is comprised of bit arrays for levels over the whole range (see Figure 3.14 for a detailed example). The *SetHDCHits* function in the **QwHitPattern** class is responsible for this mapping task.

Then the pattern recognition algorithm performs a search of the equivalent of the two-dimensional bit arrays from the event in the pattern database. One thing that needs to be pointed out is that the original requirement that all 4 layers must match a pattern in the database is reduced to 3 to allow for some tolerable inefficiency in the HDCs. Once the **treeline** is found, it will be appended to the

treelineslist. Only the hit bin position of the first and the last wire planes in that equivalent pattern from the database, which is in a given “direction”, is recorded in a valid **treeline**. This then makes possible the use of least squares fitting to solve the “left-and-right” ambiguity for each plane. Here, we start from the point where the **treelines** are obtained and walk through the code to describe the class and the functions involved to solve the “left-and-right” ambiguity and to get the **partial track**. Starting from the *QwTrackingTreeCombine.TITreeLineSort* function, the code loops over all valid **treelines** in the **treelineslist** obtained from the pattern recognition algorithm. For every valid **treeline**, since only the hit bin position from the first and the last detector layers is recorded, a “*path*” can be thus calculated by connecting those two points. The *QwTrackingTreeCombine.TICheckForX* is then called to find all the compatible hit positions along this “*path*” and to pick out the best combination of positions in terms of χ^2 , given by

$$\chi^2 = \sum_{i=1}^4 \frac{(x_i - \hat{x}_i)^2}{\sigma_i^2}, \quad (3.5)$$

from two-dimensional least χ^2 fitting of those positions. In Eq. 3.5, x_i is the hit position with the drift-distance converted directly from the drift-time while \hat{x}_i is the track position with the drift-distance calculated from the fitting of the “*path*”. The σ_i is resolution of the drift-distance in the i th plane in a given direction and is set to 0.01 cm by default for all of the wire planes. This step is quite essential because it provides an elegant solution to solve the “left-right” ambiguity and is thus worthwhile to take a look at the inside part of *QwTrackingTreeCombine.TICheckForX* function to fully understand how we implement this task. Two types of containers

exist in this function, one is called *goodHits* and the other is called *usedHits*. The key difference between those two containers is that for each detector layer, the *goodHits* can have more one hit position as long as the position stays along within the “*path width*”, while the *usedHits* only allows at most one hit position given the assumption that a valid track can only have a hit at one position in each layer. The process of filtering out the unqualified hits and putting them into *goodHits* is implemented using *QwTrackingTreeCombine.SelectLeftRightHit* and is illustrated in Figure 3.15. At this point, we have multiple hit positions in each detector layer. In order to pick out the best combination, we’ll simulate the track by picking one hit position from each layer each time and calculate the χ^2 of the track. The number of combinations we need to consider is in the order of $\mathcal{O}(n^4)$ with an average n of $\simeq 2$. This job is carried out by using a *for* loop to go through every combination and calling *QwTracking.weight_Isq* function to calculate its χ^2 . The best combination is defined when the the minimum χ^2 is reached and the hit positions from that best combination are put into *usedHits*. It needs to repeat *QwTrackingTreeCombine.TITreeLineSort* function three times, once for every wire direction x , u and v , to get the hits for later reconstruction of the *partial track*.

Finally, the *QwTracking.TITreeCombine* function is called to make use of all the hits from the *usedHits* containers of the three directions to reconstruct the **partial track**. A three-dimensional least χ^2 method is employed here (refer to Sec. 3.7 for more details).

3.6.2 VDCs

Similar to the HDCs, the first step for partial track reconstruction for the VDCs is to map the hits into a bit pattern matrix. However, a notable difference between the HDCs and the VDCs in terms of the usage of pattern recognition is that for HDCs, the concept of layer represents a wire plane and thus the algorithm is performed using data from all detectors in the same wire orientation and the same octant simultaneously, while for the VDCs, a layer describes a single wire cell, thus the algorithm needs to be done iteratively for every wire plane. This difference also leads to an extra step in the case of the VDCs, which requires one to perform matching of the **treeline** in the same wire direction for the front and back chambers in a given package.

A typical mapping process is depicted in Figure 3.16 and as can be seen, a layer is divided into $2^{maxlevel-1}$ bins (in our case, the default value of *maxlevel* is 4). An effect known as the up-down ambiguity will show up in the case of the VDCs, for the same reason as the HDCs' left-right ambiguity. Consequently, a bit pattern consisting of N layers (N is the number of wires in a VDC wire plane; in our case, N is equal to 279) will be constructed. This process of mapping is controlled by the *QwHitPattern.SetVDCHits* function. A key fact related with the VDC tracking is that the VDCs are oriented such that the nominal trajectory of a scattered electron traverses 4 to 8 layers (wire cells) in a single wire plane. Given this assumption, when identifying the valid **treeline** from the bit pattern matrix built from an event,

we'll loop through the number of layers and take 8 layers each time to search for its equivalence in the database. Since most of the layers are empty in a single event, this process can be further optimized by starting with the set where the first layer being hit is involved. For instance, if the first wire being hit is 42, the first set of 8 wires that needs to be considered is 36,37,...,41,42. Notice that the inefficiencies of the VDC wires, which is caused either by missing wires or the fact that the channel connecting to specific wire does not give out signal during that event, may cause us to bypass some of the good **treelines**. Therefore, an upper limit of missing layers is designed to address this problem by being set to 4. Furthermore, the QTR also has the tolerance of at most 1 mismatched layer but would be also categorized as missing layers as well.

All the found **treelines** in a given wire plane are stored in a **treelinelist** linked list. Then *QwTrackingTreeCombine.TITreeLineSort* is called to loop through the list of **treelines** to match wire hits to the hit in the pattern from each **treeline** and to calculate the corresponding χ^2 . By this means, the up-down ambiguity is resolved for this specific treeline. However, this could be misleading because another "ghost" **treeline** still exists in the **treelinelist** and therefore the up-down ambiguity is not quite solved yet from this perspective (see right part of Figure 3.16). We need to resort to another plane to solve the up-down ambiguity in a complete sense, which will be described later.

Next, the *QwTrackingTreeSort.rcTreeConnSort* is called for two reasons: 1) to remove **treelines** with large χ^2 and 2) to remove redundant **treelines**, *i.e.*, those

which have a portion of their wires in common.

As said before, a solution for solving the up-down ambiguity lies in the use of information from two wire planes rather than just one. This is implemented by calling *QwTrackingTreeMatch.MatchRegion3* function (see Figure 3.17), whose input parameters are two **treelinelists** with the same wire orientation from the front and back chamber respectively. The *QwTrackingTreeMatch.MatchRegion3* loops through two lists to see if the attempt to pair the front **treelines** with the back **treelines** is possible. For each pair of **treelines**, a crude straight line can be drawn given the knowledge of which wire sections were hit in each plane and the corresponding slope is thus obtained. By limiting the difference between the slope from the crude straight line and the **treelines** for each wire plane to a small range, the “ghost” **treelines**, which do not have a counterpart in the other wire plane, can be removed. Once a valid pair is found, a new **treeline** is constructed with all the hits from the front and the back **treelines** and is referred as a **treeline** in “plane 0”, for it is not linked to any particular plane. Note here that pairs of front and back **treelines** used to generate different “plane 0” **treelines** can not have any redundancies. For example, if a given front **treeline** has already been used to generate a “plane 0” **treeline** with its counterpart in the back chamber, then it can not be used to generate the second “plane 0” **treeline** with another back chamber **treeline**, if there is any.

For a single valid track, two “plane 0” **treelines** are generated, representing the u and v direction separately. Unlike the case of the HDCs, where we need to

rely on the three-dimensional least square method (refer to Sec. 3.7) to combine 3 two-dimensional **treelines** into one three-dimensional **partial track**, in the case of the VDCs, the situation becomes much simpler because there are only two directions, namely, u and v . The code loops over lists of “plane 0” **treelines** in the u and v directions separately to ensure every combination of u and v is covered. A unique corresponding plane is then deduced from both of the “plane 0” **treelines** with the following two requirements: 1) the plane is parallel with the wire direction and 2) the plane contains the “plane 0” **treeline** (see Figure 3.18). Given two non-parallel planes, a unique line can be derived from their intersection. Therefore, the VDCs **partial track** is obtained by using two “plane 0” **treelines**. The whole process is controlled by *QwTrackingTreeCombine.TITreeCombine*.

3.7 Three-Dimensional (3D) Least Square Fitting Algorithm

Two linear fitting algorithms are used in the QTR and both are based on the linear least squares approach. One is the simple two-dimensional (2D) least square method, which is employed to solve the left and right ambiguity when we find the **treeline** (see Sec. 3.6 for more details) and will not be discussed here. The other is the three-dimensional linear regression method, needed for the HDCs, which will be outlined in this section. The method is employed to find the **partial track** given three treeline segments from the u , v and x directions.

Similar to the 2D least square fitting method, we will first assume a “path” in the case of 3D. In order to describe this “path”, four parameters (x_{off} , x_{slope} , y_{off} , y_{slope}) are used to represent the slope and intercept of x and y directions in terms of z . Therefore, given a z value, the coordinates of corresponding x and y values are given by

$$x_G = x_{off} + x_{slope} \times z, \quad (3.6)$$

$$y_G = y_{off} + y_{slope} \times z.$$

The perpendicular distance between the track position and the hit position can be calculated as

$$\Delta u = \hat{x}_L \cos\theta + \hat{y}_L \sin\theta - u_{hit}, \quad (3.7)$$

where θ is the angle between the direction, which is normal to the wire orientation, and the local x axis as Figure 3.19 shows. \hat{x}_L and \hat{y}_L are the x and y coordinates of the track point under the local coordinates. u_{hit} is the drift-distance of the hit point. Remember that the calculation is in the local coordinates (as subscript L indicates in the Eq. 3.7) where the origin point is at the center of the first wire plane in that package. But let's first assume that we have a **partial track** and the **partial track** is always expressed in terms of its parameters in the global coordinate system. So by using the Eq. 3.6, the \hat{x} , \hat{y} coordinates in the global coordinate system are easy to get

$$\hat{x}_G = x_{off} + x_{slope} \times z, \quad (3.8)$$

$$\hat{y}_G = y_{off} + y_{slope} \times z,$$

where z is the location in the beam direction. Thus, we can convert global coor-

ordinates to the local coordinates in Eq. 3.8 by

$$\begin{aligned}\hat{x}_L &= y_{off} + y_{slope} \times z - y_0, \\ \hat{y}_L &= -(x_{off} + x_{slope} \times z - x_0),\end{aligned}\tag{3.9}$$

where x_0, y_0 are the wire planes' centers in the global coordinate system. By substituting Eq. 3.9 into Eq. 3.7, we get

$$\Delta u = (y_{off} + y_{slope} \times z) \cos \theta - (x_{off} + x_{slope} \times z) \sin \theta + (x_0 \sin \theta - y_0 \cos \theta - u_{hit}).\tag{3.10}$$

Given the **QwHit** class, the hit position for a particular hit is calculated as

$$u_{hit} = (wire - 1) \times \delta u + u_{drift} + u_0,\tag{3.11}$$

where u_0 is the perpendicular distance between the first wire and the center of that plane (refer to Figure B.3 in Appendix B) and δu is the perpendicular distance between adjacent wires. The u_{drift} is the drift-distance derived from the time-to-distance calibration and for here, we assume that the left-or-right ambiguity is already solved. In QTR, the function *QwHit.GetDriftPosition* will return a value equivalent to

$$u_{dp} = (wire - 0.5) \times \delta u + u_{drift}.\tag{3.12}$$

Substituting Eq. 3.12 into Eq. 3.11, we are able to write Eq. 3.11 into a more compact form

$$u_{hit} = u_{dp} - 0.5\delta u + u_0.\tag{3.13}$$

Then the difference Δu in Eq. 3.10 becomes

$$\begin{aligned}\Delta u &= (y_{off} + y_{slope} \times z) \cos \theta - (x_{off} + x_{slope} \times z) \sin \theta \\ &\quad - (-x_0 \sin \theta + y_0 \cos \theta + u_{dp} - 0.5\delta u + u_0).\end{aligned}\tag{3.14}$$

Keeping in mind that our final goal is to deduce the four parameters of the partial track: x_{off} , y_{off} , x_{slope} and y_{slope} , it is reasonable to separate the terms in Eq. 3.14 into two categories in terms of their relationship with those four parameters. Notice that the only terms that do not depend on those four parameters are the last five terms, so we can continue simplifying the formula by grouping those terms into a single term called u_{irre}

$$u_{irre} = -x_0 \sin \theta + y_0 \cos \theta + u_{dp} - 0.5\delta u + u_0. \quad (3.15)$$

Next, if we sum the quadratic value of the difference Δu over all hits, we get the expression χ^2 for a set of hits [82]

$$\chi^2 = \sum_i \left[\frac{(y_{off} + y_{slope} \times z_i) \cos \theta_i - (x_{off} + x_{slope} \times z_i) \sin \theta_i - (u_{irre})_i}{\sigma_i} \right]^2, \quad (3.16)$$

where the subscript i indicates the hit number and the quantities $1/\sigma_i^2$ act as weighting factors. Since one wire plane can contribute at most one hit, z_i and θ_i are just the plane information where the hit occurs.

To find the values of the parameters x_{off} , y_{off} , x_{slope} and y_{slope} that give rise to the minimum value of χ^2 , by setting the partial derivatives of χ^2 with respect to each of those parameters to zero, we can get four similar equations:

$$\begin{aligned} \frac{\partial \chi^2}{\partial x_{off}} &= \sum_i A_i \sin \theta_i = 0, \\ \frac{\partial \chi^2}{\partial x_{slope}} &= \sum_i A_i \sin \theta_i z_i = 0, \\ \frac{\partial \chi^2}{\partial y_{off}} &= \sum_i A_i \cos \theta_i = 0, \\ \frac{\partial \chi^2}{\partial y_{slope}} &= \sum_i A_i \cos \theta_i z_i = 0, \end{aligned} \quad (3.17)$$

where

$$A_i = \frac{(y_{off} + y_{slope} \times z_i) \cos \theta_i - (x_{off} + x_{slope} \times z_i) \sin \theta_i - (u_{irre})_i}{\sigma_i^2}.$$

These equations can be rearranged as four linear equations in terms of the four unknown parameters:

$$\begin{aligned} \sum_i \frac{(u_{irre})_i \sin \theta_i}{\sigma_i^2} &= -x_{off} \sum_i B_i - x_{slope} \sum_i B_i z_i + y_{off} \sum_i C_i + y_{slope} \sum_i C_i z_i, \\ \sum_i \frac{(u_{irre})_i \sin \theta_i z_i}{\sigma_i^2} &= -x_{off} \sum_i B_i z_i - x_{slope} \sum_i B_i z_i^2 + y_{off} \sum_i C_i z_i + y_{slope} \sum_i C_i z_i^2, \\ \sum_i \frac{(u_{irre})_i \cos \theta_i}{\sigma_i^2} &= -x_{off} \sum_i C_i - x_{slope} \sum_i C_i z_i + y_{off} \sum_i D_i + y_{slope} \sum_i D_i z_i, \\ \sum_i \frac{(u_{irre})_i \cos \theta_i z_i}{\sigma_i^2} &= -x_{off} \sum_i C_i z_i - x_{slope} \sum_i C_i z_i^2 + y_{off} \sum_i D_i z_i + y_{slope} \sum_i D_i z_i^2, \end{aligned} \quad (3.18)$$

where,

$$\begin{aligned} B_i &= \frac{\sin^2 \theta_i}{\sigma_i^2}, \\ C_i &= \frac{\sin \theta_i \cos \theta_i}{\sigma_i^2}, \\ D_i &= \frac{\cos^2 \theta_i}{\sigma_i^2}. \end{aligned} \quad (3.19)$$

Those equations can be further written in matrix form

$$\begin{pmatrix} \sum_i \frac{(u_{irre})_i \sin \theta_i}{\sigma_i^2} \\ \sum_i \frac{(u_{irre})_i \sin \theta_i z_i}{\sigma_i^2} \\ \sum_i \frac{(u_{irre})_i \cos \theta_i}{\sigma_i^2} \\ \sum_i \frac{(u_{irre})_i \cos \theta_i z_i}{\sigma_i^2} \end{pmatrix} = \begin{pmatrix} \sum_i B_i & \sum_i B_i z_i & \sum_i C_i & \sum_i C_i z_i \\ \sum_i B_i z_i & \sum_i B_i z_i^2 & \sum_i C_i z_i & \sum_i C_i z_i^2 \\ \sum_i C_i & \sum_i C_i z_i & \sum_i D_i & \sum_i D_i z_i \\ \sum_i C_i z_i & \sum_i C_i z_i^2 & \sum_i D_i z_i & \sum_i D_i z_i^2 \end{pmatrix} \times \begin{pmatrix} -x_{off} \\ -x_{slope} \\ y_{off} \\ y_{slope} \end{pmatrix}. \quad (3.20)$$

Therefore, by solving this simple linear algebra equation, the values of all four parameters x_{off} , x_{slope} , y_{off} and y_{slope} can be obtained given the hit information from the *UsedHits* container, where each hit will provide the values related with the subscript i .

In order to further reduce the impact brought by the noisy hits to the found **partial track**, an iteration process is added here: after the geometry of the **partial track** is determined from Eq. 3.20, the residual for each hit on a given plane can be calculated by using Eq. 3.14. The hit with the largest residual is then deleted from the hit list and one more fitting procedure is performed based on the remaining hits in the list to yield the final geometry parameters of the **partial track**. By applying this process, a potential noisy hit, which has not been screened out in the previous process in the QTR, is filtered out. Even if the deleted hit is a good one, the number of remaining hits (\geq) can still guarantee us to perform a good fit.

3.8 Momentum Determination

In order to obtain the four-momentum transfer Q^2 and other kinematic information, we need to loop over all given **partial tracks** in the HDCs and the VDCs to attempt connecting them together. Before the attempt to connect the HDCs and the VDCs **partial tracks**, *QwBridgingTrackFilter.Filter* function is called to filter out any unreasonable HDC and VDC candidates. Table 3.3 lists all the available filters in this function. If the combination of the HDCs and the VDCs **partial tracks** has not been filtered out by any filter, then the *status* variable will become *kPass* and *QwRayTracer.Bridge* is called to connect the HDCs and the VDCs **partial track**. The method used in *QwRayTracer.Bridge* is named as the “shooting method”. The principle behind the “shooting method” can be described as following several

TABLE 3.3: List of available filters in *QwBridgingTrackFilter.Filter* function

θ_{polar}	This filter sets the constraint on the scattering angle of the HDCs partial track . The range is $[1^\circ, 13^\circ]$. If it can not pass this filter, a fail signal <i>kFailThetaFront</i> is returned.
Z_{vertex}	Sets the constraint on the range of reconstructed target vertex in z axis from the HDCs partial track . The default range is $[-672, 628]$ cm. If failed, <i>kFailVertexZ</i> is returned.
$\Delta\theta_{polar}$	Sets the constraint on the difference between the scattering angle of the HDCs and the VDCs partial track . This can be interpreted as the bedding angle limit in QTOR magnet. The default range is $[5, 45]$ degree. If failed, <i>kFailDiffTheta</i> will be returned.
$\Delta\phi_{azimuthal}$	Sets the constraint on the difference between azimuthal angle of the HDCs and the VDCs partial track . The default range is $[-20, 20]$ degree. If failed, <i>kFailDiffPhi</i> will be returned.
$\Delta\phi_{front}$	This filter sets the constraint on the difference between azimuthal angle of $\phi_{position}$ and $\phi_{momentum}$ (illustrated in Figure 3.20) in the HDCs track only. The default range is $[-5^\circ, 5^\circ]$. If failed, <i>kFailPhiFront</i> will be returned.

steps:

1. Get the first good guess of momentum $p_{initial}$ from the geometry information of the HDCs **partial track** by assuming the electron-proton reaction is elastic without any energy loss in the target. The formula can be outlined as

$$p_{initial} = \frac{E_0}{1 + \frac{E_0}{M_p}(1 - \cos \theta)} \quad (3.21)$$

where E_0 is equal to the beam energy 1.165 GeV and θ is the polar angle of

HDC **partial track**. Also the position of that **partial track** \mathbf{r}_{front} in the front face of QTOR is obtained, which is easily calculated by projecting the **partial track** onto that plane. It is justifiable to do so because both the HDC and VDC tracks are in magnetic-field free regions, and are therefore straight line segments. The position \mathbf{r}_{back} in the back face of QTOR can also be obtained from projecting the VDCs **partial track** onto the corresponding plane.

2. Given the $p_{initial}$ and \mathbf{r}_{front} , one can "swim" through the QTOR region with the aid of a magnetic field map, which provides the value of the magnetic field of numerous at a series of intermediate points. The Runge-Kutta 4th order procedure [84] is employed here to solve the two ordinary differential equations in a numerical way:

$$\begin{aligned} \mathbf{v} &= \frac{d\mathbf{r}}{dt} \\ m_e \frac{d\mathbf{v}}{dt} &= q\mathbf{v} \times \mathbf{B} \end{aligned} \quad (3.22)$$

with the initial and boundary conditions. Consequently, the corresponding \mathbf{r}_{back} is determined.

3. two different values of momentum will enter Eq. 3.22 for every single value of $p_{initial}$: one is $p_{initial} + \Delta p$ and the other is $p_{initial} - \Delta p$. The value of Δp is set to 10 MeV by default. Therefore, two distinct values of \mathbf{r}_{back} : \mathbf{r}_{back}^+ and \mathbf{r}_{back}^- will be obtained. The momentum will be thus updated to a new value through the Newton-Raphson method:

$$P_{new} = P_{initial} - \frac{1}{2} \times \Delta p \times \frac{\mathbf{r}_{back}^+ + \mathbf{r}_{back}^- - 2 \times \mathbf{r}_{back}}{\mathbf{r}_{back}^+ - \mathbf{r}_{back}^-} \quad (3.23)$$

4. Next, by using the Runge-Kutta 4th order procedure again with the new derived momentum p_{new} , we can get the corresponding r'_{back} . If the difference between the deduced r'_{back} and real r_{back} is within the default tolerance value, we regard the connection as being successful. Otherwise, we'll repeat step 2 with the updated $p_{initial} = p_{new}$.

Notice that the tolerance is set by the *res* variable in *QwRayTracer.Bridge* function, with default value 0.2 cm and the maximum number of iterations allowed, by default, is 10. If after 10 iterations, the deduced position r'_{back} and real position r_{back} still can not match, the QTR will regard this pair of **partial tracks** as bad and will immediately stop and continue to match other pairs in the same event.

3.9 Geometry File

A fully detailed detector geometry file plays an essential role in giving the QTR capability to reflect the geometry in the real world. A full summary of the items in the geometry file is given in Appendix B.

The reconstruction of a track is first implemented in the local coordinates and then changed to the global coordinates given the knowledge of the origin of each local coordinates associated with wire planes. Thus, the locations of chamber in the VDCs and the HDCs, which are installed on rotators and located at different z locations along the beam line, need to be precisely determined. We relied on the JLab Survey and Alignment Group, which employed a Faro Laser Tracker that is

able to locate a small fiducial marker within $100 \mu\text{m}$. However, the relative position of each individual wire plane in a single chamber can not be directly measured due to the fact that the laser tracker can only measure points on the exterior of the chamber. Fortunately, those positions were rigorously controlled and measured when the chambers were built and thus should not be away from nominal values too much (within $\simeq 200 \mu\text{m}$). In the upstream area (HDCs) where the geometry numbers need the most rigorous control, an indirect self-consistency method was utilized to adjust the relative position of the wire planes to see if the change had a huge impact on the signed residual of wire planes (the signed residual is defined as the difference between hit position and track position just as Eq. 3.7 shows). An example is shown in Figure 3.21.

Furthermore, we resorted to the “projection” method to fine-tune the external geometry of the chambers. The theory behind this method is that we know the position and the shape of some components in the experiment to a very high precision, such as the collimators, the Al target and the main detectors. Then the found track could be projected back to where those components are and if the geometry of the chambers are perfect, those projected images should be exactly superimposed with the real images of those components. To see more result, please refer to Sec. 4.3.2.

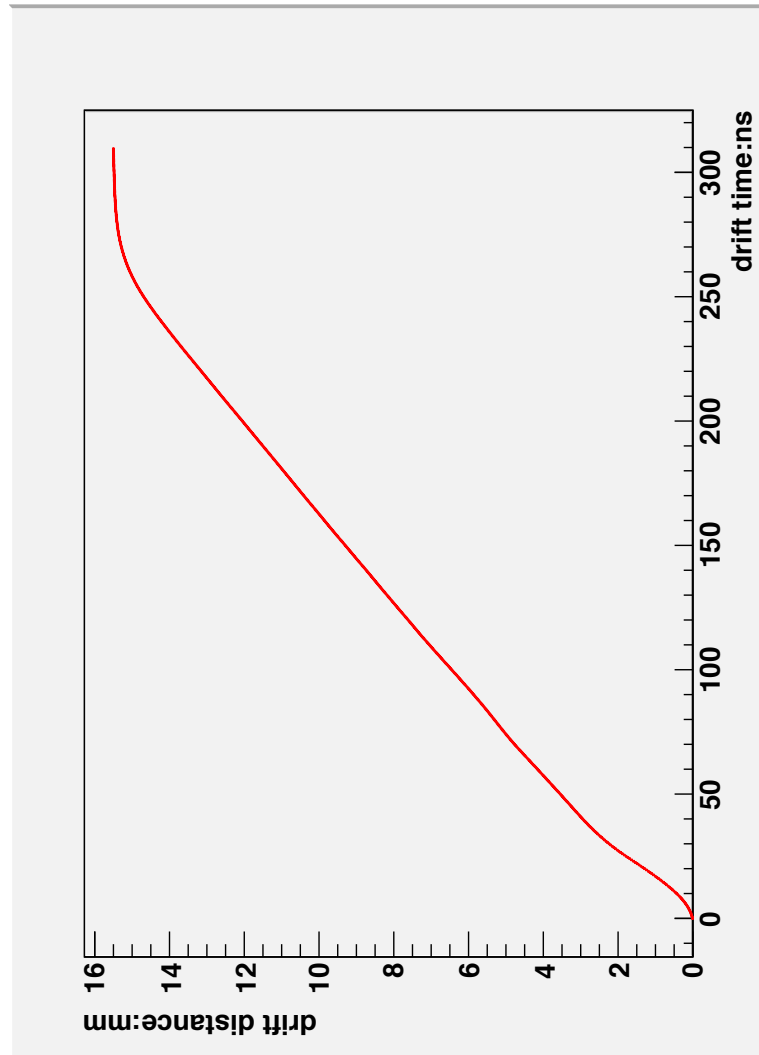


FIG. 3.7: The relationship between drift-time and drift-distance drawn from the entries in the look-up table for the VDCs. The intermediate points are so dense that the figure looks like a continuous line. However, the real data are comprised of discrete points. When calculating the drift-distance between two intermediate points, a linear interpolation is used.

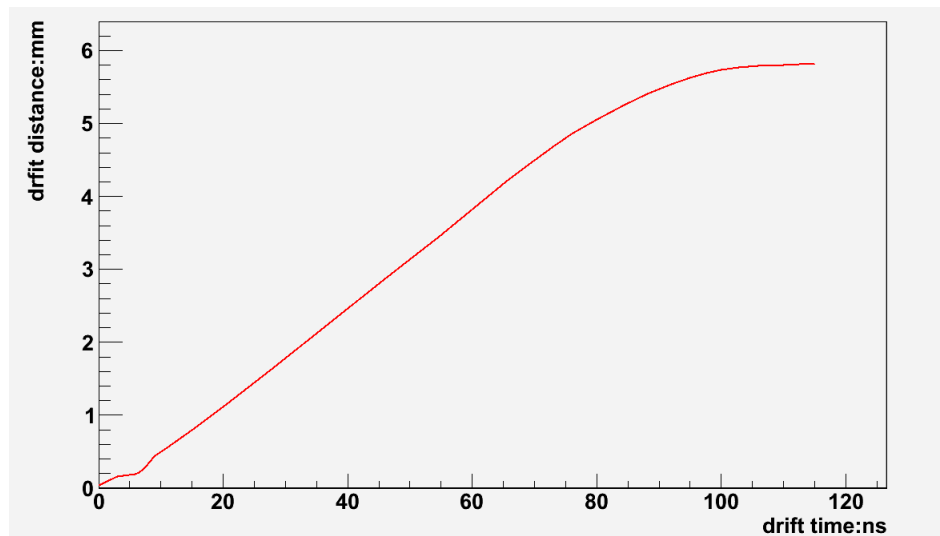


FIG. 3.8: The relationship between drift-time and drift-distance draw from the entries in the look-up table for the HDCs.

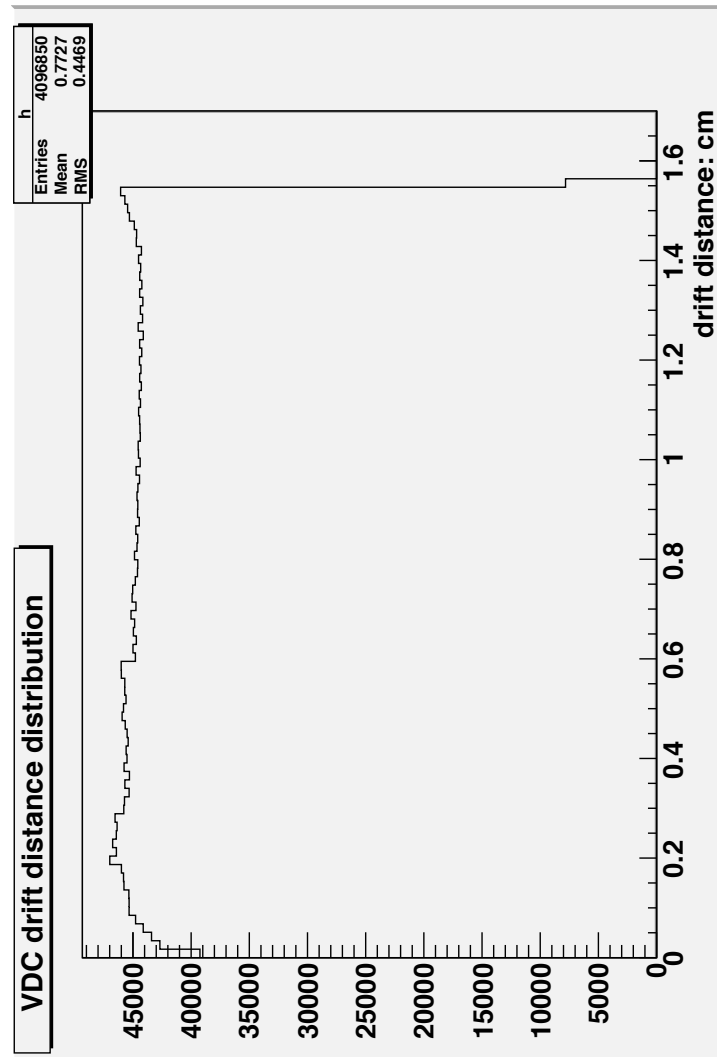


FIG. 3.9: A typical VDC drift-distance distribution obtained by numerical integration of the time spectrum.

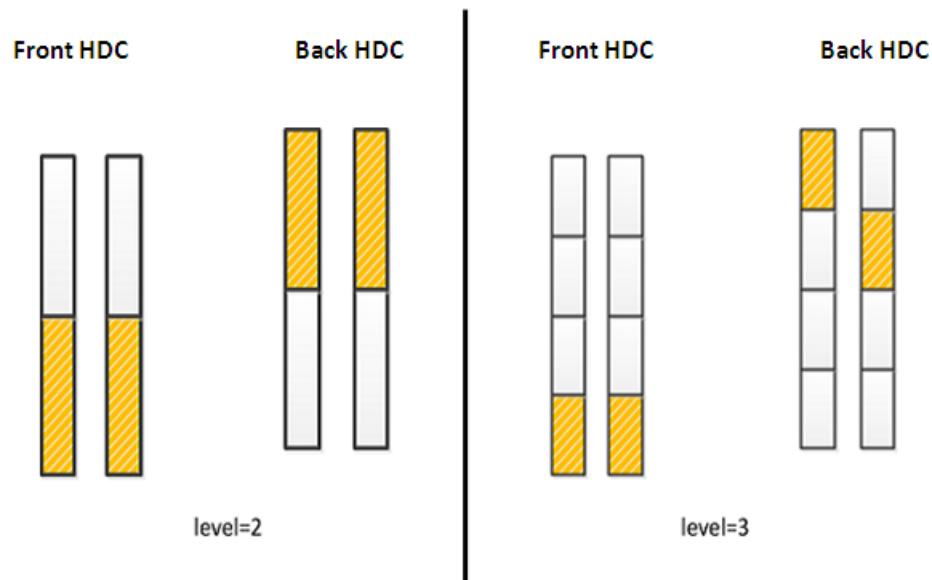


FIG. 3.10: Schematic overview of pattern database generation. Each rectangular box represents one layer (HDC wire plane) and each highlighted box represents where the particle hits the chamber. For the case of $level=2$ on the left, each layer is divided into $2^{(2-1)} = 2$ segments and the bit array value for this bit pattern is $[0, 0, 1, 1]$; An example of one of the 16 descendants is also given here on the right. The $level$ is increased to 3, so there are $2^{(3-1)} = 4$ bins in each layer. If we choose the option array to be $[0, 0, 1, 0]$ then we'll get the bit pattern shown here with bit array value $[0, 0, 3, 2]$. The pattern shown on the right is not saved because a straight line can not go through those boxes.

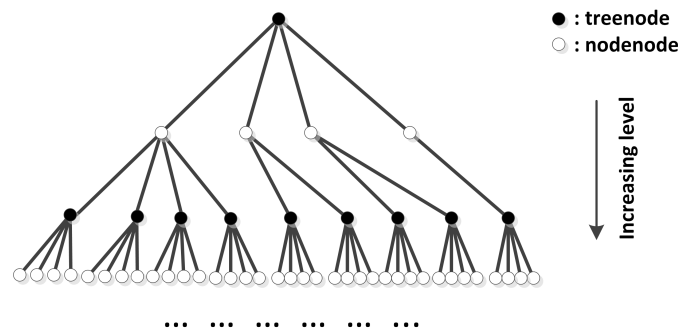


FIG. 3.11: The pattern database is organized as a tree. The treenode stores the bit information which represents a valid straight line. Each treenode has four son pointers (nodenode) pointing to the head of a linked list and each element in the linked list is a pointer to the treenode in the next level. The four son pointers describe four cases: *no shift-no flip*, *shift-no flip*, *no shift-flip*, *shift-flip*.

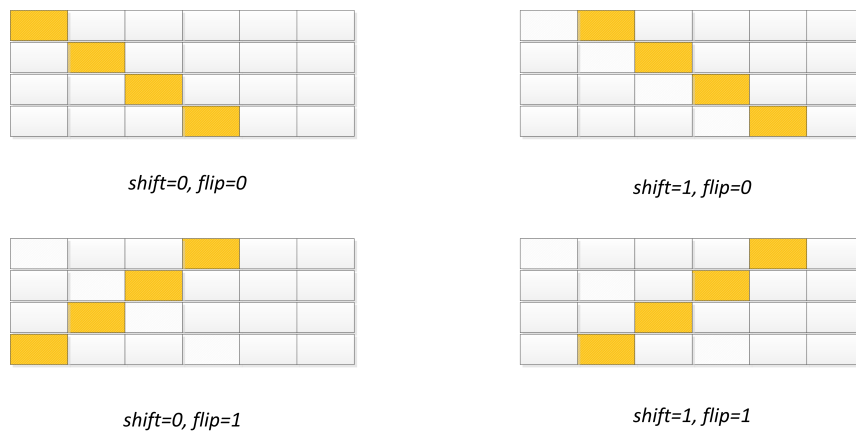


FIG. 3.12: In order to save space as well as speed up the tree search process, bit patterns with only minor difference are considered as one.

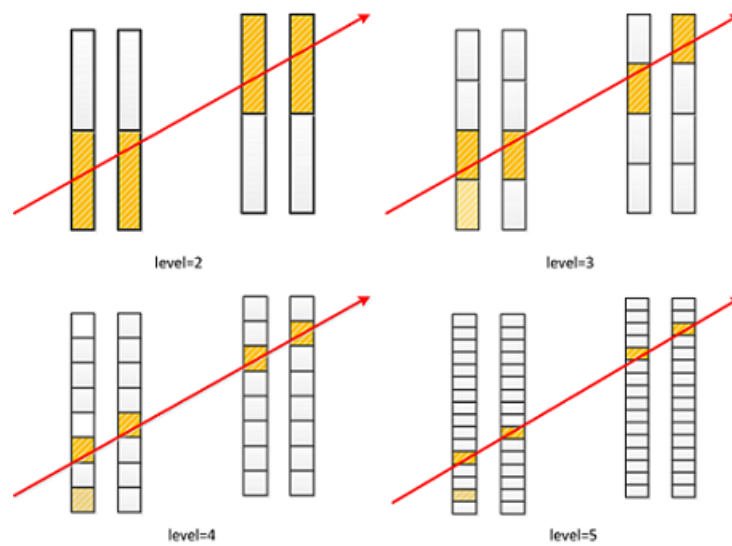


FIG. 3.13: Schematic overview of the tree-search algorithm in the case of the HDCs: four levels are shown here with increasing resolution. The light shade color box represents a noise hit while the solid color box stands for the real hit in each layer.

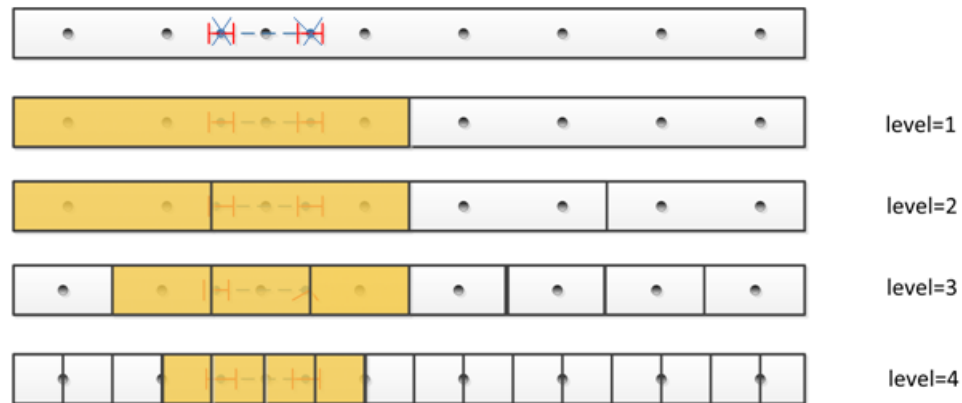


FIG. 3.14: The top diagram describes a series of sense wires (black dots) in a given single HDC layer, with a hit producing two possible hit positions (crosses), each of which has a resolution as the red bracket depicts. The default value of the resolution in the case of the HDCs is 0.05 cm. For $level = 1$, the bit array is (10); for $level = 2$, the bit array is (1100); for $level = 3$, the bit array is (01110000); for $level = 4$, the bit array is (0001111000000000). So the overall bit array for this single layer is 0001111000000000001110000110010, in order from the deepest level to the start level.

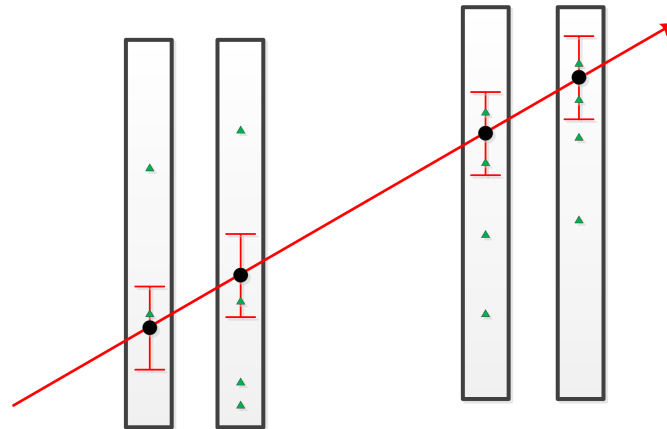


FIG. 3.15: Schematic overview of how to select the appropriate hit position according to the initial condition of a **treeline**. The red arrow represent the “*path*” and the green triangle points are the hit positions. The sense wires are not shown here. For each given detector layer, there is a range of positions which sets the criterion of selecting the hit position (green triangles).

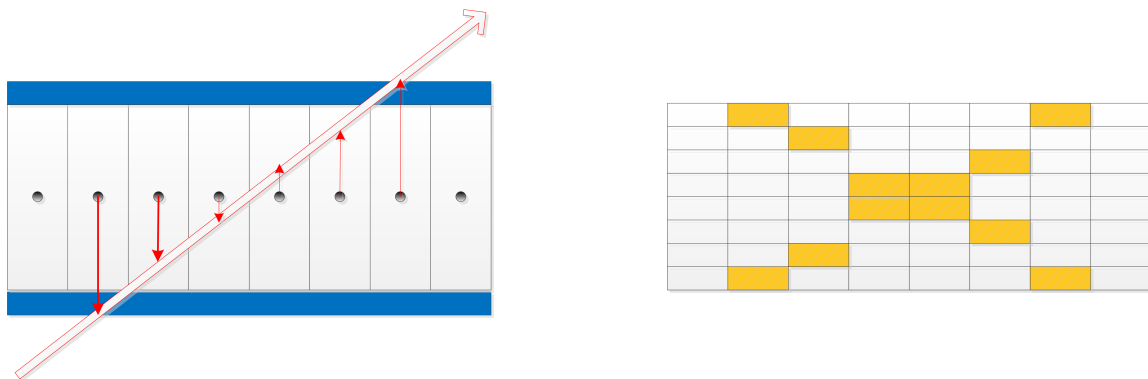


FIG. 3.16: The left figure shows how a track traverses one VDC wire plane and generates wire hits. The right figure shows how those hits are mapped into a bit pattern matrix.

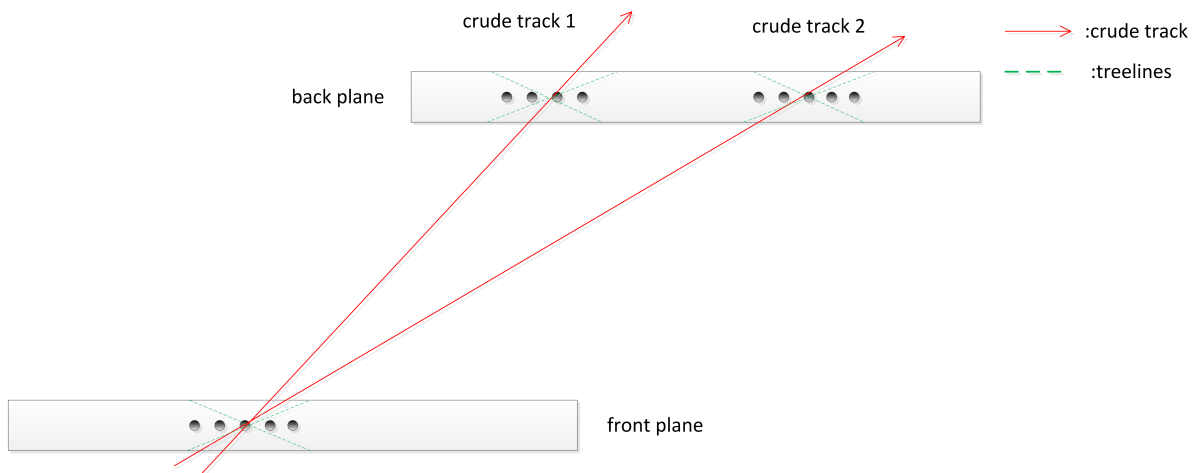


FIG. 3.17: Schematic overview of how the *QwTrackingTreeMatch.MatchRegion3* works. Two “crude” tracks (red arrows) are generated from connecting hit wire clusters in the front and back wire planes. The angle between “crude” tracks and local **treeline** is calculated. A selection based on this angle is used to find out the correct pair of **treelines** from the front and back wire planes and consequently remove the “ghost” **treelines** or “noise” track segment, depicted as crude track 1.

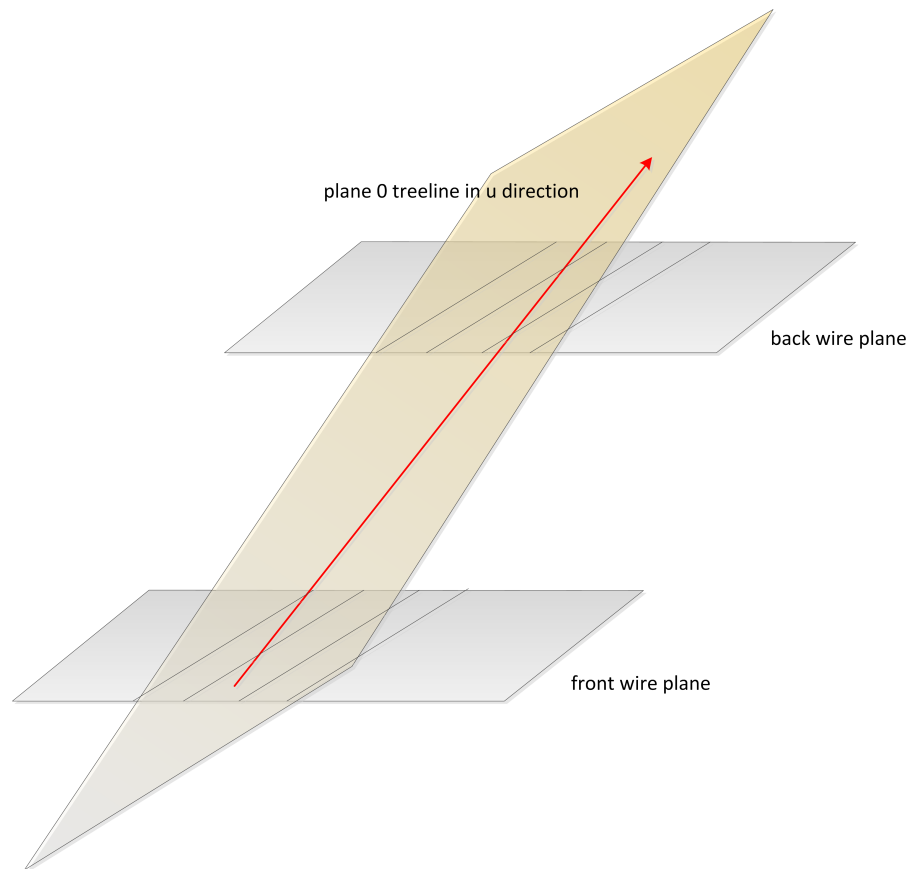


FIG. 3.18: Overview of the relationship between the unique plane (light orange) and the “plane 0” **treeline** (see red arrow). The unique plane (light orange) must be parallel to the wire orientation and must contain the “plane 0” **treeline**.

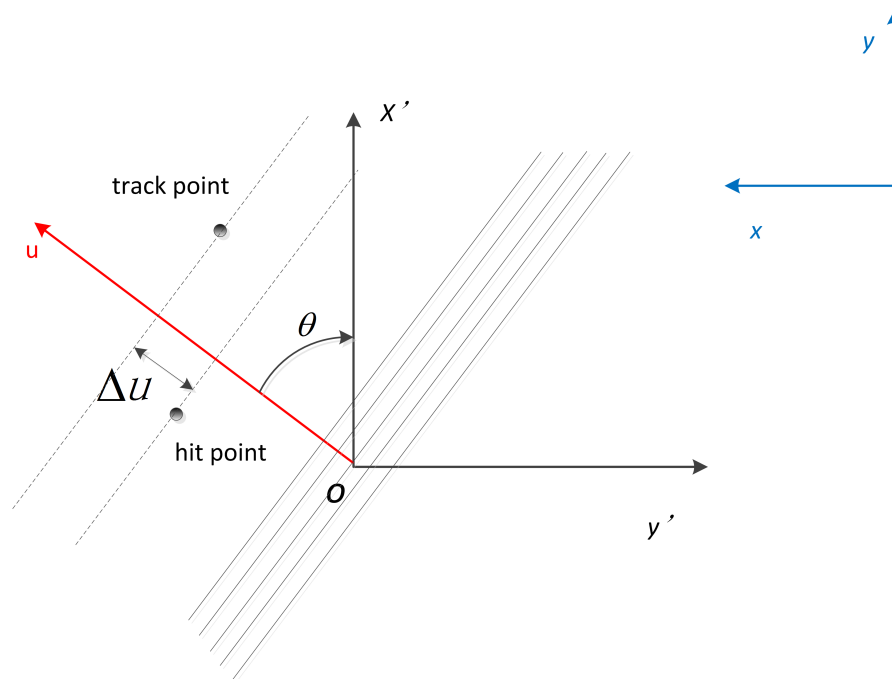


FIG. 3.19: An example to show how to calculate the Δu (as in Eq. 3.7) given a u wire plane of a HDCs at octant 3. The values of x and y coordinates for both track point and hit point are calculated in the local coordinates. θ is the angle between u axis and local x' axis. The global coordinate system is also displayed here at upper left corner.

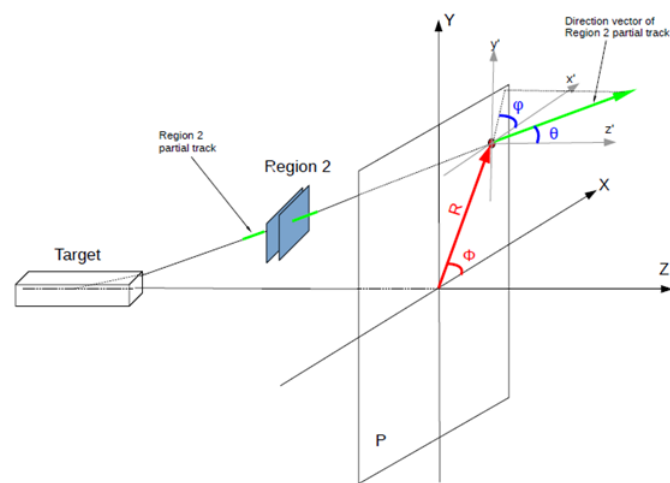


FIG. 3.20: The diagram depicts how the $\Delta\phi_{front}$ is defined (see Table 3.3). This assumes the center of the target is the origin of the track. The green line is the **partial track** of the HDCs and has polar angle θ and azimuthal angle φ . The hit position (red point) also has its own θ and ϕ . If the **partial track** comes from the target and is constructed correctly, the difference between φ and ϕ should be very small and constraining on that difference provides us a filter to remove any unreasonable HDC **partial tracks** [83].

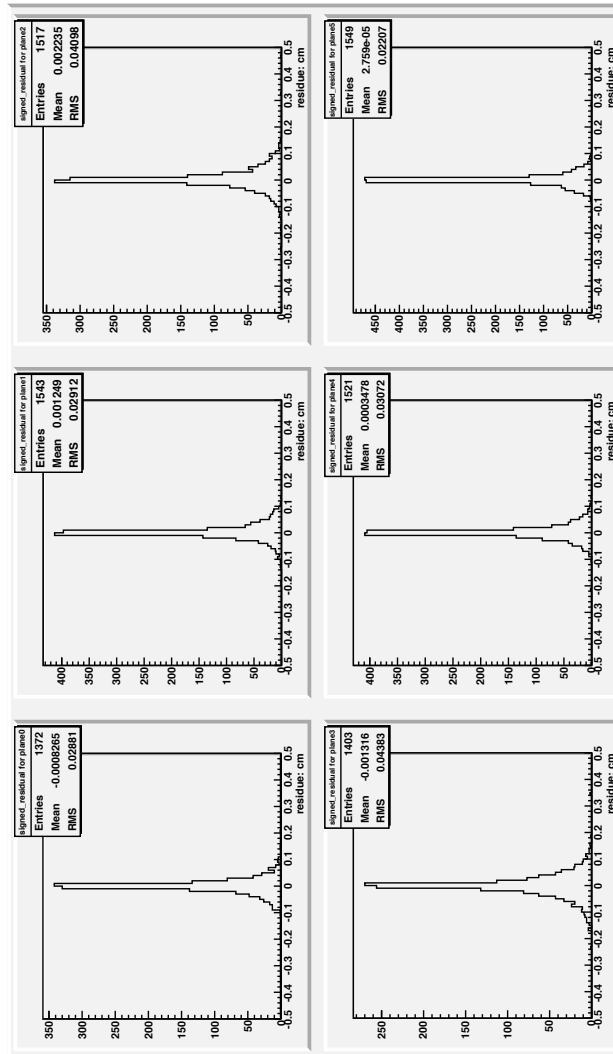


FIG. 3.21: Unlike the QTR analyzer, this method employs a so-called "brute-force" method to iteratively go through all the combinations of hit positions to create the optimal **partial track**, which has the minimum χ^2 . Once the three-dimensional track segment is found, the difference between the hit position and track position as equation(3.12) shows can be determined for every plane. This plot shows the result for the first chamber of package1 in HDC. Ideally, the real offset values for wire planes should lead to the distribution with minimum rms values.

CHAPTER 4

Tracking Data Analysis and Kinematics

4.1 Overview

The tracking data for the Qweak experiment was collected over two running periods, denoted as Run I and Run II. Each data set is analyzed using the same tracking software package but with different parameter files to represent the different configurations between various running periods, such as beam energy and QTOR current.

Tab. 4.1 presents an overview of the tracking data in each period.

In data set 1, we took measurements of Q^2 not only on the hydrogen target but also on optics targets and an aluminum target, which serve as useful auxiliary measurements to calibrate the geometry of the tracking system to ensure the

TABLE 4.1: The overview of the tracking data set

Dataset	Time	Run Number
1	January 2011	Run I
2	March 2011	Run I
3	May 2011	Run I
4	November 2011	Run II
5	January 2012	Run II
6	May 2012	Run II

correct Q^2 calculation. Systematic studies on beam raster size, beam position and QTOR current were also carried out at that time. Furthermore, the chambers were rotated to different positions to study the dependence of Q^2 on octant.

In March 2011, since the HDC could not be rotated because of being blocked by the installation of some additional shielding (the “Pb donut”), the only position measured for Q^2 was at octant 1+5. Compared to data set 1, a beam rate study was performed by adjusting the beam slit position.

In May 2011, the main goal was to study the light-weighted track distribution on all main detectors. Therefore, most of the runs were “VDC only” runs.

In November 2011, the interference between the HDCs and the additional shielding was corrected, so that the HDCs were again rotatable and consequently more rotations were performed in that period.

The measurement in January 2012 was the last major period when Q^2 was studied. In this period, most of the standard Q^2 runs, such as with the LH_2 target, were taken. For the final measurement in May 2012, a study of the Q^2 dependence on the beam angle was added.

4.2 Q^2 results

For the final precision 4% measurement of Q_W^p , the value of Q^2 needs to be measured to a precision of 0.5% or better. In this dissertation, the best result of Q^2 up to date will be presented.

The four-momentum transfer Q^2 of elastic scattering between an electron and a proton is given by:

$$Q^2 = \frac{4E^2 \sin^2 \frac{\theta}{2}}{1 + 2\frac{E}{M} \sin^2 \frac{\theta}{2}} \quad (4.1)$$

where E is the incident electron energy at the scattering vertex, θ the scattering angle and M the proton mass. In fact, for elastic scattering, the Q^2 can also be calculated by three other equations:

$$Q^2 = 4EE' \sin^2 \frac{\theta}{2} \quad (4.2)$$

$$Q^2 = \frac{4E'^2 \sin^2 \frac{\theta}{2}}{1 - 2\frac{E'}{M} \sin^2 \frac{\theta}{2}} \quad (4.3)$$

$$Q^2 = 2M(E - E') \quad (4.4)$$

Therefore, the measurement of any two of E, E' and θ will suffice to calculate Q^2 . In this dissertation, Eq. 4.1 is used to yield the value of Q^2 . The reason is that the absolute energy of the beam can be measured to $\leq 0.1\%$ precision by using Hall C's arc-energy measurement procedure [85]. However, the incident energy used in Eq. 4.1 is not equivalent to the value from the beam energy measurement, but needs to be accounted for the energy loss in the target, which will be described in more detail in Sec. 4.3.3. In addition to the precise determination of the incident

energy at the vertex, good knowledge of the locations and geometry of the tracking detectors and robust tracking software performance are requirements to yield the correct scattering angle. Furthermore, various cuts are developed and studied in order to be used as powerful tools to screen out the false tracks which will otherwise bias the result of Q^2 determination. One thing that needs to be noticed is that although it seems that the E' and therefore the VDCs are redundant if Eq. 4.1 is used, we still need VDCs, for mainly two reasons: the first is to select the elastic scattering events out of those seen by the HDCs through good track fitting in the VDCs, and the second is to make corrections for biasing due to the analog response of main detectors. Therefore all of the above topics will be discussed in the later sections.

4.2.1 Geometry of Tracking System and Projection

The scattering angle θ used in Eq. 4.1 to determine the Q^2 value, largely depends on the spatial locations of the HDCs and locations of the target and the beam. In principle, once the equation of the trajectory of scattered electrons is given by the tracking analyzer, it can be projected to any location along with the beam line as long as there's no magnetic field in the path to change its linear form into a non-linear form. The projection mainly serves a two-fold role in the Q^2 determination: one is to check the quality of reconstructed tracks from the analyzer in individual subsystems and the second is to help to tune the spatial locations of the HDCs to a high precision level. Notice that all the results in this section have had the

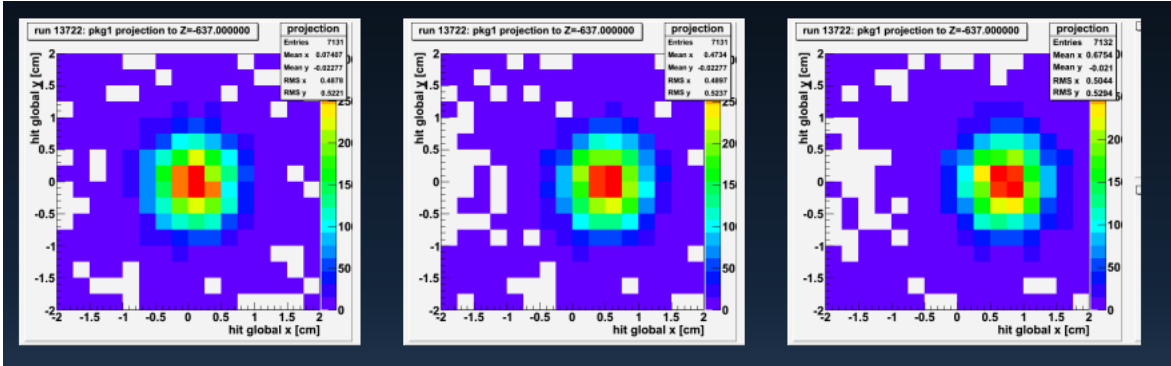


FIG. 4.1: This figure shows the projection to the aluminum target. From left to right, the position of the back HDC chamber in package 1 was moved from nominal position ($0 \mu\text{m}$) to $+600 \mu\text{m}$. The mean X value of the projection therefore shifted from 0.7 mm to 6.7 mm .

standard cuts applied, namely, the MD and the MT cuts, which will be discussed in the next section.

For the latter, a study was performed of the systematic effect of the locations of the HDC chambers on the measured Q^2 . The spatial locations of the HDC chambers used in the analysis were changed in a way that only moved the back chamber in the dispersive direction. By doing that, the scattered angle θ and the Q^2 will change accordingly. Fig. 4.1 and Fig. 4.2 show the variation of the projection to the aluminum targets (this will be discussed in more details in the next few paragraphs) and the variation of the Q^2 along with the change of position in the back chambers of the HDCs respectively. Each change is equal to $300 \mu\text{m}$ and it is already enough to see the obvious change in both projection and the value of Q^2 . By using this method, we fine-tuned the HDCs chamber to a level of hundreds of microns of confidence.

For the first purpose mentioned above, one of the aluminum thin targets or

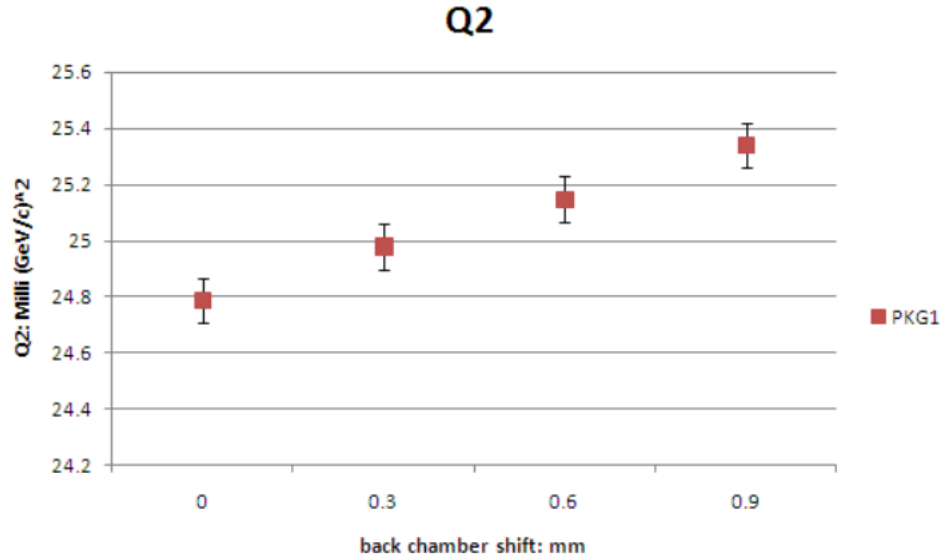


FIG. 4.2: This figure shows the Q^2 dependence on the position of the back HDC chamber in package 1. A $300 \mu\text{m}$ change can result in $\sim 0.8\%$ change on Q^2 .

one of the optics targets was used, and during those runs, the beam raster size was set to $1 \times 1 \text{mm}^2$. In this dissertation, only the results from the downstream aluminum targets are shown. The center of the downstream aluminum targets were located at $Z = -637 \text{ cm}$ (the center of the QTOR is defined as $Z = 0 \text{ cm}$, and the beam travels along the positive Z direction) with different thicknesses varying from 0.1737 to 0.7115 cm , which is equivalent to different number of radiation lengths. Fig. 4.3 shows the projection of the reconstructed partial tracks from package 1 to the plane $Z = -637 \text{ cm}$, with the measured Z vertex and χ distribution (for the definition of χ , see Eq. 3.16) in run 13722. The measured Z vertex is defined as the position along the beam axis where the perpendicular distance between the reconstructed partial track and the beam axis reaches a minimum. Tab. 4.2 gives a summary of the projection result from both packages in that run. It can be seen that with the latest geometry calibration, the measured Z vertex is

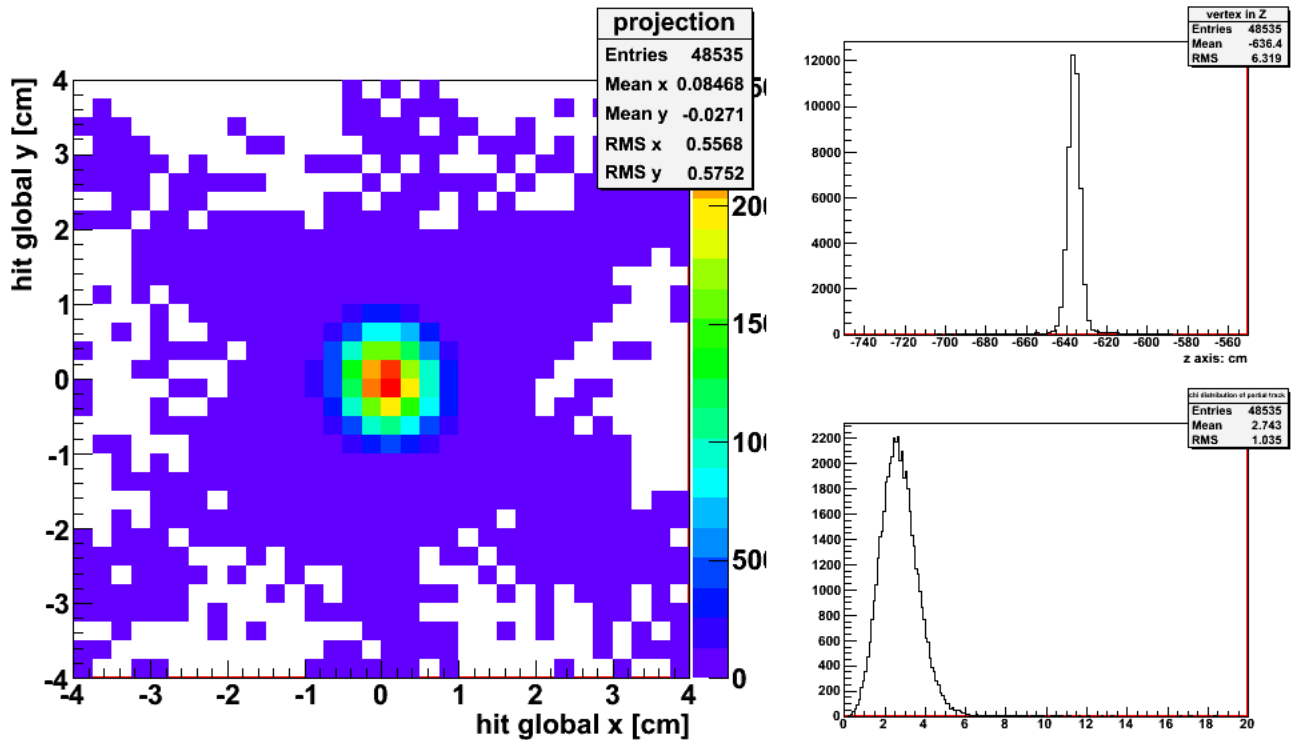


FIG. 4.3: The left graph shows the projection to the target plane where the 4% radiation length downstream aluminum target is used, from package 1 in run 13722. The statistics box shows the mean and RMS of the projected coordinates. The upper right graph is the distribution of measured Z vertex and the lower right is the χ distribution.

< 1 cm from the actual center of the target with a relatively narrow distribution.

The resolution from package 1 is generally better than that from package 2, which might be due to one “missing” plane in package 2.¹

Fig. 4.4 shows the measured vertex distribution from run 15112, where three optics targets were used. The optics target were made of carbon-foil, with a foil spacing of 16 cm for a total length of 32 cm. Each optics target is 2 mm thick. Three distinct spikes denoted as “1,3,5” were measured, with some smearing

¹The “missing” plane is plane 10 in package 2 of the HDCs; this plane could not be run at full voltage, for an unknown reason. At the reduced voltage used, the efficiency was low ($\leq 10\%$), therefore effectively making it a missing plane from track reconstruction.

TABLE 4.2: Summary of projection result to a thin Al target from run 13722

Package	Mean of X (mm)	RMS of X (mm)	Mean of Y	RMS of Y
1	0.847	5.57	-0.271	5.75
2	0.770	5.76	0.510	6.13
Package	Mean Z of Vertex (cm)	RMS of Z Vertex (cm)	Mean of χ	RMS of χ
1	-636.4	6.32	2.74	1.04
2	-637.6	6.04	2.99	1.21

TABLE 4.3: Fitted Z location for 1,3,5 optics target from run 15112.

peak	Z center (cm)	σ (cm)	Expected Z value (cm)
1	-671.88	4.60	-670.98
2	-655.40	3.89	-653.17
3	-637.41	3.84	-636.37

among peaks due to the tracking resolution. Here, the Gaussian function is used to fit each peak and the result is shown in Tab. 4.3. The center is only 1~2 cm away from the actual position of the optical target. With any future improvement of the geometry, the separation of each individual spike should become more obvious and the peak location should also be more close to the actual position.

Fig. 4.5 show a series of projection results from LH_2 target runs where different octants were covered and a 4×4 mm² beam raster was used. A summary of the measured Z vertex distribution can be found in Tab. 4.4. The center of the LH_2 target is assumed to be -653.108 cm, and the measured center is ~ 2 cm away from that value. This could be explained by some unfiltered tracks which do not come from the scattered events or the unphysical tracks reconstructed by the software. The tilted shape towards the upstream direction can also be explained by the fact that the more scattering events will occur at smaller angle because $\frac{d\sigma}{d\theta}$

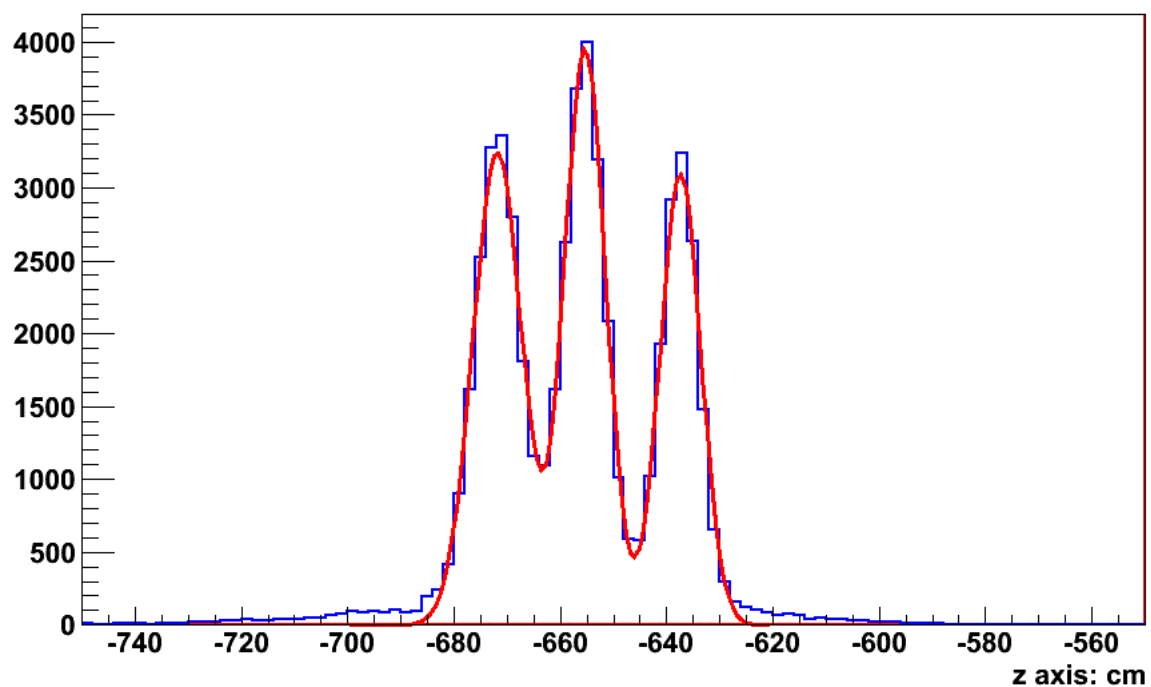


FIG. 4.4: Measured Z vertex from package 1 from run 15112 where three optics targets were used. The red curve is the result of a fit to the sum of three Gaussian distributions.

TABLE 4.4: Summary of measured Z vertex distribution

Run	Package	Octant	Mean (cm)	RMS (cm)
13653	1	1	-654.0	12.32
13653	2	5	-655.1	12.30
13671	1	8	-655.6	12.74
13671	2	4	-653.4	12.67
13674	1	2	-655.3	12.91
13674	2	6	-653.6	12.50
13676	1	3	-654.4	12.82
13676	2	7	-653.2	12.41

gets larger at smaller θ . With more rigorous filters developed in future, such as the matching filter (see Sec. 4.2.2) or improved tracking software, the difference between the measured and the real should be smaller. The RMS value indicates how well the length of the target is measured. Since the length of our LH₂ target is 35 cm, the ideal RMS value, assuming the uniform scattering, can be calculated as

$$Z_{RMS} = \sqrt{\frac{1}{L} \int_{-\frac{L}{2}}^{\frac{L}{2}} z^2 dz}, \quad (4.5)$$

where L is the length of the target. Therefore, the ideal value for the RMS is ~ 10 cm and the measured RMS is ~ 13 cm.

Unlike the projection from runs using aluminum or optics targets, the Z plane chosen to project the tracks to here is the primary collimator. As Fig. 4.5 shows, almost all the reconstructed tracks were confined within the aperture of the primary collimator with $Z=-370.719$ cm, which is expected, and is also a useful metric of the quality of the tracking system. The projection results from the other seven octants can be found in Appendix D.

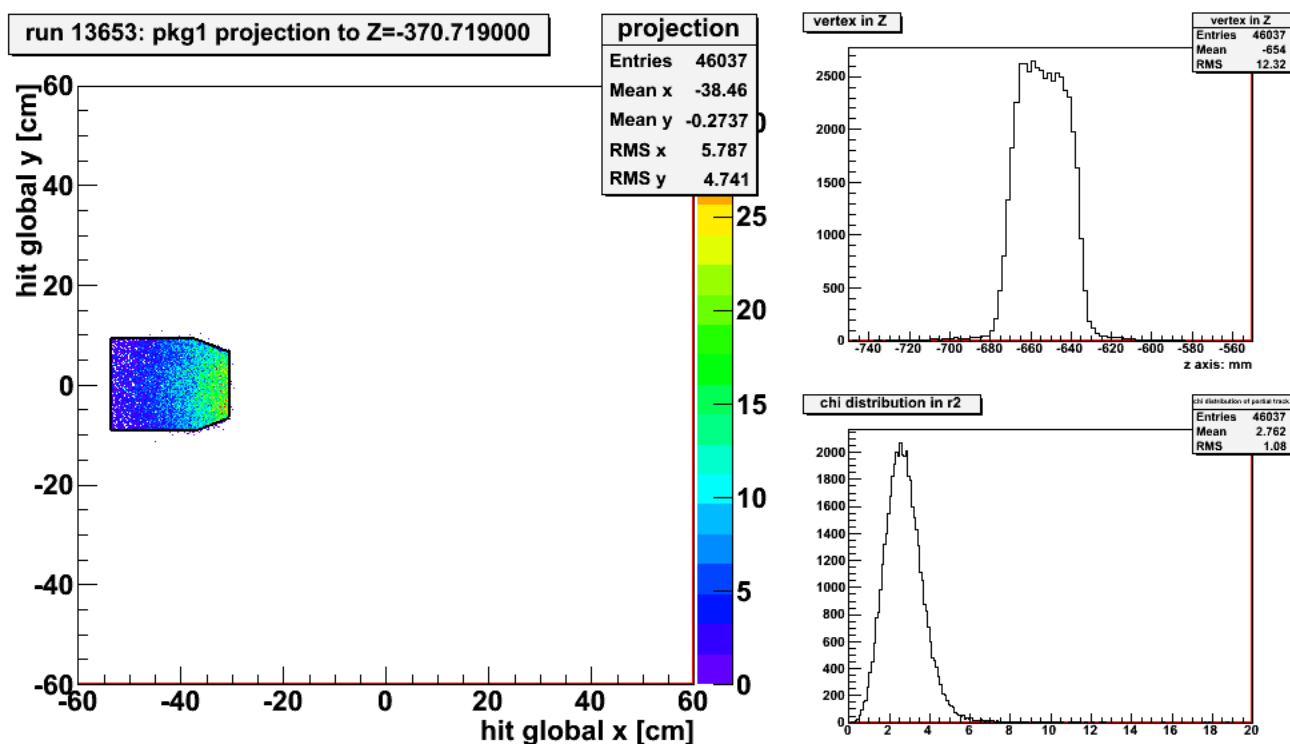


FIG. 4.5: Projection result from package 1 in run 13653 where octant 1 is covered. This was a run using the full LH₂ target. The left pnael is projection to Z of primary collimator. The upper right plane is the distribution of measured Z vertex and the lower right is the χ distribution.

4.2.2 Cuts

Various cuts have been developed to reject poorly-fit or non-elastic scattering tracks from the analyzer. The cuts being used in this dissertation include the main detector cut (MD cut) and a HDC multiple tracks cut (MT cut).

The MD cut is a cut that requires that the main detector in the appropriate octant actually fired. It is implemented through the use of the time spectrum of signals from the main detectors. Since the tracking system can only cover one octant pair at one time, we need to decide which main detector's TDC signal needs to be looked at. The adopted cut requires that both PMTs on the given main detector have fired at the "prompt" time, but does not check the ADC values. Fig. 4.6 shows the cut used in the latest tracking data analysis. Fig. 4.7 and Fig. 4.8 shows the θ and ϕ distribution from events from a typical hydrogen target run where the TDC signal is within and outside the main detector's "prompt" window respectively. It can be seen from both plots that more outliers are found for events where the TDC signal is outside our defined "prompt" window.

The MT cut is a cut that sets an upper limit on the number of valid hits in the HDCs region. Since the tracking analyzer has a poor capability of finding the correct track if two or more tracks go through the same package of detectors at the same, it is necessary to implement this cut in our analysis to make sure that the track is coming out of a clean single event. Since the minimum number of hits required for a reconstructed track in one package of the HDC is 9, so the threshold

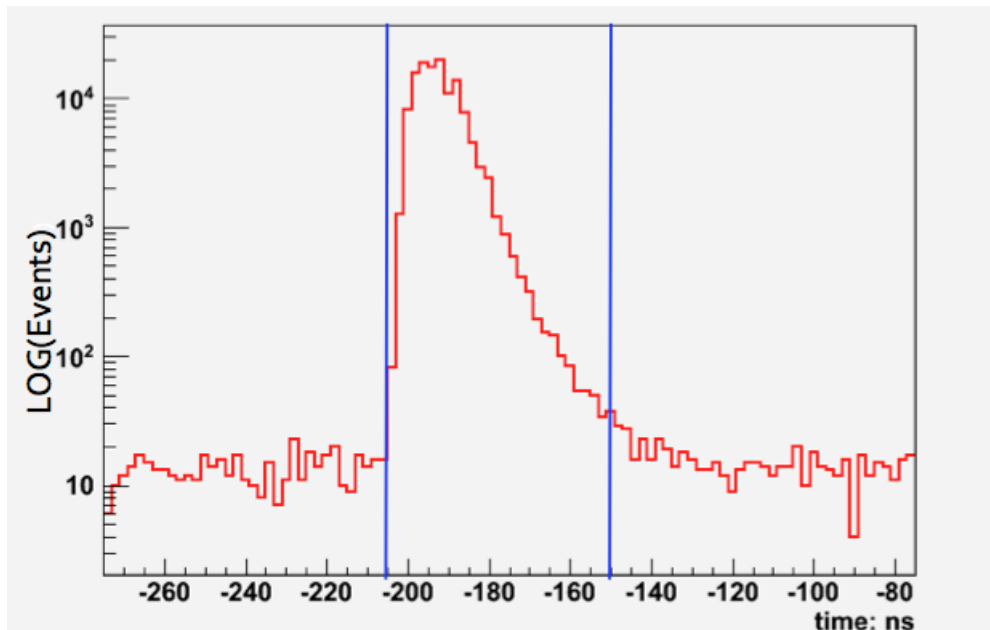


FIG. 4.6: The histogram shows the time distribution in one of the two PMTs in main detector 1. Only hits between the two blue vertical lines are considered as being valid hits.

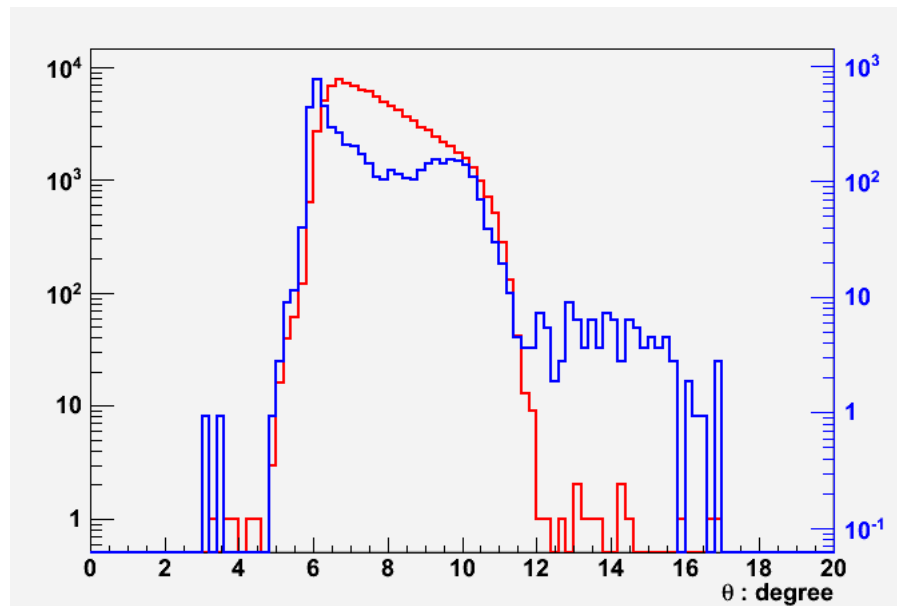


FIG. 4.7: The histogram shows the θ distribution of reconstructed tracks from the events where the TDC time in the main detector is within the “prompt” window (red) and events where the time is out of that window (blue). The left and right axes use different scales and the right axis shows the scale of the histogram in blue. The scheme of double axes is the same for the Fig. 4.8 to Fig. 4.10.

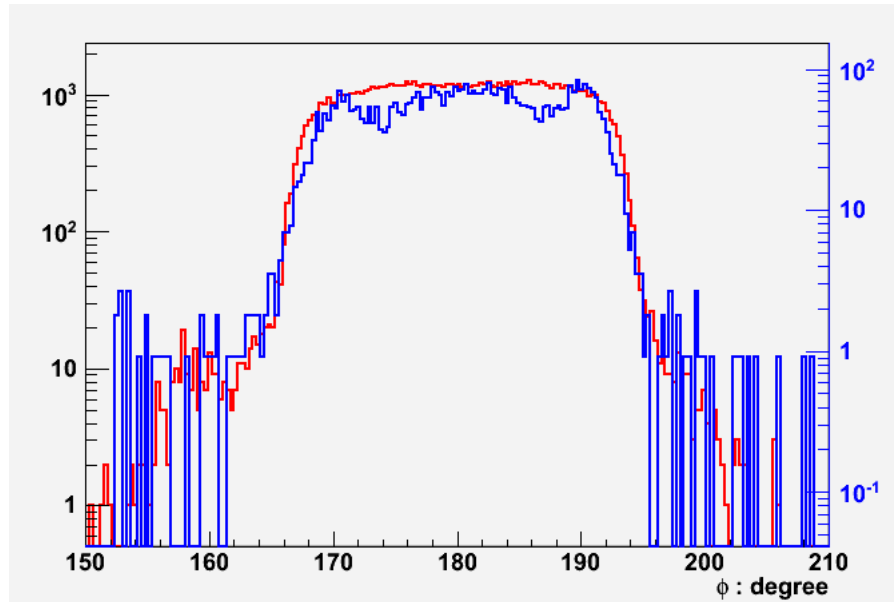


FIG. 4.8: The histogram shows the ϕ distribution of reconstructed tracks from the events where the TDC time in the main detector is within the “prompt” window (red) and events where the time is out of that window (blue).

is set to be 18, which is twice that value. From Fig. 4.9, it can be seen 18 is quite a loose cut, where the multiple-track event only accounts for $\leq 3.2\%$ of total events, so it is a small effect. Similar to the MD cut, Fig. 4.10 and Fig. 4.11 also shows that with the MT cut, the distributions of θ and ϕ are more narrow and have less outliers.

In addition to the MD and the MT cuts, other types of cuts can also be used to select the good-fit and elastic tracks from the initial results from the analyzer. Among them, the most notable ones are DirectionThetaOff, DirectionPhiOff, PositionThetaOff and PositionPhiOff cuts. Before explaining the definition of those cuts, let's first look at how the value of θ and ϕ relating with those cuts are defined. The θ and ϕ correspond to the polar and azimuth angles. The partial track found in the VDCs has its own θ_3 and ϕ_3 and if being projected to the back plane

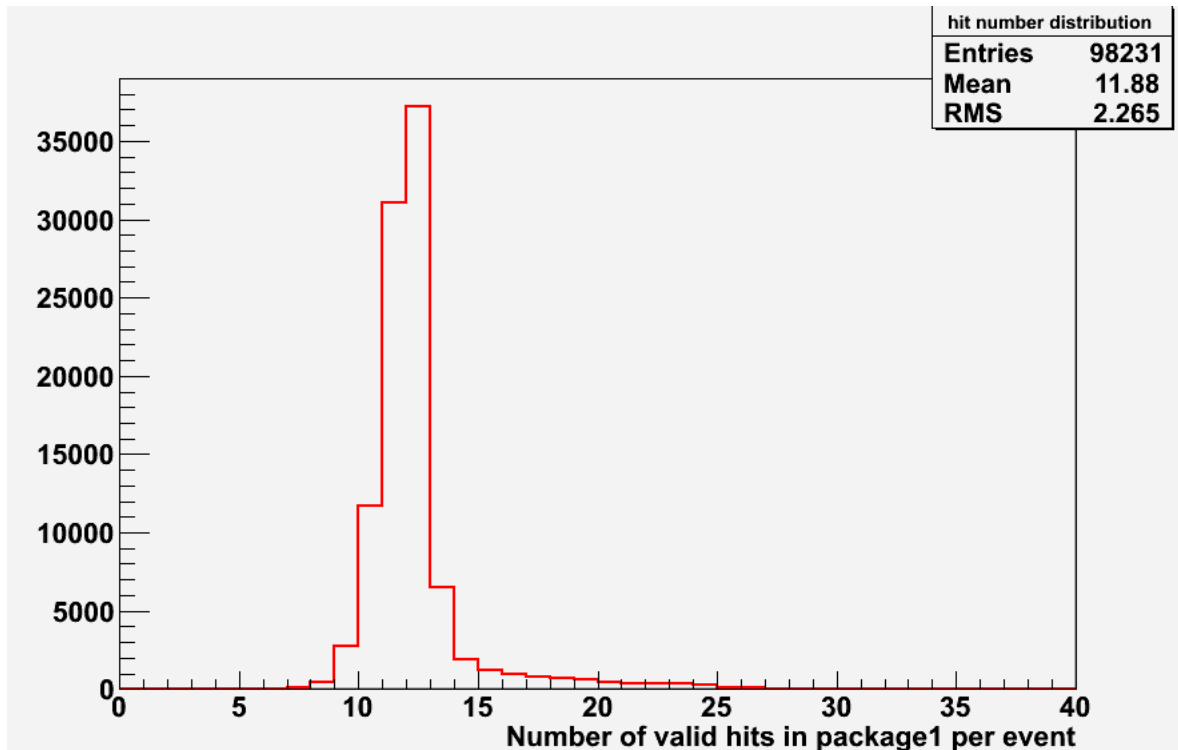


FIG. 4.9: The histogram shows the distribution of valid HDC hits (“valid hit” means its distance is bigger than 0 and it is the first hit on that wire) for events from package 1 in run 13653.

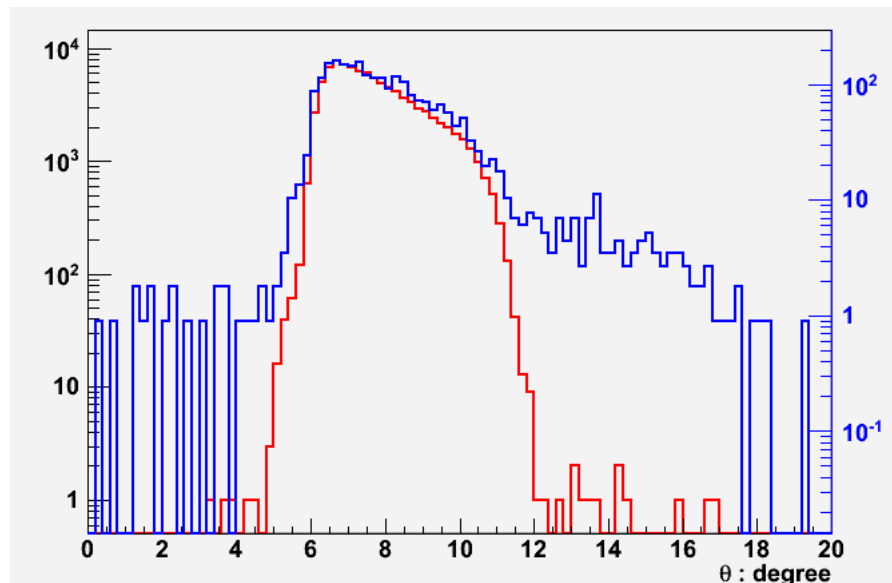


FIG. 4.10: The histogram shows the θ distribution of reconstructed tracks from the events where the number of valid hits in the HDCs is smaller than the MT cut (red) and events where the number is bigger than the cut (blue).

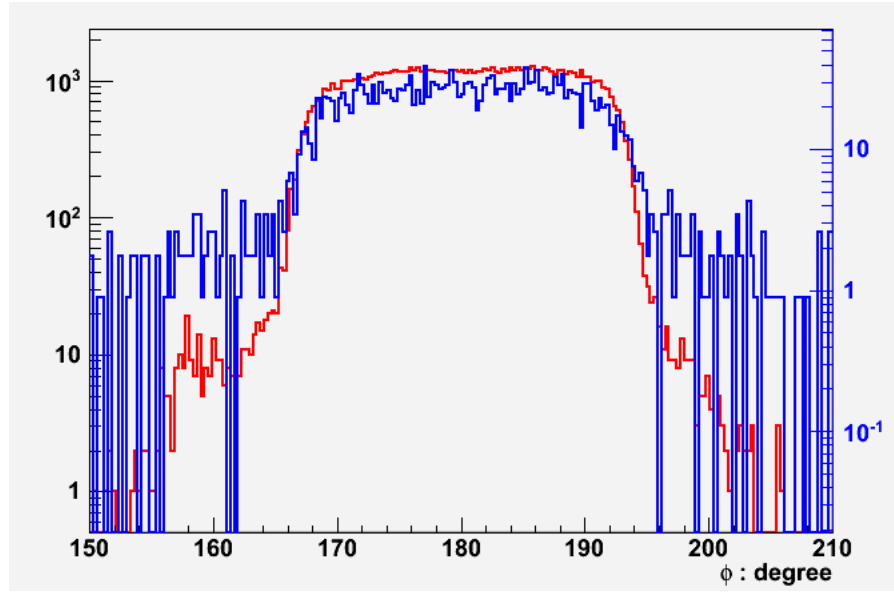


FIG. 4.11: The histogram shows the ϕ distribution of reconstructed tracks from the events where the number of valid hits in the HDCs is smaller than the MT cut (red) and events where the number is bigger than the cut (blue).

of the QTOR, which is a virtual position at $Z = 577$ cm and served as a reference plane, a point with polar coordinates (θ_3^0, ϕ_3^0) is obtained. However, we can not compare the same quantities from the partial track found in the HDC because there is a magnetic field between the HDCs and the VDCs. Therefore, we need to let the partial track of the HDC travel through the entire magnetic field and then calculate its θ_2' , ϕ_2' , θ_2^0 and ϕ_2^0 , the last two of which requires that the track is projected to the same plane where θ_3^0 and ϕ_3^0 are calculated. Then the cuts are just based on the difference between each pair of those four values. For instance, the DirectionThetaOff is simply equal to

$$\Delta\theta = \theta_3 - \theta_2'. \quad (4.6)$$

The Fig. 4.12 shows the distribution of one of those matching variables $\Delta\theta$ for a typical hydrogen target; the shape is close to a Gaussian curve and therefore

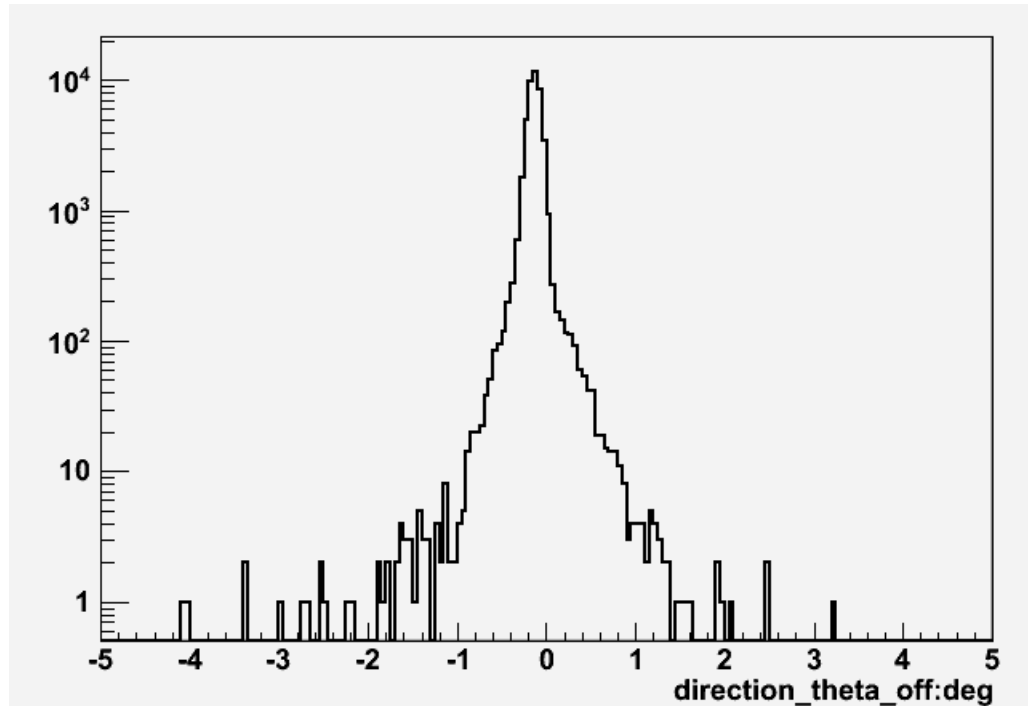


FIG. 4.12: The histogram shows the distribution of the DirectionThetaOff variable in package 1 in run 13653. The y axis is in logarithmic scale.

a cut using the width σ can be developed in the future to select the appropriate events.

4.3 Systematic Uncertainties

In order to study the impact on Q^2 brought by various systematic factors, we took a lot of different testing runs by deliberately changing the factors we wanted to study. In this section, I'll discuss these distinct systematic factors impacts on the value of Q^2 .

4.3.1 Beam Properties

The first thing that needs to be studied is how a change of beam properties will influence the measured Q^2 . Those beam properties include beam position, raster size, beam rate and beam angle.

Beam Raster Size

The study was carried out by changing the beam raster size from $1 \text{ mm} \times 1 \text{ mm}$ to $5 \text{ mm} \times 5 \text{ mm}$. During that data-taken period, all other beam properties were kept relatively stable. The result is shown in Fig. 4.13 and a linear fit is performed. The maximum slope is 0.0025 ± 0.0083 in units of $\text{m}(\text{GeV})^2/\text{mm}^2$ in package 2. If we assume 1σ deviation for the worst scenario, the slope would be $0.0108 \text{ m}(\text{GeV})^2/\text{mm}^2$. Since the beam raster size is $4 \times 4 \text{ mm}^2$ for LH_2 target runs, this indicates the effect brought by the beam raster size from a $0 \times 0 \text{ mm}^2$ case to our nominal situation is only $\sim 0.043 \text{ m}(\text{GeV})^2$, which is $< 0.2\%$ of Q^2 and therefore is a negligible effect on the Q^2 value. Both fitted slopes are consistent with zero, as expected since we had no reason to expect a dependence of $\langle Q^2 \rangle$ on the raster size and this was also confirmed in simulation.

Beam Position

The study was performed by changing the beam position at the target in the X and Y directions separately. The data set was collected at two distinct tracking

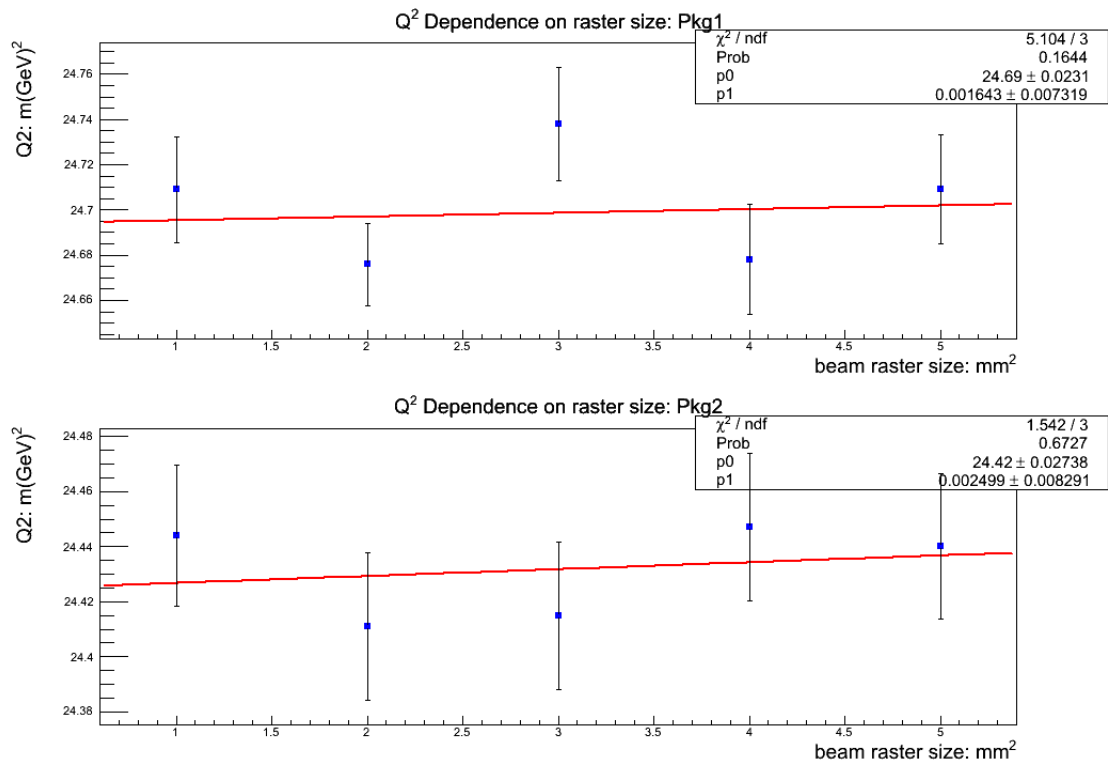


FIG. 4.13: This plot shows the correlation between Q^2 and the beam raster size for both packages in runs 13653-13657. The p0 and p1 in the statistical box are the intercept and slope of the linear fit. Both fitted slopes are consistent with zero.

detectors positions: one was octant 1&5 and the other was octant 3&7. The first plot, Fig. 4.14 shows the result of changing the beam position in the X direction in steps of 1 mm when the detectors were at octant 1 and 5. The relationship is almost linear and when the beam is moved to the positive X direction, the Q^2 in package 2 increases. This is all as expected because as the beam moves in the positive X direction, it also moves away from package 2 at octant 1. Consequently, the scattering angle observed in the package 2 increases, resulting in bigger Q^2 . Since package 1 is in the opposite octant, all the behavior is opposite for package 1. Using the same analysis method as in the beam raster size study, the linear fit indicates that the maximum slope is $0.107 \text{ m(GeV)}^2/\text{mm}$ if 1σ is added. The nominal position of the beam is believed to be controlled within $\simeq 100 \mu\text{m}$, which is equivalent to $0.0107 \text{ m(GeV)}^2/\text{mm}$ and $\sim 0.4\%$ of Q^2 . In the production running, only the pair of Q^2 from opposite octants will be extracted, therefore due to the cancellation effect, the error brought by the beam position should be expected to be even less than that number. Fig. 4.14 shows the result when beam position changes along the Y direction. It is expected that the impact on the Q^2 is quite small. Both measured slopes are consistent with zero as expected. The largest slope (1σ added) is $0.0283 \text{ m(GeV)}^2/\text{mm}$ and it is equal to $\sim 0.1\%$ of Q^2 .

A similar study was carried out when the detectors were at octant 3 and 7. The beam position moved in the Y direction. The result is in Fig. 4.16 and it indicates a 0.5% uncertainty in Q^2 if the uncertainty of the beam position is controlled within $100 \mu\text{m}$. Again, like octant 1&5, only the pair of Q^2 will be extracted, which results

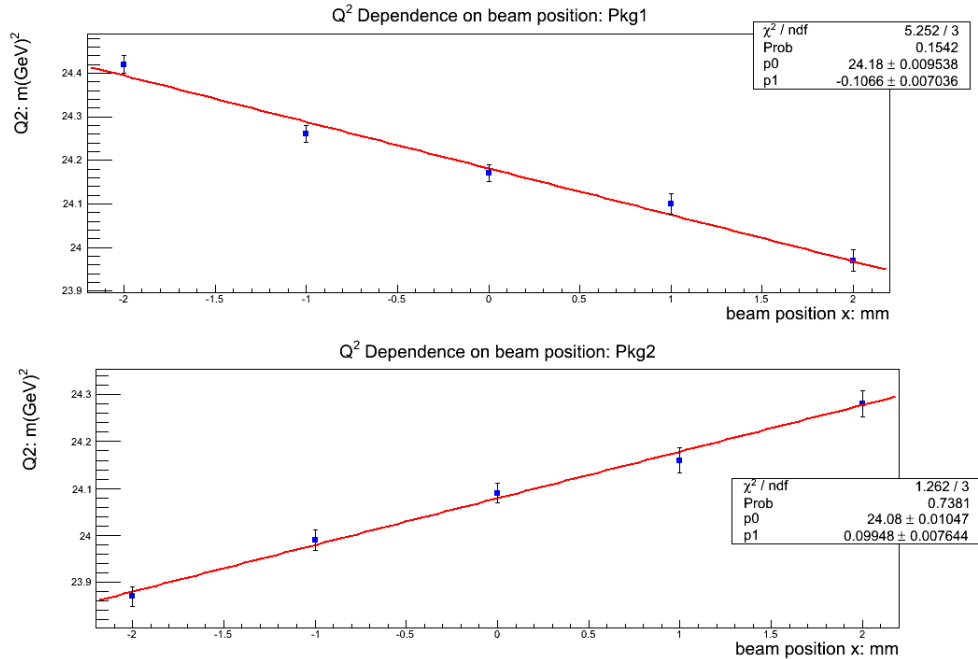


FIG. 4.14: This plot shows the correlation between Q^2 and the beam position in the X direction when detectors are at octant 1 and 5. The run numbers are 14955-14961. Package 2 is at octant 1 while package 1 covers the opposite octant.

in smaller correction due to the change of beam position.

The Tab. 4.5 also shows the rate of the change of Q^2 when the beam moves along with the direction that is the same as how the tracking detectors are placed. The magnitude of the rate itself is quite consistent, which is as expected. The result from GEANT 4 simulation is also listed here [86], and since the uncertainty of the simulation is $\sim 0.02 \text{ m(GeV)}^2/\text{mm}$, the difference between the real data and the simulation is within 1σ . This again follows what one would expect. Notice that for octants other than those on which the study were carried out, the same magnitude of slope are assumed and therefore the average number in Tab. 4.5 will be applied for the other eight octants.

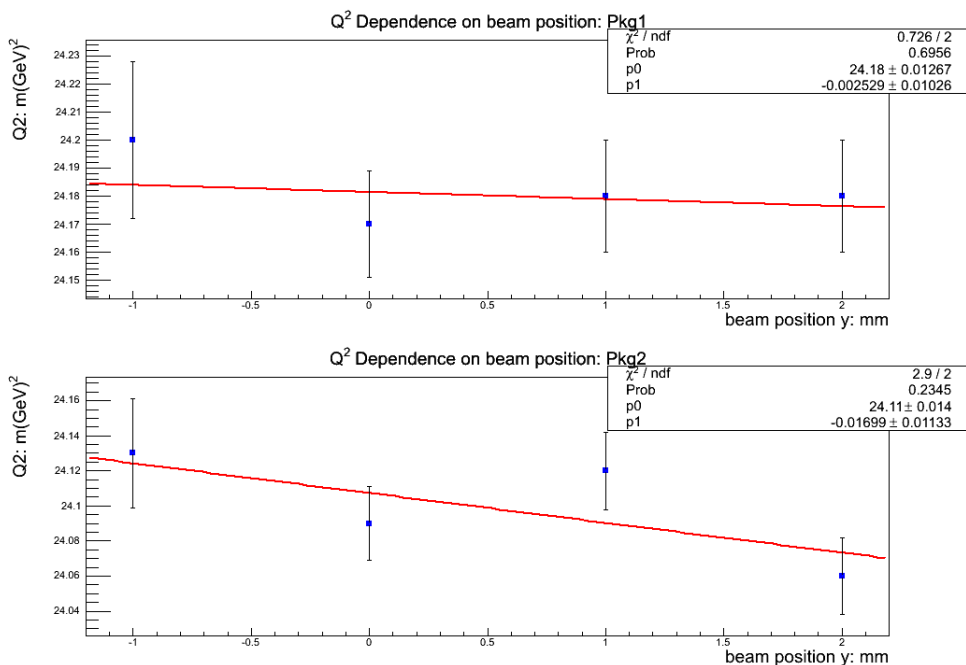


FIG. 4.15: This plot shows the correlation between Q^2 and the beam position in the Y direction when detectors are at octant 1 and 5. The run numbers are 14963-14969. Package 2 is at octant 1 while package 1 covers the opposite octant.

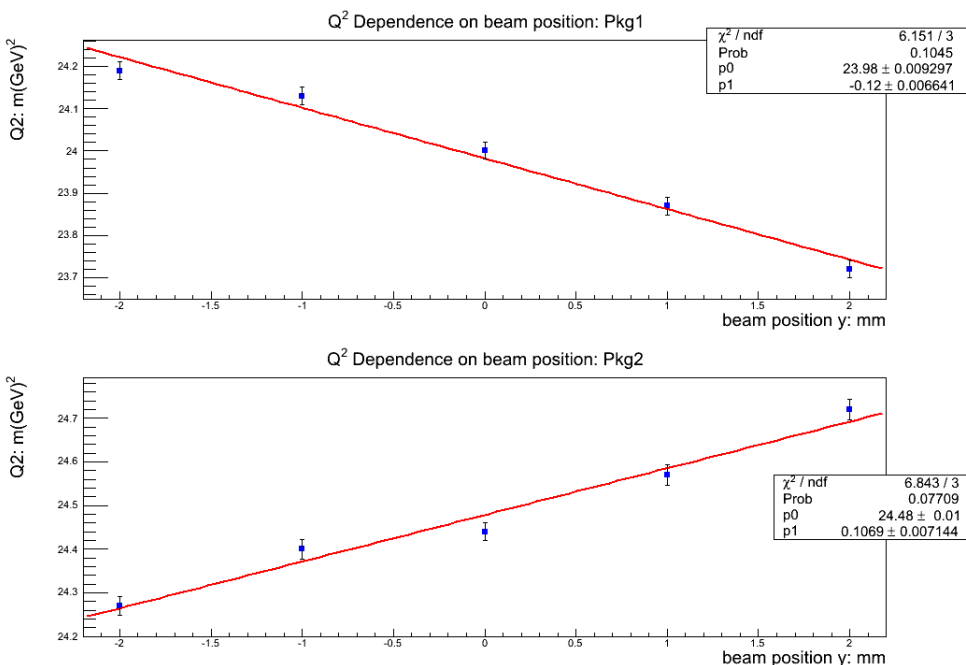


FIG. 4.16: This plot shows the correlation between Q^2 and the beam position in the Y direction when detectors are at octant 1 and 5. The run numbers are 15070-15080. Package 2 is at octant 7 while package 1 covers the opposite octant.

TABLE 4.5: The summary of slopes for beam position study.

Octant	Slope (m(GeV) ² /mm)	Simulation (m(GeV) ² /mm)
1	99.5±7.6	120.0± 7.0
5	106.6±7.0	115 ± 7.0
3	120.0±6.6	108 ± 7.0
7	107.0±7.1	125.0 ± 7.0
average	109.0±3.5	117± 3.5

Beam Rate

Since the beam current used in event-mode is only on the order of 50 pA, it is hard to measure its absolute rate, so we decided to use the HDCs' "FAST OR" rates as the proxy to measure the beam rate. The "FAST OR" rate is the sum of the rate of 16 wires (one half of an HDC plane) of one plane of the HDC. The first beam rate study was carried out in November 2011 and was repeated in January 2012. The result for both packages can be found in Fig. 4.17 and Fig. 4.18 respectively. In the first study, the rate was changed from 15 kHz to 45 kHz (15,27,36, 45 kHz) and the second study was from 40 kHz to 120 kHz. From the first study, the largest slope, appearing in the package2, is 0.00508 m(GeV)²/kHz, if 1 σ deviation is assumed. This also indicates that the difference brought by the beam rate going from 0 kHz to 45 kHz is ~ 0.20 m(GeV)², which is $< 0.8\%$ of Q^2 . For the second run, the result indicates that the difference brought by the beam rate going from 0 kHz to 120 kHz is ~ 0.12 m(GeV)², which is $< 0.5\%$ of Q^2 .

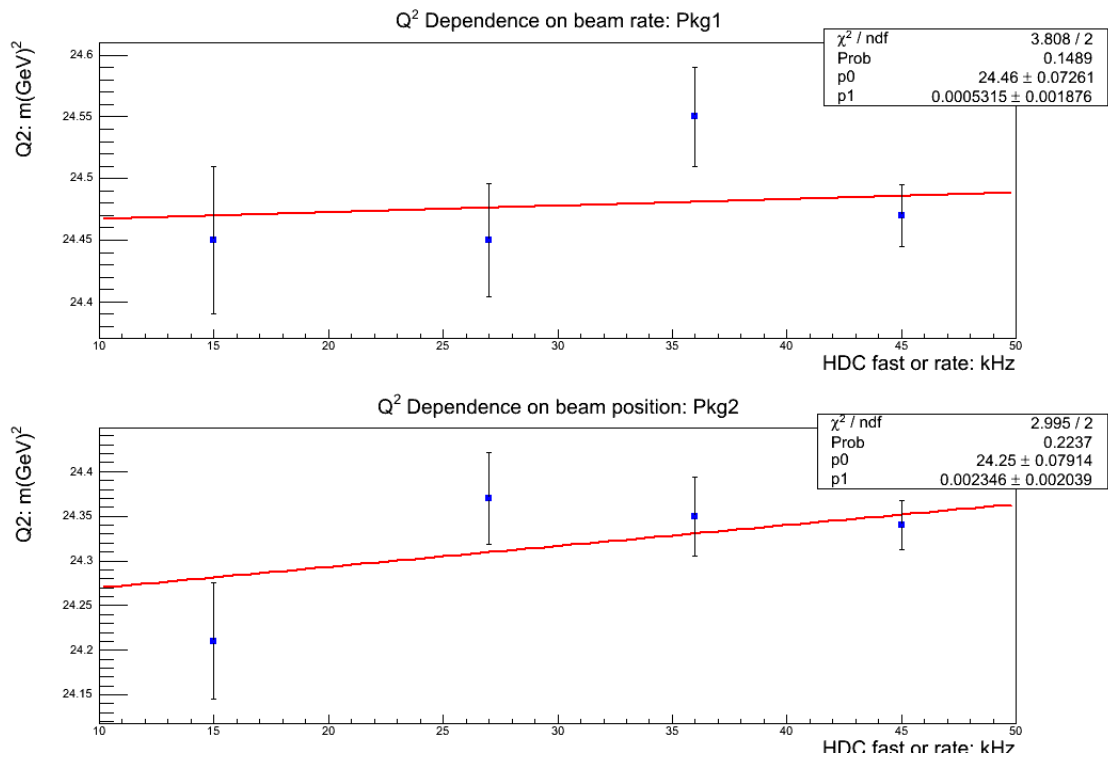


FIG. 4.17: This plot shows the correlation between Q^2 and the HDCs' "FAST OR" rate, which is used as a proxy for beam rate at such low current, for both packages in runs 13723-13726.

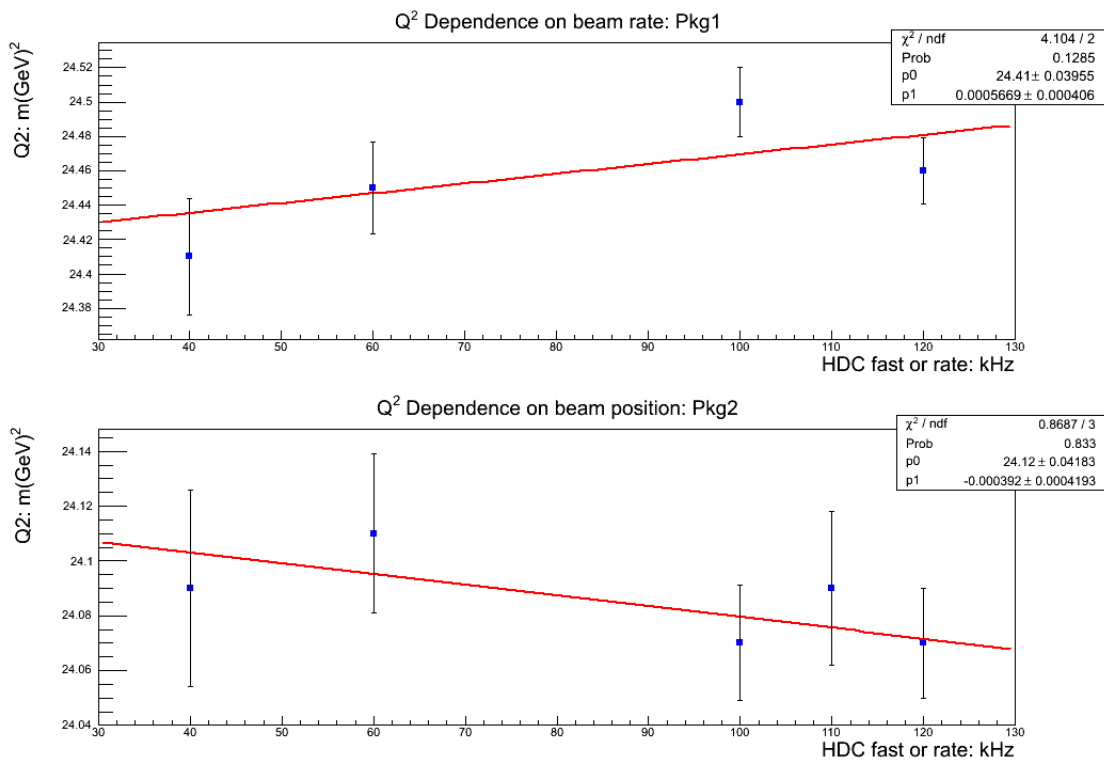


FIG. 4.18: This plot shows the correlation between Q^2 and the HDCs' fast or rate, which is used as a proxy for beam rate at such low current, for both packages in runs 15137-15141.

Beam Angle

The fourth study related with a beam property was completed by changing the beam angle from $-600 \mu\text{rad}$ to $+600 \mu\text{rad}$ in steps of $300 \mu\text{rad}$ in the X , Y direction separately. Fig. 4.19 shows the result when octant 3 and 7 were covered and the beam angle was changed in the Y direction. Only data for package 2 is available because one of the VDCs in the package 1 malfunctioned due to a “pinched” gas line that prevented gas from flowing and therefore prevented the chambers from running under full voltage for those runs. A test when the beam angle in the X direction was changed was also carried out and the result can be seen in Fig. 4.20. The slopes, acutally, are consistent with zero and are much smaller than the values from simulation study, which is around $0.434 \pm 0.014 \text{ m}(\text{GeV})^2/\text{mrad}$. The reason for this discrepancy is because in the QTR software, the scattering angle θ is determined as the difference between trajectory seen by the HDCs and the nominal beam axis, which is not the case if the beam axis is tilted. Since we can not determine the beam incident angle at the scattering point from the tracking data, the θ derived from QTR software, is not accurate if the beam angle is tilted. In order to get a correct value for this study, we would need to use Eq.4.4 to calculate the Q^2 .

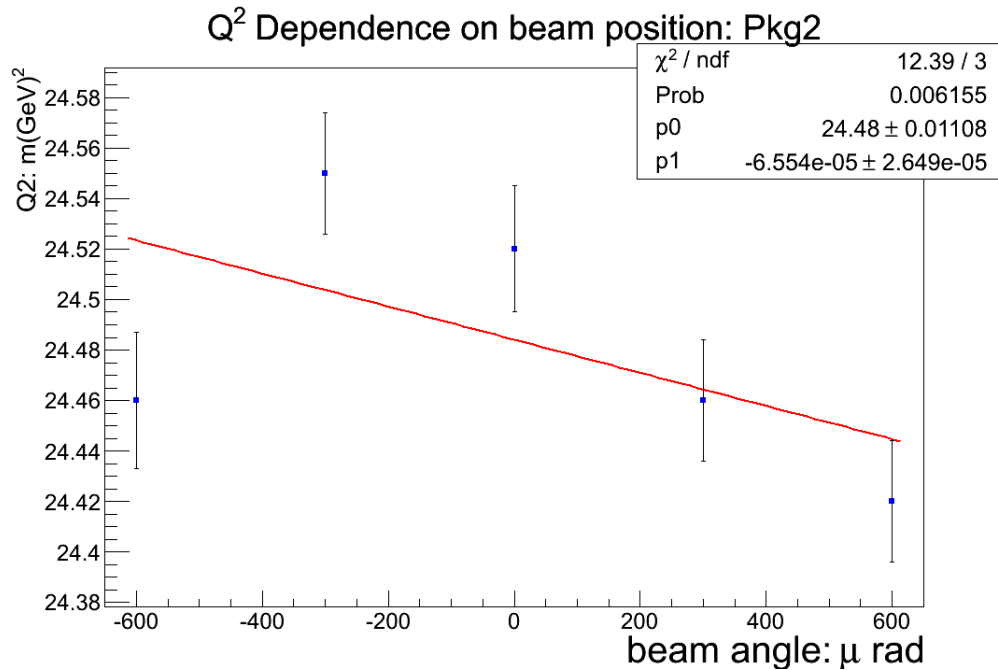


FIG. 4.19: This plot shows the correlation between Q^2 and the beam angle in the Y direction. The run numbers are 18497-18505, when tracking chambers were put in the octant 3 and 7 locations.

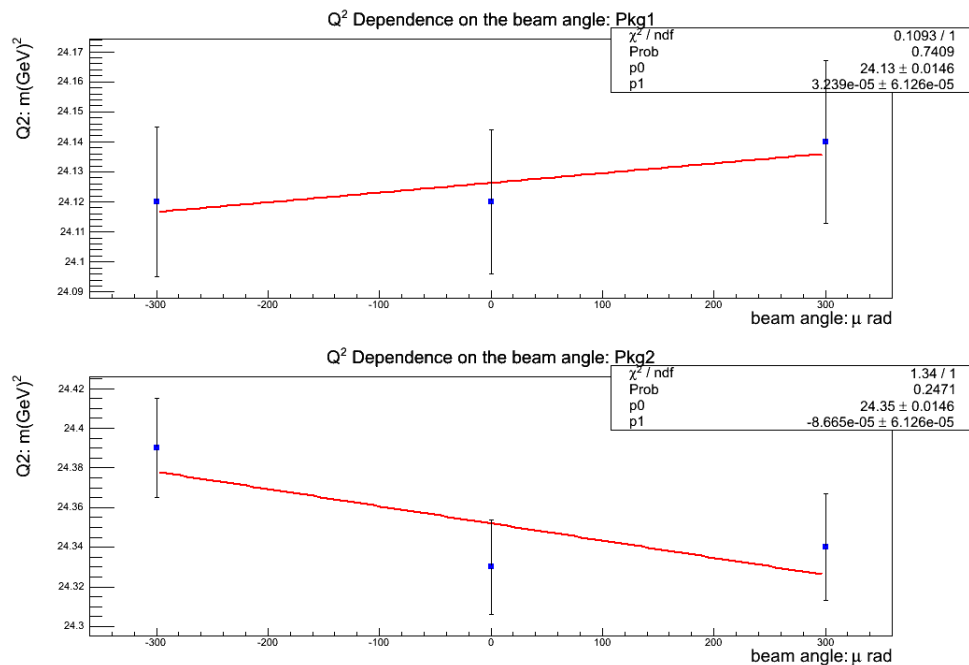


FIG. 4.20: This plot shows the correlation between Q^2 and the beam angle in the X direction. The run numbers are 18570-18573, when tracking chambers were put on the octant 1 and 5 locations.

4.3.2 Beam energy measurement

In Eq. 4.1, the energy used to calculate Q^2 is the incident energy at the scattering vertex. In order to get the most precise value, we need to know the beam energy before the beam enters the target as well as the energy loss in the target. In this section, how we calculated the incident beam energy and its result will be discussed and the next section will focus on the energy loss. Eight dipoles in the arc section of Hall C beam line are used to bend the incident beam by a total of 34.3° . During the energy measurement, those dipoles are switched on and the current in the magnet is varied to set the position of the beam going along the center of those magnets. Two pairs of harp scanners, which are made of tungsten wires, were placed at the entrance and the exit of the arc respectively to measure the initial and final position and direction of the beam. With the known entering and exiting position and direction of the beam, combined with the magnetic field integral from the eight dipoles², the beam energy can be therefore deduced. Four energy measurements were carried out during the whole data-taking period. The result can be found in Tab. 4.6 and the error for the measurement was mainly due to the knowledge of the integrated magnetic field. It can be seen that the biggest uncertainty on this measured value is only $\sim 0.1\%$, which is equal to $\sim 0.2\%$ uncertainty for Q^2 .

²the magnetic field integral of only one dipole is measured and the values of the other 7 dipoles are assumed to be the same.

TABLE 4.6: Results from beam energy measurements

Time	Value (MeV)	Uncertainty (MeV)	Run Period
January 2011	1160.33	1.1	Run I
May 2011	1160.44	1.1	Run I
December 2011	1158.27	1.1	Run II
May 2012	1159.48	1.1	Run II

4.3.3 Energy loss in the target

As mentioned in Sec. 4.2, the energy E used in Eq. 4.1 is not the value from Hall C's arc-energy measurement, therefore one needs to subtract the energy loss in the target to arrive at the vertex energy. The energy loss is due to ionization, internal Bremsstrahlung and multiple scattering. The amount of energy loss can not be measured directly from the experiment, so we had to resort to simulation to give us the precise value. The Qweak's Geant3 and Geant4 teams carried out the simulation task separately. The simulation deliberately assumes the scattering vertex is at the end of the target in order to calculate the energy loss through the entire LH₂ target. The result from Geant3 and Geant 4 simulation shows a 11.4% difference in the total loss of energy (68.0 MeV compared to 60.6 MeV). However, since the scattering event randomly occurs in the target for the real experiment, another simulation was carried out to chose the vertex randomly along the length of the target and the result shows the mean pre-scattering energy is 1155 MeV for both Geant3 and Geant4, which means a 5 MeV loss. Consequently, the difference of the energy loss by using the Geant3 and Geant4 is $5 \times 11.4\% = 0.57$ MeV, which is equal to a $\sim 0.1\%$ uncertainty of Q^2 .

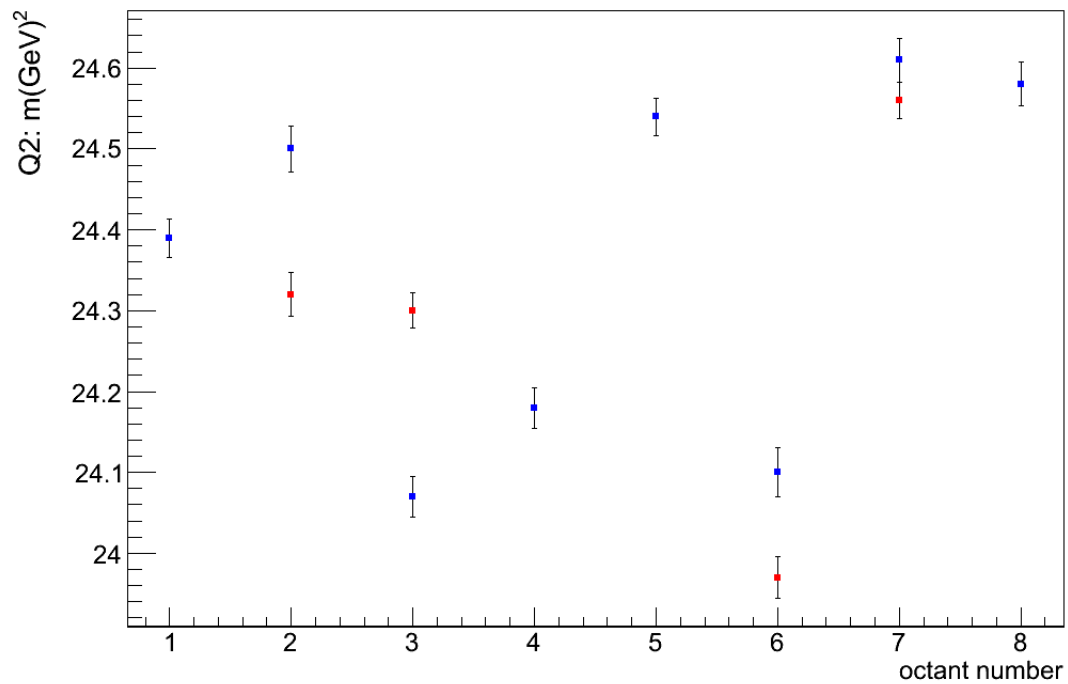


FIG. 4.21: This plot shows the correlation between Q^2 and the octant position. The run numbers are 13671-13681. The red points are results when the detectors are at “reversed” position.

4.3.4 Octant Variance

Since neither the locations of the detectors and collimators nor the QTOR magnetic field have perfect azimuthal symmetry (despite them being designed to be symmetric), the Q^2 is not consistent along with the octant-pair number. Instead, it shows an octant-to-octant variations in mean Q^2 . Fig. 4.21 shows the variation. However, for the final extraction of Q_W^p , only the pair-wise result of Q^2 is used, so the pair-wise result is also shown in Fig. 4.22.

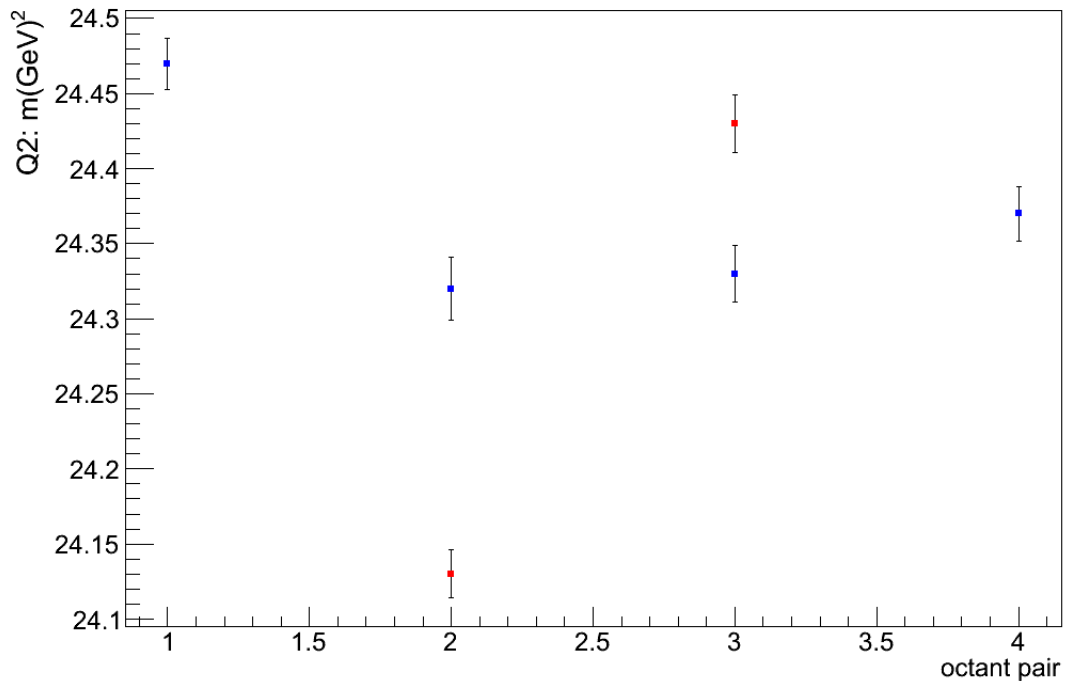


FIG. 4.22: This plot shows the correlation between Q^2 and the octant pair. The run numbers are 13671-13681. The red points are results when the detectors are at “reversed” position.

4.3.5 Stability

The biggest uncertainty of Q^2 comes from the run-to-run instability, especially over different data-taking periods. Fig. 4.23 shows the Q^2 result for several runs under some similar conditions, like positions of the tracking detectors, etc. The biggest uncertainty, from Fig. 4.23 is $\sim 1.3\%$. Different factors can contribute to this variation, for instance, one of wires in the back chamber at HDC was known to be broken during the data-taking period in January of 2012, which caused the low efficiency of partial track reconstruction where that broken wire was involved. Consequently, a bias of Q^2 was generated out of the tracking software. However, the source for this $\sim 1.3\%$ uncertainty has not been identified yet.

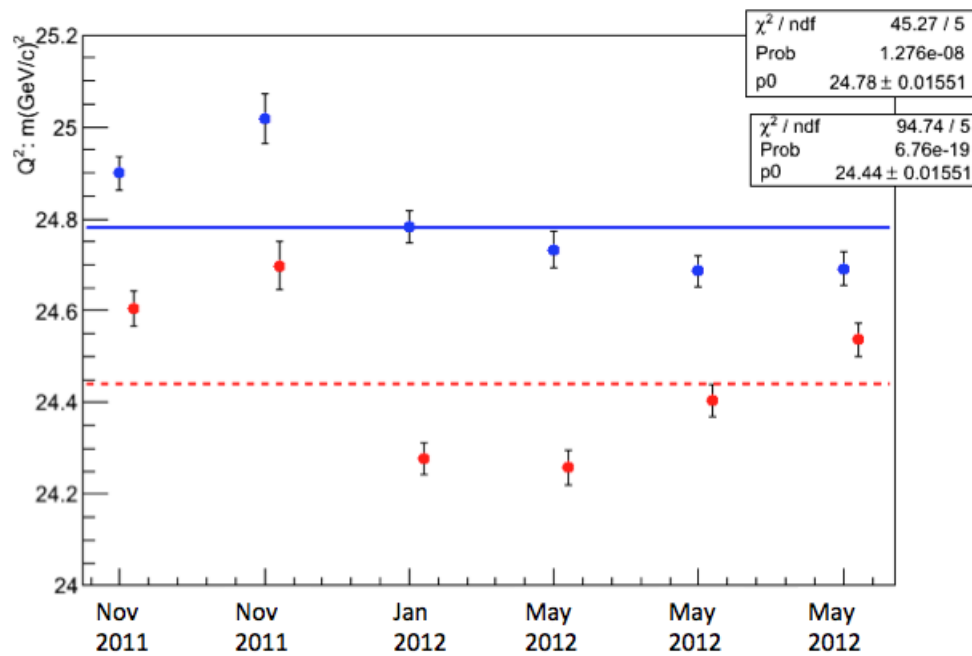


FIG. 4.23: This plot shows the Q^2 values from both packages at the same location (octant 1&5) from three different data-taking period, which spans 7 months. The blue represents the data from package 1 while red represents package2. The statistic box above is the result from data of package 1.

4.4 Light-weighting effect on Q^2

The Q^2 measured under the event mode can not be used as the final Q^2 value to extract Q_W^p in Eq.1.29 because the parity asymmetry was measured under the current mode, which is the value integrated over a window while the Q^2 discussed in this chapter was measured under the event mode. Therefore, in order to apply this correction, we need to resort to the concept of light-weighting Q^2 , which is the average Q^2 over the entire main detectors weighted by the number of the photo-electrons produced by the main detector PMTs at different locations. The correction that needs to be applied to the event-mode Q^2 to get the effective Q^2 is $\sim 1\%$ [87], which is quite close to 1.2%, the expectation from GEANT4 simulation [88].

Another important assumption is used here that the rate distribution, namely, the weighting function must be consistent from low to high current. Since the tracking detectors can not be used at high current, the scanner consequently becomes the instrument to detect the variation of the rate distribution. Several runs were taken at both low and high current and the study shows a relatively stable rate distribution and the fluctuation of the distribution only results in a 0.09% change on the effective Q^2 [89].

4.5 The Summary of Error Sources for Q^2

A summary of error sources which contribute to the uncertainty in the value of Q^2 as of this writing is in Tab. 4.7. In this table, all the errors related with the beam properties are discussed in Sec. 4.3.1. However, since those studies were carried out in only one pair of octants, we need to assume the same errors are also applied to other octants. For some properties, like beam raster size and beam rate, this seems quite reasonable. For other octant-related beam properties, like beam position and beam angle, a sine interpolation is necessary. Therefore, all the errors related to beam properties in Tab. 4.7 are all-octant averaged. All the other errors summarized in Tab. 4.7 are also averaged values for all eight octants. Among those uncertainties, the biggest resources are the stability and octant pair variation: for the stability, various recent studies indicate that we could possibly ignore the problematic Run I data when the error is quite big [90]. Instead, we used the real data from Run II to calibrate the Geant4 simulation first. After the real and synthetic data matched, we changed the parameters to be consistent with Run I to get the result. In this way, the error source from stability is "hybrid": simulation from Run I and measured data from Run II. Consequently, we are confident that this error source could be reduced below 1%. If the statement holds true, the total error for Q^2 would be 1.6% (shown as value in the parenthesis in Tab. 4.7).

TABLE 4.7: Contributions to the uncertainty in $\langle Q^2 \rangle$

Source	$\Delta \langle Q^2 \rangle / \langle Q^2 \rangle$
Statistics	0.1%
Beam Energy	$\leq 0.1\%$
Beam Raster Size	$\leq 0.1\%$
Beam Position	0.2%
Beam Rate	$\leq 0.1\%$
Beam Angle	0.1%
Energy Loss in Target	0.1%
Octant pair variation	1%
Geometry effect	0.3%
Stability	2%
Cuts	0.5%
Total	2.3%(1.6%)

4.6 Path Forward to 0.5% precision

As mentioned in the proposal, the error bar for Q^2 for the final 4% Qweak measurement is 0.5%. In order to reach that goal, we still need to reduce the current error by 1%. Simulation could be resorted to understand the reasons for the error for some sources such as the stability and octant pair variation. If necessary, we could use the simulation data itself to generate the error contribution for those sources. The cuts could also be investigated and refined. If all this works well, the Q^2 with an error bar of 0.5% should be reached. At the time of writing of this thesis, these efforts are still underway by the collaboration.

CHAPTER 5

Parity Data Analysis

5.1 Overview of the Data

The data of the Qweak experiment was collected over nearly two years, from June 2010 to May 2012. After initial commissioning of the apparatus and beam, the “production” data-taking took place. The production data were divided into three stages, known as the “25% measurement”, “Run 1” and “Run 2”. The first is named for the expected precision on the proton’s weak charge that it will provide, and represents the first 20 days of data-taking. This was followed by Run 1, which took place from Feb 2011 to May 2011. After a 6 months shutdown of the accelerator, Run 2 began and lasted from Nov 2011 to May 2012. Each data set was “blinded” by an independent blinding factor, so later they could be analyzed and the results could be revealed independently. The initial “blinded” results of the 25% measurement have been reported in the PhD theses of Katherine

Mayers [58] and John Leckey [55]. In this dissertation, a more up-to-date and unblinded result of the 25% measurement of the Q_W^p is presented.

As mentioned before, three variables need to be measured or known (see Eq. 1.28) in order to calculate Q_W^p : the physics asymmetry (A_{LR}^p), the Q^2 and $B(Q^2)$. The precise measurement of A_{LR}^p requires us to measure the polarization and to correct for any helicity-correlated false asymmetry and backgrounds in the raw asymmetry (A_{Raw}^p). This chapter will be mainly focused on the measurement of A_{LR}^p , and the other two observables, Q^2 and $B(Q^2)$, are discussed in chapter 4 and chapter 6 respectively.

Before discussing details of the calculation of the Q_W^p , several terms, which will be mentioned repeatedly in later sections, need to be defined here. “IN” and “OUT” refer to the status of the IHWP (refer back to Chapter 2 for the definition of this term) when the data was taken. “IN+OUT” means the sum of the result from two opposite IHWP settings, which will provide a “null test” to see if any false asymmetry due to the beam properties is largely removed. “IN-OUT” is the difference between those two IHWP settings and should be equal to the true raw physics asymmetry. For the data itself, the term “runlet” is used to describe about ~ 6 minutes of data in a run, which is also equal to the maximum limit of 2 GB per file of raw data on disk. A “run” is normally equal to ~ 1 hour of data and a “slug” is a term to describe a collection of data in a given IHWP setting. Typically the data in a slug is ~ 8 hours of data.

All data presented in this dissertation from the 25% measurement repre-

sented only one configuration of the other slow-reversal device, the “Double Wien”, therefore the true beam helicity for each slug was determined just by the IHWP setting.

5.2 Data Processing Scheme for Parity Data

The raw data, which is saved as a CODA file, is firstly decoded using the Qw-Analysis software into the data formats, which can be read and analyzed later by the ROOT software. The MySQL database is chosen here to store the output of the root files and also to provide a convenient channel to read the data. All the data can be accessed by using various softwares that support the MySQL; the smallest unit that can read from the database is a runlet. In other words, if some analysis needs to be done quartet by quartet, you have to bypass the database and instead examine the rootfiles directly. The next step is to apply the linear regression method to correct for any helicity-related false asymmetries and the new results were also stored in the database marked with the specific number of the regression scheme being used. The whole data process scheme in this experiment for parity data is summarized in a flow chart in Fig. 5.1

5.3 Data Quality

The first step of all is to check the quality of the collected data. There were numerous reasons that could cause bad quality data, such as a hardware failure,

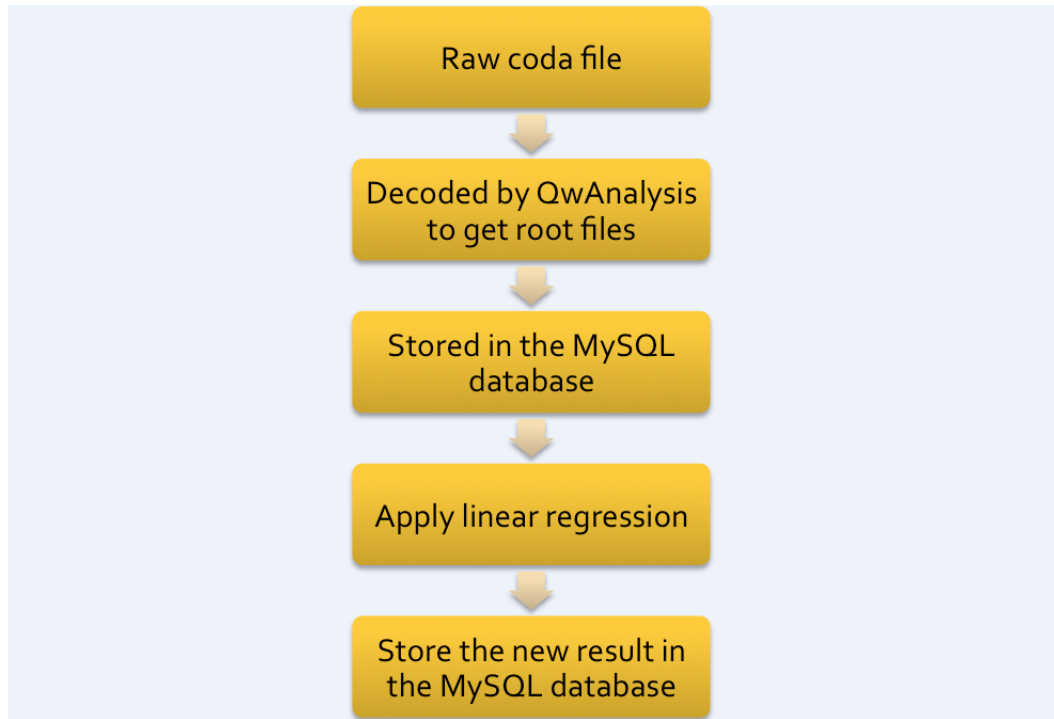


FIG. 5.1: Data process scheme in the Qweak experiment for parity data.

beam trips, beam ramps and excursion of the beam from the nominal positions, *etc.* Three different types of cuts are available in the analysis. The most basic one is the hardware cut, which is aimed at removing the data that fail to pass the general hardware integrity checks. Each channel of a given readout electronics has an error code and this error code could be combined to indicate that one of the subsystems has a problem. For instance, combined BPMs and MD signals could use the combined error code to check if any of its components has a hardware issue. The causes of the error code in a given channel include saturation of the signal, inconsistency of the output, incorrect increment of the sequence number, *etc.* The single event cut, which is more focused on the performance of each individual subsystem compared to the hardware cut, sets the valid range for data

from those subsystems (BCMs, BPMs, ...), which effectively excludes an event in which the beam behaves outrageously. The last type of cut is named the stability cut. This cut is used to remove the data which were taken when the beam was quite unstable, such as during beam ramps (when the beam recovered to the standard current after the beam trip occurred), beam trips, beam position excursions and main detector yield fluctuations. Unlike the single event cut, this cut uses a 5 second buffer of data to calculate its root mean square value to see if the value is within the preset range. If not, all the data within that 5 second buffer is marked with a stability cut error. More details related to this event cut framework can be found in [91].

All the collected data at the runlet level were labeled into three categories in the database in terms of their qualities: good, suspect and bad. For the analysis in this dissertation, the criterion used for defining the suspect and bad runlets are listed in Tab. 5.1. Notice that the first two slugs in the 25% measurement, slug 29 and slug 30, will not be considered for the analysis in this dissertation because the beam current was $< 100 \mu A$ current in $> 95\%$ of the runlets from those two slugs. For the rest of the slugs, the “good” runlets after removing the bad and suspect ones accounts for 87% of the total data recorded.

TABLE 5.1: the criterion of the data quality

	Beam Current	Charge Asymmetry (A_q)
suspect	$< 100 \mu A$	> 10 ppm
bad	unusable data ¹	> 100 ppm

¹The instruments, like QTOR or a main detector were off.

5.4 The Measurement of the Raw Asymmetry A_{raw}

After the data quality check, the next natural step is to get the raw asymmetry A_{raw} before any correction. To measure the correct yield for a single PMT, the pedestal is firstly removed from the raw yield and then the yield is normalized to the beam charge. Since there are 8 Main Detectors and 16 PMTs, different combinations can be formed to measure A_{raw} . The simplest one is called $A_{mdallpmtavg}$ and can be outlined as

$$A_{mdallpmtavg} = \frac{1}{16} \sum_{i=1}^{16} A_i, \quad i = 1, 2 \dots 16 \quad (5.1)$$

where A_i is the asymmetry measured by a single PMT.

For the other two methods, one concept, the tube weighting w_i , needs to be defined by using the following formula:

$$w_i = \frac{1}{Y_i}, \quad i = 1, 2 \dots 16 \quad (5.2)$$

where Y_i is the mean value of the yield from a single PMT. The basic idea is for a larger number of events received, which is quantified by Y_i , the statistical error should be smaller. The two methods that use w_i are called $A_{mdallbarsavg}$ and $A_{mdallbars}$. For $A_{mdallbarsavg}$, each bar's asymmetry is calculated first,

$$Y_i = \frac{w_{i_pos} Y_{i_pos} + w_{i_neg} Y_{i_neg}}{w_{i_pos} + w_{i_neg}}, \quad (5.3)$$

$$A_i = \frac{Y_i^+ - Y_i^-}{Y_i^+ + Y_i^-}, \quad i = 1, 2 \dots 8, \quad (5.4)$$

where *pos* and *neg* refers to the two PMTs for a specified bar i . Then similar to Eq. 5.1, the total asymmetry $A_{mdallbarsavg}$ is calculated by taking the average of all

eight A_i .

$A_{mdallbars}$, which calculates a single value by taking all 16 PMTs' weighted yields, can be outlined as:

$$Y = \frac{\sum w_i Y_i}{\sum w_i}, \quad i = 1, 2 \dots 8, \quad (5.5)$$

$$A_{mdallbars} = \frac{Y^+ - Y^-}{Y^+ + Y^-}. \quad (5.6)$$

For the 25% measurement, the difference between the results using those three methods were found to be quite small, in the order of ~ 1 ppb. So in this dissertation, the simplest method, $A_{mdallpmtavg}$ is used for later calculation.

5.5 Polarization

During the 25% measurement period, only the Møller polarimeter was used to measure the absolute beam polarization (the Compton polarization was still being commissioned). The results with only statistical errors are shown in Fig. 5.2. The first measurement was taken 10 days before the first slug that is included in the 25% measurement and is considered to have suffered from a high voltage issue in the lead-glass detector and also a different laser spot was used on the polarized source photocathode, so it will not be included here. Furthermore, considering the impact brought by the variation of beam position, the value in Fig. 5.2 needs to be corrected in terms of the beam position to provide a final value. This correction has been done on a run-by-run basis and the result is shown in Fig. 5.3. An additional 0.37% systematic uncertainty is attached to each slug to represent the run-to-

run unknown uncertainties, which makes the extracted polarization 88.07%. In addition to the typical systematic uncertainties for the Møller measurement, an additional uncertainty, which is due to a turn-to-turn short in one of the four coil packs in quad3, which is one of the quadrupole magnets in the Møller polarimeter, found by the Møller group in spring of 2011, also needs to be addressed. The full impact is still under the investigation and an additional 1% correction from a simulation study is applied to the measured value and a conservative additional $\approx 1\%$ systematic error is added to get the final extraction of the beam polarization [92]:

$$P_e = (88.95 \pm 0.19_{stat.} \pm 0.93_{sys.} \pm 0.89_{Q3-sys})\% \quad (5.7)$$

5.6 Corrections for Helicity-related Beam Properties

Any change of beam properties with beam helicity state can introduce the so-called false parity asymmetries. In order to remove this effect, the following formula is used:

$$A_{reg} = A_{meas} - \sum_{i=1}^n \left(\frac{\partial A}{\partial P_i} \right) \delta P_i, \quad (5.8)$$

where P_i stands for different beam parameters: position (X , Y), angle (X' , Y'), energy (E). Their helicity-correlated difference, denoted as δP_i , was measured continuously by using the BCMs and BPMs while the data were collected. Tab. 5.2 shows a summary of those differences during the 25% measurement. Since the beam modulation system was not available during the 25% measurement [93], the detector sensitivities of beam parameters $(\partial A)/(\partial P_i)$ had to be calculated by

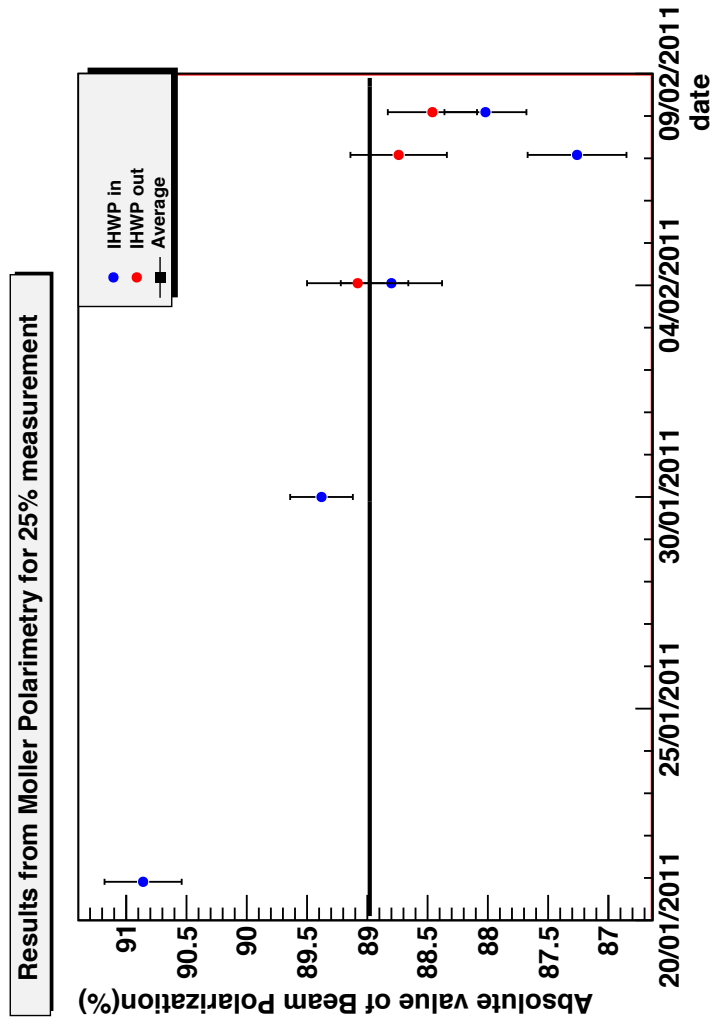


FIG. 5.2: Møller Polarimetry results for the 25% measurement; online results with only statistical error bars.

using a multidimensional regression scheme in which the raw asymmetry was fitted to linear dependencies on the various beam parameters P_i , which varied “naturally” during the data-taking. As typical results, the sensitivities to position X and position Y for different MDs in slug 35 are shown in Fig. 5.4 and Fig. 5.5 respectively. The general shape of the fitting curve is expected because of the different positions of individual main detectors. For instance, MD1 and MD5 are

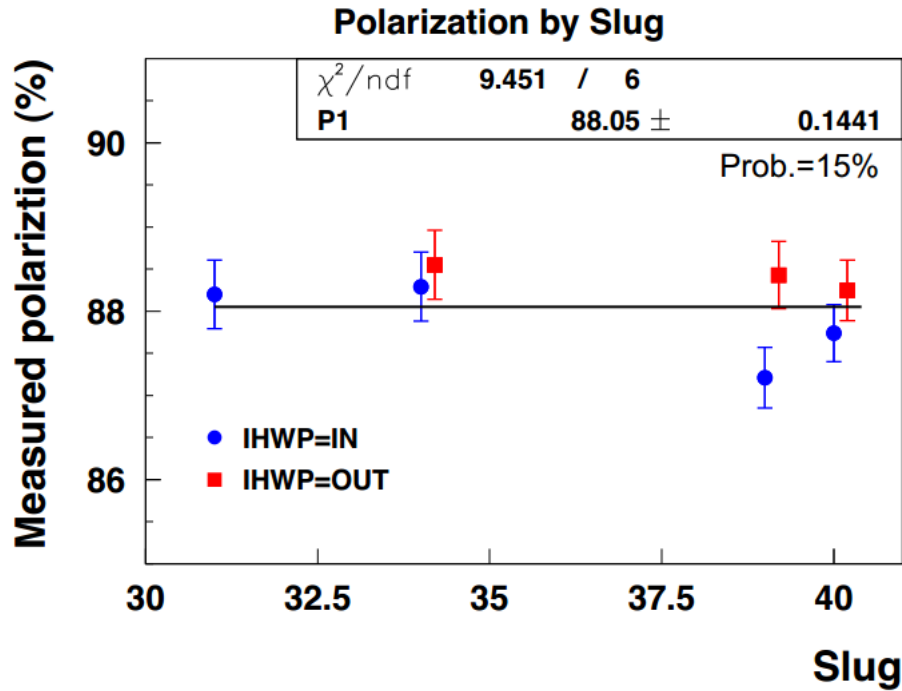


FIG. 5.3: Møller Polarimetry results for the 25% measurement, after correction for beam-related effects.

positioned horizontally, so they are quite sensitive to the change in the X direction while MD3 and MD7, which are in the vertical position, are mostly sensitive to any change in Y direction.

In the Qweak experiment, different sets of devices along the beamline are available to measure the beam parameters. The locations of all those devices can

TABLE 5.2: Helicity-correlated differences in the 25% measurement averaged out on the slug basis for two different IHWP states.

Helicity-correlated difference	IHWP IN	IHWP OUT
Target X difference (nm)	-11.7 ± 1.2	-7.9 ± 1.1
Target Y difference (nm)	92.4 ± 2.8	-34.0 ± 2.9
Slope X difference (nrad)	0.36 ± 0.04	0.15 ± 0.04
Slope Y difference (nrad)	2.24 ± 0.07	0.88 ± 0.07
Energy (ppb)	-19.4 ± 0.6	-16.7 ± 0.6

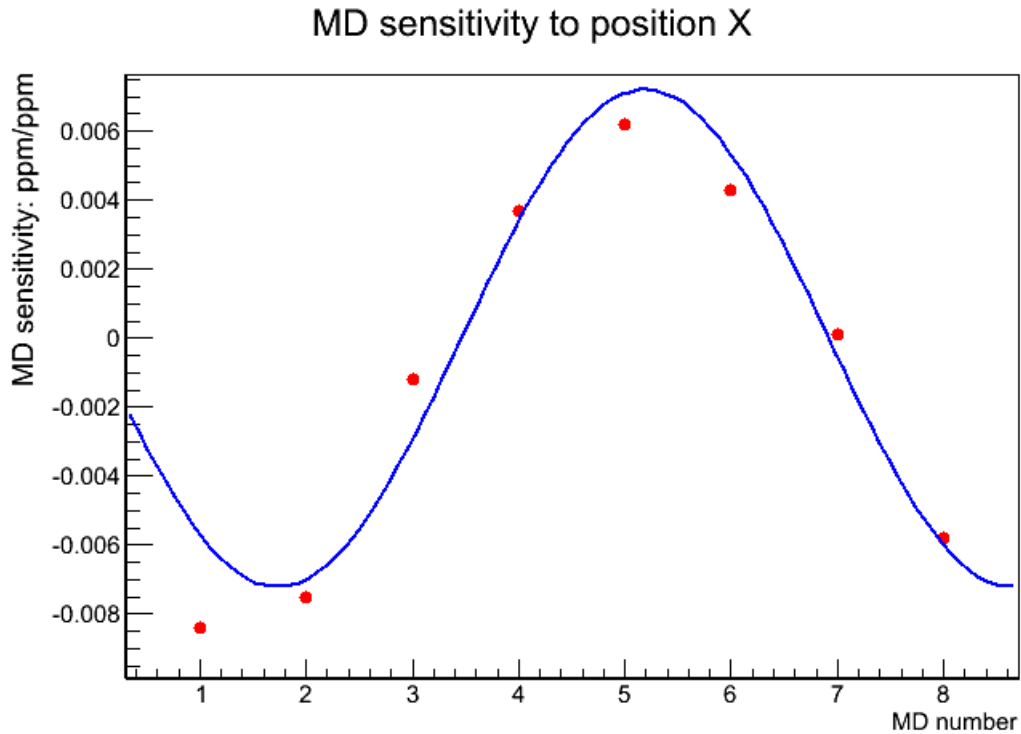


FIG. 5.4: MD sensitivity to position X for individual Main detectors in slug 35. The statistical error bar for each measurement is only in the order of 10^{-5} , so it is not drawn here.

be found in Appendix C. For the position and angle (X , X' , Y , Y'), two options are used: 1) either use BPM pairs (3h04 and 3h09/3h09b) to project to the target or 2) directly use target variables (targetX, targetY, targetXSlope, targetYSlope³). For energy E , two options are also present to measure its value: 1) use BPM 3c12X, which is located the largest dispersion position in the beam arc or 2) use combined results of BPM 3c12X, targetX and targetXSlope as an energy calculator. The second option is potentially better because it uses more BPMs to decouple the sensitivities to the beam position and to the beam energy from the detectors while the drawback is that any error occurring to any one of those BPMs will cause an

³These variables are determined by using the fit result from signals from the following BPMs: 3H09B, 3H09, 3H08, 3H07B and 3H07A.

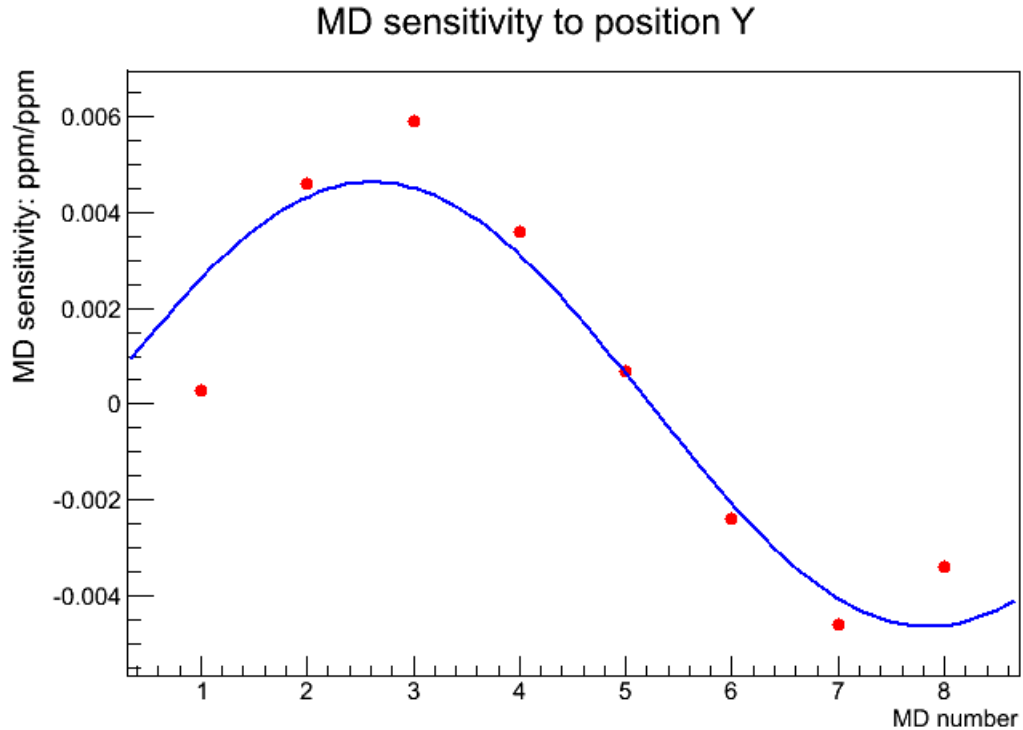


FIG. 5.5: MD sensitivity to position Y for individual Main detectors in slug 35. The statistical error bar for each measurement is only in the order of 10^{-5} , so it will not be drawn here.

invalid event. In addition, the beam charge asymmetry (A_Q) can also be chosen to add to the variable set in order to remove any nonlinearity effect in the main detector yield. Last but not least, the asymmetry observed in the upstream Lumis, can also be used as a variable in regression. Consequently, a total number of ten different regression schemes were considered in this thesis.

Detailed comparison between those distinct regression schemes for the 25% measurement have been carried out. Here, only five regression schemes' results are displayed for the purpose of studying the effect brought by using different regression variables. Their names and variables are listed in Tab. 5.3.

Unlike the std, 5+1 and set3 regression schemes, where the value of the

TABLE 5.3: Variables used in std, 5+1, set3, set5, set6 and set7 regression schemes.

std	set5	set7
target X	BPM 3h09b	BPM 3h09
target Y	BPM 3h04	BPM 3h04
target X'	BPM 3c12X	BPM 3c12X
target Y'		
energy calculator		
5+1	set3	set6
target X	target X	BPM 3h09b
target Y	target Y	BPM 3h04
target X'	target X'	BPM 3c12X
target Y'	target Y'	A_Q
energy calculator	BPM 3c12X	
A_Q	A_Q	

position and angle are given by the corresponding calculated variables, set5, set6 and set7 use the combinations of two BPMs to represent the position and angle:

$$\text{position-like} = \text{bpm3h09(b)} + \text{bpm3h04}$$

$$\text{angle-like} = \text{bpm3h09(b)} - \text{bpm3h04}$$

The first comparison is carried out between 5+1 and set3 where the only difference is how the energy is measured. The total corrections to the raw asymmetry for both two schemes are shown slug-by-slug in Tab. 5.4. Notice that the correction to the asymmetry is always in the unit of ppb for all the comparisons in this section, unless otherwise specified. From the Tab. 5.4, it can be concluded that the choice of the energy variable has almost no impact on the regressed asymmetries for this dataset.

⁴The value of the corrections for the IHWP out status was multiplied by -1 in order to correct the sign for the half-wave plate status.

TABLE 5.4: Total corrections of 5+1 and set3 to raw asymmetry, in ppb, for two correction schemes. All the total corrections shown in the next few tables are handled in the same way.

slug	correction (5+1)	correction (set3)
31	79.61	79.61
32	-38.50	-38.46
33	13.42	13.42
34	-38.73	-38.73
35	49.48	49.48
36	-58.87	-58.87
37	44.43	44.43
38	-69.24	-69.24
39	15.85	15.85
40	-72.74	-72.74
total	-321.87 ⁴	-321.87

The next comparison is to see how the choice of BPM pairs will change the asymmetry. The comparison between set5 and set7 is shown in Tab. 5.5 and it can be seen that the largest difference is only ~ 4 ppb. Therefore, the choice of whether to use BPM 3h09b or BPM 3h09 almost does not affect the final result. The result of the comparison between target BPMs (set3) and BPM pairs (set6) is shown in Tab. 5.6 and it seems that using the target BPMs will typically bring larger correction (1 \sim 10 ppb) to the regressed asymmetry. The largest discrepancy comes from whether the charge asymmetry is used during the regression or not, which could be as large as 20 ppb, as seen in Tab. 5.7. If the charge asymmetry is used, the width of the asymmetry is reduced significantly. However, since the reason for this effect is still under investigation and since the reason for a sensitivity to A_Q is not understood, to be conservative, regression schemes that are used in this dissertation are those without using the charge asymmetry during

TABLE 5.5: Total corrections of set5 and set7 to raw asymmetries, in ppb, for two correction schemes.

slug	correction (set5)	correction (set7))
31	74.45	78.21
32	-31.89	-31.80
33	16.06	15.69
34	-27.87	-27.33
35	23.05	24.09
36	-51.37	-51.17
37	18.06	16.25
38	-57.20	-56.69
39	-13.75	-13.33
40	-56.06	-55.92
total	-193.36	-187.4

TABLE 5.6: Total corrections of set3 and set6 to raw asymmetries, in ppb, for two correction schemes.

slug	correction (set6)	correction (set3))
31	79.61	76.98
32	-38.46	-28.95
33	13.42	0.26
34	-38.73	-36.12
35	49.48	44.46
36	-58.87	-57.56
37	44.43	38.09
38	-69.24	-69.07
39	15.85	3.60
40	-72.74	-72.38
total	-321.11	-273.51

TABLE 5.7: Total corrections of set5 and set3 to raw asymmetry, in ppb, for two correction schemes.

slug	correction (set5)	correction (set3)
31	74.45	76.98
32	-31.89	-28.95
33	16.06	0.26
34	-27.87	-36.12
35	23.05	44.46
36	-51.37	-57.56
37	18.06	38.09
38	-57.2	-69.07
39	13.75	3.60
40	-56.06	-72.38
total	-193.36	-273.51

TABLE 5.8: Asymmetry under different regression schemes for slugs 31-40, in ppb.

Regression Scheme	Asymmetry	Error
Raw	-173.70	29.53
Std	-200.62	29.44
Set5	-194.41	29.48
Set7	-193.38	29.42

the regression. They are std, set5 and set7. In Tab. 5.8, the asymmetry with the error for those regression schemes are listed for slugs 31-40, and the difference between the asymmetries for different schemes is within ~ 7 ppb.

5.7 Corrections for Backgrounds

Even if the helicity-related false asymmetry is kept to a minimum level to our best knowledge, we still need to remove various background noise sources, which contribute to the measured parity-violating asymmetry. The formula to yield the

physics asymmetry is given by

$$A_{ep} = \frac{A_{meas}/P_e - \sum_i f_i A_i^{bkgd}}{1 - \sum_i f_i}, \quad (5.9)$$

where f_i is called the dilution factor and is defined as the ratio between the main detector light yield from the background source i and the total observed yield

$$f_i = \frac{Y_i^{bkgd}}{Y_i^{bkgd} + Y_i^{signal}}. \quad (5.10)$$

For this experiment, the biggest background source comes from the aluminum target window, which accounts for a $\simeq 20\%$ correction to the physics asymmetry A_{ep} . Other sources, like $N \rightarrow \Delta$ inelastic events, the transverse component in beam polarization and soft backgrounds will also be considered in the data analysis in this dissertation.

5.7.1 Aluminum Target Window and Dilution

Since the target used in the experiment includes upstream and downstream aluminum windows, our detected events include electrons from inelastic, elastic or even quasielastic scattering between the beam electrons and aluminum in those windows. As can be seen in Eqs. 5.3-4, in order to assess the aluminum background correction to the physics asymmetry, two parts need to be evaluated: the asymmetry A_{Al} and the dilution factor f_{Al} .

Unlike the A_{ep} , the asymmetry A_{Al} is also determined by the weak charge of the neutron, which is -1 at tree level. Therefore, the A_{Al} is around ten times bigger than A_{ep} and a detailed theoretical prediction for A_{Al} can be found in [94]. Ten

slugs of data were taken to study the magnitude of A_{Al} by using the 4% downstream aluminum target with beam at $15\sim 30 \mu A$ for the 25% measurement between 01/26/2011 and 02/03/2011. The regressed value for A_{ep} was found to be $1.66 \pm 0.17_{stat}$ ppm and is shown in Fig. 5.6 slug-by-slug. After further correcting for beam polarization, QTOR transport and beamline backgrounds (discussed later), a radiative correction must also be applied due to the additional radiative energy losses in the aluminum as well as the hydrogen target. The magnitude of the radiative correction is obtained from simulation. The final aluminum asymmetry for the 25% measurement is 1.76 ± 0.26 ppm [58].

The dilution factor f_{Al} is defined as the ratio in the main detector's acceptance between the rate of scattering occurring in the aluminum target window and the total rate of scattering from the filled hydrogen target. Two methods were used to measure this quantity: the first is to use an empty target and directly measure the rate from the aluminum target window; the second method is to use the target full of cold gas with varying density, which is used to indirectly obtain the scattering rate from the aluminum target window by extrapolating to the vacuum. Data were collected by using both methods during the Run 1. A low beam current $\sim 1 \mu A$ was used in the empty target method to protect the aluminum window and thus event mode data-taking was adopted in those measurements. A reference target made of carbon was also used as a reference target during these studies to account for the potential systematic changes during individual runs, such as the difference in the pedestal of BCMs at different beam current or at different time. The mea-

sured value from both methods were compared and they agree with each other adequately (a 1% difference) at 0.03226 ± 0.00236 [95].

The impact of uncertainties from asymmetry in the aluminum target window to the physics asymmetry can be summarized in the following relationships:

$$\left(\frac{dA_{ep}}{A_{ep}}\right)_{A_{Al}} = -\frac{dA_{Al}}{A_{ep}} \times \frac{f_{Al}}{1 - \sum_i f_i}, \quad (5.11)$$

$$\left(\frac{dA_{ep}}{A_{ep}}\right)_{f_{Al}} = \frac{df_{Al}}{(1 - \sum_i f_i)^2} \times \frac{A_M/P_e + (-1 + \sum_{i \neq Al} f_i)A_{Al} - \sum_{i \neq Al} A_i f_i}{A_{ep}}. \quad (5.12)$$

For our case, $A_{Al} \sim 10A_{ep}$ and $f_{Al} \sim 0$, then Eqs. 5.11-12 can be simplified to

$$\left(\frac{dA_{ep}}{A_{ep}}\right)_{A_{Al}} = \frac{A_{Al}}{A_{ep}} \times \frac{f}{1 - f} \times \frac{dA_{Al}}{A_{Al}} \simeq 10f_{Al} \frac{dA_{Al}}{A_{Al}}, \quad (5.13)$$

$$\left(\frac{dA_{ep}}{A_{ep}}\right)_{f_{Al}} \simeq df_{Al} \times \frac{A_{Al}}{A_{ep}}. \quad (5.14)$$

With our measured values, the uncertainties from the asymmetry and the dilution factor are 9.8 ppb combined. A more detailed calculation will be discussed in Sec.5.9.

5.7.2 Inelastic Backgrounds

The inelastic scattering between the electron and the proton contributes to A_{LR} through the electroweak excitation of the $\Delta(1323)$ baryon resonance

$$N \xrightarrow{V} \Delta, \quad (5.15)$$

where N is the nucleon and $V = \gamma, W^\pm, Z^0$. In the Qweak experiment, this transition is probed by the electromagnetic ($V = \gamma$) and neutral weak ($V = Z^0$), where Δ eventually decays into a nucleon and a π . Although the QTOR magnet was

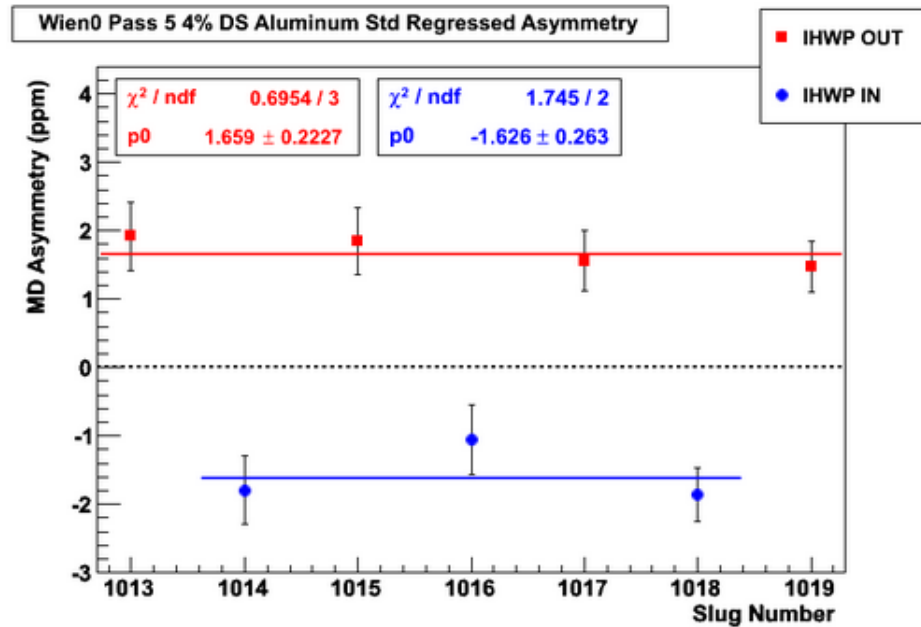


FIG. 5.6: The regressed value of the parity-violating asymmetry of aluminum for the 25% measurement. The p_0 values are the fit values for all of the slugs in each IHWP status assuming a constant value.

used to bend most of the inelastic electrons away from the acceptance of the main detector, which led to a tiny fraction (as high as $\sim 0.2\%$) of the rate seen by the main detector, the inelastic asymmetry is expected to be Q^2 -dependent, given by $A \approx 10^{-4} Q^2 / (\text{GeV})^2$ [96]. At $Q^2 \sim 0.026(\text{GeV})^2$, this indicates that this asymmetry is ~ 10 times bigger than the elastic asymmetry and the estimated correction from this asymmetry becomes non-negligible and therefore needs to be measured. Notice that the value of $\sim 0.2\%$ inelastic rate percentage is derived from an initial crude simulation. The total detected rate is firstly compared between simulation and experimental data to make sure they are about the same, so the percentage of the inelastic rate in the total rate derived from the simulation should be consequently close to its counterpart under normal experimental

running situations.

In order to measure the inelastic asymmetry, the magnet current was reduced to 6700 A to produce the maximum rate of inelastic scattering in the main detector. A total of 20 hours of data was taken in February of 2011. Another two sets of data with higher statistics were taken in April of 2011 and December of 2011 respectively. The latest result from John Leacock's analysis [97] showed that

$$A_{inel} \approx -3.02 \pm 0.97 \text{ ppm}, \quad (5.16)$$

where the uncertainty is purely statistical. The dilution factor f_{inel} was also determined from simulation to be $(2.00 \pm 0.05) \times 10^{-4}$ at the nominal beam current 8921 A in that analysis. Considering the dilution and A_{inel} leads to -3.02 a correction with an error 0.97.

5.7.3 Soft Backgrounds

In the Qweak experiment, photons and neutrons that hit the main detectors were the two major soft backgrounds and their sources mainly came from two places: one was primary electrons interacting in the beamline and the other was electromagnetic showers, created by the scattered electrons, on the collimators and the shielding wall. The effect of the soft background from the beam line was measured by using a thick tungsten "shutter" to block one of the octants of the primary collimators (octant 7), thereby blocking most of the scattered electrons from the target and leaving the beamline background only. The signal in the main detector was measured after and before the "shutter" was moved in, which allowed us to

calculate the dilution factor by

$$f = \frac{\textit{background}}{\textit{background} + \textit{signal}}. \quad (5.17)$$

The analysis of Run 1's data, which was carried out in May 2011, showed that the dilution factor, averaged over various raster sizes ($3\text{mm}^2 \rightarrow 5\text{mm}^2$), was $(0.193 \pm 0.064)\%$. The asymmetry from the beam line is estimated indirectly by using the background monitors and upstream lumis to measure the asymmetry and then scale this down by a certain factor. This method is based upon the assumption that the ratio between the beam line asymmetry and asymmetry observed by the main detectors is a fixed value. The value for the beam line asymmetry is measured to be -5.5 ± 11.5 ppm. This octant plug technique, however, could not measure the dilution from the showers created by the elastically scattered electrons hitting the edges of the collimators and shield walls; we refer to this as the QTOR transport background. Therefore, in order to measure the total QTOR transport background, special tests were carried out to use the main detector as the trigger in event-mode. The basic idea behind this test is that both the main detector and trigger scintillator could detect the charged particles, while only the main detector could perceive high-energy photons indirectly (see Sec. 2.7.1). Consequently, the signal from neutral backgrounds was revealed by subtracting the signal in the scintillator from that in the main detector. More details of this measurement can be found in [98]. The preliminary result in [98] also showed that the contribution from the "soft backgrounds" is $\sim (1 \pm 0.5)\%$ to the total yields in the main detector. The asymmetry for this kind of background is estimated to

be $\sim 0 \pm 200$ ppb.

5.8 Transverse Asymmetry

In addition to the corrections from various backgrounds, there are still some other corrections that need to be considered before arriving at the physics asymmetry. One of those examples is the parity-conserving transverse asymmetry B_n . In ep scattering, B_n arises when the polarization is in the transverse direction with respect to the momentum and is due to the imaginary part of the 2γ exchange amplitude [99]. Consequently, for a given main detector, the measured asymmetry can be written as

$$A_{measured}(\phi_{det}) = |P| A_{PV} + |P_T| B_n \sin(\phi_{det} - \phi_s) + B_{other}, \quad (5.18)$$

where $|P_T|$ is the transverse polarization in the beam, ϕ_{det} is the azimuthal angle of that given detector, ϕ_s is the phase offset and B_{other} is all the other background. Consequently, if our main detector system was perfectly symmetric in the azimuthal direction, B_n is expected to be canceled out when signals from all the eight detectors are averaged out. Special tests were performed to quantify this effect by using the beam with fully transverse polarization either in horizontal or vertical direction. Then the collected data from all eight main detectors with distinct azimuthal angle ϕ_{det} were used to fit to the function [100]

$$A_{det} = |P_T| B_n \sin(\phi_{det} - \phi_s) + C, \quad (5.19)$$

where C represents the effect due to any broken symmetry which could not be canceled out when averaging all the signals. Fig. 5.7 shows an example of fitting the asymmetry from vertical and horizontal transverse LH₂ data sets. The preliminary analysis from LH₂ data showed that the magnitude of the transverse asymmetry was [100]

$$B_n = (-5305 \pm 71_{stat.} \pm 150_{sys.}) \text{ ppb}. \quad (5.20)$$

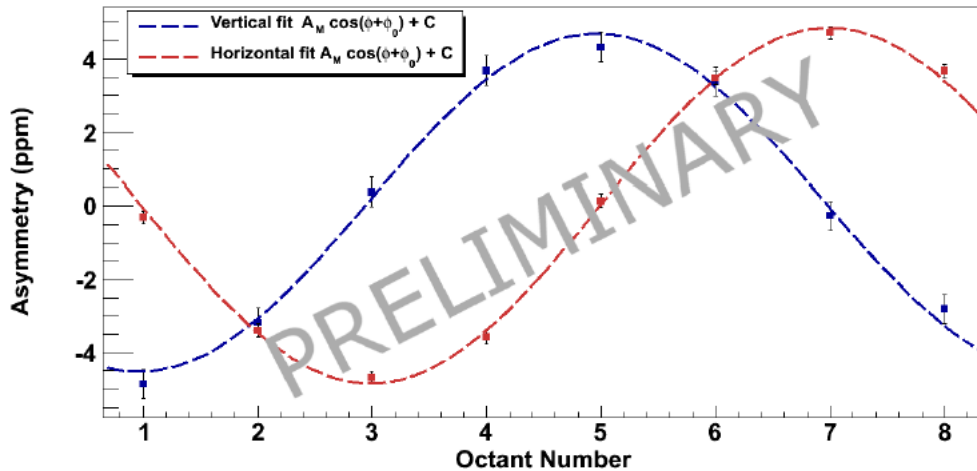


FIG. 5.7: The fitting of the raw asymmetry against the octant number on the elastic horizontal and vertical transverse LH₂ data sets.

The total leakage from the transverse component of the beam is then calculated by summing over the product of the residual polarization and the residual term C , which are calculated assuming the beam is either at 100% vertical or horizontal transverse polarization. Notice that the residual polarization $P_{horizontal}$ and $P_{vertical}$ during longitudinal data taking were measured by fitting the ratio of the measured ϕ -dependent asymmetry during longitudinal to the measured asymmetry during full transverse running and they were found to be $(3.8 \pm 0.9)\%$ and

TABLE 5.9: Summary of the values of the “null” test and the true physics asymmetry for slugs 31-40 before and after the standard regression scheme is applied, in ppb.

	(IN+OUT)/2	(OUT-IN)/2
Raw	70.35 ± 29.58	-173.70 ± 29.53
Standard	67.60 ± 29.53	-200.62 ± 29.44

$(4.2 \pm 0.9)\%$ respectively [101]. The final false asymmetry result is determined to be

$$\Delta A_{trans} = 0.47 \pm 3.88 \text{ ppb} \quad (5.21)$$

5.9 Physics Asymmetry

As discussed in Sec.5.6, different regression schemes can be used to correct the false parity asymmetries brought by the helicity-correlated difference and the comparison in Tab.5.8 shows only as large as 7 ppb difference between different regression schemes. In this dissertation, the standard regression scheme is used as the final scheme to correct the false asymmetry. Fig. 5.8 and Fig. 5.9 shows the results before (“raw”) and after the regression is applied. The “IN+OUT” and “OUT-IN” values are also summarized in Tab.5.9. Notice that 70.35 ppb value of the “IN+OUT” is deviated from 0, which is expected from theoretical point of view, it still falls into 95% confidence level by taking into account the error bars.

In order to obtain the true physics asymmetry from $A_{measured}$, which is the asymmetry after regression applied, Eq.5.9 is needed to correct the contributions from various background noise sources, which are discussed in Sec.5.7. A sum-

TABLE 5.10: Summary of the error on each individual background correction in ppb and its relative uncertainties on A_{ep} for the 25% measurement, in ppb.

Background	Asymmetry (ppm)	Dilution factor	Total correction (ppb)
Aluminum	1.76 ± 0.26	0.0323 ± 0.0024	56.9 ± 10.11
Inelastic	-3.02 ± 0.97	0.0002 ± 0.0000	-0.6 ± 0.2
Beamline	-5.50 ± 11.50	0.00193 ± 0.0006	-10.62 ± 23.02
QTOR _{trans}	0.00 ± 0.20	0.0010 ± 0.0005	0.0 ± 0.2
Total		0.034	45.7 ± 25.14

mary of each background's asymmetry and its dilution factor is shown in Tab.5.10.

Using Eq.5.9 and information from Tab.5.10, the physics asymmetry is calculated to be:

$$A_{ep} = -280.79 \text{ ppb.} \quad (5.22)$$

Furthermore, the contribution of each error source to A_{ep} can be calculated using the following two equations:

$$\left(\frac{dA_{ep}}{A_{ep}}\right)_{A_i} = -\frac{dA_i}{A_{ep}} \times \frac{f_i}{1 - \sum_k f_k}, \quad (5.23)$$

$$\left(\frac{dA_{ep}}{A_{ep}}\right)_{f_i} = \frac{df_i}{(1 - \sum_k f_k)^2} \times \frac{A_M/P_e + (-1 + \sum_{k \neq i} f_k)A_i - \sum_{k \neq i} A_k f_k}{A_{ep}}, \quad (5.24)$$

where the subscript i corresponds to the i th background and the total uncertainty from source i then can be calculated as

$$\left(\frac{dA_{ep}}{A_{ep}}\right)_i = \sqrt{\left(\frac{dA_{ep}}{A_{ep}}\right)_{A_i}^2 + \left(\frac{dA_{ep}}{A_{ep}}\right)_{f_i}^2}. \quad (5.25)$$

A breakdown of the absolute and relative uncertainties to A_{ep} from each individual source is given in Tab. 5.11. The final physics asymmetry therefore is:

$$A_{ep} = -280.79 \pm 34.26_{stat.} \pm 27.37_{sys.} \quad (5.26)$$

TABLE 5.11: Summary of each individual correction and its relative uncertainties on A_{ep} for the 25% measurement, in ppb.

Source	Correction error	Contribution to dA_{ep}/A_{ep}
Statistical	34.26	12.2%
Polarization	5.50	1.96%
Aluminum background	10.11	3.6%
Inelastic background	0.20	0.07%
Beam line background	23.02	8.2%
QTOR _{tran}	0.20	0.07%
Regression	8.14	2.9%
Transverse	4.49	1.6%
Total	43.85	15.6

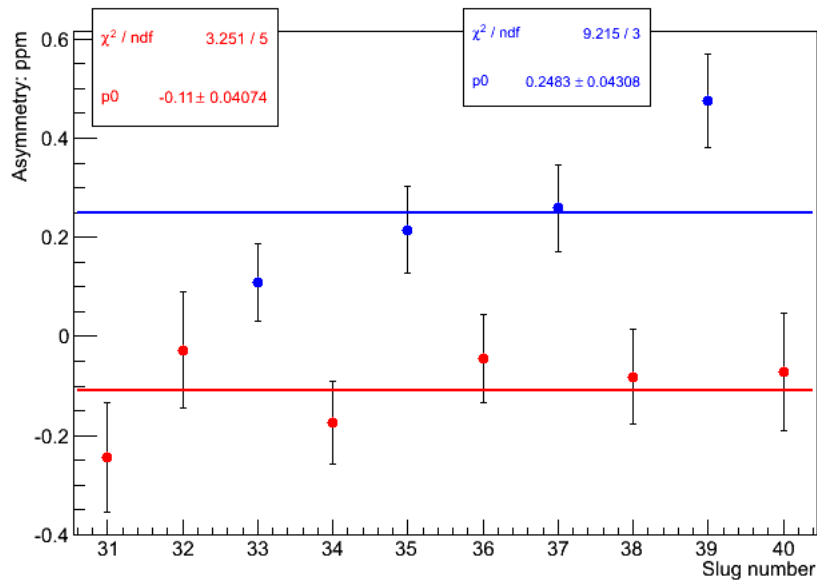


FIG. 5.8: Raw asymmetry A_{ep} for slugs 31-40. The red points are the results when the IHWP status is out while the blues are results when IHWP is in. The $p0$ in each statistical box shows the average values of asymmetries for those two different IHWP status.

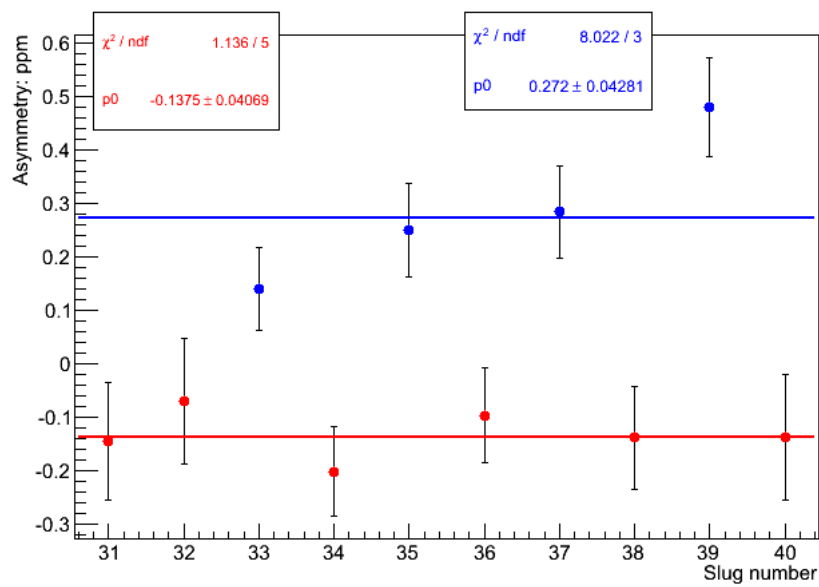


FIG. 5.9: Asymmetry A_{ep} for slugs 31-40, after applying the standard regression scheme. The red points are the results when the IHWP status is out while the blues are results when IHWP is in. The p_0 in each statistical box shows the average values of asymmetries for those two different IHWP status.

CHAPTER 6

Result and Outlook

6.1 The 25% measurement of Q_W^p

The final elastic asymmetry, after all corrections are applied, is $-280.79 \pm 34.26_{stat.} \pm 27.37_{sys.}$ from Sec.5.9 at $Q^2 = 0.025 \text{ GeV}^2$. This new result, combined with other PVES experiments' data, is plotted in Fig. 6.1. Notice that the value and error bar plotted in Fig. 6.1, $A_{PV} = -279 \pm 35_{stat.} \pm 31_{sys.}$, which is the official result of the collaboration, as published in [50], is slightly different from those in this dissertation. But this few ppb difference will not affect the validity of the final values at the current precision. The value of Q_W^p at $Q^2 = 0$, can be extrapolated through the following equation:

$$A_{LR}^p/A_0 \simeq Q^2 Q_W^p + Q^4 B(Q^2), \quad (6.1)$$

where the meaning of each item has been discussed in Sec.1.6. Fig. 6.1 shows the global fit combined other PVES experiment where the value of Q^2 ranges

from 0.025 (GeV/c)^2 to 0.63 (GeV/c)^2 . Notice that this global fit is under the forward limit angle assumption, which means the angle dependence of the hadronic form factor contribution has been removed from the asymmetry by the amount of $A(\theta, Q^2) - A(0^\circ, Q^2)$. By using this method, the two dimensional function of $A(\theta, Q^2)$ is collapsed into a one dimensional function $A(Q^2)$ and therefore can be conveniently plotted and fitted. In addition to removing the angle dependence, the γZ correction, which is the biggest theoretical correction, also needs to be taken care of. The γZ correction can be divided into two parts: one part is dependent on Q^2 and beam energy E and will vanish when both those two quantities are zero; the other part is intrinsic and will survive when $Q^2 = 0$ and $E = 0$. What we need to remove for every asymmetry is the first part. As discussed in Sec.1.7, the most updated result shows the correction at the kinematics of Qweak is $7.8 \pm 0.5\%$ [21]. The value of Q_W^p obtained after all those correction, is $Q_W^p(\text{PVES}) = 0.064 \pm 0.012$, which is consistent with the prediction from the standard model $Q_W^p(\text{SM}) = 0.0710 \pm 0.0007$ with a higher precision than any other previous experiment.

6.2 More recent results and path to the 4% result

The rapid progress in recalculating the correction from γZ box leads to decreasing uncertainties and also help us to interpret the Q_W^p better. The latest up to date result can be found in Qweak collaboration's papers. There are still several factors

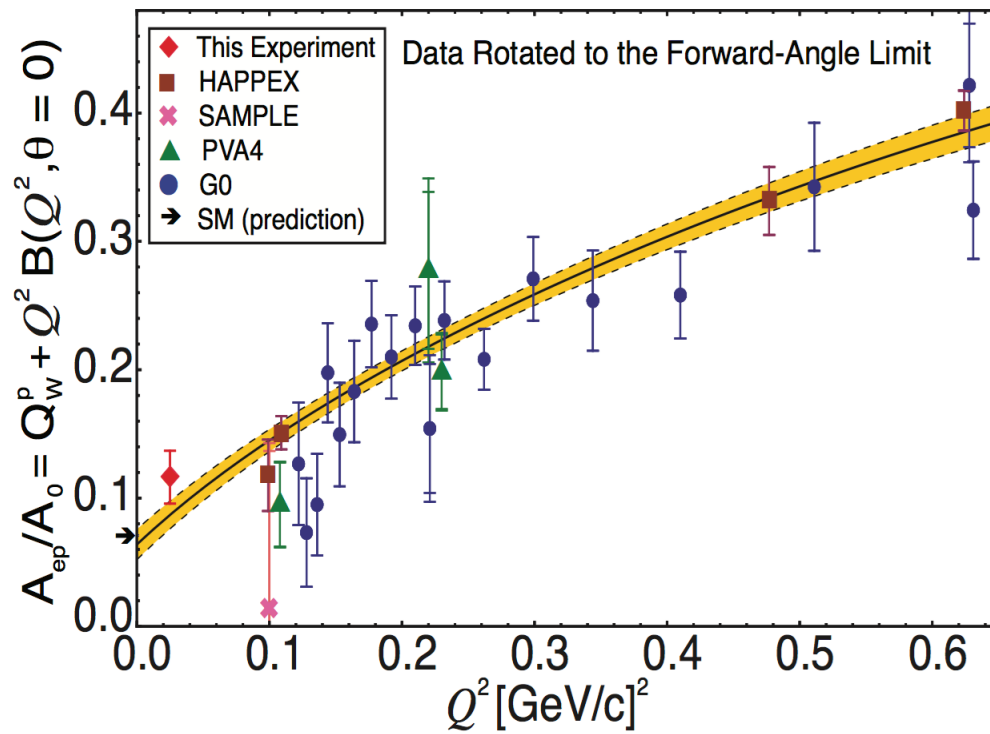


FIG. 6.1: Current world data from parity-violating electron-proton experiments, including Qweak's 25% result, with the extrapolation to $Q^2 = 0$ to get the value of Q_w^p .

needed to be improved in order to meet the original 4% Q_W^p goal. These includes, but are not limited to: 1) statistics: all the data-taken periods have already been finished by the May of 2012 (refer to Sec.5.1 for more information); what has been showed and analyzed in this dissertation only includes data from 25% measurement. Therefore, with more data being analyzed, the error from statistics is expected to be greatly reduced to close to the proposed value of 2.1%. 2) beam polarization: the proposed error is 1% and the current error stays at 2% 3) Q^2 : the latest result shows the error of Q^2 is limited to 1.6%. By futher investigating the data and combining with the simulation result, we expect that the stability and octant variant error sources can be reduced. 4) aluminum and beamline background: those two items currently are the two biggest systematic error sources (3.6% and 8.2% each) contributing to the dA_{ep}/A_{ep} . The proposed values for all the backgrounds is 0.5%. Therefore, in order to meet the final goal, much effort needs to be put to better understand the data and reduce the errors.

APPENDIX A

Details of Parameter Files and Running Options in QTR

The QTR relies upon a lot of pre-configured parameter files to precisely reconstruct track. A lot of running options have also been provided in order to make it convenient for people to use the QTR. This Appendix provides a list of the important parameter files as well as the most common options available when the tracking analyzer is run.

A.1 Parameter Files

For each type of tracking detector, there are four kinds of parameter file needed to be loaded:

- The Geometry File (**qweak_new.geo**): This file contains the positions in lab coordinates of each detector for HDCs and VDCs. Local information, such as the number of wires in each individual detector, the angle of wire orientation, the active size of the detector, can be also found in this file. More details can

be found in Sec. 3.9.

- The t_0 map (**R3_timeoffset.map** and **R2_timeoffset.map**): This file contains the t_0 correction value for every wire in VDCs. More details are discussed in Sec. 3.4.2.
- The drift-time to drift-distance tables (**R2_TtoDtable.map** and **R3_TtoDtable.map**): The algorithm used to map the drift-time into the corresponding drift-distance, required that we built a look-up table in order to do a quick conversion. The first text map contains the look-up table for HDCs while the second for VDCs. More details are discussed in Sec. 3.4.3.
- The electronics map (**qweak_R2.map** and **qweak_R3.map**): These two files contain important information which help to link each electronic channel with a specific corresponding physical element, such as package, plane and wire, for HDCs and VDCs, respectively.

A.2 Running Options

Below is the list of the most common running options:

- **-r run number**: This option specifies the dataset with the given run number to analyze.
- **-e event**: This option specifies the event number to analyze. A range of events can be specified by separating the start event number and end event number with a semicolon, such as 1:100. The start event number can be even omitted, like :100 to tell the QTR to analyze the event from the first event until event 100. If this option does not appear in the command line, the QTR will analyze all the events in the dataset.

- - -disable-by-type *subsystem name*: This option specifies the name of the subsystem one wants the QTR to ignore. For VDCs, the *subsystem name* is *QwDriftChamberVDC* while for HDCs, the name is *QwDriftChamberHDC*.
- - -disable-wireoffset {YES|NO}: Sets the option of turning on or off the *SubtractWireOffset* functions. For more information, see Sec. 3.4.2.
- - -use-tdchits {YES|NO}: If 1(YES) is chosen, a TDC-based Root file will be created. Otherwise, the normal wire-based Root file is constructed.
- - - R3-octant *octant number*: This option is used to load the specific octant geometry information for VDCs.
- - - R2-octant *octant number*: This option is used to load the specific octant geometry information for HDCs.
- - -QwTracking.regenerate {YES|NO}: This option specifies if one wants to create the pattern database. The default value, which is recommended, is 0(NO) unless numbers in the geometry map are changed.
- - -QwTracking.disable-momentum {YES|NO}: This option specifies if one wants to reconstruct the full track by connecting the HDCs and VDCs **partial tracks**. The default value is 1(YES).
- - -QwTracking.disable-tracking {YES|NO}: If choosing 1(YES), the QTR will ignore all the tracking jobs. In other words, only the drift-time and drift-distance information will be obtained while no **treelines** will be reconstructed.

APPENDIX B

Details of Geometry File in QTR

This Appendix provides a full summary of all entries which are used to describe a given wire plane. To make numbers in the geometry file easier to be maintained and more readable, each package is assumed to be placed at octant 3. The units used in the geometry file are cm for length and degree for angle. A typical line corresponding to a given wire plane in the geometry file typically has 23 entries, they're listed in order as follows:

1. name: this entry gives wire plane an alias, like *VDC_leftfront* in order for people to better recognize wire plane when reading the geometry file
2. type: indicates the type of detector. For the HDCs and the VDCs, this entry is always *drift*.
3. z: this entry specifies the z position of the wire plane in the global coordinates.
4. rotational angle about global x: the VDCs are oriented in such a way that the whole local coordinate system needs to rotate about the global x axis a certain degree (See Figure ??). This entry records value of this "tilt" angle. For the HDCs, since the wire plane is perpendicular to the beam axis, this

entry is thus 0.

5. spatial resolution: this entry describes how accurate is the drift-time timing information.
6. tracking resolution: this entry is used to represent the hit resolution when mapping the drift-distance from an event into corresponding bit patterns (refer Sec. 3.6.1 for more details).
7. slope matching: this is limit of the slope difference used in the process of matching the **treelines** from front and back chambers in the case of the VDCs (refer Sec 3.6.2 for more details).
8. package: this entry specifies which package this wire plane belongs to. We use letter u (up) and d (down) to represent package 1 and package 2, respectively.
9. region: region number where 3 stands for the VDCs and 2 for the HDCs.
10. type: detector type. d for both the HDCs and the VDCs.
11. direction: the wire direction in the plane. For the VDCs, there are two directions: u and v ; for the HDCs, three directions can be found: x , u and v .
12. x : x position of wire plane in the global coordinates.
13. y : y position of wire plane in the global coordinates.
14. the width of active area in local x : for both the VDCs and the HDCs, the longer edges are always placed parallel to the local y axis.
15. the width of active area in local y .
16. the width of active area in local z .

17. wire spacing: this entry records the perpendicular distance between adjacent wires.
18. position of the first wire: this entry is the distance between the location of the first wire and the local coordinates' origin (see Figure ?? to Figure B.4 for more details).
19. $\cos \theta$: θ is the angle between uv and local xy coordinates (See Figure ?? to Figure B.4 for more details).
20. $\sin \theta$: see item 19.
21. rotational angle about global z : similar to item 3, this entry is the rotational angle of the whole local coordinates about global z axis.
22. number of wires: this records how many wires in a given wire plane.
23. plane ID: this ID tag is used to keep track of each individual wire plane in the QTR.

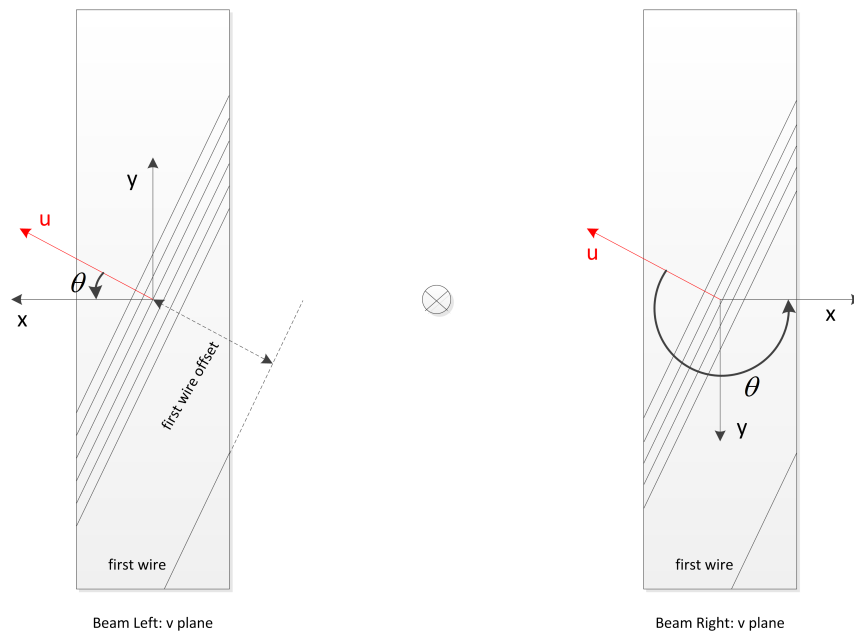


FIG. B.1: The layout of two v planes from both packages in the VDCs. In the geometry map, the package 1 is placed at octant 5 (beam right) while all the numbers are read from octant 3, which can be obtained by rotating the package 1 by 90° in counterclockwise direction from octant 5. Similar to the package 1, the numbers of package2 saved in the geometry file is also read from octant 3 and this is obtained by rotating 90° in clockwise direction from octant 1. The u direction is perpendicular to the wire orientation and pointing from wire with small number to wire with big number. θ is the counterclockwise rotational angle from u to local x and its cos and sin value are saved as item 19 and 20 in the geometry file. For two v planes in the VDCs, the nominal values of θ are 26.565° (beam left) and 206.565° (beam right).

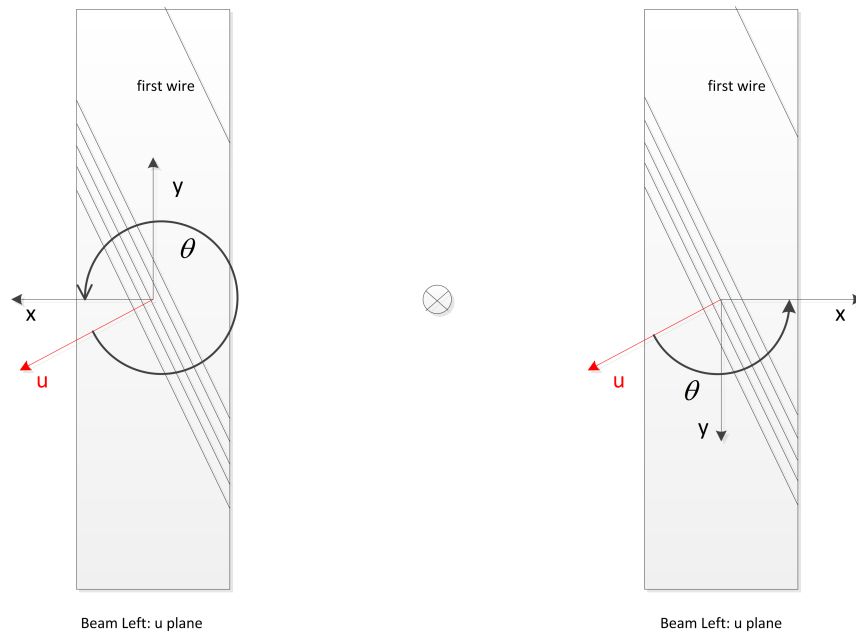


FIG. B.2: The layout of two u planes from both packages in the VDCs. Unlike ??, the wire orientation is changed as well as the position of the first wire. So the nominal values of θ are adjusted to 333.435° (beam left) and 153.435° (beam right) accordingly.

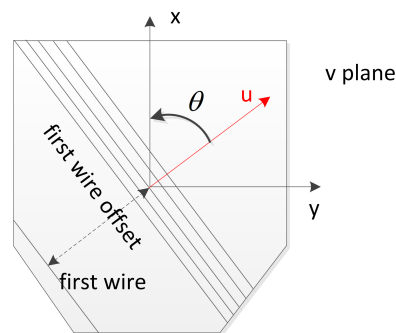


FIG. B.3: The layout of one u plane in the HDCs. It is placed at octant 3 where all the numbers are read. Unlike the mirror image relationship between two opposite octants in the VDCs, the octant is just the rotational image of the opposite one in the HDCs, which leads to the same treatment of both packages. Similar to VDCs, the u is perpendicular to the wire orientation and always points from first wire to the last wire. The θ for u plane is 153.435° .

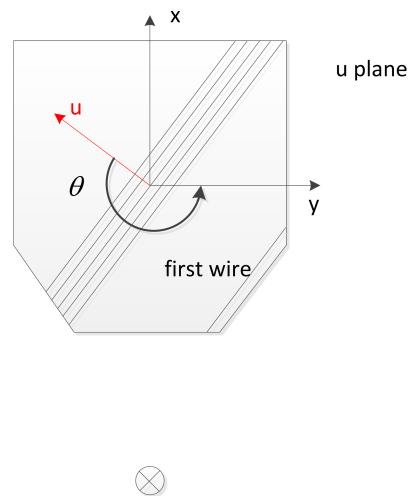


FIG. B.4: The layout of one v plane in the HDCs. It is placed at octant 3 where all the numbers are read. The θ for u plane is 216.87° . Notice that there are three directions in HDCs and only u (B.3) and v are drawn here, the x is ignored for it being simple.

APPENDIX C

Hall C beamline apparatus layout

This section displays the side view of the layout of all the Hall C apparatus along the beamline. Notice that the names of the apparatus in this figure are different from the names used in this dissertation. The name discrepancies for some of apparatus mentioned in this dissertation are listed below.

- IPM3H04A: BPM3h04
- IPM3H09: BPM3h09
- IPM3H09B: BPM3h09B
- IBC3H05: Hall C BCM1
- IBC3H05A: Hall C BCM2

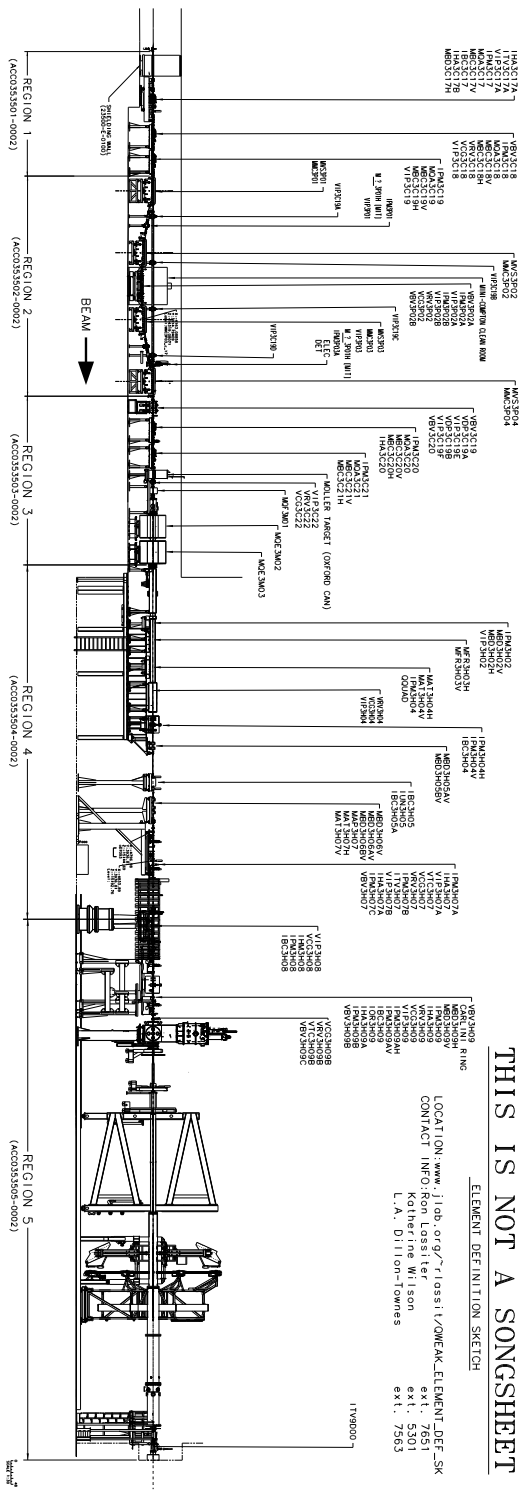


FIG. C.1: The side view of the layout of apparatus along the Hall C beamline.

APPENDIX D

Projections of Reconstructed Tracks for all Octants

This section displays the result of projecting the HDC tracks to collimator 2, and the hydrogen target from a series of runs where where all eight octants were covered (See Sec. 4.2.1).

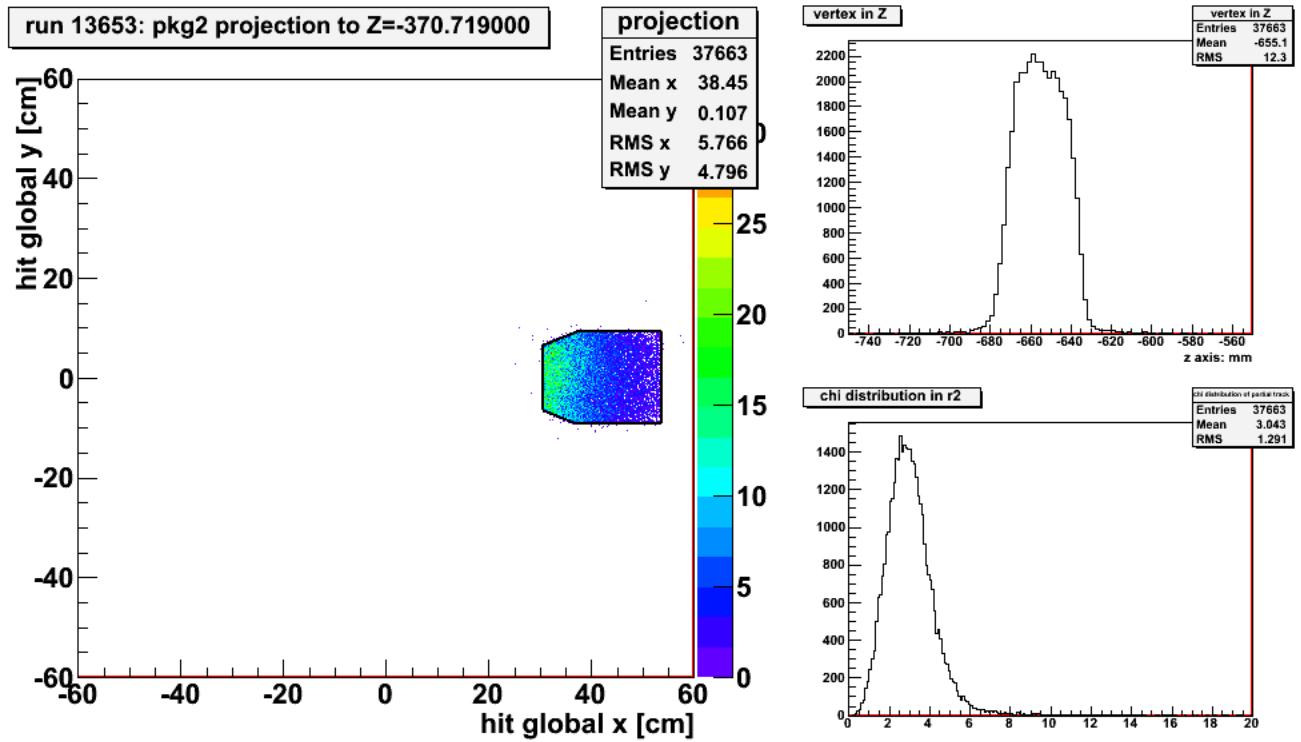


FIG. D.1: Projection result from package 2 in run 13653 where octant 5 is covered.

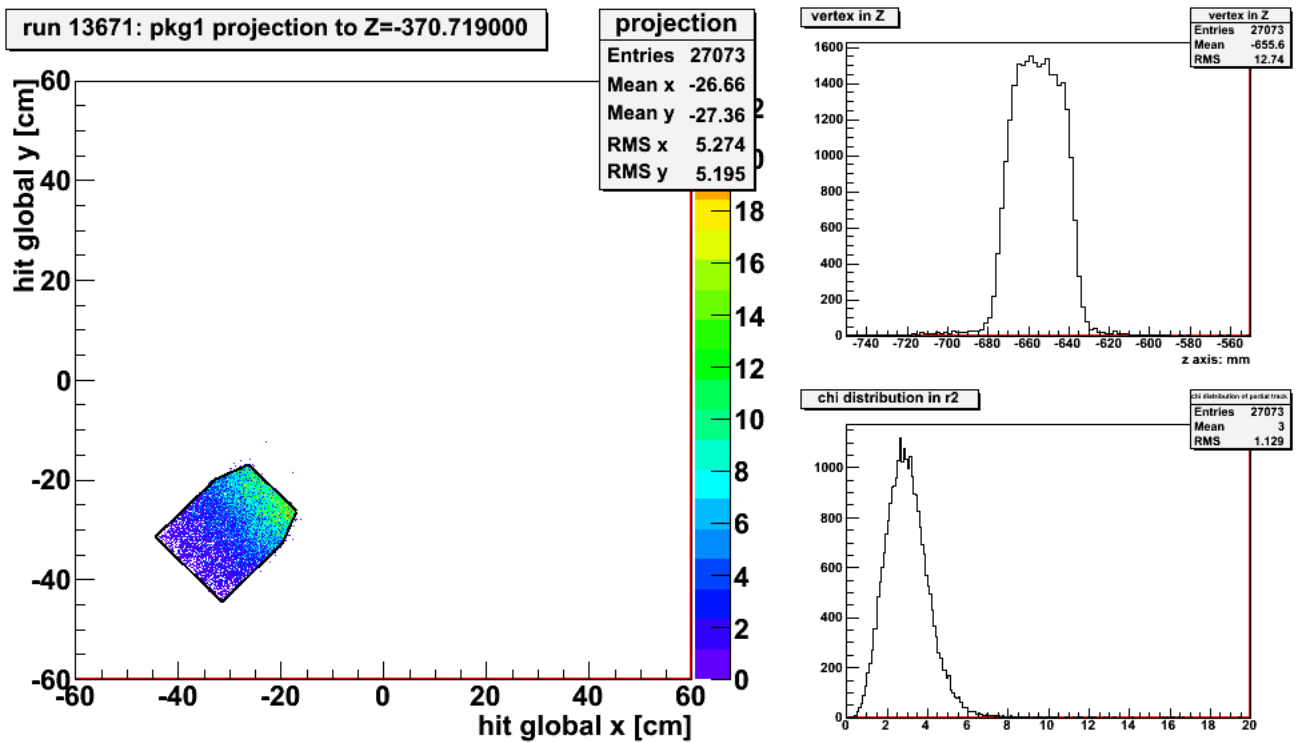


FIG. D.2: Projection result from package 1 in run 13671 where octant 8 is covered.

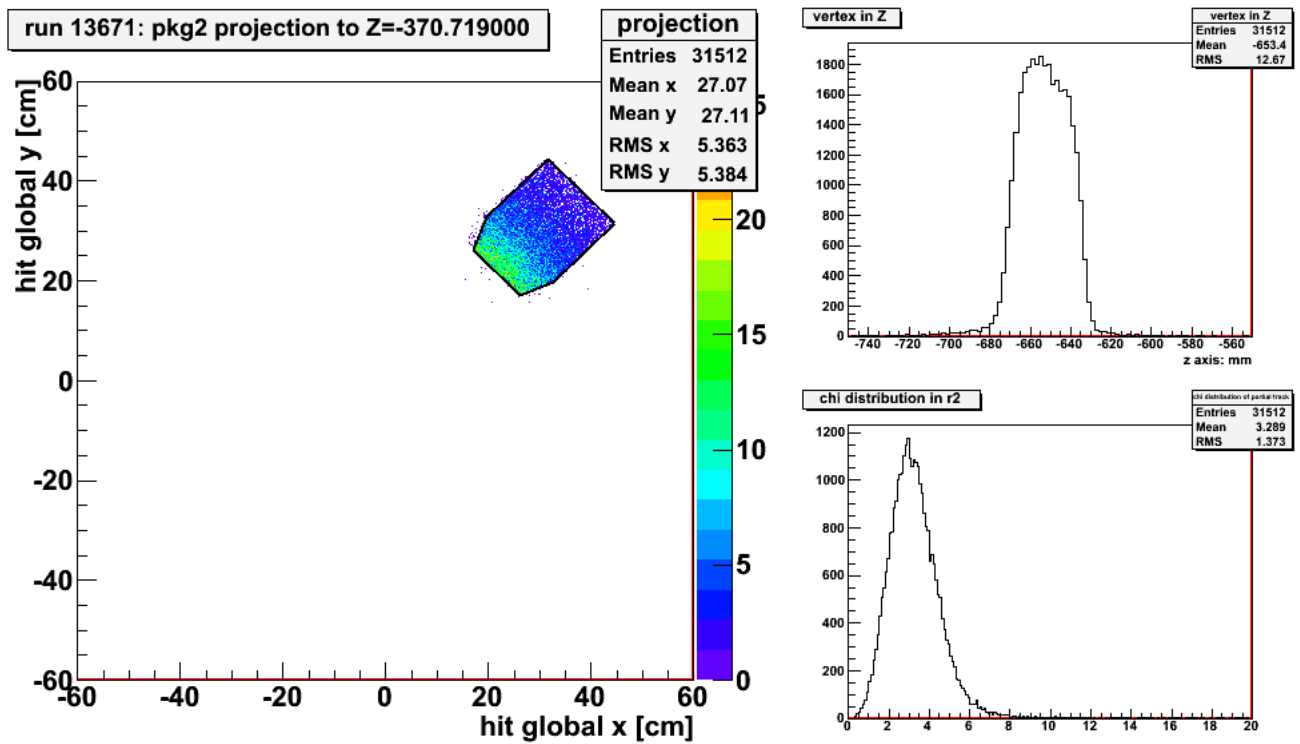


FIG. D.3: Projection result from package 2 in run 13671 where octant 4 is covered.

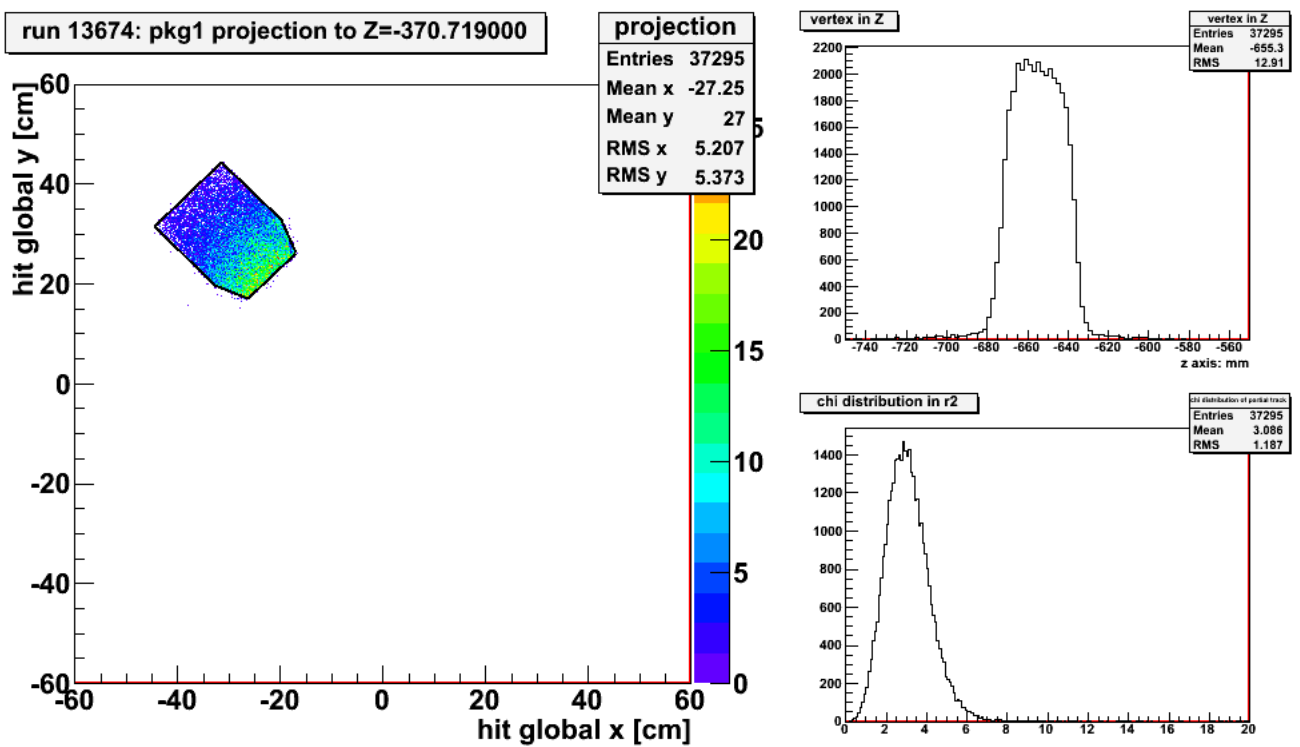


FIG. D.4: Projection result from package 1 in run 13674 where octant 2 is covered.

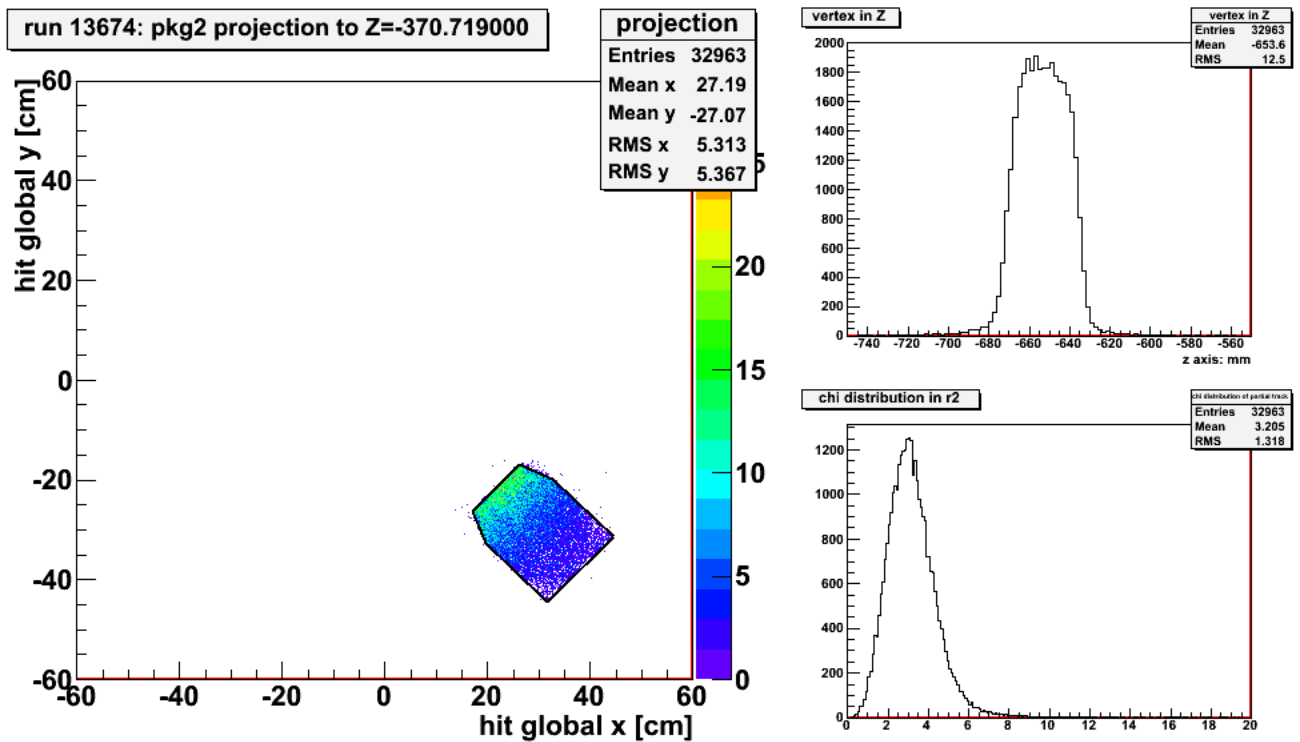


FIG. D.5: Projection result from package 2 in run 13674 where octant 6 is covered.

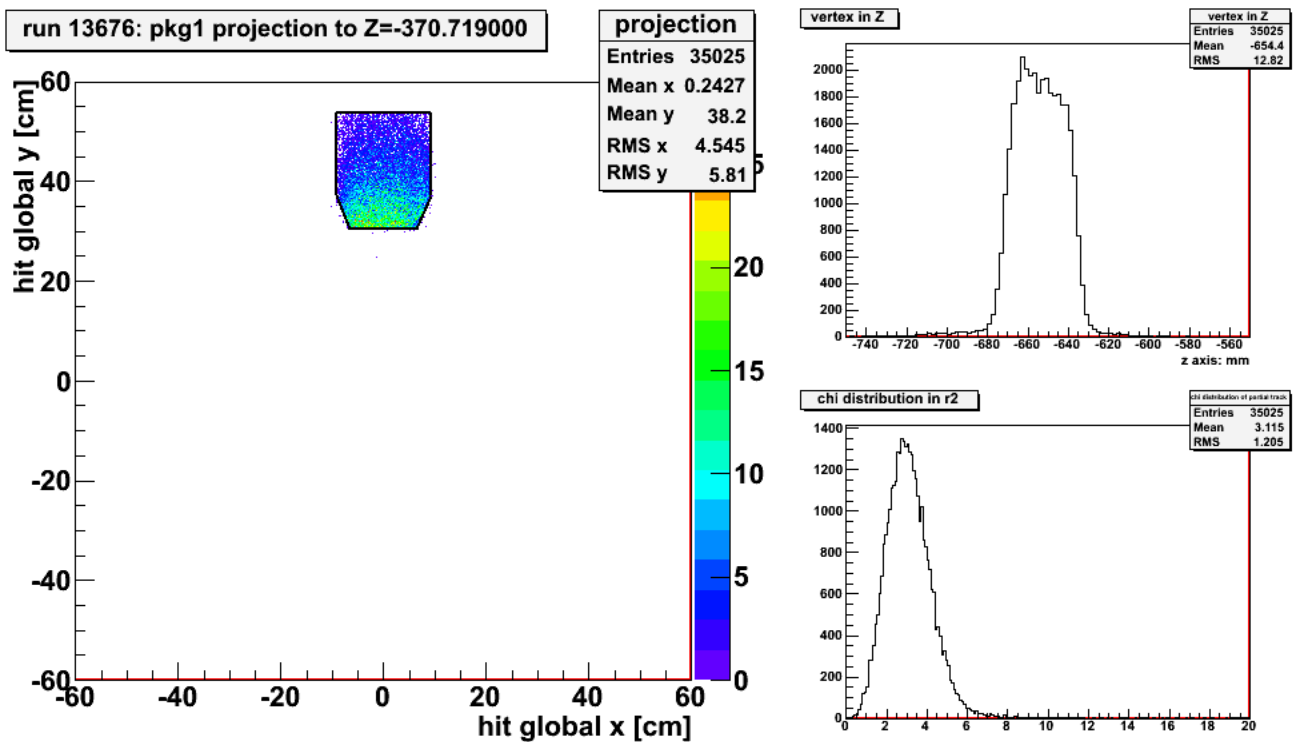


FIG. D.6: Projection result from package 1 in run 13676 where octant 3 is covered.

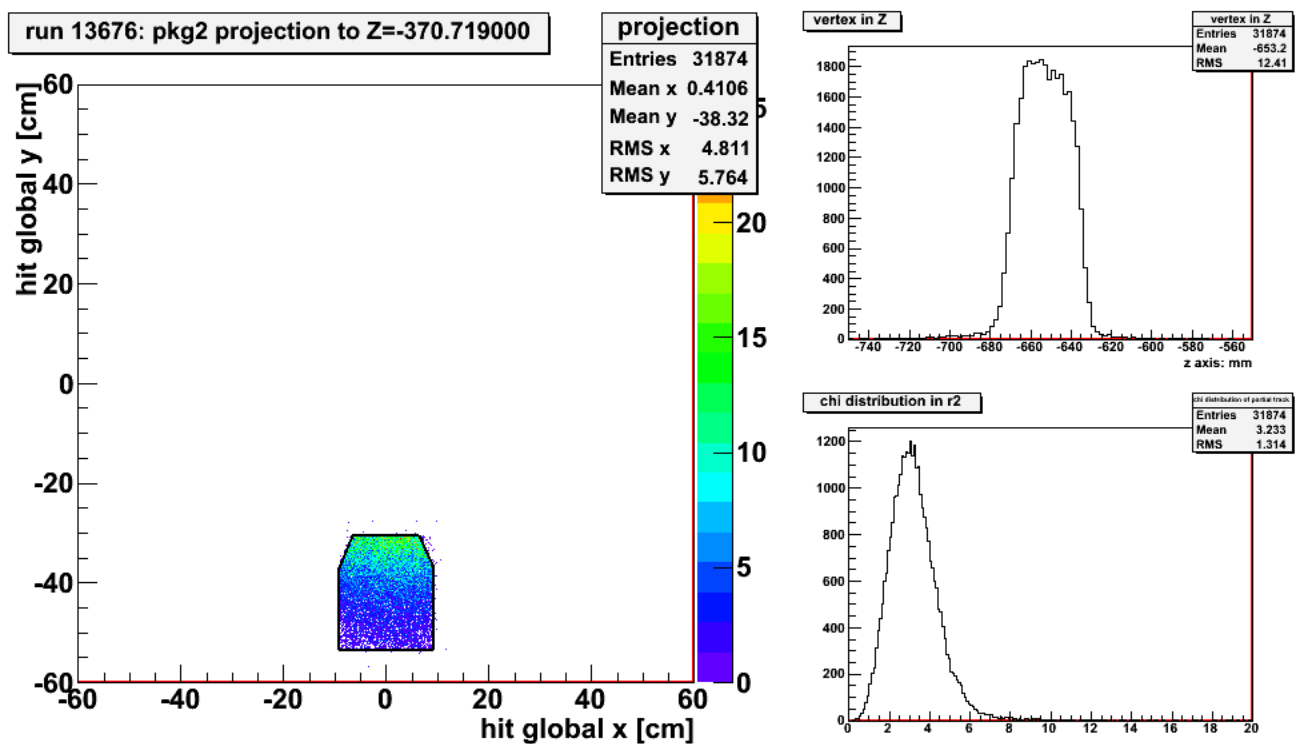


FIG. D.7: Projection result from package 2 in run 13676 where octant 7 is covered.

APPENDIX E

Personal Contributions to Qweak

For hardware, I was involved with building and calibrating the VDCs at the College of William and Mary from 2007 to 2010.

I became an expert on the tracking software. Initially, this work included the track reconstruction only in the VDCs using the cosmic rays. This led to the optimization of the VDCs. When the commissioning started, I made numerous improvements to the QTR, which efficiency and precision of the linking the partial tracks between each tracking system improves significantly. I also kept constantly updated the geometry of the tracking system in order to make them more consistent with the reality.

The analysis of the Q^2 as well as the 25% dataset was my independent work.

BIBLIOGRAPHY

- [1] G. Aad *et al.* Observation of a new particle in the search for the standard model higgs boson with the {ATLAS} detector at the {LHC}. *Physics Letters B*, 716(1):1 – 29, 2012.
- [2] Sheldon L. and Glashow. Partial-symmetries of weak interactions. *Nuclear Physics*, 22(4):579 – 588, 1961.
- [3] Steven Weinberg. A model of leptons. *Phys. Rev. Lett.*, 19:1264–1266, Nov 1967.
- [4] A. Salam. *Elementary Particle Theory*. Almquist and Wiksells, Stockholm, 1969.
- [5] Robert Mann. *An Introduction to Particle Physics and Standard Model*. CRC press, first edition, 2009.
- [6] F.J. Hasert *et al.* Observation of neutrino-like interactions without muon or electron in the gargamelle neutrino experiment. *Physics Letters B*, 46(1):138 – 140, 1973.
- [7] Parity nonconservation in inelastic electron scattering. *Phys.Lett.*, B77:347–352, 1978.
- [8] G. Arnison *et al.* Experimental observation of isolated large transverse energy electrons with associated missing energy at $s=540$ gev. *Physics Letters B*, 122(1):103 – 116, 1983.

- [9] M. Banner *et al.* Observation of single isolated electrons of high transverse momentum in events with missing transverse energy at the cern pp collider. *Physics Letters B*, 122(5-6):476 – 485, 1983.
- [10] Robert G. Sachs. Nucleon electromagnetic form factors at high momentum transfer. *Phys. Rev. Lett.*, 12:231–233, Mar 1964.
- [11] Kent Paschke, Anthony Thomas, Robert Michaels, and David Armstrong. Strange vector form factors from parity-violating electron scattering. *Journal of Physics: Conference Series*, 299(1):012003, 2011, and references therein.
- [12] M.J. Musolf *et al.* Intermediate-energy semileptonic probes of the hadronic neutral current. *Physics Reports*, 239(1):1 – 178, 1994.
- [13] R. D. Young, R. D. Carlini, A. W. Thomas, and J. Roche. Testing the standard model by precision measurement of the weak charges of quarks. *Phys. Rev. Lett.*, 99:122003, Sep 2007.
- [14] Shi-Lin Zhu, S. J. Puglia, B. R. Holstein, and M. J. Ramsey-Musolf. Nucleon anapole moment and parity-violating ep scattering. *Phys. Rev. D*, 62:033008, Jul 2000.
- [15] Jens Erler, Andriy Kurylov, and Michael J. Ramsey-Musolf. Weak charge of the proton and new physics. *Phys. Rev. D*, 68:016006, Jul 2003.
- [16] M. Gorchtein and C. J. Horowitz. Dispersion γ Z-Box Correction to the Weak Charge of the Proton. *Phys. Rev. Lett.*, 102:091806, Mar 2009.
- [17] C. J. Horowitz M. Gorchtein and M. J. Ramsey-Musolf. In *AIP Conf. Proc.*, volume 1265, page 328, 2010.

- [18] A. Sibirtsev, P. G. Blunden, W. Melnitchouk, and A. W. Thomas. γZ corrections to forward-angle parity-violating ep scattering. *Phys. Rev. D*, 82:013011, Jul 2010.
- [19] Rislow Benjamin C. and Carlson Carl E. Contributions from γZ box diagrams to parity violating elastic $e-p$ scattering. *Phys. Rev. D*, 83:113007, Jun 2011.
- [20] Mikhail Gorchtein, C. J. Horowitz, and Michael J. Ramsey-Musolf. Model dependence of the γZ dispersion correction to the parity-violating asymmetry in elastic ep scattering. *Phys. Rev. C*, 84:015502, Jul 2011.
- [21] N. L. Hall, P. G. Blunden, W. Melnitchouk, A. W. Thomas, and R. D. Young. Constrained $\gamma - Z$ interference corrections to parity-violating electron scattering. *Phys. Rev. D*, 88:013011, Jul 2013.
- [22] J.A. Tjon, P.G. Blunden, and W. Melnitchouk. Detailed analysis of two-boson exchange in parity-violating e-p scattering. *Phys.Rev.*, C79:055201, 2009.
- [23] Andrzej Czarnecki and William J. Marciano. Polarized Moller scattering asymmetries. *International Journal of Modern Physics A*, 15:2365, 2000.
- [24] Jens Erler and Michael J. Ramsey-Musolf. Weak mixing angle at low energies. *Phys. Rev. D*, 72:073003, Oct 2005.
- [25] C. Bouchiat M.-A. Bouchiat. Parity violation in atoms. *Rep. Prog. Phys.*, 60:1351–1396, 1997.
- [26] Anthony *et al.* Observation of parity nonconservation in møller scattering. *Phys. Rev. Lett.*, 92:181602, May 2004.

- [27] Zeller *et al.* Precise determination of electroweak parameters in neutrino-nucleon scattering. *Phys. Rev. Lett.*, 88:091802, Feb 2002.
- [28] Marcela Carena, Alejandro Daleo, Bogdan A. Dobrescu, and Tim M. P. Tait. Z' gauge bosons at the Fermilab Tevatron. *Phys. Rev. D*, 70:093009, Nov 2004.
- [29] Precision electroweak measurements on the z resonance. *Physics Reports*, 427(5-6):257 – 454, 2006.
- [30] W.-M. *et al.* Yao. Review of Particle Physics. *Journal of Physics G*, 33:1, 2006.
- [31] Abe *et al.* High-precision measurement of the left-right Z boson cross-section asymmetry. *Phys. Rev. Lett.*, 84:5945–5949, Jun 2000.
- [32] Precision electroweak measurements on the Z resonance. *Phys.Rept.*, 427:257–454, 2006.
- [33] J. Benesch *et al.* The MOLLER Experiment: An Ultra-Precise Measurement of the Weak Mixing Angle Using Møller Scattering. 2014.
- [34] E. A. Paschos and L. Wolfenstein. Tests for Neutral Currents in Neutrino Reactions. *Phys. Rev. D*, 7:91–95, Jan 1973.
- [35] I.C. Cloet, W. Bentz, and A.W. Thomas. Isovector EMC effect explains the NuTeV anomaly. *Phys.Rev.Lett.*, 102:252301, 2009.
- [36] W. Bentz, I.C. Cloet, J.T. Londergan, and A.W. Thomas. Reassessment of the NuTeV determination of the weak mixing angle. *Phys.Lett.*, B693:462–466, 2010.

- [37] P.L. Anthony et al. Precision measurement of the weak mixing angle in Moller scattering. *Phys.Rev.Lett.*, 95:081601, 2005. <http://www-group.slac.stanford.edu/com/e158/press-release.htm> Press Release.
- [38] M.A. Bouchiat and C.C. Bouchiat. Weak Neutral Currents in Atomic Physics. *Phys.Lett.*, B48:111–114, 1974.
- [39] M.A. Bouchiat, J. Guena, L. Hunter, and L. Pottier. Observation of a Parity Violation in Cesium. *Phys.Lett.*, B117:358, 1982.
- [40] C.S. Wood, S.C. Bennett, J.L. Roberts, D. Cho, and Carl E. Wieman. Precision measurement of parity nonconservation in Cesium. *Can.J.Phys.*, 77:7–75, 1999.
- [41] I. Lindgren and J. Morrison. *Atomic Many-Body Theory*. Springer-Verlag, Berlin, 1986.
- [42] S.G. Porsev, K. Beloy, and A. Derevianko. Precision determination of electroweak coupling from atomic parity violation and implications for particle physics. *Phys.Rev.Lett.*, 102:181601, 2009.
- [43] JoAnne L. Hewett and Thomas G. Rizzo. Low-energy phenomenology of superstring-inspired E6 models. *Physics Reports*, 183:193 – 381, Nov 1989.
- [44] Paul Langacker, Mingxing Luo, and Alfred K. Mann. High-precision electroweak experiments: A global search for new physics beyond the standard model. *Rev. Mod. Phys.*, 64:87–192, Jan 1992.
- [45] M.J. Ramsey-Musolf. Low-energy parity violation and new physics. *Phys.Rev.*, C60:015501, 1999.

- [46] W. Buchmüller, R. Rühl, and D. Wyler. Leptoquarks in lepton-quark collisions. *Physics Letters B*, 191(4):442 – 448, 1987.
- [47] H. Abramowicz et al. Search for first-generation leptoquarks at HERA. 2012.
- [48] M.J. Ramsey-Musolf and S. Su. Low Energy Precision Test of Supersymmetry. *Phys.Rept.*, 456:1–88, 2008.
- [49] F. Abe et al. Limits on quark-lepton compositeness scales from dileptons produced in 1.8 TeV $p\bar{p}$ collisions. *Phys.Rev.Lett.*, 79:2198–2203, 1997.
- [50] D. Androic et al. First Determination of the Weak Charge of the Proton. *Phys. Rev. Lett.*, 111(14):141803, 2013.
- [51] Y.C.Chao et al. *J.Physics.:Conf.Ser.*, 299:012015, 2011.
- [52] J. Benesch J. Clark J. Hansknecht R. Kazimi D. Machie J. Grames, P. Adderley and M. Poelker. Two wien filter spin flipper. In *Proceedings of the 2011 Particle Accelerator Conference*, 2011.
- [53] G. Smith et al. Qweak Liquid Hydrogen Target:Preliminary Design and Safely Document. Qweak document: Qweak-1041-v2, Aug 2009.
- [54] W. Falk and L. Lee. Magnetic Verification of the G^0 Superconducting Magnet System. A contribution to the TRIUMF Annual Report 2002, G^0 document: G0-02-089, Dec 2002.
- [55] John Leckey. *The First Direct Measurement of the Weak Charge of the Proton*. PhD thesis, College of William and Mary, 2011.
- [56] Garfield. <http://garfield.web.cern.ch/garfield/>.

- [57] Istituto Nazionale di Fisica Nucleare Technical report. A prototype frontend ASIC for the readout of drift tubes of CMS barrel muon detector. <http://www.pd.infn.it/cms/DTFB/electronics/frontend/homepage.html>.
- [58] Katherine E. Myers. *The First Determination of the Proton's Weak Charge Through Parity-Violating Asymmetry Measurements in Elastic $e+p$ and $e+Al$ Scattering*. PhD thesis, George Washington University, 2012.
- [59] F.J. Barbosa, E. Jastrzembski, J. Proffitt, and J. Wilson. The Jefferson Lab high resolution TDC module. In *Nuclear Science Symposium Conference Record, 2002 IEEE*, volume 1, pages 135 – 139 vol.1, nov. 2002.
- [60] Struck Innovative Systeme. <http://www.struck.de/sis3801.htm>.
- [61] CODA. https://coda.jlab.org/wiki/index.php/Main_Page.
- [62] R. Carlini *et al.* The Qweak Experiment Jeopardy Proposal. Qweak document: Qweak-703-v5, Dec 2007.
- [63] Julien Bergoz and Bergoz. Current monitors for particle beams. *Nuclear Physics A*, 525(0):595 – 600, 1991.
- [64] J. Musson. BCM 5 and 6 Electronics. Qweak document: Qweak-1435-v1, Jun 2011.
- [65] D. Mack. BCM Normalization Issues Part II: Calibrations and Linearity. Qweak document: Qweak-1369-v1, Mar 2011.
- [66] D. Mack. Potential Effect of BPM Non-Linearity. Qweak document: Qweak-1493-v1, Oct 2011.
- [67] John Leacock. private communication, 2012.

- [68] A. Slaughter. Parity Violation in High-Energy Electron Scattering: Data Analysis for the G^0 Experiment. College of William and Mary Senior Honors Thesis, 2004. Undergraduate Thesis.
- [69] M. Hauger *et al.* *Nucl. Instrum. Methods Phys. Res., Sect.A*, 462:382, 2001. [arXiv:nuclex/9910013].
- [70] H.R. Band *et al.* *Nucl. Instrum. Methods Phys. Res., Sect.A*, 400:24, 1997.
- [71] M. Loppacher. https://hallcweb.jlab.org/polwiki/images/5/54/Loppacher_moeller_thesis.pdf. Qweak-PolWiki.
- [72] A. Narayan. A Diamond Micro-strip Electron Detector for Compton Polarimetry. Qweak document: Qweak-1526-v1, Oct 2011.
- [73] HERMES Collaboration K. Ackerstaff *et al.* *Nucl. Instr. and Methods.*, A417:230, 1998.
- [74] C/C++ Standard Template Library Programmer's Guide. <http://www.sgi.com/tech/stl/>.
- [75] Boost Library. <http://www.boost.org/>.
- [76] W. Deconick. <https://qweak.jlab.org/wiki/index.php/Geometry>.
- [77] J.H. Lee. F1TDC and its Multihit Histograms. Qweak document: Qweak-1604-v2, Feb 2012.
- [78] K.G. Fissum *et al.* Vertical drift chambers for the Hall A high-resolution spectrometers at Jefferson Lab. *Nuclear Instruments and Methods in Physics Research Section A: Accelerators, Spectrometers, Detectors and Associated Equipment*, 474(2):108 – 131, 2001.

- [79] Schulz H D and Stuckenberg H J. In *Proc. Topical Conf. on Application of Microprocessors in High Energy Physics Experiments*, volume 81-07. CERN, 1981.
- [80] Dell' Orso M and Ristori L. A highly parallel algorithm for track finding. *Nucl. Instrum. Methods A*, 287:436–438, 1990.
- [81] Battaiotto P *et al.* The tree-search processor for real-time track pattern recognition. *Nucl. Instrum. Methods A*, 287:431–435, 1990.
- [82] Philip R. Bevington. *Data Reduction and Error Analysis for the Physical Sciences*. New York: McGraw-Hill, 2002.
- [83] Jie Pan. Momentum determination in qtr. Technical Report, JLab, 2010.
- [84] Press W H *et al.* *Numerical Recipes in C: The Art of Scientific Computing*. Cambridge: Cambridge University Press, 1993.
- [85] C. Yan, R. Carlini, and D. Neuffer. Beam energy measurement using the Hall C beamline. Prepared for 1993 IEEE Particle Accelerator Conference (PAC 93), Washington, DC, 17-20 May 1993.
- [86] V. Gray. Beam position and angle scans in GEANT4. Analysis & Simulation. ELOG 877, Feb 2013.
- [87] Jie Pan. Light/ Q^2 distributions per octant from tracking data and a comparison of two light-weighting methods. Tracking, Oct 2012.
- [88] Jie Pan. Simulated Q^2 and light distributions. Tracking, Oct 2012.
- [89] Jie Pan. *Towards a Precision Measurement of Parity-Violating e-p Elastic Scattering at Low Momentum Transfer*. PhD thesis, University of Manitoba, 2012.

- [90] D. Armstrong. personal communication, 2016.
- [91] R. Beminiwattha. Qweak Event Cut Framework. Qweak document: Qweak-1682-v1, Jun 2012.
- [92] D. Gaskell and J. Magee *et al.* Wien-0 polarization. Møller. ELOG 97, Apr 2012.
- [93] Josh Hoskins. *Determination of the Proton's Weak Charge via Parity Violating Electron Scattering*. PhD thesis, College of William and Mary, 2014.
- [94] T.W. Donnelly, M.J. Musolf, W.M. Alberico, M.B. Barbaro, A. De Pace, and A. Molinari. Parity-violating quasielastic electron scattering. *Nuclear Physics A*, 541(4):525 – 577, 1992.
- [95] J. Magee. Corrected 25% Aluminum Dilution. Analysis & Simulation. ELOG 744, Sep 2012.
- [96] H.W. Hammer and D. Drechsel. Parity violating pion electroproduction off the nucleon. *Z.Phys.*, A353:321–331, 1995.
- [97] John D. Leacock. *Measuring the Weak Charge of the Proton and the Hadronic Parity Violation of the $N \rightarrow \Delta$ Transition*. PhD thesis, Virginia Tech, 2012.
- [98] R. Beminiwattha. Neutral Background. Qweak document: Qweak-1549-v2, July 2012.
- [99] B. Pasquini and M. Vanderhaeghen. Resonance estimates for single spin asymmetries in elastic electron-nucleon scattering. *Phys.Rev.*, C70:045206, 2004.

- [100] B. Waidyawansa. Preliminary Beam Normal Single Asymmetry Results from the Qweak Experiment. Qweak document: Qweak-1601-v7, Jun 2012.
- [101] B. Waidyawansa. Transverse uncertainty for 25% Qweak. Analysis & Simulation. ELOG 758, Oct 2012.